Coventry University

DOCTOR OF PHILOSOPHY

Selective electroless copper deposition by applying a gradient magnetic field

Danilova, Sofya

Award date:
2020

Awarding institution:
Coventry University

Selective electroless copper deposition by applying a gradient magnetic field

by

Sofya Danilova

December 2019

Coventry
University

A thesis submitted in partial fulfilment of the University's requirements for the Degree of Doctor of Philosophy

Content removed on data protection grounds

Certificate of Ethical Approval

Applicant:

Sofya Danilova

Project Title:

A fundamental study into novel methods to selectivity metallise materials using a magnetic field to enable more sustainable processing in high value manufacturing sectors (reviewed)

This is to certify that the above named applicant has completed the Coventry University Ethical Approval process and their project has been confirmed and approved as Medium Risk

Date of approval:

15 November 2019

Project Reference Number:

P95804

Abstract

Selective metallisation of non-conductive materials is a manufacturing process which is often used in the electronics industry to create printed circuit boards, radio-frequency identification tags, solar panels and other devices. Selective metallisation is often achieved by a combination of blanket metal deposition and photolithography processes. However, photolithography is an expensive and time-consuming process which generates hazardous waste. A range of methods of selective metal deposition are currently being developed in order to replace the photolithography process.

In the present work, a novel approach of selective electroless copper deposition was investigated. Electroless deposition of copper onto non-conductive material requires prior catalyst deposition. The concept of this research was to apply a gradient magnetic field during catalyst deposition and attract the catalyst exclusively to areas of maximum magnetic field strength, meaning subsequent electroless plating should also occur only at these areas. This approach requires the catalyst for electroless plating to be magnetic. Therefore, this research project focussed on the following areas:

- Synthesis of magnetic catalyst Fe_3O_4-Ag composite nanoparticles by a range of procedures and characterisation of their size, composition, crystal structure, magnetic properties and catalytic activity;
- The fabrication of the magnetic template and simulation of the magnetic field distribution across the substrate surface;
- Deposition of the magnetic catalyst onto the non-conductive substrate via gradient magnetic field application and characterisation of the catalyst in solution and on the substrate surface after deposition;
- Selective electroless copper plating onto the surface of the non-conductive substrates that were selectively catalysed by the novel magnetic catalyst and characterisation of the coatings.

Selectively deposited copper lines with a width of 400 µm were obtained using this novel approach of selective metallisation. This research project proves that selective electroless copper deposition can be achieved by gradient magnetic field application.

Acknowledgements

First of all I am very thankful to Prof. Andrew Cobley, my Director of Study. He gave me the opportunity to conduct this research and supported me throughout the whole journey with his knowledge, experience and optimism. Thank you for encouraging me and believing in me, this work would not be possible without your guidance and support.

I would like to thank Dr. John Graves, my second supervisor, who shared his knowledge and experience with me and supported this research all the way through. I am also very grateful to Dr. Alex Pedchenko for giving me a greater understanding of the theory of magnetism.

I am very grateful to the Future Transport and Cities Research Institute and especially to Director Dr. Carl Perrin for funding my PhD and conference attendance. I want to thank other staff at Coventry University for their support, including: Nick Turner, Camelia Dijkstra, Niall Smyth, Steve Alitt, Steve Damms, Collin Thorneycroft, Simon Stenhause, Luke Stirrup, Luke Trodden, Alan Greenwood, Daniel Dugdale, Raluca Barza and the whole Functional Materials group.

I would like to acknowledge the help of COST eMINDs which organised multiple training courses and gave me the opportunity to do parts of my research at the Autonomous University of Barcelona. I want to thank Dr. Eva Pellicer and Prof. Jordi Sort for accommodating me during these visits and supporting my research. I am very grateful to the staff and students of Nottingham Trent University especially Dr. Gareth Cave and his group, who helped me with nanoparticle synthesis and analysis.

Finally, I want to thank my family for their unfailing support throughout the whole of my journey through education, from school to completing my PhD. I would never be here without you. Most importantly I want to thank my beloved husband. Thank you for believing in me and proof reading my work all the way through.

There are many more individuals who have helped me through this journey and I will be always grateful to all of you.

Publications

The following publications were produced from the present research:

Patent:

- A. J. Cobley, S. Danilova, Material deposition in a magnetic field, International Publication Number WO 2017/118853 A2, 2017, World Intellectual Property Organisation.

Publications:

- S. Danilova, J. E. Graves, A. J. Cobley, Magnetic Field Enabled Selective Metallisation of Dielectric Substrates, The Journal of the Institute of Circuit Technology, 11(1), 12-16, 2018.
- S. Danilova, J. E. Graves, A. J. Cobley, Selective electroless metallization of non-conductive substrates enabled by a Fe_3O_4/Ag catalyst and a gradient magnetic field, Materials Letters, 219, 170-173, 2018.
- S. Danilova, J. E. Graves, E. Pellicer, J. Sort, A. J. Cobley, Selective Metallization of Non-Conductive Materials by Patterning of Catalytic Particles and the Application of a Gradient Magnetic Field, ECS Transactions, 85(4), 69-78, 2018.

In preparation:

- S. Danilova, J. E. Graves, G. V. W. Cave, J. Sort, E. Pellicer, A. J. Cobley, Selective electroless plating on non-conductive materials by applying a gradient magnetic field, SPIE Conference Proceedings.

List of Figures

List of Tables

List of abbreviations

CV – cyclic voltammetry

DLS – dynamic light scattering

EDTA - ethylenediaminetetraacetic acid

EDX – energy dispersive X-ray diffractometry

FEMM - finite element method magnetics

HRTEM – high resolution transmission electron microscopy

ICP – inductively coupled plasma

MHD – magnetohydrodynamic

PCB – printed circuit board

PEEK - polyether ether ketone

RO – reverse osmosis

SDR – spinning disc reactor

SE2 – secondary electrons

TEM – transmission electron microscopy

VSM – vibrating sample magnetometry

XRD – X-ray diffractometry

Table of content

Introduction

Electroless plating is a process of metal deposition from an aqueous-based solution. Electroless plating is often used to metallise non-conductive materials like plastic, glass, ceramics, and fabric. Prior to electroless plating, the surfaces of non-conductive materials need to be activated by a catalyst. The most commonly used catalyst is a colloid consisting of palladium and tin (Pd/Sn).

The metal deposited in the electroless plating process usually covers all of the exposed surfaces of the immersed substrate. However, for some applications selective metallisation is required (Figure 1) [1,2]. For example, in the electronics industry, selective Cu metallisation is used in order to obtain conductive tracks or interconnects in large-scale integrated circuits, printed circuit boards, photovoltaics, and antennas (Wi-Fi and near-field communication).

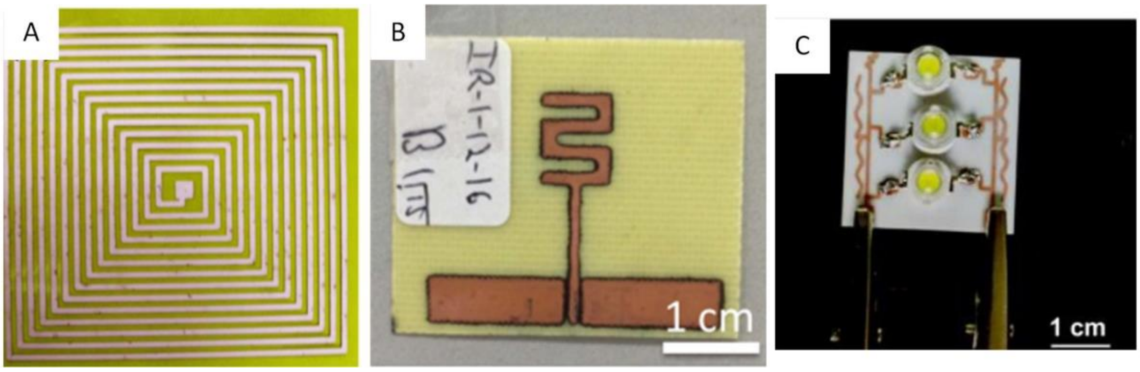

Figure 1. Examples of selective electroless plating used for the following applications: A – a near field antenna [3], B – a Wi-Fi antenna [4], C – high-powered light emitting diodes connected by copper tracks [5].

Often the photolithography process is used in order to obtain selective metallisation [6,7]. In this process the photoresist is deposited onto the substrate (Figure 2, A). The photoresist consists of resin, a photoactive compound and a solvent. After deposition onto the substrate, the resist is baked in order to remove the solvent. Subsequently, the resist is exposed through the photomask by UV-light (Figure 2, B). The photomask consists of transparent and opaque regions. The light only goes through transparent regions and the part of the photoresist being exposed. Depending on the type of resist –positive or negative – the part of the photoresist exposed to light will become more or less soluble, respectively. After this the soluble part of the photoresist can be removed by the developer (Figure 2, C). After this stage, depending on the manufacturing process the metal can be deposited onto the substrate or if metal was deposited prior to photolithography it can be etched (Figure 2, D). The photoresist can then be completely removed by the solvent (Figure 2, E). If the metal was deposited on top of the photoresist, removal of photoresist will also cause the metal to be removed. If the etching of metal was used, only metal under photoresist will remain on the substrate and selective metallisation has been achieved.

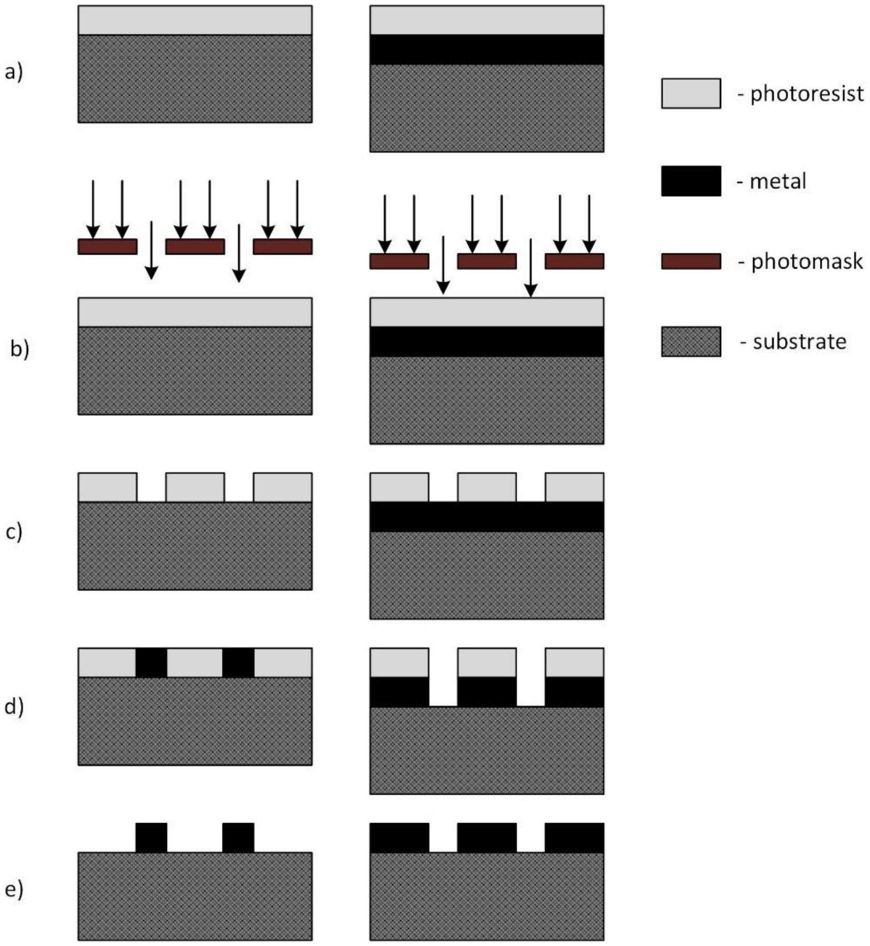

Figure 2. Schematic presentation of the steps of the photolithography process. A – positive photoresist deposition onto the bare substrate (left) and onto the pre-deposited metal (right) , B – exposure of the photoresist by light through the photomask, C – developing of the pattern, D – deposition of metal (left) and etching of metal (right), E – stripping the photoresist.

The main disadvantage of this approach is the cost – 30% of the device manufacturing cost is due to photolithography [8]. In addition, the process produces a large amount of organic and inorganic waste. Currently a variety of alternative processes are being developed in order to replace the photolithography process. These methods usually involve patterning of catalyst deposition so that the subsequent electroless copper plating occurs only at the areas where the catalyst was deposited. The most studied processes are:

- Laser-assisted patterning [9–12]. In this approach the substrate surface is selectively excited by a laser (Figure 3, A). There are a range of modifications of this method. For example, the catalyst solution can be spin-coated onto the substrate first. Then, the required parts are annealed by a laser and the rest of the catalyst is removed. However this approach still requires the use of expensive equipment for generation of the laser beam.
- Ink-jet printing [13–16]. The catalyst ink is printed on the surface in the required pattern (Figure 3, B). The main challenges in this technology are to create an ink viscous enough to maintain its shape on the substrate after printing and at the same time be fluid enough to be extracted from the printer nozzle. This leads to the limitation that small element sizes cannot be achieved by this method. Often, annealing of conductive ink is required prior to electroless plating. This is conducted at elevated temperatures which restricts the choice of materials to those which are resistant to these high temperatures. Also this technique requires individual printing of each line, so the pattern is obtained line-by-line and not simultaneously. This restricts high-volume selective metallisation production.
- Contact printing [17,18]. Some templates e.g. polydimethylsiloxane (PDMS) are made in a required pattern. Then the catalyst solution is deposited on the template (for example by dip-coating) and after, the template is placed on the substrate surface to transfer the catalyst (Figure 3, C). The main disadvantage of this technique is the contact of the template with the surface of the substrate, which can often lead to surface contamination.

All of the described methods have certain limitations and would not be able to replace photolithography entirely. That is why the photolithography process still dominates in the fabrication of selectively metallised nonconductive materials.

In the present research, a unique alternative method of selective electroless copper plating of non-conductive material was investigated. The idea of the research was to apply a gradient magnetic field behind the non-conductive substrate during catalyst deposition and electroless metal deposition. The catalyst is attracted by the magnet and will deposit at the regions of maximum magnetic field influence. Subsequent electroless Cu plating appears in a pattern that precisely follows that of the magnetic field.

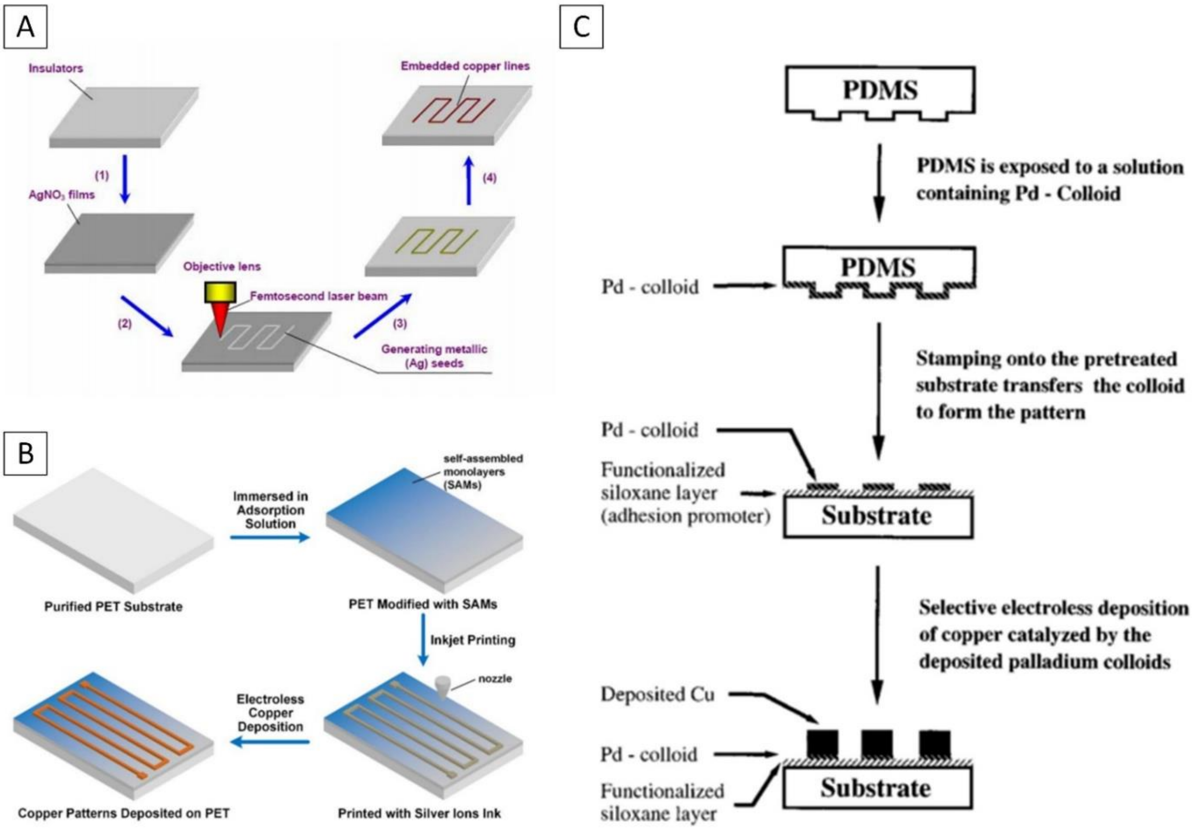

Figure 3. Schematic representation of the working principle of methods of selective metallisation A – laser-assisted [10], B – ink-jet printing [16], C – contact printing [19].

There are no previously published works describing similar research, therefore the goal of this study was to investigate whether the described process is even possible. The electroless copper (Cu) plating process was investigated because it is widely used in the electronics industry and because Cu is not magnetic, so the process of metal film formation should not be influenced by the magnetic field. For example, another commonly used electroless plating process uses Ni-P, which contains Ni that is a ferromagnetic metal and would thus not be amenable to the current method. Electroless Cu is often deposited on epoxy laminate for printed circuit board (PCB) manufacturing and therefore a typical PCB epoxy laminate was used as a non-conductive substrate. The most commonly used Pd/Sn catalyst is not magnetic and therefore modifications of the catalyst were required in order to make it attracted to the magnetic field.

Therefore the aim and objectives of this research are the following:

Aim: investigate whether electroless copper plating can be selectively deposited on non-conductive material by applying a gradient magnetic field.

Objectives:

- Synthesise a catalyst for the electroless copper plating process which can also be attracted by a magnetic field;
- Research how the magnetic field gradient can be created and applied during catalyst deposition and electroless copper plating;
- Selectively deposit the catalyst onto the non-conductive substrate by applying a gradient magnetic field in a pre-determined pattern;
- Deposit copper onto the selectively catalysed non-conductive substrate by the electroless plating process and analyse the obtained deposit (if a coating is achieved)

The following thesis consists of eight chapters. The first chapter is the literature review, which presents an overview of the literature on the theory of electroless plating and its initialisation, basics of magnetic fields and approaches to patterning and methods of nanoparticles synthesis. The second chapter of the thesis is the methodology, which describes the methods used in the following experiments. The third chapter describes preliminary study experiments, where the magnetic field was applied during the standard electroless plating procedure. The fourth chapter covers experiments on synthesis of magnetic catalyst nanoparticles. In the fifth chapter the magnetic nanoparticles were used as a catalyst for selective electroless plating and were deposited using a single permanent magnet. In the sixth chapter, the magnetic field distribution across the substrate was simulated and simulation of the template which allowed patterning of the magnetic field was attempted. The seventh chapter shows the final experiments in which selective electroless plating was performed using the template developed in chapter six and the magnetic catalyst nanoparticles which produced the best results in chapter five. The eighth and final chapter includes conclusions from the work and future work suggestions. The work also contains two appendices – the first is the ethics application for the project and the second is the peer-reviewed paper published from the present work.

Chapter 1. Literature review

Part 1. Electroless plating

1.1.1 Overview of the electroless deposition process

The electroless plating process involves the deposition of metal from aqueous solution without application of an external electric power source. Non-conductive materials can be metallised by this process, unlike electrodeposition which can only deposit metal onto conductive surfaces. Prior to electroless plating, the catalyst needs to be deposited onto the substrate. Then, metal ions are reduced on the catalysed substrate surface to form a deposited layer. The Cu metal itself then becomes a catalyst for further deposition, which allows for the formation of layers with different thicknesses. Often, immersion plating is mistakenly referred to as electroless deposition. The difference is that in immersion plating, the more noble metal replaces the atoms of another metal from the substrate surface and no reducing agent is employed. The process cannot be performed on non-conductive materials and the subsequent coating is relatively thin with a weaker adhesion to the substrate compared to electroless plating [6]. Further comparison of electroless, electrodeposition and immersion plating is presented in Table 1.

Table 1. Comparison of electroless plating, electrodeposition and immersion plating.

The compared characteristics	Electroless plating	Electrodeposition	Immersion plating
Typically obtained thickness of the deposited layer	Below 50 µm [20] (below 5 µm for electroless Cu)	Up to 1 mm	Below 1 µm [6]
Driving force	Chemical/ electrochemical reaction of metal ion with reducing agent	Electric current	Displacement reaction
Type of substrates	Conductive and nonconductive	Conductive	Metallic substrate with a less noble metal than the desired metal coating
The uniformity of the coating	Uniform	Not uniform	Uniform

1.1.2 Bath composition

Electroless deposition is used to obtain films of Ni, Cu, Co, Ag, Pd, and Pt [2], as well as their alloys. The most studied and commonly-used deposition systems are electroless Cu, Ni-P and Ni-B deposition. The main components of the electroless plating bath are:

1) Source of metal ion. Salts of the required metal are used: acetate, chloride and sulfate.
2) Reducing agent. This reduces the metal ion. The choice of reducing agent depends on the required rate of deposition, ability to reduce metal on the catalytic surface and desire to obtain the alloy material. For example, in order to obtain a Ni-B layer, sodium borohydrate is used, while for a Ni-P layer sodium hypophosphite is required.
3) Complexing agent. This prevents metal precipitation which allows operation at a higher pH, at which some electroless plated metals are deposited (e.g. electroless copper). It helps to avoid bath decomposition if dust is present and slows the rate of reaction to make it more practical [21]
4) An adjuster of pH. During the electroless plating reaction H^+ and OH^- ions are either formed or consumed so the pH of the solution changes during the reaction. The electroless deposition process occurs without external electric power, so the pH should be adjusted to make the reaction thermodynamically favourable.
5) Source of energy. In order to make the reaction possible, energy should be passed to the reagents. For electroless plating, heat is the source of energy. With an increase of the temperature the reaction rate increases.

1.1.3 Electroless Cu plating

Most of the electroless Cu plating baths which are used commercially and were investigated by research use formaldehyde as a reducing agent and ethylenediaminetetraacetic acid (EDTA) as a complexing agent. Alternatives have included dimethylamine borane, hypophosphite and glycolic acid as reducing agents and malic acid, succinic acid, tartrate, citrate, triethanolamine and ethylenediamine as complexing agents [22]. Baths which contain formaldehyde and EDTA operate at a basic pH and elevated temperature. The overall electroless Cu plating reaction is [23]:

$$Cu(EDTA)^{2-} + 2HCHO + 4OH^- \rightarrow Cu^0 + H_2 + 2H_2O + 2HCOO^- + EDTA^{4-} \qquad (1)$$

Often the electroless plating process is described in terms of the mixed potential theory [6,24–26]. According to this theory, two simultaneous independent processes occur on the catalyst surface – cathodic and anodic reactions. In the case of electroless plating, the cathodic reaction is a metal (Cu) reduction [26]:

$$Cu(EDTA)^{2-} + 2e^- \rightarrow Cu^0 + EDTA^{4-} \tag{2}$$

The anodic reaction is reducing agent (formaldehyde) oxidation [26]:

$$2HCHO + 4OH^- \rightarrow 2HCOO^- + H_2 + 2H_2O + 2e^- \tag{3}$$

The potential at which anodic (I_R) and cathodic (I_M) currents are equal is an equilibrium potential. The equilibrium potential (E_{MP}) or mixed potential is between cathodic (E_m^0) and anodic (E_R^0) equilibrium potentials (Figure 4, A). Often mixed potentials are described by Evan's diagrams, where they lie on the intersection of the cathodic and anodic process branches (Figure 4, B).

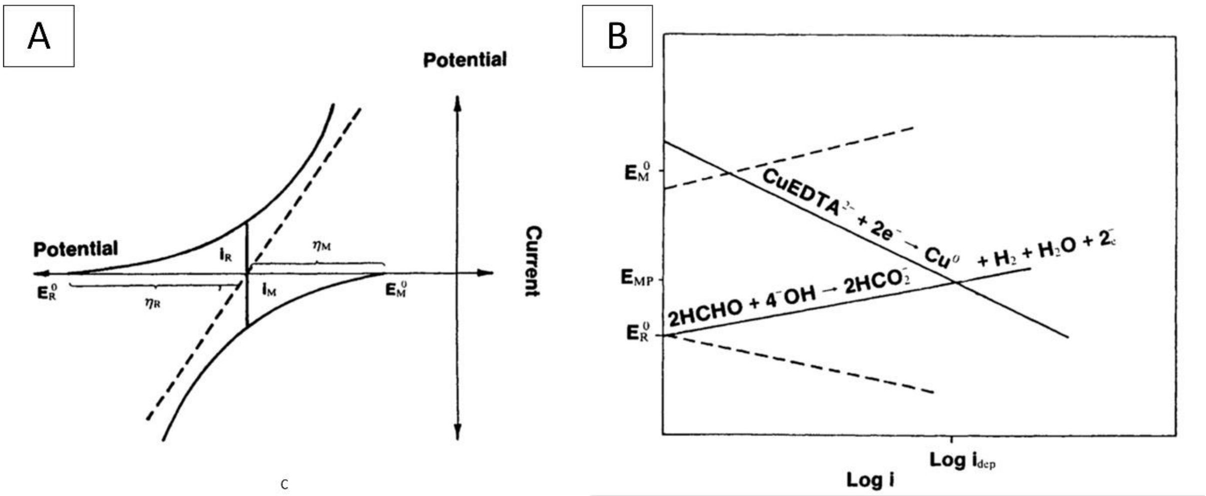

Figure 4. A - Current-potential curves of the cathodic and anodic reactions of the electroless Cu plating process, b – Evan's diagram of the electroless Cu plating process [6].

The original mixed potential theory claims that the anodic and cathodic reactions are independent, however, further works [6,24,27,28] showed that both reactions are interconnected in the electroless Cu plating process.

The anodic reaction (formaldehyde oxidation) provides electrons for the cathodic reaction (Cu reduction), so the kinetics of the process of electroless plating are controlled by the kinetics of formaldehyde oxidation [6], while the cathodic reaction activates formaldehyde reduction in the steady state [27,29]. The approach of viewing electroless plating as consisting of two independent reactions is still used, for example in investigations of catalytic activity of the metals for formaldehyde oxidation, where only the anodic reaction is studied.

1.1.4 Cathodic reaction mechanism – Cu reduction

Although the mechanism of the reaction of Cu reduction is commonly agreed upon, some aspects of this mechanism are still unclear. The main question is from which form Cu ions are reduced: complexed (CuEDTA) or ionic (Cu^{2+}). Some work suggests Cu reduction from the complexed form [22]:

$$Cu(EDTA)^{2-} \rightarrow Cu(EDTA)^{2-}_{ads} \tag{4}$$

$$Cu(EDTA)^{2-}_{ads} + e^{-} \rightarrow Cu(EDTA)^{3-}_{ads} \tag{5}$$

$$Cu(EDTA)^{3-}_{ads} + e^{-} \rightarrow Cu(EDTA)^{4-}_{ads} \tag{6}$$

$$Cu(EDTA)^{4-}_{ads} \rightarrow Cu^{0} + EDTA^{4-} \tag{7}$$

Bindra suggests that Cu(EDTA) dissociates prior to reduction, though it is unclear whether it dissociates into a bulk solution first and then adsorbs onto the catalyst surface or a process of dissociation occurs after adsorption [24].

Paunovic [30] suggests that Cu exists in the solution in both complexed and non-complexed forms. Therefore the reaction of Cu reduction from its ions is:

$$Cu^{2+} + e^{-} \rightarrow Cu^{+} \tag{8}$$

$$Cu^{+} + e^{-} \rightarrow Cu^{0} \tag{9}$$

If the Cu is complexed, it dissociates prior to reduction:

$$Cu(EDTA)^{2-} + 2e^{-} \rightarrow Cu^{2+} + EDTA^{4-} \tag{10}$$

$$Cu^{2+} + 2e^{-} \rightarrow Cu^{0} \tag{11}$$

Bath decomposition (uncontrollable Cu reduction) is usually associated with the presence of Cu^{2+} ions [6,31], meaning their concentration in solution should be controlled.

According to Shacham-Diamand [22], decomposition happens by the following mechanism:

$$2Cu^{2+} + HCHO + 5OH^{-} \rightarrow Cu_2O + 3H_2O + HCOO^{-} \tag{12}$$

The initiation of this reaction does not require the catalyst and therefore the reaction can happen spontaneously and the Cu_2O will be formed in the bulk solution.

1.1.5 Anodic reaction mechanism – formaldehyde oxidation

The formaldehyde oxidation reaction is the rate determining step of the electroless plating process [32]. The reaction of formaldehyde oxidation is activation controlled [32,33] and depends on the nature of the catalyst metal. Firstly, hydrogen evolution only happens on the surface of certain metals like Cu, Ag and Au, but there is no gas formed when the reaction happens on the Pt or Pd surface due to the hydrogen adsorption onto their surfaces [32]. This indicates that the reaction proceeds differently. Also, the shape of the polarization curves of formaldehyde oxidation are dependent on the nature of the catalyst metal [29]. Both factors indicate that different mechanisms of formaldehyde oxidation are possible.

It is in agreement that the following reactions of formaldehyde oxidation occur on Cu, Ag and Au surfaces [21]:

$$2HCHO + 4OH^- \rightarrow 2HCOO^- + H_2 + 2H_2O + 2e^- \qquad (13)$$

And on Pt and Pd surfaces [26]:

$$HCHO + 3OH^- \rightarrow HCOO^- + 2H_2O + 2e^- \qquad (14)$$

Potential catalyst metals for formaldehyde oxidation such as Ni, Re and Cd are oxidised at the high pH values that electroless Cu baths operate and cannot be used as catalysts for the reaction [29].

It was proposed that oxidation of formaldehyde can occur by both mechanisms simultaneously, but on different metals in which case one mechanism will be preferential to the other [26].

The hydrogen atoms released during the reaction can recombine or be oxidised [26]:

$$\dot{H_{ad}} + OH^- \rightarrow H_2O + e^- \qquad (15)$$

$$\dot{H_{ad}} + \dot{H_{ad}} \rightarrow H_2 \uparrow \qquad (16)$$

1.1.6 Kinetics

The kinetics of electroless plating are often described by the following equation [6,23]:

$$r = k[Cu^{2+}]^a[OH^-]^b[HCHO]^c[EDTA]^d \qquad (17)$$

Where r –the rate of Cu deposition, k – experimentally determined rate constant, a – d – the reaction orders of the respective reagents.

There are no consistent data on the rate of the reaction, as the experiments were performed in different conditions and different rates of reactions were observed [6].

Another description of the reaction kinetics involves an Arrhenius type equation, which claims that the rate of deposition depends only on the concentration of methylene glycol anions and none of the other reagents[34]

$$r = Aexp\left(-\frac{\Delta E}{RT}\right)[CH_2(OH)_2] \tag{18}$$

Also, many research groups observed an induction time [30,31,35,36] prior to the beginning of the actual deposition. Dumesic et al explained this as the reduction of the oxide formed on the catalyst surface prior to use [31], Kuznetsov et al associate it with formaldehyde adsorption onto the catalyst surface [35]. Another possible reason is that the system needs to reach the mixed potential before plating can start which depends on bath pH and ligand nature [30].

The plating rate is faster at the start of the deposition process when the deposition is catalysed by catalyst and at the later stage when the catalyst is completely covered by deposited Cu which starts to autocatalyse subsequent deposition. This happens due to different mechanisms of formaldehyde oxidation taking place on different metals as discussed earlier [31].

The overall kinetics of electroless copper plating are affected by the following factors:

- The nature of the catalyst – it influences formaldehyde oxidation;
- Time – the rate of the reaction is not uniform and slows down with time first due to the change in the autocatalytic reaction and then due to the decrease in the concentration of reactants;
- Mass transport – this effect is only significant when the deposition rates are high, the stirring is low and the concentration of Cu ions is low [31], because only the reaction of Cu reduction is limited by diffusion [31–33]. Mass transport does not affect formaldehyde oxidation or hydroxide ion supply due to the excess formaldehyde and mobility of hydroxide ions [31].
- Composition of the bath and deposition conditions; the pH (Figure 5, A), temperature (Figure 5, B), choice of reducing agent, metal and ligand all affect the thermodynamic conditions of the system and therefore the kinetics of the reaction. The pH and temperature are usually optimised depending on the bath composition. Examples of optimisation are presented in Figure 5.

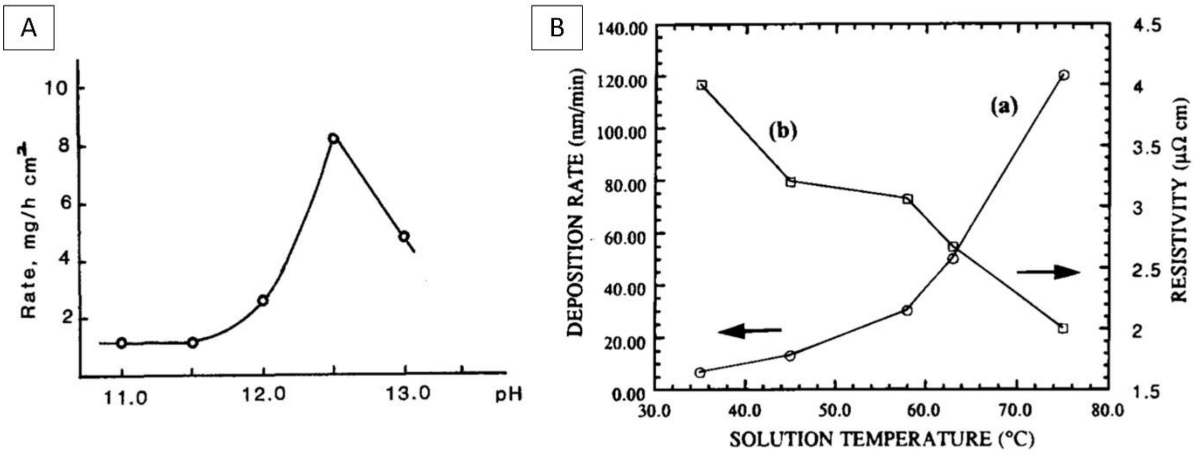

Figure 5. Examples of dependence of the rate of electroless copper deposition on A – pH of the solution [21], B - temperature of the solution [23].

1.1.7 Thermodynamics

The chemical reaction is spontaneous when the Gibbs energy is negative [37].

$$\Delta G^{o} < 0, \tag{19}$$

$$\Delta G^{o} = -zFE^{o} \tag{20}$$

$$E^{0} = E_{c} - E_{a} \tag{21}$$

where ΔG^o – Gibbs energy, z – number of electrons, F – Faraday constant, E^o – standard cell potential, E_c - standard potential of cathodic reaction, E_a – standard potential of anodic reaction.

Table 2. Standard potentials of formaldehyde oxidation and Cu reduction reactions [22].

Reaction	E° vs SHE (V)
$2HCHO + 4OH^{-} \rightarrow 2HCOO^{-} + H_2 + 2H_2O + 2e^{-}$	0.32 (pH 12)
$Cu(EDTA)^{2-} + 2e^{-} \rightarrow Cu^{0} + EDTA^{4-}$	-0.216

The reaction of Cu reduction is spontaneous [37]. However, this also means that Cu reduction can occur in the bulk solution. Therefore, complexing agents (e.g. EDTA) are used in order to decrease the Cu reduction potential and increase the Gibbs energy (Table 2), preventing spontaneous Cu deposition.

The potential of the reaction depends on the pH of the solution. This interaction is usually described by Pourbaix diagrams. For reactions of Cu reduction and formaldehyde oxidation the potentials are lower at basic pH (Figure 6) so the thermodynamic driving forces are higher.

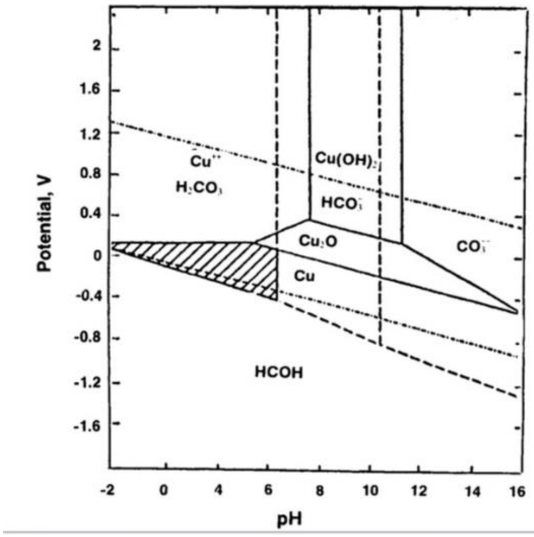

Figure 6. Combined Pourbaix diagram of carbon-water and copper-water systems [6].

The process of reductant oxidation is accompanied by the consumption of OH^- which changes the pH of the solution.

In order to control the deposition, stabilizers and complexing agents are used. In addition, the concentration of the reducing agent and the temperature should be controlled in order to avoid spontaneous reactions.

1.1.8 Catalysts for formaldehyde oxidation

The catalyst for the electroless plating process influences the rate determining step – formaldehyde oxidation. The catalyst influences the mechanism of the reaction, its kinetics as well as the hydrogen evolution process. The most investigated metals to catalyse formaldehyde oxidation are from groups 10 (Ni, Pd, Pt) and 11 (Cu, Ag, Au) of the periodic table [29,32,38–40]. Their alloys and composite nanoparticles can also be used [6]. In order to compare catalyst performance the following approaches were used.

1) Observed copper deposit

The simplest approach is to perform electroless Cu plating using the investigated catalyst. The performance of the catalyst is then judged by the presence of the deposited Cu film. The more quantitative version of the method is to measure the quantity of the deposited Cu (Figure 7). This can be done by measuring the weight of the substrate before and after deposition [41], or by measuring the amount of deposited Cu by atomic adsorption spectrometry [42,43], inductively coupled plasma analyses [44] or quartz crystal microbalance [45,46]. The higher the weight gained per cm^2 the higher the activity of the catalyst. The rate of deposition can then be calculated from the data.

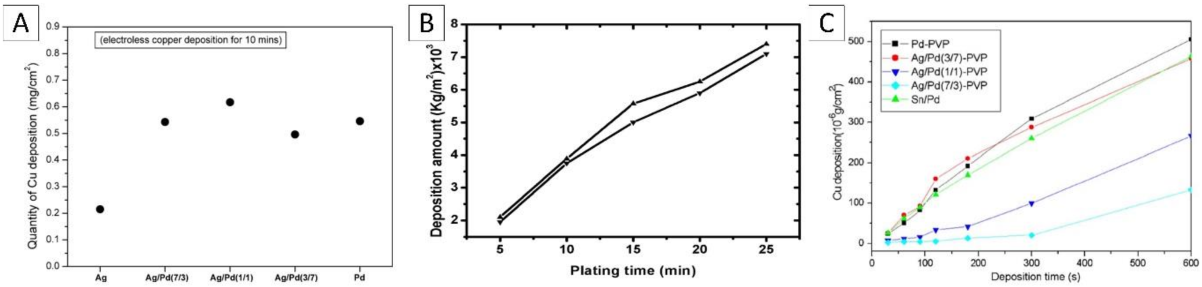

Figure 7. The quantity of deposited copper obtained by using novel catalysts A – Ag, Pd and its mix [43], B – Ag [41], C - Ag, Pd and its mix [45].

2) Electrochemical characterisation of the formaldehyde oxidation process

The performance of the catalyst can also be characterised by a range of electrochemical techniques. The most often used techniques are linear sweep voltammetry (Figure 8, A, B) [26,29,47] and cyclic voltammetry (CV) [26,32,40,48] (Figure 8, C, D). Both techniques are performed using a three-electrode system which includes a counter electrode (usually Pt), working electrode (the investigated electrode) and reference electrode. The measurements are usually conducted in a formaldehyde solution at basic pH to mimic the conditions of the electroless plating bath in the absence of the Cu either in stabilized or ionic form. Sometimes additives are also added. A potential is applied in a certain range and the current density is measured. In the case of CV, after reaching the end of the set potential, the recording continues in the reverse direction.

If the metal is active toward formaldehyde oxidation the current will increase at the anodic part of the measurement. At Figure 8, C the background current is also shown – the measurement was performed in a sodium hydroxide solution without formaldehyde, which means that the current rise was associated with formaldehyde oxidation only.

A higher current density does not necessarily indicate higher catalytic activity. Therefore further analysis of obtained data is required. Ohno [29] plotted the potentials for each metal at constant current density and claimed that the metals with the lowest potentials are better catalysts than those with higher potentials (Figure 9, A). He also plotted activation energy against the obtained potentials though for formaldehyde oxidation no linear correlation between the two values was found (Figure 9, C).

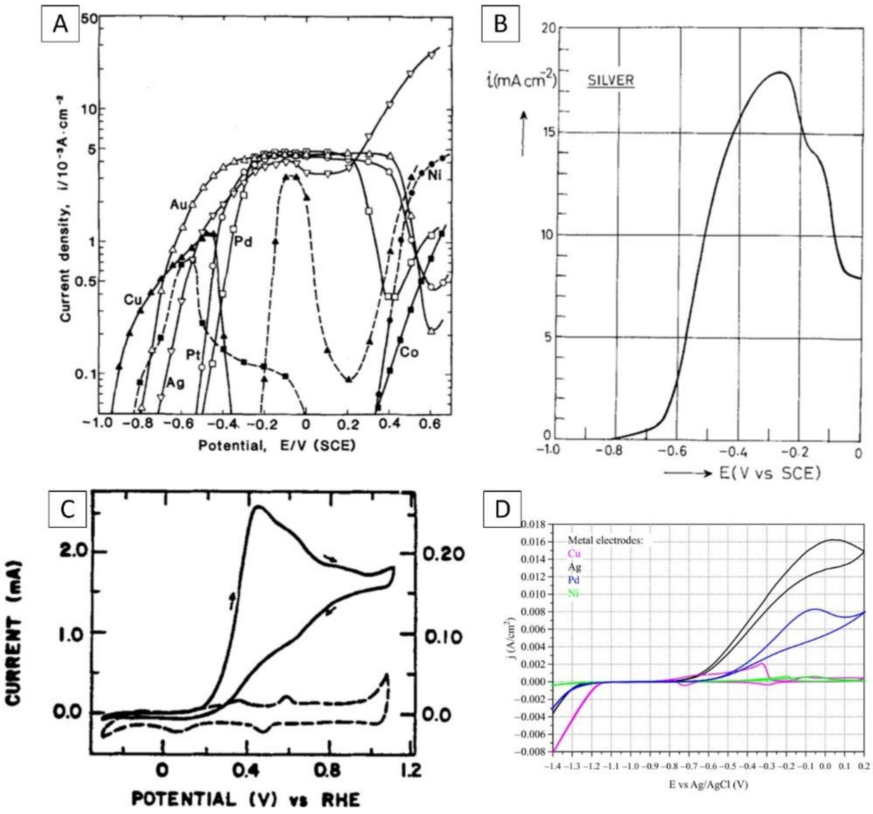

Figure 8. The results of linear sweep voltammetry (A, B) and CV (C, D) experiments on formaldehyde oxidation which were performed in the solutions: A – 0.1 M formaldehyde, 0.175 M Na_2EDTA, pH 12.5, 25 °C [29], B – 0.1 M formaldehyde, 0.15M NaOH, 25 °C [26], C – 0.1 M formaldehyde, 1 M NaOH, 25 °C [32], D – 0.3 M formaldehyde, pH 13 [40].

First Capon and Parson [38] and later Bindra [32] plotted the relative catalytic activity (the ratio of height of cathodic peak to the average current of the anodic part of the measurement) against the metal formate heat formation (Figure 9, B). The catalysts at the "top" of the volcano are theorised to have the best performance, though it is a more qualitative than quantitative method. In addition, Cu, which is positioned at the "bottom" of the volcano plot is active toward formaldehyde oxidation as the process becomes autocatalytic after initiation.

Other methods which were used to evaluate catalytic activities were Tafel plots [46,49]– similar to the CV and linear sweep voltammetry the current density was compared to evaluated activity. Some measured the change of the current [50] and the change of potential [30,35] in the studied solution over time. Through change of potential the period before plating started can be accounted for, which indicated the time required for each catalyst to start the catalysation process. However, the measurement should start straight after the electrode has contact with the solution, because the surface changes start immediately and affect the measured potential.

The measurements of current were compared on the assumption that higher current density means more efficient catalytic activity.

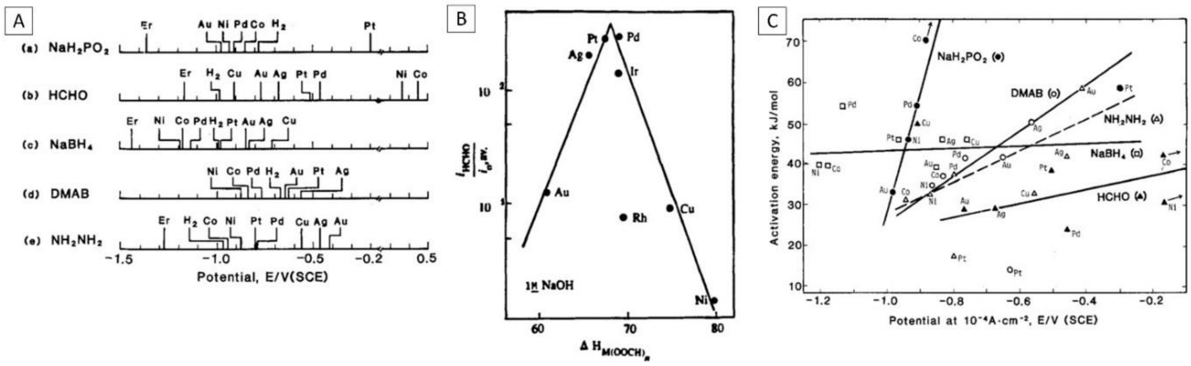

Figure 9. The methods of the catalytic activity investigations A, C from the work [29], B from [32]. A – The comparison of potential of investigated catalysts at the constant current density value for the various reducing agents, B – the comparison of the oxidation current vs enthalpy of formates of catalyst metals; C – comparison of activation energies vs potentials at the constant current value for the various reducing agents.

Therefore, a range of electrochemical measurements can be used to evaluate the catalytic activity of the materials, however there is no accepted interpretation that can quantitatively indicate whether one metal is more catalytic than another. The data can be interpreted by several approaches and should be viewed in conjunction with the results of actual Cu plating: using the measured amount of deposit and the presence of deposited copper.

1.1.9 Catalyst formulation

The most commonly used catalyst is Pd/Sn [6,51,52]. Typically the catalyst consists of Pd nanoparticle coordinated by Sn ions. Sn ions stabilize the colloid or solution by electrostatic interactions. When the substrate is immersed in the Pd/Sn dispersion the catalyst deposits uniformly on the substrate surface.

Regardless of the effectiveness of the Pd/Sn formulation, alternative catalysts are still being investigated. Pd/Sn sometimes does not have high stability and can decompose [14,53]. Also for ink-jet printing, more viscous formulations of catalyst are required. Therefore a range of research has focussed on developing more stable Pd catalysts [14,53,54]. They mainly focus on alternative ways of Pd stabilization.

The main disadvantage of the Pd/Sn catalyst is its price, which is a result of the use of expensive Pd. Composite nanoparticles which contain Pd and a cheaper catalyst metal (Cu or Ag) are also being investigated [42,43,47,55–57]. The performance of this type of catalyst is comparable with

Pd and sometimes even slightly higher [43]. Pd-free catalysts are also of great interest to many research groups at present [41,58–62].

Other methods use deliberately synthesised nanoparticles as a catalyst. The advantage of this method is that the shape and size of nanoparticles can be controlled which potentially can be tuned to achieve the best performing catalytic activity [46,63]. However, controllable synthesis of nanoparticles also requires use of some stabilizers which can potentially affect the activity of the nanoparticles towards formaldehyde oxidation.

In order to avoid particle agglomeration during drying the nanoparticles are usually used in the same solutions as synthesised [53,61,62,64], which means that the products of reaction are also present during catalyst deposition and can remain on the substrate surface.

The reported quantities of deposited electroless copper are presented in Table 3. They ranged from 0.3 to 0.84 mg/cm^2 for the standard Pd/Sn catalyst and from 0.25 to 0.8 mg/cm^2 for newly-developed Ag catalyst. The range is very broad and there is overlap for both catalysts. Therefore, the comparison of the performance of catalysts is not possible between different published works.

Table 3. The quantities of deposited Cu after 10 min of electroless Cu plating by using different catalysts.

Type of catalyst	**Quantity of deposited Cu, mg/cm^2**	**References**
Ag	0.25	[43]
Ag	0.8	[62]
Ag	0.35	[61]
Ag	0.37	[41]
Pd	0.55	[43]
Pd/Sn	0.45	[45]
Pd	0.5	[45]
Pd/Sn	0.84	[62]
Pd/Sn	0.37	[41]
Pd/Sn	0.3	[25]

CV measurements of Ag nanoparticles in formaldehyde solution were performed in several works (Table 4, Figure 10). Nanoparticles were loaded by drop-coating or dip-coating onto the working electrode. The measured oxidation peak was obtained at a range of potentials, which if measured vs Ag/AgCl electrode is around 0. The recorded current densities are different from work to work and depend on the electrode preparation and measurement conditions.

Table 4. The comparison of the conditions of CV or linear sweep voltammetry experiments for investigation of Ag nanoparticles catalytic activities towards formaldehyde oxidation.

Number	Method of nanoparticles deposition	Concentration HCHO, M	Concentration NaOH or KOH, M	Scan rate, mV/sec	Reference electrode	Ref.
1	Dip-coating	0.1	0.1	1	Ag/AgCl	[45]
2	Dip-coating	0.1	0.1	10	Ag/AgCl	[64]
3	Dip-coating	0.1	0.1	10	Ag/AgCl	[61]
4	Drop-coating with Nafion	1.0	1.0	100	SCE	[65]

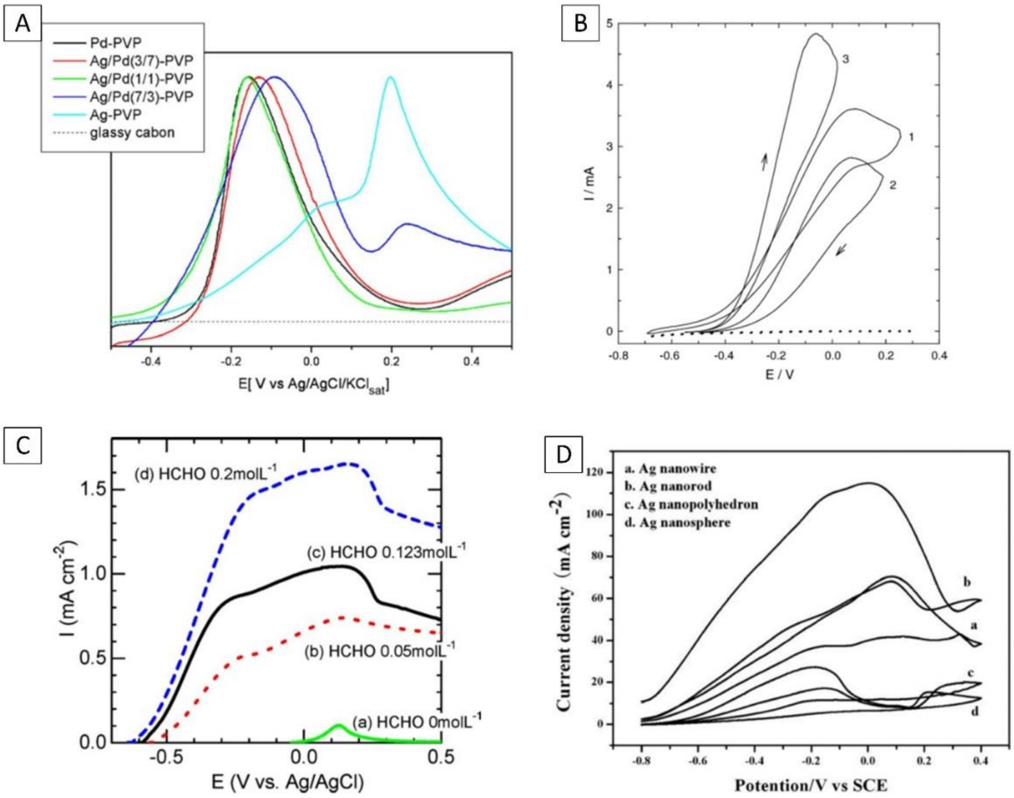

Figure 10. The CV and linear sweep voltammetry measurement of Ag nanoparticle activity towards formaldehyde oxidation at the conditions described in Table 3. A – 1, B – 2, C – 3, D – 4.

1.1.10 Selective surface catalysation

The works reviewed in sections 1.1.8 – 1.1.9 were performed using blanket catalyst deposition where catalyst is distributed evenly across the substrate surface, which results in complete copper coverage of the substrate surface. The catalyst deposits from the solution through particle adsorption onto the substrate surface or particle formation on the surface and both depend on the catalyst solution formulation and the functionalisation of the substrate surface.

Selective electroless metal deposition can often be achieved by selective catalyst deposition or selective surface activation as was mentioned in Introduction. The reproduction of the required pattern is the main requirement.

When the catalyst solution deposits selectively e.g. by contact or ink-jet printing, often a "coffee-ring" effect can be observed where more catalyst is present at the edges of the pattern which results in uneven copper plating across the patterned area (Figure 11). This occurs due to the difference in evaporation rate of the solvent at the edges of the pattern and at the centre or due to capillary forces.

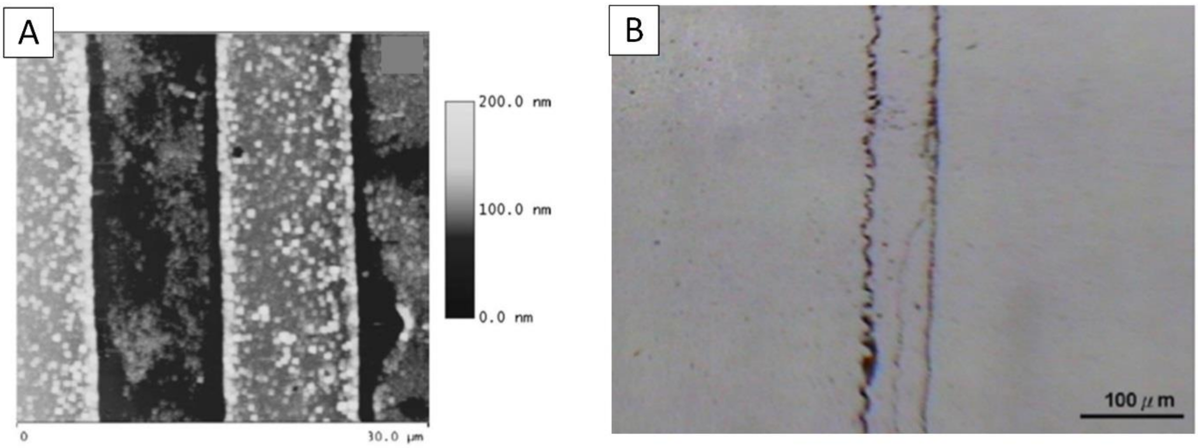

Figure 11. The images of selective plating where the coffee-ring effect was observed. The metallisation was done by A – microcontact printing [18], B – ink-jet printing [14].

Often the different methods of selective surface initiation allow control over catalyst density per substrate surface area. This process requires optimisation otherwise non-continuous plating will be obtained. For example, in laser-assisted surface activation the laser-activated areas were located too far from each other which meant subsequent electroless plating did not result in a continuous line (Figure 12, A). A similar effect was observed when the surface was initiated by aerosol activation – the resultant copper plating was not continuous across the activated area

(Figure 12, B). In ink-jet printing when the spacing between droplets was too large the pattern of lines were not reproduced correctly (Figure 12, C).

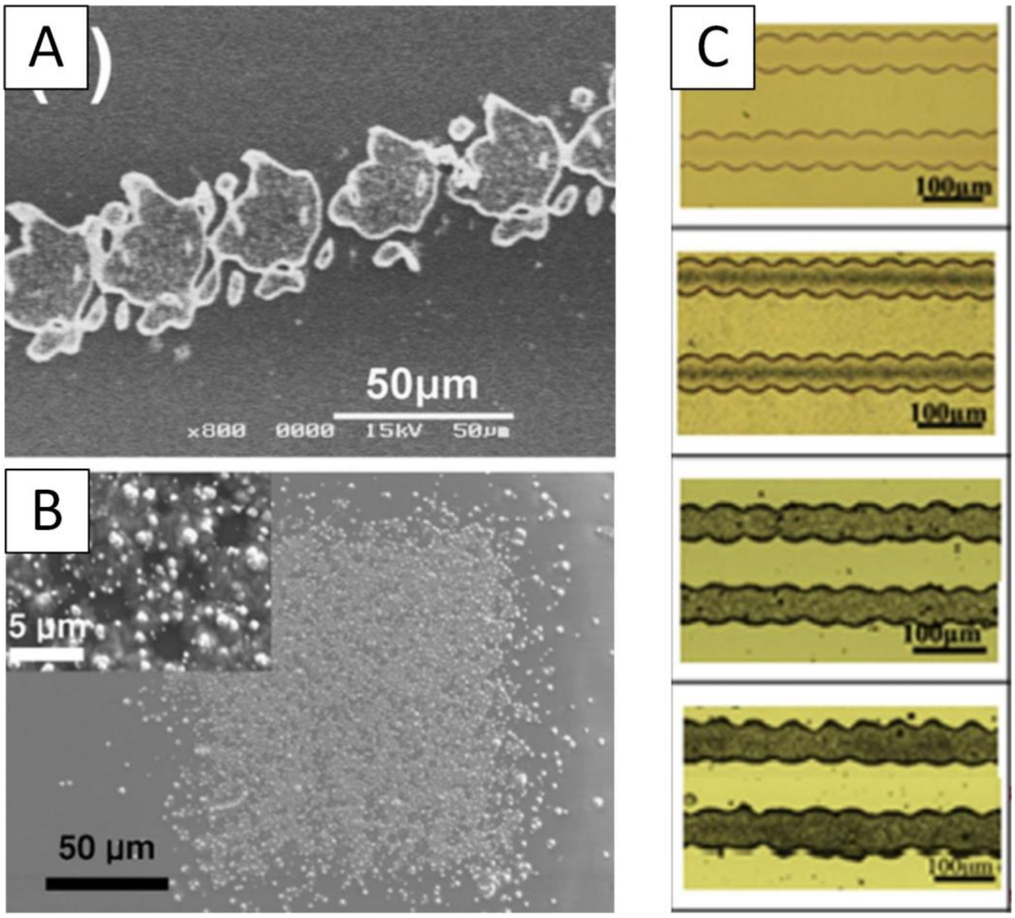

Figure 12. The SEM (A, B) and optical microscope images (C) of the selective electroless plated layers showing non-continuous or deformed patterns obtained by the methods: A – laser-assisted metallisation [66], B – aerosol catalyst deposition [67], C – ink-jet printing.

When a novel method of selective metallisation is developed it requires some modifications in the catalyst solution or dispersion. Often nanoparticles are synthesised in order to use as a surface activator. If the catalyst particles do not have narrow size distribution, the subsequent electroless plating will grow unequally across the initiated area depending on the size of the catalyst particles, which results in higher roughness of the deposited layer (Figure 13, A-C). This also affects the reproduction of the pattern when patterns with fine features are required (Figure 13, D).

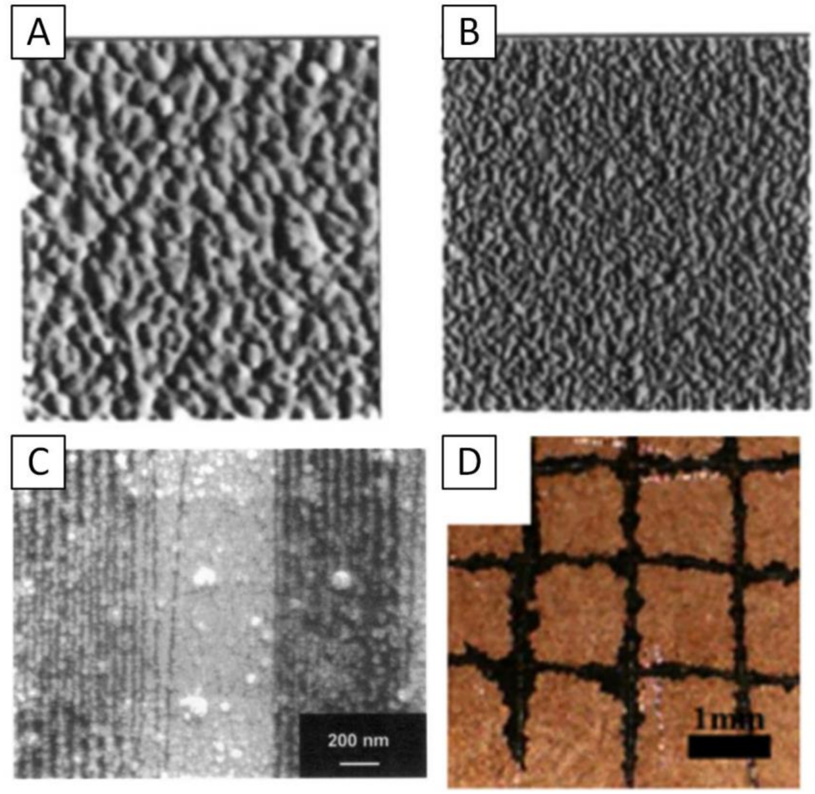

Figure 13. The SEM and optical microscopy images of the electroless Ni (A-C) [67] and Cu (D) [68] deposited by using nanoparticles. A, C – the nanoparticles had broad size distribution and deposited A – blanket, C – selectively; B – the nanoparticles had narrow size distribution; D – selective copper deposition with particles with broad size distribution.

Therefore, the following requirement for the selective catalyst deposition can be concluded:

1) The catalyst should be distributed evenly across the portion of the surface required for metallisation;

2) The density of the catalyst distribution across the substrate surface should be optimised so that the electroless plated metal forms a continuous layer where required;

3) If nanoparticles are used as a catalyst, the size distribution of the particles should be as narrow as possible.

1.1.11 Conclusion

The electroless copper plating process was reviewed. The electroless bath should contain a metal salt, complexing and reducing agents, as well as pH adjusters and other additives. The deposition process is influenced by the electrolyte composition, pH and temperature of deposition.

In the electroless solution the metal ions are coordinated by the complexing agent, which prevents the metal from being reduced spontaneously. The reducing agent is oxidised on the substrate surface and donates electrons to the complexed metal ion, then the metal reduces and deposits on the substrate surface. The process can be viewed as two independent reactions of formaldehyde oxidation and metal reduction, though in reality the reactions are interdependent.

The rate determining reaction is formaldehyde oxidation. The rate of the reaction changes during the electroless plating process and slows down when the reaction becomes autocatalytic. Mass transport does not significantly influence the rate of the electroless copper plating process. The mechanism of reaction depends on the nature of the catalyst which catalyses the oxidation process.

The catalyst should be deposited prior to electroless plating if metallisation of non-conductive material is required. Usually, a Pd/Sn catalyst is used however it can be replaced with a number of catalysts of different formulations. As alternative catalysts, metals from groups 10 and 11 of the periodic table can be used. Ag is a promising catalyst which is cheap and well-studied. It is often used in nanoparticle form.

The catalytic activity of the catalyst can be characterised by the actual Cu deposition process or electrochemical techniques like CV, linear sweep voltammetry and Tafel plots. However, the data obtained from electrochemical techniques requires further interpretation.

Often, in order to achieve selective metallisation the catalyst is deposited selectively on the substrate. In that case more parameters of the deposited catalyst should be considered including: equal distribution of catalyst across the surface, “dense” distribution of the catalyst and uniformity of the catalyst nanoparticle size.

Part 2. Magnetic field

1.2.1 Overview of magnetic field properties

When moving in an external magnetic field $\vec{B}$, each individual charge experiences a force acting on it which can be described by the following equation (Lorentz force):

$$\vec{F} = q(\vec{E} + \vec{v} \times \vec{B}) \tag{22}$$

where q – the charge of the particles, E – the electric field, B – magnetic field, v – velocity of the particle. B also called a **magnetic flux density** or magnetic induction.

As can be derived from the Lorentz equation, the magnetic field is acting on a moving charge q (if v=0 then Lorentz force is purely electric F=qE and there is no contribution of the magnetic field) by producing a [Lorentz] force F, which is perpendicular to both the direction of particle movement ($\vec{v}$) and the external magnetic field $\vec{B}$. The electric and magnetic fields are vector fields which are changing with space and time.

In materials, the magnetic moment arises from the movement of electrons. The electrons moving in their orbitals is what produces the local magnetic field. The spin of the electron contributes to the magnetic moment as well.

Magnetic moment describes the torque which is exerted on an object from a magnetic field. The alignment of the magnetic moment under an external field defines the properties of the material: if all local magnetic moments are aligned in an opposite direction to the direction of the external field the material is **diamagneti**c. This type of material will be slightly repelled by a magnet. The higher the strength of the magnetic field applied the higher the repulsion will be.

In **paramagnetic** material the magnetic moments are aligned in the direction of the magnetic field and are proportional to the applied magnetic field. Paramagnetic materials are weakly attracted by magnets. These types of materials follows Curie's law:

$$M = C\frac{B}{T}, \tag{23}$$

where M – magnetisation of the material, C – Curie's constant, B – magnetic field and T – the temperature.

Typical magnetisation curves for paramagnetic and diamagnetic materials are presented in Figure 14.

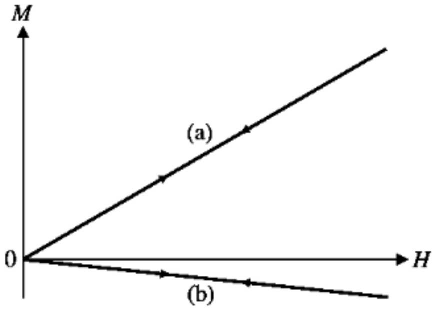

Figure 14. Typical plot of magnetisation of material vs applied magnetic field strength, A – for paramagnetic material, B – for diamagnetic material [69].

Ferromagnetic materials have a strong attraction to a magnetic field. This is due to the long-range ordering – where unpaired electron spins are aligned in the same direction. These regions with aligned electrons are called domains. Without an external magnetic field, domains can be aligned in different directions but when the magnetic field is applied the domains align with the magnetic field until all non-aligned domains disappear and a saturation point is reached. After that point if the magnetic field increases the magnetisation does not change. This is shown on the B-H diagram as the magnetisation saturation point (M_s) (Figure 15). After the magnetic field is removed, the material still possesses a certain degree of magnetisation. The magnetic field required to demagnetize the material is called coercivity which is characterised by the presence of the hysteresis loop (H_c). The amount of magnetisation retained after removing the magnetic field is called its remanence (M_r).

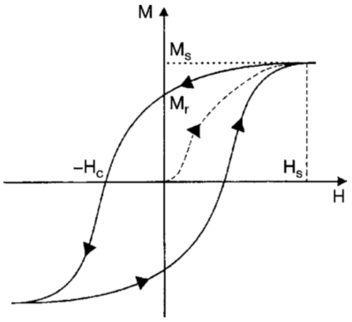

Figure 15. Typical plot of magnetisation of material vs applied magnetic field strength for ferromagnetic material [70].

Magnetisation of the material is the density of the magnetic dipole moment in it:

$$M = \frac{\mu}{V} \tag{24}$$

where μ is magnetic dipole moment and V is the volume.

When the magnetic material consists of several types of atoms some of which are not ferromagnetic, more complex interactions with the magnetic field arise. When the magnetic field is applied, the magnetic moments align antiparallel. If the magnetic moments for both types of alignment are equal then they mutually cancel. This type of material is called **antiferromagnetic**. If the predominant alignment is parallel to the magnetic field then the material is **ferrimagnetic**. The magnetisation of these types of material is lower than in ferromagnetic materials, however the behaviour is often similar to ferromagnetic material [71].

The ability of the material to be magnetised in the magnetic field is characterised by its magnetic susceptibility:

$$\chi = M/H \tag{25}$$

where χ is susceptibility, M is variation of magnetization, and H is applied field.

Higher values of susceptibility mean higher magnetisation of the material. Some values of magnetic susceptibilities are presented in Table 5.

Table 5. The values of magnetic susceptibility of some materials.

Name	**Formula**	**Magnetic susceptibility, cm^3/mol**
Copper	Cu	-5.46
Silver	Ag	-19.5
Palladium	Pd	+540
Iron sulfate	$FeSO_4$	+12400
Iron	Fe	Ferromagnetic

The units of measurement of magnetic values are presented in Table 6.

Table 6. The conversion of main magnetic units between SI and Cgs.

Quantity	**Symbol**	**SI unit**	**Cgs unit**
Magnetic induction	B	10^{-4} Tesla [T]	1 Gauss [G]
Magnetic field strength	H	$10^3/4\pi$ A/m	1 Oersted [Oe]
Magnetic moment	μ	10^{-3} J/T or A m^2	1 emu
Magnetisation	M	10^3 J/T m^3 or A/m	1 Oe or emu/cm^3

1.2.2 Magnetic properties of nanoparticles, measurement

The properties of ferromagnetic materials are different between the bulk and the nanoparticle forms. The main distinction of nanoparticles from the bulk material is the higher surface area of the former. The smaller the size of the particles the greater the percentage of the atoms are on the surface rather than in the bulk. For ferromagnetic materials the atoms located on the surface are less coordinated which increases their magnetic moment. However, the surface is more subjected to impurities and crystallinity imperfections. The surface state of the particles influence their magnetic properties. Often on the surface layer a dead magnetic layer is present which does not contribute to the magnetisation of the particles.

For Fe_3O_4 the magnetisation value of the bulk material is 93 emu/g [72]. For the nanoparticles, a range of values have been reported (Figure 16). The crystallinity [73], concentration of Iron [74] and the monodispersity [74] can all affect the measured values.

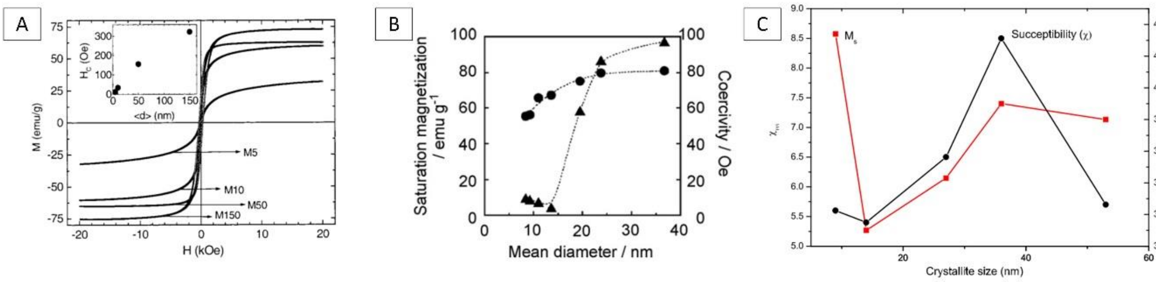

Figure 16. The magnetic saturation values for the Fe_3O_4 nanoparticles of different sizes from works A - [75], B - [72], C - [76].

The size of nanoparticles influences significantly the magnetisation saturation, with most literature reporting a decrease in magnetisation saturation with decreasing nanoparticle size. The coercivity of the particles also decreases with decreasing size. At a certain critical diameter, a particle becomes a single domain and with further reduction of the particles' size they act as a large single paramagnetic atom which can be quickly magnetised but cannot retain magnetisation. This means that the particles become **superparamagnetic**.

1.2.3 Influence of the magnetic field on electroless plating and electrodeposition processes

1.2.3.1 Electromagnetic interactions

The magnetic moments of electrons align in the magnetic field. Therefore processes which involve electric charge transfer can be altered by the magnetic field. These include electrochemical processes like corrosion, displacement reactions, electroless plating and electrodeposition. The magnetic field interacts with the electric current and intensifies convection. It can be described by the Lorentz force [77]:

$$\overline{F_L} = \bar{J} \times \bar{B} \tag{26}$$

where j – electric current density and B - magnetic induction.

Due to the vector nature of the constituents the value of Lorentz force depends on the mutual orientation of current and magnetic field. If the magnetic field and current density are parallel the Lorentz force is zero, while a perpendicular position gives a maximum effect on convection [78]. For this reason, the influence of the magnetic field applied perpendicular to the electric current flow will increase convection in the electrochemical cell. Due to unequal current distribution near the electrode surface micro flows arise, which is known as the magnetohydrodynamic (MHD) effect [78].

In the electrodeposition process, mass transport in the solution near the substrate surface improved when the magnetic field was applied [77] which leads to decreased thickness of diffusion layer and facilitates more equal chemical distribution. Enhanced convection affects morphology of the deposited layer [79]. The magnetic field increases the amount of nucleation seeds formed as well as the thickness of the layer [80].

In electroless plating the MHD effect increases the rate of the deposition (Figure 17, A), which affects the deposit morphology [81,82]. The deposited layer can become more rough (Figure 17, D) due to the increase in mass-transport and more dense (Figure 17, B, C) due to the quicker removal of the hydrogen from the surface which causes formation of air holes in the deposit.

Magnetic fields applied parallel to an electrode could decrease grain size of the deposited material [82] and lead to changes in layer density. The layer density can be varied by addition of the complexing agent, causing it to either decrease or increase [82]. Kinetics are also affected by the magnetic field. It was found that the induction period of electroless Ni plating was affected by introduction of the external magnetic field (Table 7) [83].

Table 7. Effect of magnetic field on induction period of electroless Ni plating [83].

Temperature, °C	Concentration of Ni, M	Induction period, min		
		0 T	0.15 T	0.2 T
57	0.076	0.00	0.05	0.00
48	0.076	0.12	0.19	0.20
39	0.076	1.20	0.99	0.98
31	0.076	2.18	2.02	2.21
31	0.038	1.23	1.28	1.54
31	0.114	2.83	2.07	2.81
31	0.152	3.84	3.28	3.76

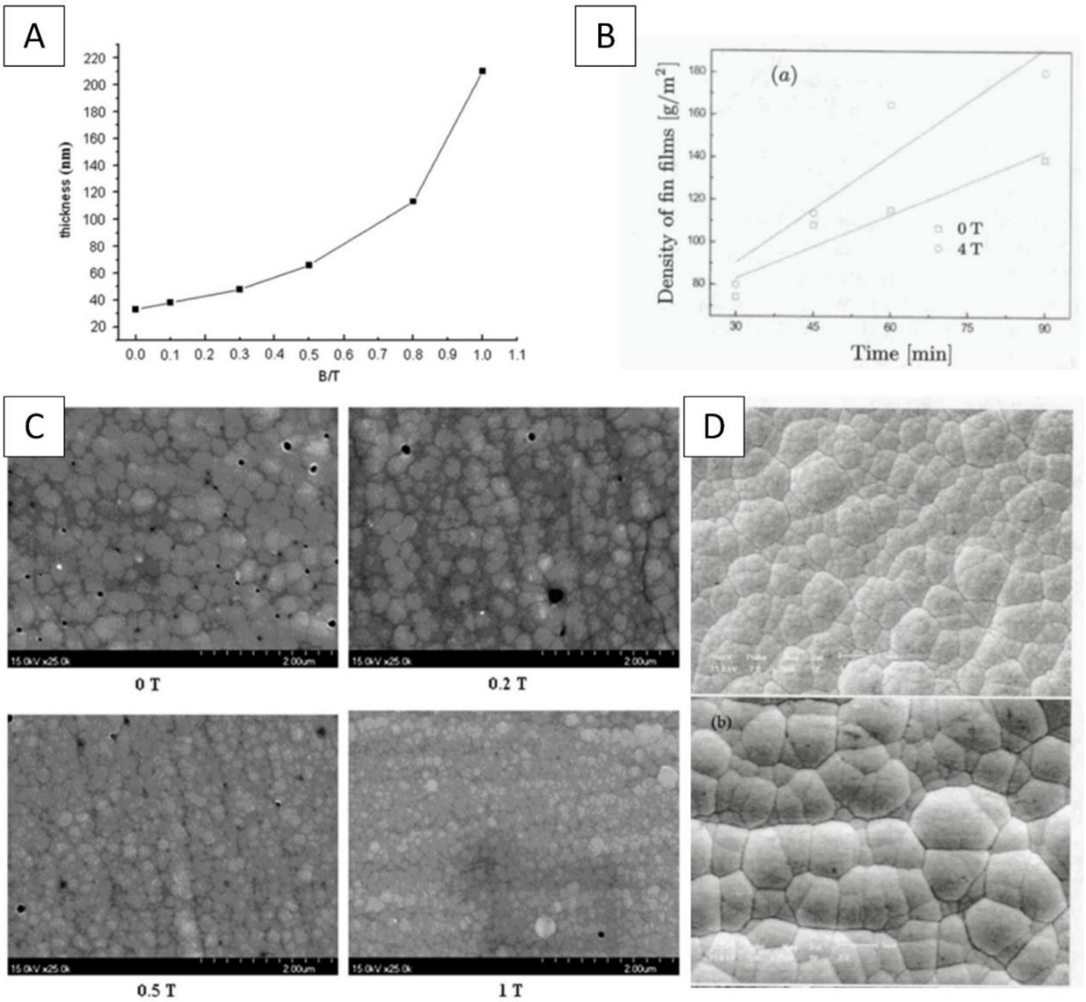

Figure 17. The effect of the magnetic field on the electroless deposition process. A – the thickness of deposited layer of Co-W-P [82], B – the density of deposited layer of Ni-P [81], C – the density of deposited layer Co-W-P [82], D – morphology of the deposited layer of Ni-P [81].

Some authors attribute all the changes mentioned above to the change in nucleation and early growth stages of the deposited layer under the applied magnetic field [82]. They also suggest that if higher magnitude magnetic fields generate a gradient magnetic field then new forces are involved in solution convection, which are known as micro-MHD.

Reported experiments on the effect of the magnetic field on electroless plating were performed using electrolyte-containing ferromagnetic species such as Co and Ni. However, little research has been done on electroless plating of non-magnetic species. The confusion can be caused by misuse of the term "electroless" [84] when in reality the process was a displacement reaction (immersion plating) [85] or electroplating [86].

1.2.3.2 Electrophoretic interaction

Magnetic fields also interact with paramagnetic species in solution [87]. Magnetisation of material is proportional to the strength of the applied magnetic field and the magnetic susceptibility of material [88].

$$M = xH \tag{27}$$

where M - magnetization of material, H - strength of magnetic field, χ - volume magnetic susceptibility.

The response of the material to the magnetic field depends on the magnetic susceptibility of the material. Paramagnetic material has positive magnetic susceptibility and is attracted by a magnetic field. Diamagnetic materials have negative susceptibility and are weakly repelled by a magnetic field. The cause of paramagnetic particle attraction is unpaired electrons in the d- or f-orbitals, which align in a magnetic field. The rare earth elements (from Ce to Yb), Fe, Pt and Pd groups and actinides are paramagnetic. Rare-earth metals have higher magnetic susceptibility due to unpaired f –orbital electrons (maximum 14 electrons). Other elements have unpaired d-orbital electrons (maximum 10 electrons) which decreases the magnetic interaction force [70].

Magnetic fields influence a moving charge by following equation [70].

$$\vec{F} = q\vec{v}\,\mathrm{x}\,\vec{B} \tag{28}$$

where is q – particle charge, v – particle velocity and B – magnetic field strength.

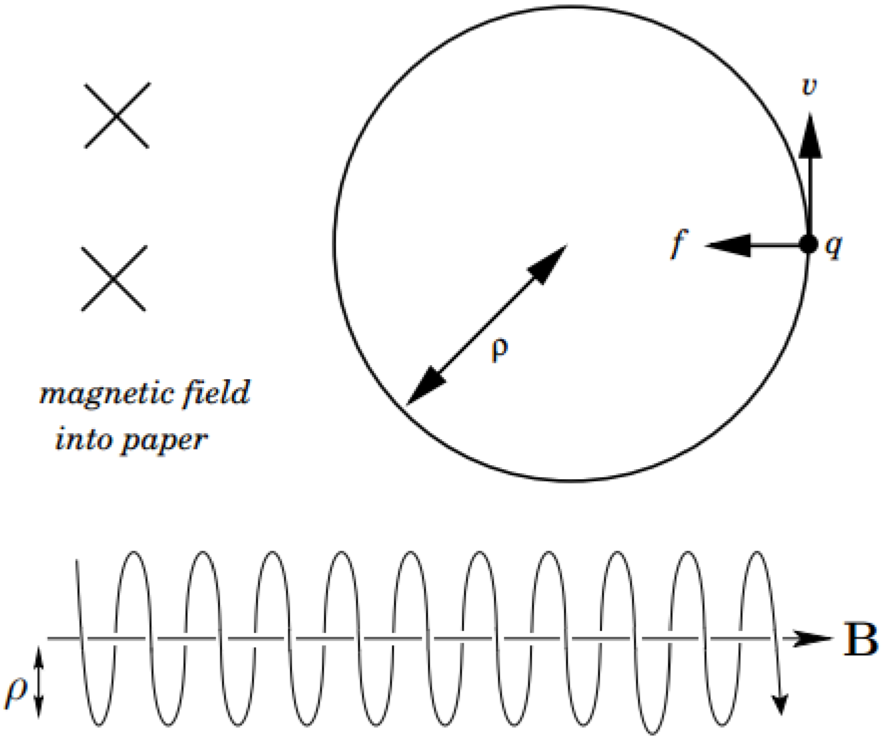

Figure 18. Circular and spiral motion of a particle in a magnetic field.

If the charged particle moves perpendicular to the magnetic field the particle will not be accelerated or decelerated by the field but will start to move in a circular motion (Figure 18) with radius $R = \frac{m\, v_\perp}{|q|B}$ (gyroradius or Larmor radius [89]). It will improve mass transport in solution but not cause the particles to be attracted. The attraction is possible when particles move parallel to the magnetic field.

No significant effect was found on the distribution of paramagnetic species under the application of a uniform magnetic field [87]. However, some researchers suggest that magnetic ions respond to a gradient magnetic field in solution not independently but as a group [79,90]. In a non-uniform magnetic field, a Kelvin force appears which tends to drive the paramagnetic species to the higher magnetic strength areas of the solution. In addition, in deposits of alloys of elements with different magnetic susceptibilities, the stoichiometry changes [82].

This approach was used to obtain patterned deposition of metal during the electrodeposition process. In order to intensify the effect of the gradient magnetic field, smaller magnets were used [91–93]. However, the diffusion of the paramagnetic species from the high strength magnetic force areas should also be taken in consideration [94].

1.2.3.3 Patterning electrochemical deposition under a magnetic field

Permanent magnets [95,96] or a ferromagnetic material grid [97,98] are usually used to create a pattern. There are two types of patterning possible: direct and reverse. Direct patterning is created when paramagnetic species are used as a depositing material (Table 8). Ions attracted by the magnetic field form a thicker deposit on the areas with a maximum strength of magnetic field. The deposition at the area of maximum magnetic field strength has been found to be rougher [96] and more dense [99] than on the areas with minimal magnetic influence. It was observed that a decrease in hydrogen bubble generation [100–102] is a possible contributing factor to the improvement of the layer density.

Table 8. Overview of published results from direct selective electrodeposition in a magnetic field.

Metals	**Concentration, M**	**Substrate**	**Strength of magnetic field, mT**	**Thickness of deposited metal under magnets/between magnets, μm**	**Deposition time**	**Ref.**
Co^{2+}	1.00	Metal foil	400	distinctive	10 min	[103]
Cu^{2+}	1.00	Metal foil	400	0.45/1.8 distinctive	10 min	[83]
Ni^{2+}	1.00	Metal foil	400	distinctive	10 min	[83]
Zn^{2+}	1.00	Metal foil	400	Barely distinctive	10 min	[83]
Cu^{2+}	0.10	Au on glass	500	distinctive 0.5/0.25	75.4 sec	[104]
Cu^{2+}	0.30	Au on glass	500	distinctive 0.17/0.14	29.5 sec	[104]
Cu^{2+}	0.57	Au on glass	500	distinctive 0.15/0.05	18.4 sec	[104]
Cu^{2+}	0.75	Au on glass	500	distinctive 0.1/0.01	16.0 sec	[104]
Cu^{2+}	1.00	Au on glass	500	no presence of pattern	12.8 sec	[104]
CoFe	0.0065 each element	Glass disc covered by Au	500	distinctive	390 sec	[99]

All experiments were conducted with a horizontally placed substrate in order to exclude the effect of natural convection. The gradient magnetic field is applied perpendicular to the substrate surface. The influence of different parameters on the patterning was investigated. It was found that solutions with higher metal concentration produce a less distinguishable pattern [79]. Some researchers [79] suppose that all molecules including solvent and additives contribute to the magnetic susceptibility of the whole electrolyte solution. However, others conclude that only the nature of the metal ion is responsible for the patterning process [103]. The arrangement of the patterning elements as well as time of deposition were not found to have an effect on the patterning process [103]. The patterns were estimated by visual inspection of samples (Figure 19), profilometry [104] and cross sectional SEM imaging [103,104].

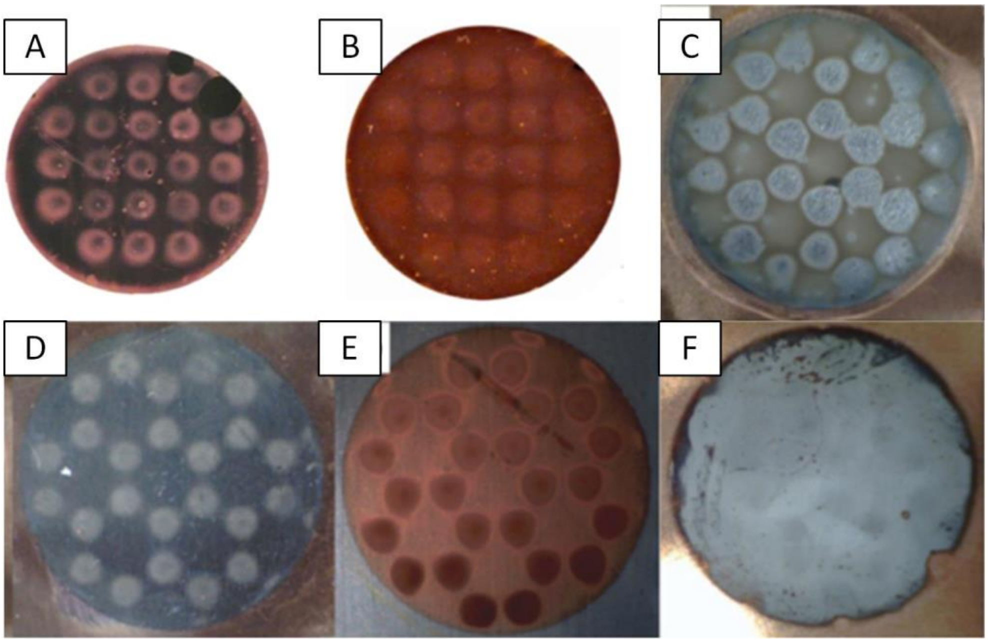

Figure 19. The optical images of pattern deposits obtained by applying a gradient magnetic field during electrodeposition. A – Cu deposit from 0.1 M solution [104], B – Cu deposit from 1 M solution [104], C – Co deposit from 1 M solution [103], D – Ni deposit from 1 M solution [103], E – Cu deposit from 1 M solution [103], F – Zn deposit from 1 M solution [103].

In addition, several experiments were performed in order to obtain a reverse pattern (Table 9). The solution consists of depositing metal ions and strongly paramagnetic but electrochemically inert ions. The paramagnetic species are attracted by the magnetic field and displace electroactive ions. A gradient in atom concentration is created and metals start to deposit at the areas with minimum magnetic influence.

Table 9. Overview of published results from reverse selective electrodeposition in a magnetic field.

Metal/ additive	**Concentration, M**	**Substrate**	**Strength of magnetic field, mT**	**Thickness of deposited metal under magnets/between magnets**	**Time of deposition, sec**	**Ref.**
Cu^{2+}/ Dy^{3+}	0.1/1	Metal foil	300	Averagely distinctive	1200	[102]
Zn^{2+}/Dy^{3+}	0.1/1	Metal foil	300	50nm/100nm	300	[102]
Co^{2+}/Dy^{3+}	0.1/1	Metal foil	300	Badly distinctive		[102]
Ni^{2+}/Dy^{3+}	0.1/1	Metal foil	300	Badly distinctive		[102]
Bi^{3+}/Mn^{3+}	0.01/0.09	Au	500	Distinctive	90	[104]

In the case of inverse patterning the magnetic susceptibility of the depositing metal also influences the deposition process. However, in this case it is desirable that the depositing metal is diamagnetic or slightly paramagnetic so the magnetic field attracts only inert species.

In addition, applying an external magnetic field may improve the quality of pattern [79,105]. This effect may be attributed to enhanced overall convection.

Overall, patterns were successfully obtained for a range of materials including Cu, Zn, Ni, Bi, Co and Fe. The theory behind the process is well discussed [79,103], but there is no common agreement on the nature of the forces attracting the depositing metal ions. The accuracy and reproducibility of pattern formation was not explored. The size of the patterns are in the millimetre scale whereas the sub-micron patterning was not attempted [104].

No published evidence of patterning electroless deposition under an applied gradient magnetic field was found. Because electroless deposition is achieved without applying external electric power the only effect present is the micro-MHD effect which only slightly intensifies the reaction of deposition but is not expected to cause the patterning effect. The Kelvin forces are much smaller in magnitude than thermal motion, which could negatively affect the process of patterning by electroless deposition. Also in electroless copper plating most of the Cu^{2+} ions are present in the complexed form Cu[EDTA]. The complex decomposes near or on the substrate surface, where the reduction process happens. Therefore, the patterning effect of the magnetic field on the electroless plating is expected to be negligible if present at all.

1.2.5 Nanoparticle deposition patterning by gradient magnetic field application

Prior to the electroless plating process the surface of the substrate is activated by the catalyst. The most commonly used catalysts include Pd, Pt, Au or Ag. The catalysts for electroless plating can be deposited from their dispersions where the catalysts exist in nanoparticle form.

The patterning of magnetic nanoparticles in a gradient magnetic field was previously studied (Figure 20). It is often used in biomedical research to pattern cells labelled by magnetic nanoparticles (Figure 20, A-C) [106–111]. A magnet alone or a magnet with a template is used in order to arrange the cells or particles in the required geometry.

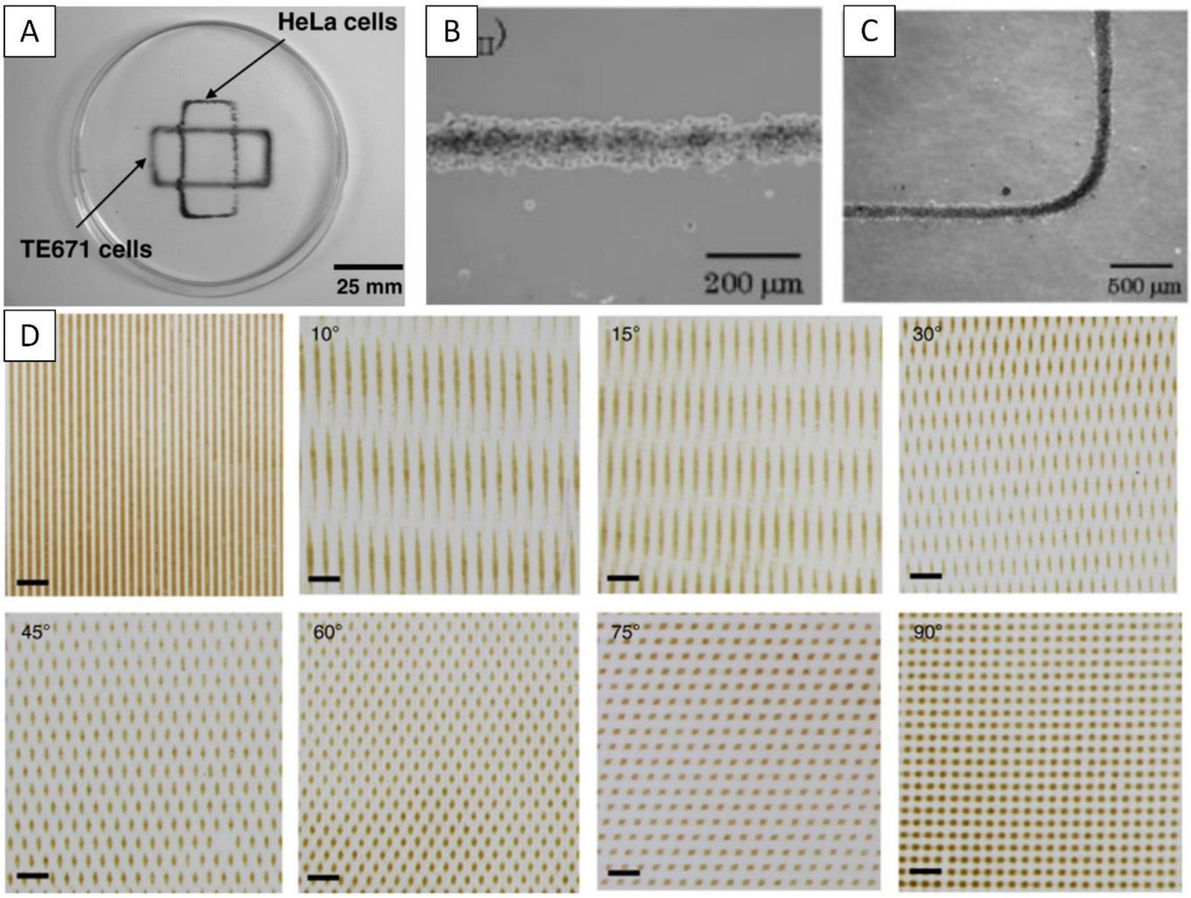

Figure 20. Patterning of the magnetic cells and particles by applying a gradient magnetic field A - [107], B, C - [110], D - [112].

The final geometry can be affected by the concentration of the magnetic particles or cells (Figure 21, A) : the higher the concentration the thicker the lines that were obtained because more magnetically labelled cells were attracted by the magnetic field [110]. Also the distance between the magnet or magnetic template and the substrate surface on which the magnetic particles or labelled cells deposit affects the patterning (Figure 21, B, C) [106,111]. The magnetic field strength decreases with distance and less magnetic species can be attracted.

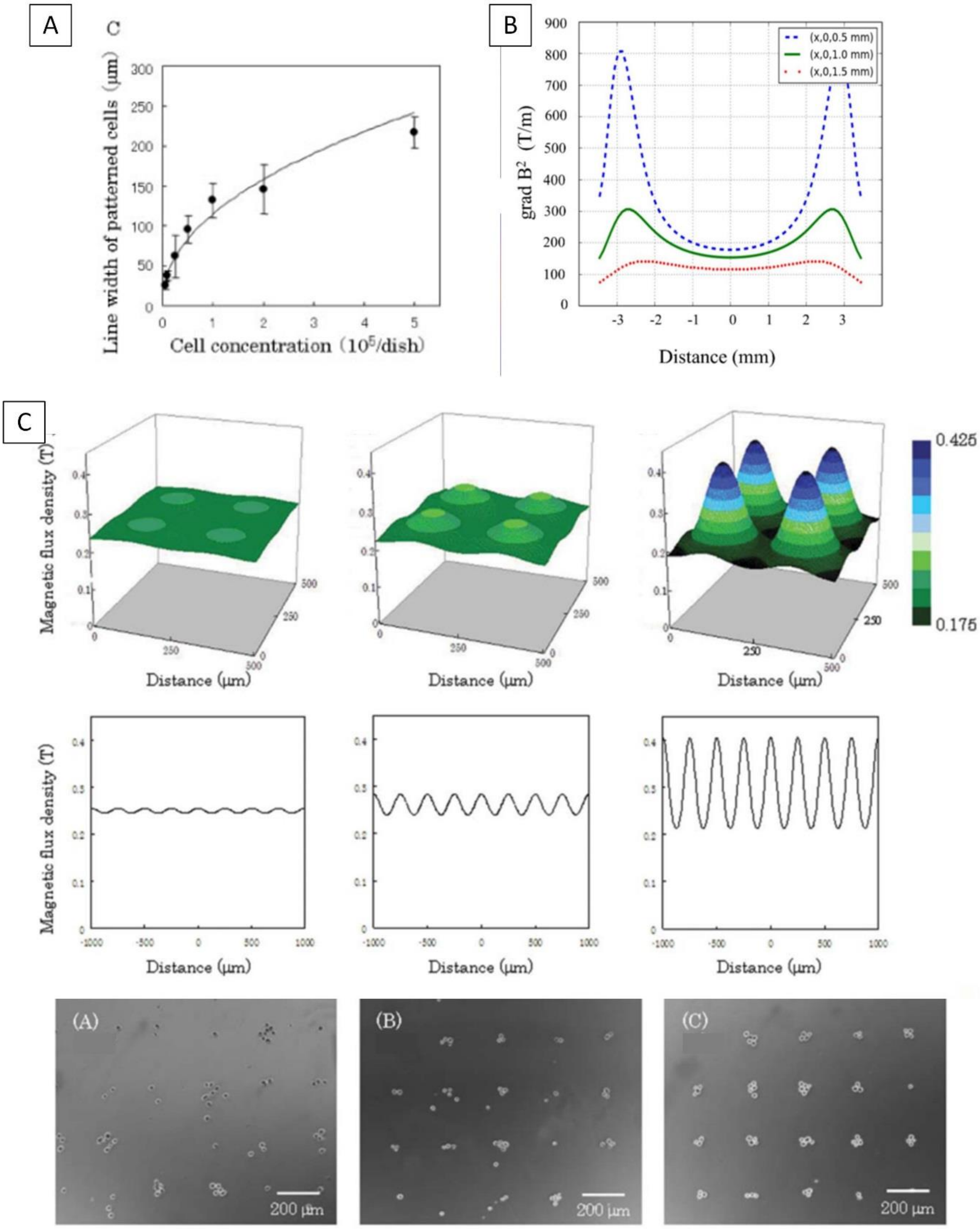

Figure 21. The influence of different parameters on the patterning by a gradient magnetic field A – the influence of the deposited cell concentration [110], B – the influence of the distance between magnet and the substrate on the magnetic flux density gradient [108], C – the influence of the distance between magnet and the substrate on the magnetic flux density [113].

The magnet is usually placed perpendicular to the substrate surface so that the south or north pole of the magnet is facing the substrate surface. The distribution of the magnetic particles on the substrate after deposition in the magnetic field was studied. Often particles aggregate in the magnetic field along the lines of the magnetic field [112,113] or they can also form three-dimensional aggregates [107,109].

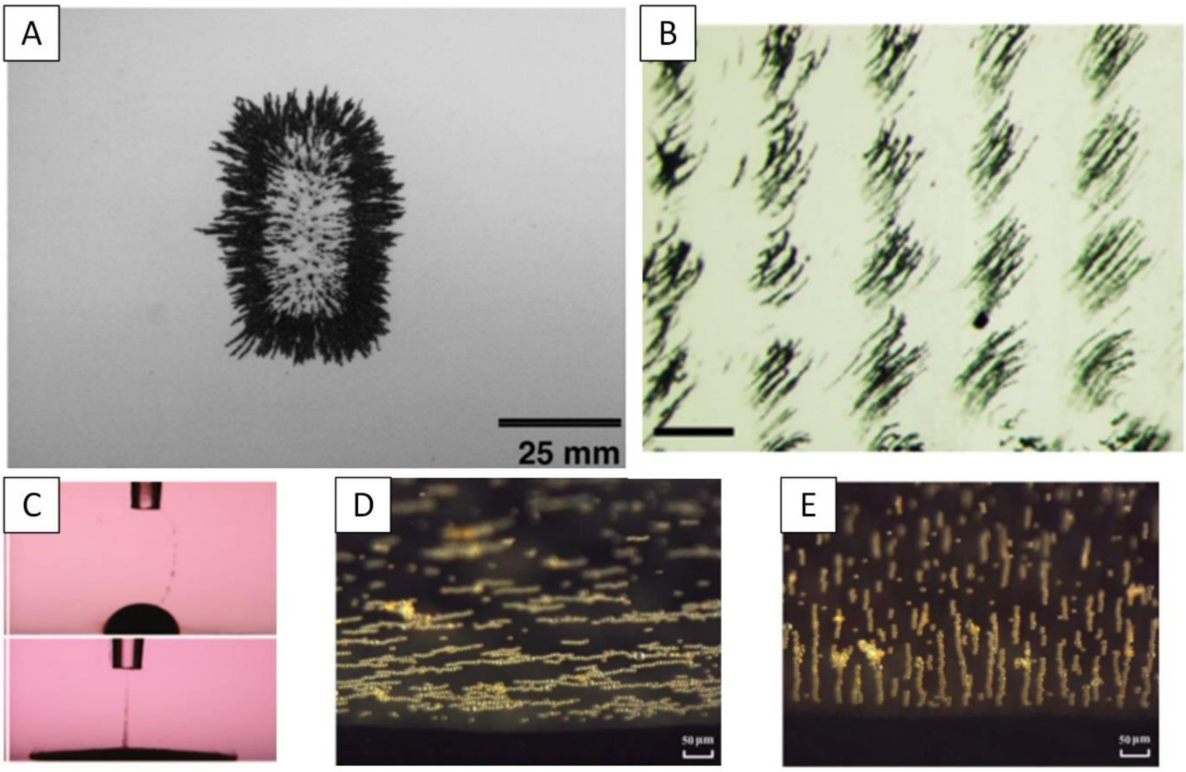

Figure 22. Three-dimensional arrangement of the magnetic particles in the magnetic field. A – [114], B – [115], C – top – the deposition under the magnetic field influence, bottom – deposition without magnetic field [109], D, E – [111].

1.2.6 Conclusion

Magnetic materials can be characterised in terms of magnetization, magnetic susceptibility, coercivety and remanence. The magnetic field can influence electrochemical processes and improve convection due to the magnetohydrodynamic effect. The effect is higher if more electric charge movement is involved in the process, as is the case in electrodeposition. The forces of attraction on static ions by the magnetic field is low. Metal deposited in the electrodeposition process can be patterned by applying a gradient magnetic field due to the current flow, however electroless plating cannot be patterned in this way.

The magnetic field can attract nanoparticles. Previous works have documented the patterning of nanoparticles by gradient magnetic fields. Nanoparticles can also be used to catalyse electroless plating. None of the reviewed work suggests further deposition on the patterned magnetic particles or cells. This research is the first to attempt the use of nanoparticles patterned by the magnetic field to catalyse the process of electroless deposition in order to achieve selective metallisation. Magnetic catalysts have also never been used for electroless plating. The method of synthesis of the magnetic catalysts will be discussed in the next part of this chapter.

Part 3. Synthesis of composite nanoparticles

1.3.1 Method classification

Composite nanoparticles are particles with a diameter in the range of 1 – 100 nm and which consist of two or more compounds and have the combined properties of each individual part. The composites can be arranged in either a core-shell shape or have the shape of Janus particles (Figure 23).

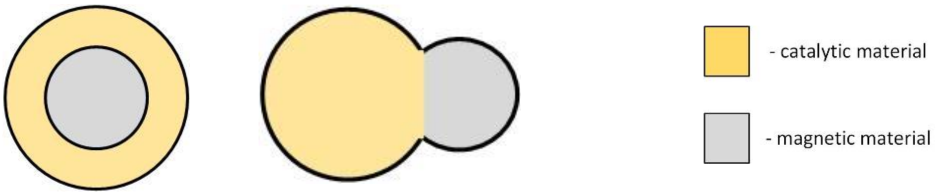

Figure 23. Schematic representation of core-shell (left) and Janus (right) particles.

Composite materials have a range of applications due to their unique properties, which arise from the combination of the two types of material. For example, Fe_3O_4 – Ag composites have magnetic (Fe_3O_4) and catalytic (Ag) properties. In order to synthesise composite nanoparticles, the synthesis procedures of each individual type of particle are usually combined.

For the present research the composite consisting of Fe_3O_4 and Ag was chosen for investigation. Fe_3O_4 particles have ferrimagnetic properties which are close to the ferromagnetic properties of Fe. They are often used for patterning deposition in a gradient magnetic field. The Ag was chosen due to its catalytic properties towards formaldehyde oxidation. It is a promising cheap alternative to the often used Pd catalyst.

There are a range of classifications of methods of nanoparticle synthesis. One of the most common classifications is to divide all synthesis methods into either a top-down or a bottom-up approach. Top-down synthesis of nanoparticles includes a range of techniques which allow for breakdown of the bulk material into small particles of nanometre size. However, these methods often result in non-uniform size distribution and an irregular shape of the particles.

The bottom-up approach allows for control of the synthesised particles size and shape. Also a functional layer can be obtained on the nanoparticle surface. Therefore, only bottom-up synthesis will be further reviewed.

1.3.2 The methods of Fe_3O_4-Ag composite nanoparticle synthesis

The composites consist of two types of particles, therefore often one type of particle is synthesised first (Fe_3O_4) and then the second particle (Ag) is synthesised in the presence of the first. This can be done via a one-pot procedure where, after Fe_3O_4 synthesis, the pre-cursors of Ag are added straight into the same solution, which contains the products of the reaction and the Fe_3O_4 nanoparticles. The particles can also be obtained by simultaneous synthesis of both Fe_3O_4 and Ag in one pot. Another approach is to wash the Fe_3O_4 first and then add the Ag precursor to the freshly re-dispersed solution.

It should be noted that some of the discussed methods describe synthesis of particles exceeding 100 nm size, which means technically they cannot be classified as nanoparticles (typically particles with a diameter below 100 nm). However, because in many works these particles are still referred to as a nanoparticles they will also be designated as such in the current work.

1.3.2.1 Synthesis methods of Fe_3O_4 nanoparticles for Fe_3O_4-Ag composites

In the two step synthesis procedure Fe_3O_4 nanoparticles are synthesised first. A range of methods have been reported for the synthesis of Fe_3O_4 nanoparticles [114–117] although only some of them were used during synthesis of the Fe_3O_4-Ag composites.

1) Precipitation or co-precipitation method

Usually a mix of Fe^{2+} and Fe^{3+} salts or Fe^{2+} salts only are used as a precursor. They can be dissolved in water or in organic media. A base (often NH_4OH or NaOH) is also added to the solution. An example of Fe_3O_4 formation from Fe^{2+} ions [118,119] is:

$$Fe^{2+} + 2OH^- \rightarrow Fe(OH)_2 \tag{29}$$

$$3Fe(OH)_2 + \frac{1}{2}O_2 \rightarrow Fe(OH)_2 + 2FeOOH + H_2O \tag{30}$$

$$Fe(OH)_2 + 2FeOOH \rightarrow Fe_3O_4 + 2H_2O \tag{31}$$

From a mix of Fe^{2+} and Fe^{3+}:

$$Fe^{2+} + 2Fe^{3+} + 8OH^- \rightarrow Fe_3O_4 + 4H_2O \tag{32}$$

The size of the nanoparticles can be adjusted by changing the pH, precursor salts, the base, temperature and time of the reaction. In addition, additives are employed to functionalise the Fe_3O_4 surface or to control growth. In order to obtain Fe_3O_4 for further composite synthesis the works reported particles sizes of 50 nm and below: 10 nm [120,121]; 13 nm [122]; 20 nm[123]; 51 nm [124]. Typical transmission electron microscopy (TEM) images of the Fe_3O_4 nanoparticles obtained by this method are presented in Figure 24.

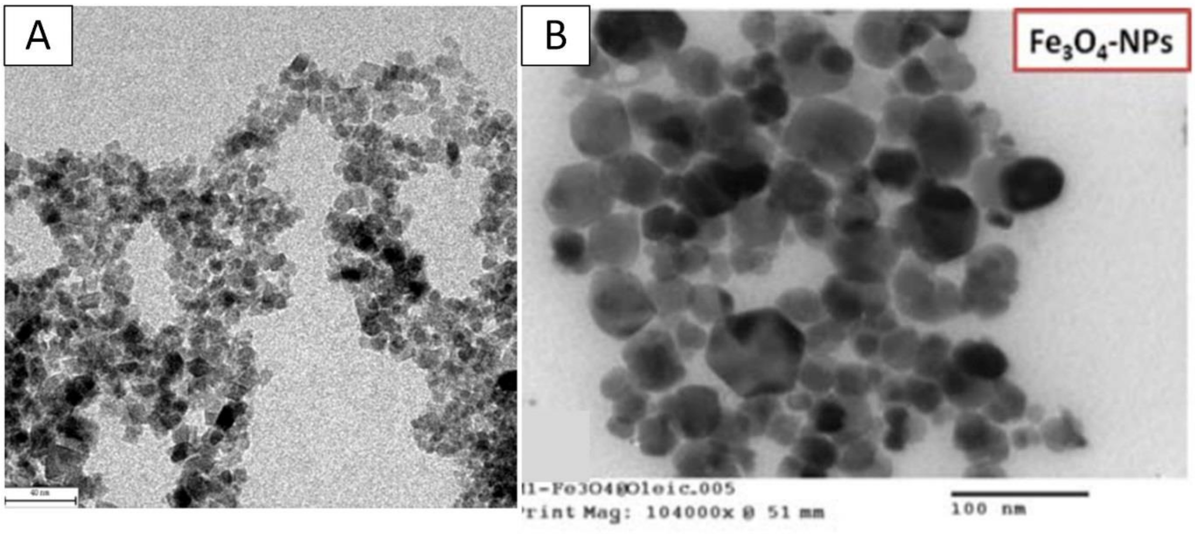

Figure 24. TEM images of Fe_3O_4 nanoparticles synthesised by the co-precipitation method from works A - [121], B – [123].

2) Solvothermal

The Fe^{3+} salt is dissolved in water (hydrothermal synthesis) or an organic solvent (solvothermal synthesis). The solution usually contains a base or a reagent which will result in base formation e.g. ammonium acetate:

$$NH_4CH_3CO_2 + H_2O \rightarrow CH_3COOH + NH_4OH \tag{33}$$

Surfactants can also be added to the mixture to control nanoparticle growth. The mixture is then placed in a Teflon-lined stainless-steel autoclave and heated up to 160-200 °C for a few hours (8-24h). During the reaction, part of the Fe^{3+} ions can be reduced to Fe^{2+} by a mild reducing agent e.g. ethylene glycol according to the following equation:

$$2(HOCH_2)_2 \leftrightarrow 2CH_3CHO + 2H_2O \tag{34}$$

$$2CH_3CHO + 2Fe^{3+} \leftrightarrow (CH_3CO) + 2Fe^{2+} + 2H^+ \tag{35}$$

$$Fe^{2+} + 2OH^- \leftrightarrow Fe(OH)_2 \tag{36}$$

The existence of the Fe in both ferric and ferrous oxidation states enables magnetite formation [116,125]:

$$2Fe(OH)_3 + Fe(OH)_2 \leftrightarrow Fe_3O_4 + 4H_2O \tag{37}$$

Usually relatively large particles of sub µm size are obtained with a round shape: 200 nm, 400 nm and above (Figure 25).

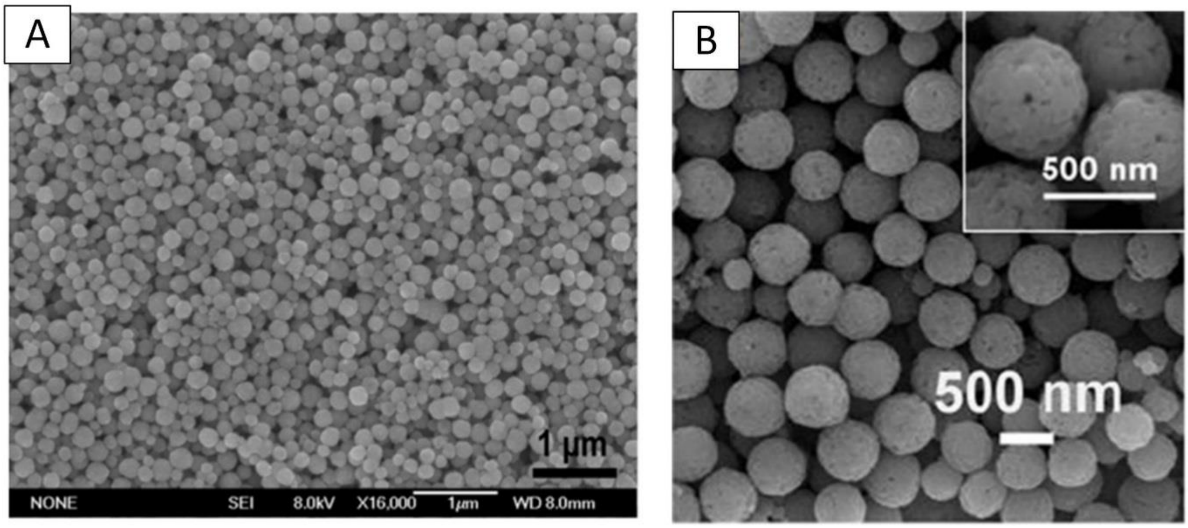

Figure 25. Scanning electron microscopy (SEM) (A) and TEM (B) images of the Fe_3O_4 synthesis via the solvothermal method from works [126,127].

3) Decomposition/solvothermal synthesis

Fe_3O_4 can also be obtained by thermal decomposition of $Fe(acac)_3$ (acac = acetylacetonate), or $Fe(CO)_5$. The most widely used method of decomposition-solvothermal synthesis in the presence of oleylamine and oleic acid was first proposed by Sun [103]. This method is used for simultaneous synthesis of Fe_3O_4 and Ag in order to form a composite. For this reason, the solution also contains the Ag precursor and stabilizers such as polyvinylpyrrolidone (PVP), oleic acid and dodecandiol. After mixing, the obtained liquid is placed in a sealed container and subjected to high pressure and temperature treatment or microwave irradiation. The obtained composite particles are presented at Figure 26. Usually Janus-like particles are obtained by this method and the size of the biggest particle does not exceed 15 nm. In TEM images, the particles with higher electron density (Ag) appear darker than the particles with lower electron density (Fe_3O_4) [128]. However, the particles usually have quite low values of magnetisation saturation which do not exceed 10 emu/g which is probably due to the small size of the particles.

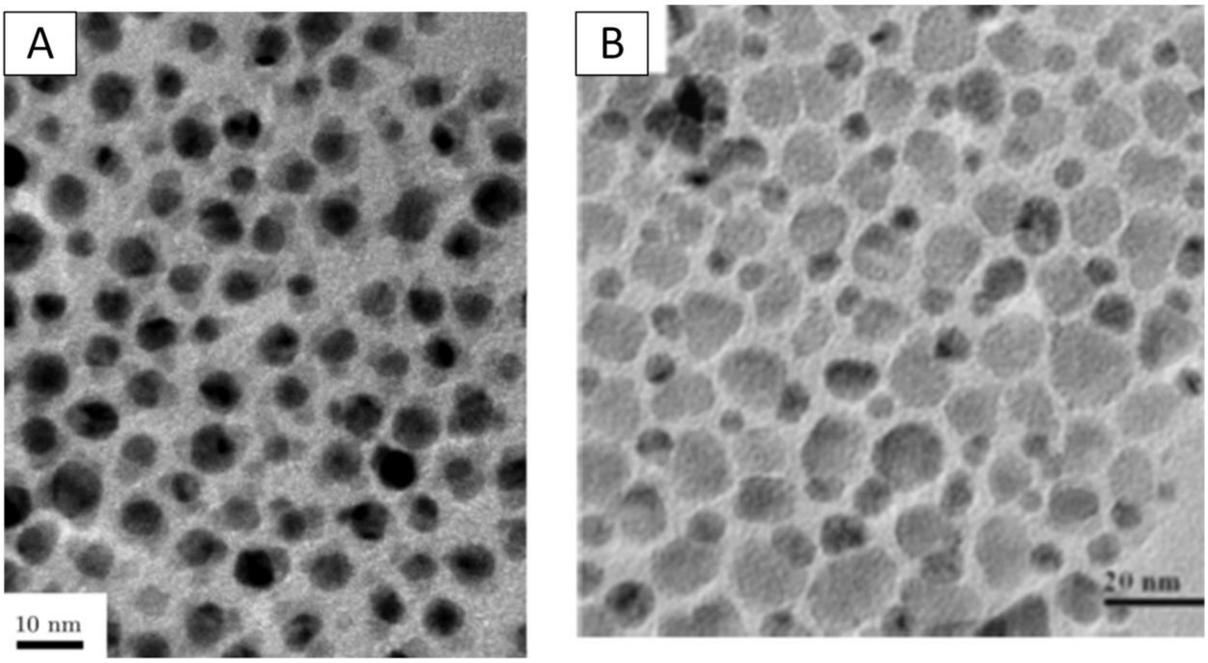

Figure 26. TEM images of the Fe_3O_4 – Ag nanoparticles synthesised via the thermal decomposition/solvothermal method from works: A -[129], B - [130].

1.3.2.2 The synthesis of Fe_3O_4-Ag composites

Ag can be reduced from Ag salt by using $NaBH_4$ (Figure 27, A, B) according to the reaction [131]:

$$AgNO_3 + 2NaBH_4 \rightarrow Ag + H_2 + B_2H_6 + NaNO_3 \quad (38)$$

The reduction by $NaBH_4$ can be accompanied with PVP as a stabilizer (Figure 27, C, D). Previous works have shown that both Fe_3O_4 and Ag are present in the composite obtained by the reduction with $NaBH_4$ though there was not enough evidence to confirm the core-shell structure as some claimed.

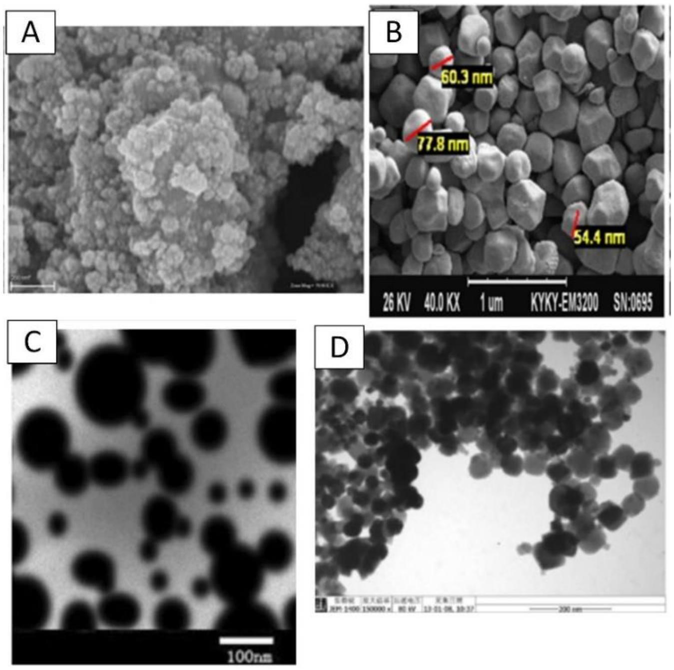

Figure 27. SEM (A [132], B [124]) and TEM (C [133], D [134]) images of the Fe_3O_4-Ag nanoparticles, where Ag obtained by $NaBH_4$ reduction, C, D – in the presence of PVP.

The presence of both Fe_3O_4 and Ag in composites was confirmed by energy-dispersive X-ray spectroscopy (EDX) [132,134], x-ray diffractometry (XRD) [124,133] and by measuring interplanar distance in high-resolution transmission electron microscopy (HRTEM) images [134].

Ag^+ can also be reduced by other organic molecules: a range of amino acids (tyrosine, arginine (Figure 28, A) [135], histidine [136]), glucose (Figure 28, B) [137], tartaric acid (Figure 28, C) [138], (3-Aminopropyl)triethoxysilane [121], (3-Aminopropyl)trimethoxysilane [122] and vinifera extract (Figure 28, D) [139]. The obtained particles usually have a composite structure, confirmed by XRD [93,96,97], EDX [93, 97], and selected area diffraction pattern [97].

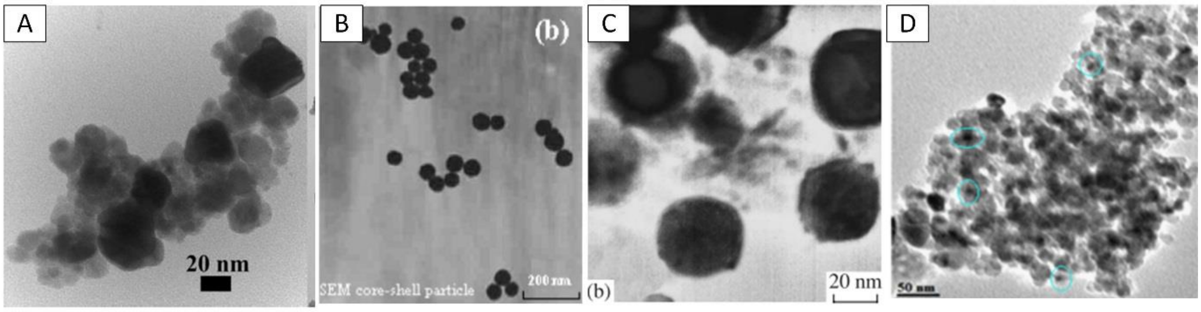

Figure 28. TEM (A, D) and SEM (B, C) images of the Fe_3O_4-Ag nanoparticles obtained by Ag reduction with A – arginine [93], B – glucose [95], C – tartaric acid [96], D – vinifera extract [97].

Often, visible absorption spectra are reported for composite Fe_3O_4-Ag nanoparticles (Figure 29, A-C). The peaks are typically observed in the range of 400-500 nm. However, peaks in a similar range can also be observed in Ag nanoparticles (Figure 29, D-F) and will be shifted depending on the size and shape of the particles, while Fe_3O_4 nanoparticles do not have characteristic absorption peak in a visible spectrum. Therefore, this analysis can confirm the presence of Ag though it does not necessarily mean that the composite Fe_3O_4-Ag was formed or that Fe_3O_4 is even present in the sample.

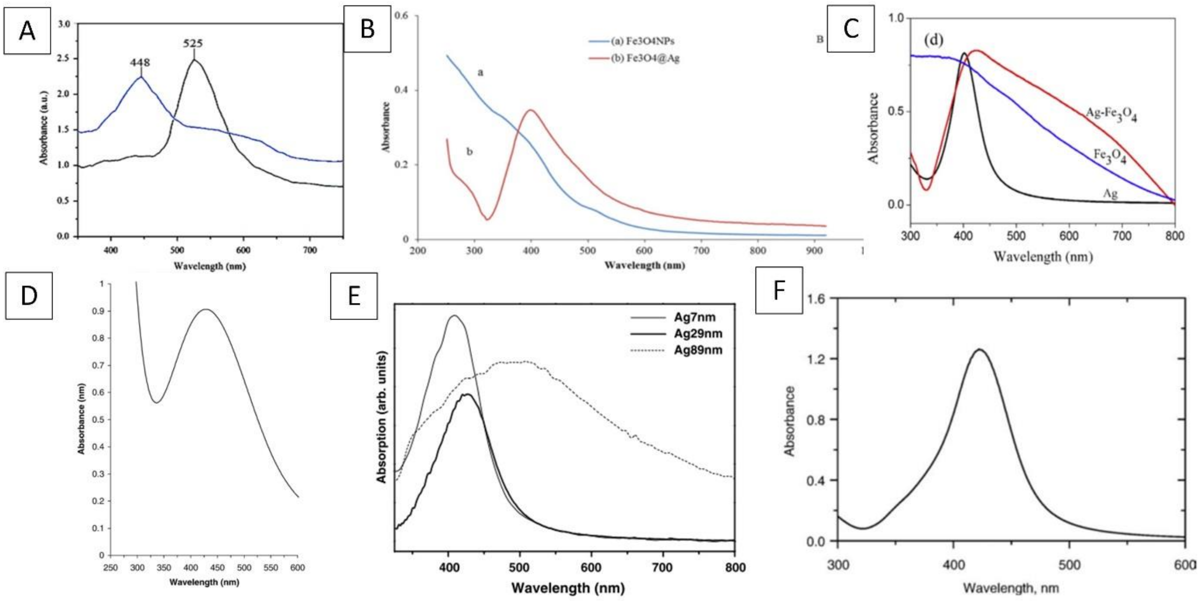

Figure 29. Visible absorbance spectrum of the composite Fe_3O_4-Ag: A - [139], B - [124],C - [134]; and Ag nanoparticles: D - [140], E - [141], F - [142].

In order to obtain a core-shell structure of nanoparticles, intermediate layers are often used between Fe_3O_4 and Ag: these can include carbon (Figure 30, A), TiO_2 (Figure 30, B) and SiO_2 (Figure 30, C). These layers can prevent particle agglomeration (C) or promote Ag precursor adsorption (TiO_2, SiO_2). The layer can also protect Fe_3O_4 from an acidic environment. The composites synthesised by using additional layers have definite core-shell structures.

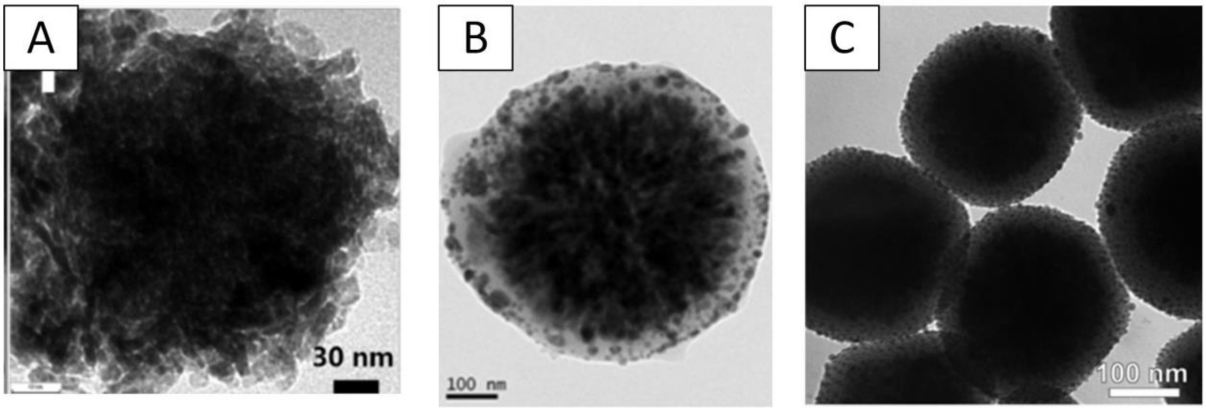

Figure 30. TEM images of Fe_3O_4-Ag core-shell nanoparticles with intermediate layer of A – carbon [143], B – TiO_2 [144], C – SiO_2 [126].

The most effective way to prove the core-shell structure formation is to do a mapping of the elements by EDX (Figure 31). This allows visualisation of the position of the elements in the image.

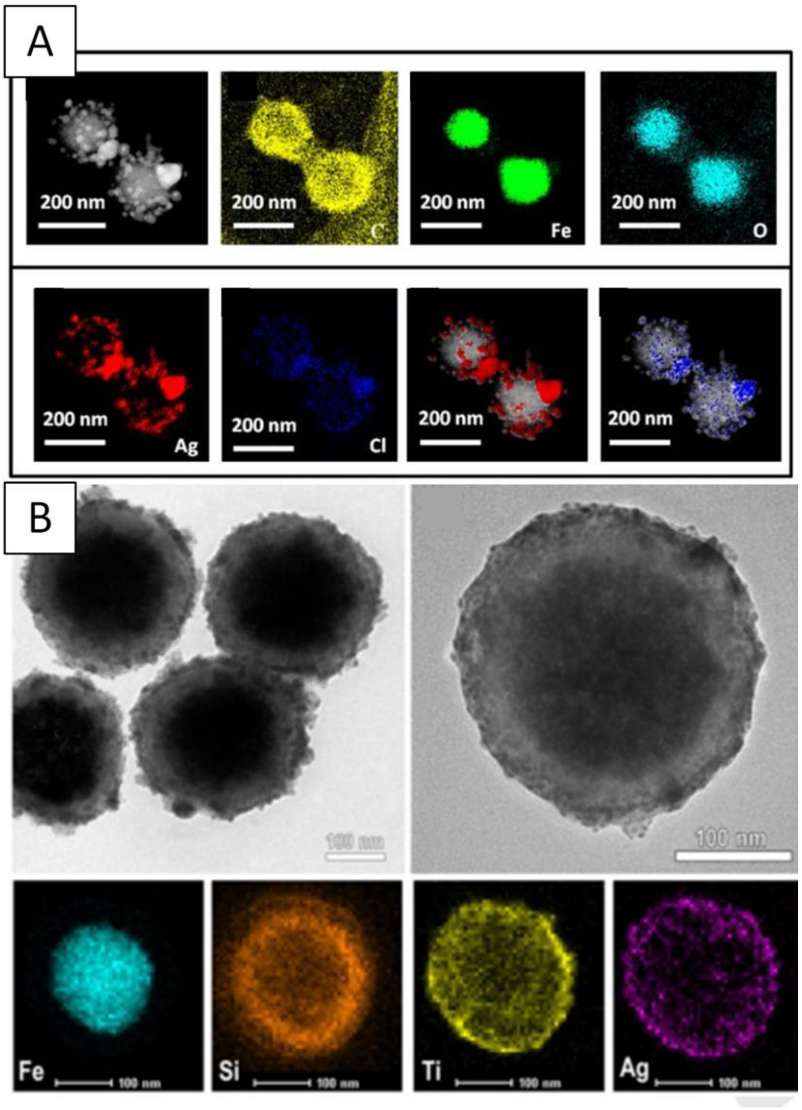

Figure 31. Element mapping of the composite nanoparticles by EDX analysis A – of the Fe_3O_4 – C – Ag nanoparticles [145], B – of the Fe_3O_4-SiO_2-TiO_2-Ag nanoparticles [146].

1.3.3 Scaling-up the synthesis of nanoparticles

Often the works which describe the methods of synthesis do not report the yield of the synthesis reaction. However, low yield can limit the application of the particles and increase their price. Even with high yield some processes are hard to scale-up in order to achieve an adequate amount of catalyst to conduct the required number of experiments.

Therefore, often special equipment is used in order to quickly synthesise large amount of nanoparticles by the bottom-up approach. The main problem associated with scaling-up the synthesis procedure is how to provide mixing of the solution during synthesis such that the reagents distribute equally and monodispersed particles can be synthesised. One of the methods which allows adequate mixing of solutions and scaling-up of the synthesis procedure is use of the spinning disc reactor (SDR) [147,148].

The reagents are mixed on the spinning disc (Figure 32, A) and form a thin film on the disc due to centrifugal forces. This intensifies the mass transfer during the reaction. The reacted mixture eventually leaves the disc due to centrifugal forces and is collected. In this way, the products of the reaction are excluded during synthesis and only unreacted reagents are supplied onto the disc in a controlled way.

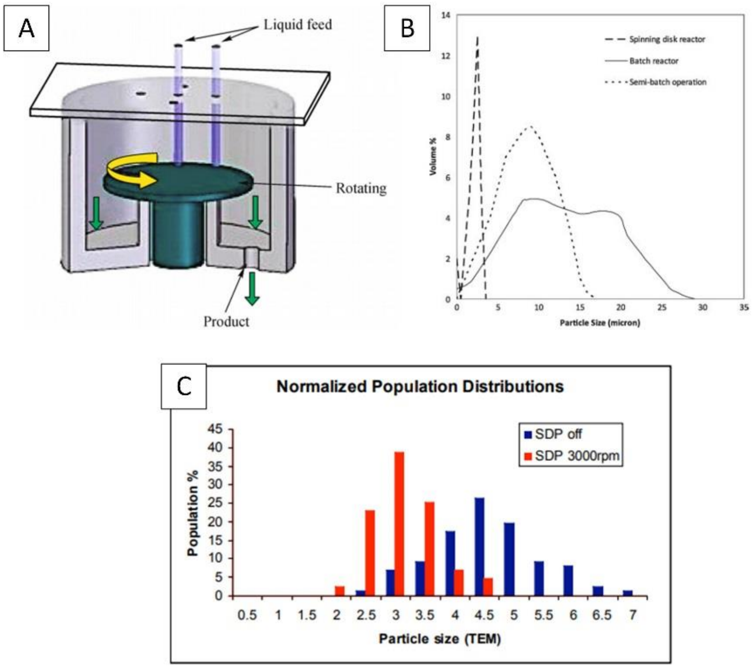

Figure 32. A – the set-up of the SDR [148], B – comparison of the nanoparticles size synthesised by conventional and SDR methods [147], C – comparison of the particles size distribution synthesised without disc rotation and at the rotation 3000 rpm [149].

By this approach Fe_3O_4 nanoparticles were synthesised [147,149]. It was reported that the size of the particles are reduced compared to the conventional co-precipitation method of synthesis (Figure 32, B). The size of the particles can also be altered by changing the rotation speed on the spinning disc (Figure 32, C).

1.3.4 Reproducibility of the nanoparticles synthesis

There are a large amount of works describing nanoparticle synthesis procedures, however reproducibility of the synthesis is rarely discussed or reported. The difficulties with synthesis reproduction can first of all arise due to the inaccurate reporting of the published preparation procedure. For example a paper was published by Gong et al [120] on the synthesis of Fe_3O_4-Ag core-shell nanoparticles. However, the amount of Ag precursor suggested in the paper would not be sufficient to cover the Fe_3O_4 nanoparticles and this synthesis procedure was found to be questionable by another research group [150]. It is rarely highlighted, but information regarding the synthesis procedure is often missing in the reports and insufficient for reproduction of the work.

Changes in nanoparticles can happen during drying and storage. Due to their high surface area the nanoparticles often have surface contamination [151] and oxide film formation [152,153] which affects their properties. The particles can agglomerate during storage. Particle transformations with aging were summarised by Baer [152]. (Figure 33, A). However, these issues are often underreported which makes it difficult to reproduce the synthesis.

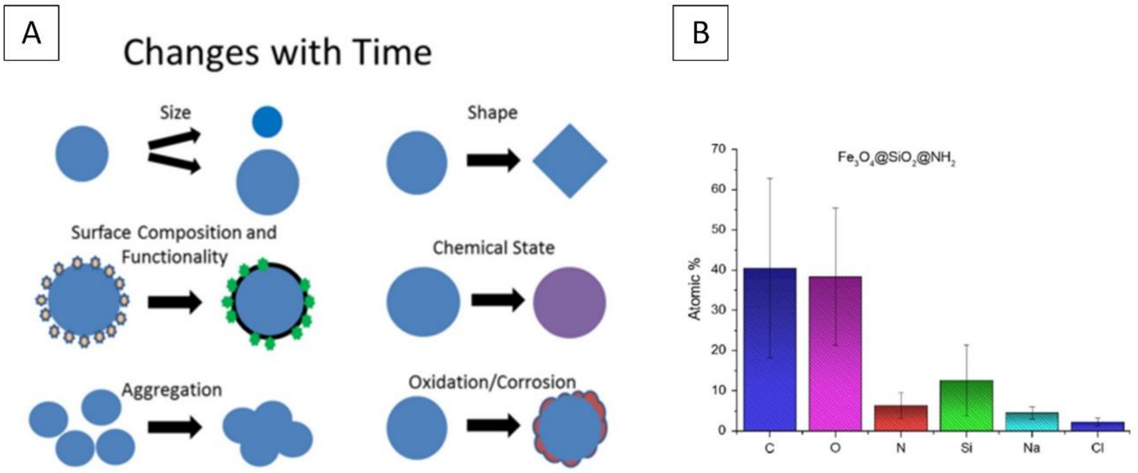

Figure 33 A – The chemical and physical changes of nanoparticles with time [152]. B – the results of inductively-coupled plasma (ICP) analysis of the composition of particles synthesised in different batches [154].

Even when the synthesis is reproduced by the same research group, variation can be observed batch to batch (Figure 33, B) [151,155].

As the issues are rarely reported with nanoparticle synthesis, the reproducibility of the syntheses should be controlled in order to ensure reproducibility of the other nanoparticle properties [151–153].

1.3.5 Methods of nanoparticles dispersion

Colloid nanoparticle dispersions consist of two phases: liquid (dispersant e.g. water) and solid (particles). Usually, dispersions are characterised by the size of the dispersed particles as shown in Table 10, although the systematisation may vary.

Table 10. The classification of dispersion by the size of dispersed solid particles [156].

Particle size, mm	10	1	10^{-1}	10^{-2}	10^{-3}	10^{-4}	10^{-5}	10^{-6}	$<10^{-6}$
Classification	Coarse dispersion (visible by naked eye)			Fine particulate dispersion			Colloidal dispersion		Solution
Total surface area, m^2/cm^3	$6x10^{-4}$	$6x10^{-3}$	$6x10^{-2}$	0.6	6	60	600	6000	

The nanoparticles can be used for their applications as synthesised. However to avoid the influence of the reaction products on the performance the particles can also be washed, dried and re-dispersed. In addition, when the particles are re-dispersed from the dry powder, the concentration can be precisely controlled.

In order to disperse particles in a liquid, magnetic or mechanical stirring can be used. The nanoparticles can agglomerate during drying and in order to break the chemical bonds other ways of dispersion should be considered for example ultrasonication and milling.

The concentration of the particles in dispersion affects their behaviour in the colloid. In “diluted” colloids the particles experience only Brownian motion and do not have interaction with neighbouring particles until collision. They can be called “vapour-like” colloids [157]. As the concentration of nanoparticles increases in the solution, the particles have more neighbouring particles with which to interact. They experience attractive and repulsive forces.

In order to overcome the attraction, electrostatic repulsion forces can be introduced into the colloid (the particles possess the surface charge and repel each other) or steric stabilization can be used (the particles are covered with a polymer molecule which sterically keeps particles apart so that Van der Waals forces cannot arise).

When the particle concentration increases the particles constantly experience interactions with neighbouring particles and this is called a solid-like colloid.

Often sedimentation can occur in colloid solution due to gravitational forces (Figure 34, B, C). The gravitational force acting on the particle is:

$$F_g = (4/3)\pi R^3 \Delta\rho g \tag{39}$$

where R – the particle radius, Δ ρ is the difference between the density of dispersant and particles, g is the acceleration due to gravity.

When this force exceeds the value of kT (k is the Boltzmann constant and T is the absolute temperature) the sedimentation of individual particles will occur. This sediment is usually hard to re-disperse due to the close position of the particles to each other and the resultant chemical bonds between them.

The particles can also experience flocculation (Figure 34 G-I) – the physical process of agglomeration which often can happen with sterically stabilized particles. Often this is because either a) the layer of polymer on the particles surface is too thin and cannot prevent particle interaction or b) excess polymer in the dispersion which causes particles to be attracted to each other, driven by osmotic pressure. Also bridging flocculation can occur when the polymer binds to several particles simultaneously due to incomplete surface coverage. When particles are strongly attracted to each other, a coagulation process can occur (Figure 34 D-F). Often coagulation and flocculation are used as synonymous terms, as no clear definition of each term exists. The colloid can exist in the states as shown in Figure 34.

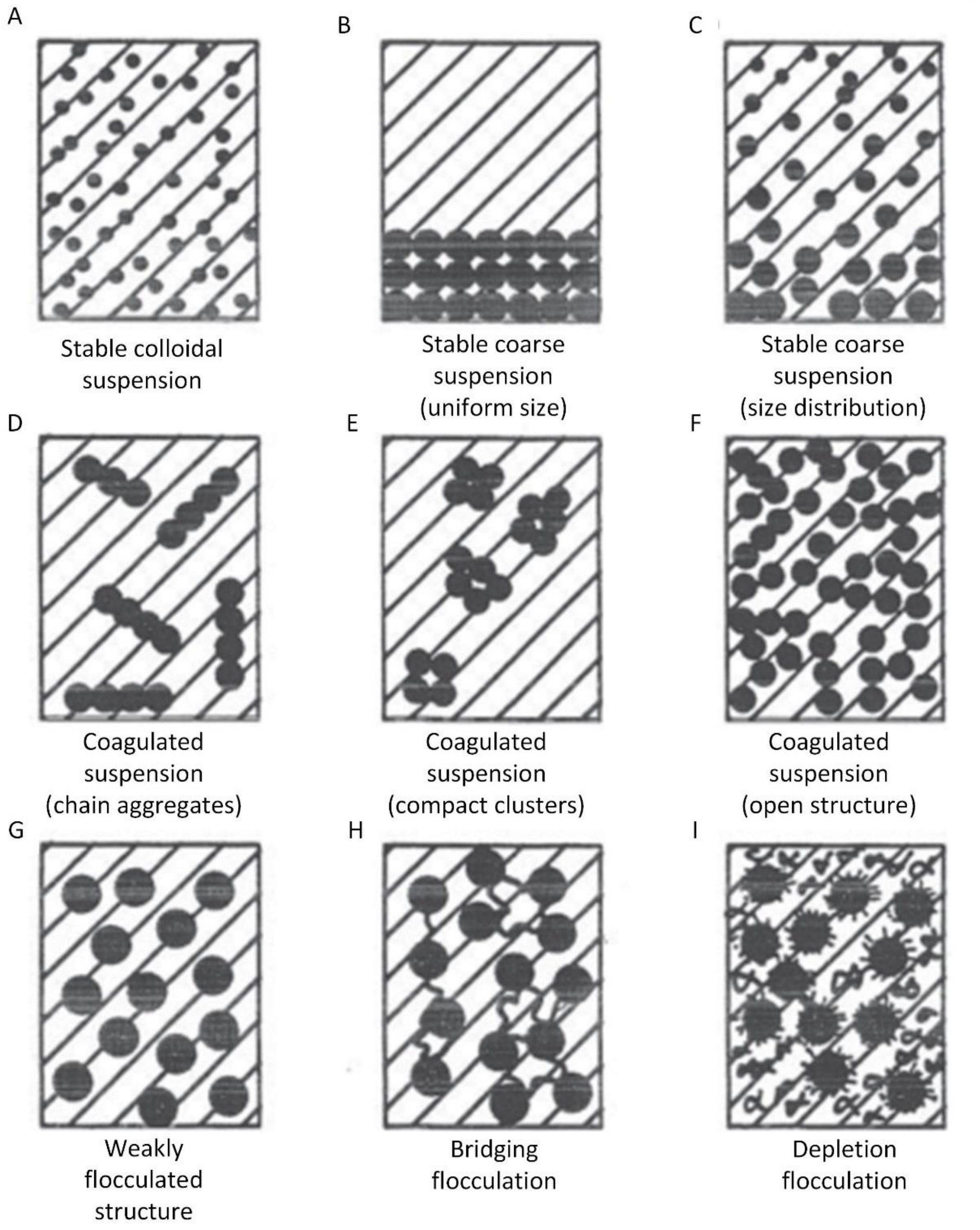

A Stable colloidal suspension

B Stable coarse suspension (uniform size)

C Stable coarse suspension (size distribution)

D Coagulated suspension (chain aggregates)

E Coagulated suspension (compact clusters)

F Coagulated suspension (open structure)

G Weakly flocculated structure

H Bridging flocculation

I Depletion flocculation

Figure 34. The possible distribution of the particles in the colloid dispersion [157].

1.3.6 Conclusion

There are a number of works that show that electrodeposition can be patterned by applying a gradient magnetic field. However, this requires interaction of an externally induced electric current with a gradient magnetic field, which is not present during normal electroless plating.

There is no evidence in the literature to suggest that selective deposition of metal during electroless plating via the application of a gradient magnetic field has been performed before. However there are a few premises to this study:

- the magnetic nanoparticles can be deposited selectively by applying a gradient magnetic field;
- catalyst nanoparticles can be used as a catalyst for the electroless copper plating process;
- the nanoparticles can be synthesised in such a way that they possess both magnetic and catalytic properties

Therefore, the present work focussed on:

1) Synthesis of magnetic-catalyst nanoparticles. There are range of synthesis procedures for composite Fe_3O_4-Ag nanoparticles. The surface area of the nanoparticles and their catalytic activity increase with a decrease in particle size. However, the magnetization saturation value decreases with nanoparticle size unless superparamagnetic nanoparticles are obtained. The superparamagnetic nanoparticles will be ideal for selective metallisation as their small size will allow for creation of precise patterns as well as allowing for a high surface area and catalytic activity. However, the methods of synthesis of these particles require the use of high temperature, high pressure and organic solvents which contradicts the idea of creating an environmentally more friendly process. Therefore, water-based syntheses at temperatures below 100 ^{o}C are considered.

2) The catalyst characterisation. The particle size, composition and crystal structure should be analysed in order to prove that the correct material was synthesised. After this, the magnetic and catalytic properties will be assessed. The catalytic activity of the particles should be characterised by both electrochemical methods and electroless Cu plating, as the electrochemical method does not give exact quantitative measurement and gives only a qualitative measure of the ability to catalyse the plating reaction.

3) As there has been no research performed on magnetic catalysts for electroless plating, the distribution of the catalyst under the magnetic field on the substrate surface and the quality of the subsequent electroless plating (its continuity and morphology) will be analysed in the present work.

Chapter 2. Methodology

2.1 Overview

This chapter contains the methods of electroless plating, synthesis methods of magnetic catalyst nanoparticles, methods of dispersion and methods of template fabrication and holder fabrication. The chapter will cover the following aspects of the methodology:

- The electroless plating of Cu onto the laminate substrate is a standard procedure which was modified during the research and the standard procedure is described.
- During the research it was found that the magnetic field does not have any patterning effect on electroless plating of Cu, therefore it was decided that replacing the standard Pd catalyst with a catalyst that is ferromagnetic would be a better option. The synthesis of the novel ferromagnetic catalyst is described.
- The catalyst for electroless plating usually deposits on the substrate surface from the solution or dispersion. The methods of catalyst nanoparticle dispersion preparation by ultrasonication and filtration are described.
- The methods of magnetic field application during catalyst deposition and electroless plating are described. First, the attachment of the single permanent magnet is described. Then, the simulation and fabrication of the template which is 'patterning' the magnetic field is detailed. Finally, a holder was made - which helped to keep the magnet, magnetic template and the substrate in the same place during deposition and protect it from the solutions.
- The characterisation techniques which were used throughout the research are described as well as the sample preparation for the analysis.
- The conclusion describes the final developed method of selective metallisation by applying a gradient magnetic field during electroless Cu plating.

The overall scheme of the performed research is presented at Figure 35. It started with standard electroless plating under a magnetic field influence. Then, the novel magnetic catalyst was synthesised and dispersed. The magnetic template and holder were then fabricated. At the end, selective electroless plating was performed by using the magnetic template and the novel magnetic catalyst.

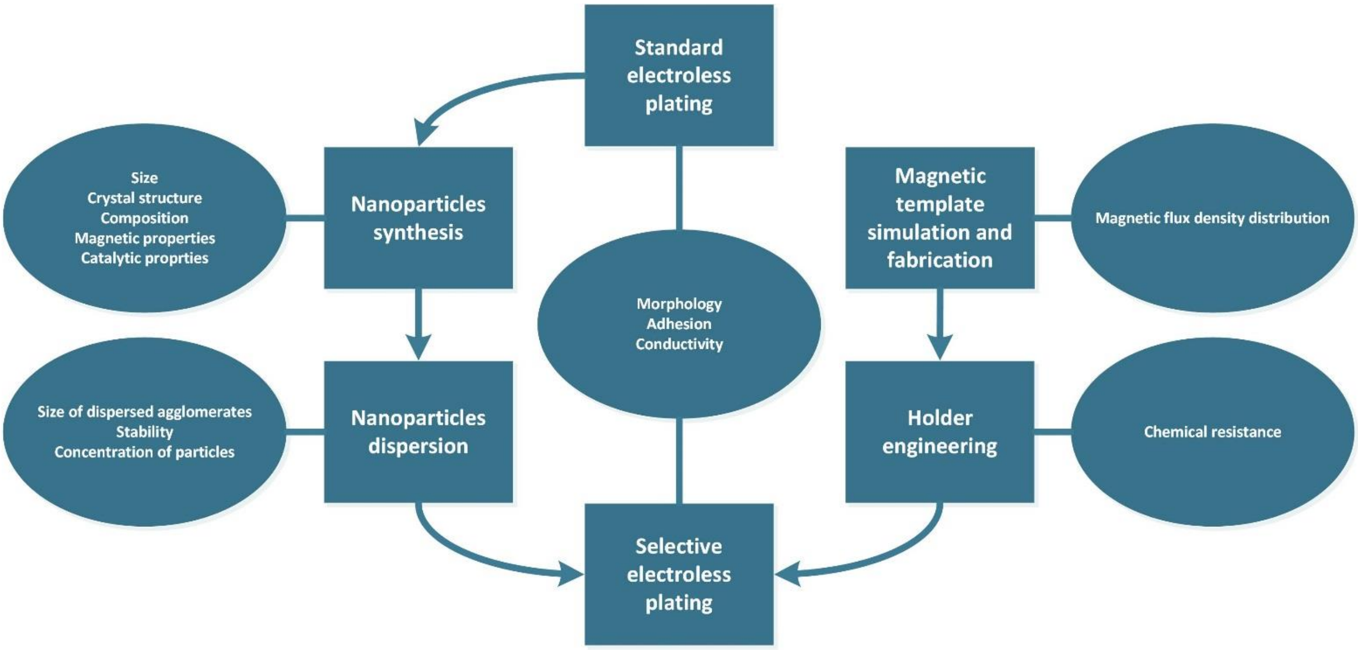

Figure 35. The overall scheme of the methodology.

2.2 Electroless Cu plating on non-conductive material

The procedure used in the current work for electroless plating of Cu onto non-conductive material was used in other studies [27,31,158]. Laminate substrate was first cut into 30 x 30 x 3 mm pieces.

The standard electroless Cu plating process (which was used as the control) has the following steps: substrate pre-treatment; catalyst deposition and electroless Cu plating. The plating line is depicted in Figure 36.

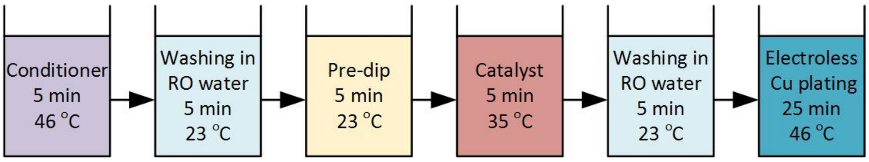

Figure 36. Schematic representation of stages of electroless Cu plating process including pre-treatment.

The reagents used to make the solutions were purchased from Dow Electronics.

Table 11. The reagents used in the electroless Cu plating process and their composition.

Name of the component	**Composition*, vol %**	**Present chemical**
Circuposit Conditioner 3320A	25 – 40	Glycolic acid
	7.0 - 10.0	P-toluenesulphonic acid, containing a maximum of 5% H_2SO_4
	5 – 7	Octylphenoxypolyethoxyethanol
	5 – 7	Sulphuric acid
	3 - 5	Ammonia, anhydrous
	3 – 5	Isopropanol
	0.25 - 0.5	Methoxyacetic acid
Circuposit Pre-Dip 3340/4400	12.5 – 15	Sodium hydrogensulphate
	60 - 80	Sodium chloride
Catalyst 3344/4444	15 – 20	Stannous Chloride
	7 - 10	Hydrochloric acid
		Pd source and concentration is not disclosed
3350 A - 1	25 - 40	Copper dichloride
3350 M - 1	20 – 25	Tetrasodium ethylene diamine tetraacetate
	60 - 80	Sodium chloride
Cuposit Y - 1	25 - 40	Formaldehyde
	1 – 2.5	Methanol
Cuposit Z - 1	40 - 60	Sodium hydroxide

* The composition as provided by the supplier.

The solutions were made according to the following procedure:

1) *Conditioner solution preparation procedure*:

The water purified by reverse osmosis (RO water) in amount 450 ml and 50 ml Circuposit Conditioner 3320A (the information about all reagents used in the procedure is shown in Table 11) were mixed and heated to 46°C while vigorously stirring.

2) Pre-dip solution preparation procedure:

Circuposit Pre Dip 3340/4400 (135 g) was dissolved in 420 ml RO water until clear. Then the solution was made up to 500 ml using RO water. The solution was operated at room temperature (on average 23 ^{o}C).

3) Pd catalyst solution preparation procedure (only for Chapters 3 and 7):

Circuposit Pre-Dip 3340/4400 (135 g) was dissolved in 450 mL RO water and stirred until clear. Then, 10 ml of Circuposit Catalyst 3344/4444 and 3 ml Cataposit 449 were added. During continuous stirring the solution was heated up to 35^{o}C.

4) Electroless copper plating solution preparation procedure:

Circuposit 3350 M-1 (75 ml), 5 ml Circuposit 3350 A-1 and 5.25 ml Cuposit Z-1 were added to 410 ml RO water during vigorous stirring. Then the solution was heated up to 46^{o}C and 5.7 ml Cuposit Y-1 was added.

The obtained electroless copper deposit was characterised by:

- scanning electron microscopy – for morphology evaluation of the deposited copper.
- resistance measurement – used in order to confirm that the coating is conductive.
- adhesion testing – this was performed on part of the sample in order to compare the plating adhesion to the surface of the non-conductive substrate (see Section 2.7 for more details).

2.3 Nanoparticle catalyst synthesis

The standard Sn/Pd catalyst does not have ferromagnetic properties [88] and therefore was not attracted by the magnet. As a replacement, a novel magnetic catalyst was synthesised (the results are described in Chapter 4) that comprised of magnetic (Fe_3O_4) and catalytic (Ag) particles by the following procedures (Table 12):

- The magnetic Fe_3O_4 nanoparticles (S1, S2) were synthesised first and then the Ag was reduced in the presence of Fe_3O_4. The concentration of the Ag precursor was varied.
- The one-pot synthesis of nanocomposite and functionalization of particles during the synthesis by polyvinylpyrrolidone (S3) and arginine (S4).
- The core-shell particles were synthesised by locating the reducing agent at the magnetic nanoparticle surface (S5).

Table 12. Summary of all nanoparticle synthesis procedures used in this work.

Code name of the nanoparticles	Synthesis of Fe_3O_4	Synthesis of Ag	Additives	Reference
S1	Precipitation reaction of $FeSO_4$ and NH_4OH			[114]
S1 – 1; S1 – 2; S1 – 3; S1 - 4	S1 at different amount	Reduction of $AgNO_3$ at different concentrations by $NaBH_4$		[124,132]
S2	S1		Reaction carried out on spinning disc reactor	
S2 – 3; S2 - 4	S2	Reduction $AgNO_3$ at different concentrations by $NaBH_4$		
S3	Co-precipitation $FeSO_4$ and $FeCl_3$ by NH_4OH	Reduction $[Ag(NH_3)_2]NO_3$ by $NaBH_4$	Polyvinylpyrollidone	[133]
S4	Precipitation of $FeSO_4$ by arginine	Reduction of $AgNO_3$ by arginine Reduction $[Ag(NH_3)_2]NO_3$ by SnCl	Arginine	[135]
S5	S1	Reduction of $AgNO_3$ by arginine Reduction $[Ag(NH_3)_2]NO_3$ by SnCl	SiO_2	[159]

2.3.1 Iron oxide synthesis

- **Procedure 1 (S1)**

NH_4OH solution of concentration 25%, Sigma Aldrich in amount 20 ml was added drop-wise to a RO water solution of 0.01 M $FeSO_4 x 7 H_2O$, Fisher Scientific. The mixture was magnetically stirred for 1 hour at room temperature. Then the solution was filtered and washed with RO water 3 times. Collected materials were left to dry overnight at 50 ^oC in the oven.

- **Procedure 2 (S2)**

Synthesis was conducted using a SDR. The scheme of the SDR is presented in Figure 37, A and the disc itself in Figure 37, B. In short, both of the reagents were pumped with a speed of 60 ml/min and were supplied at the centre of the spinning disc. The disc rotated with a speed of 3000 rpm. During the rotation the reagents are mixed and moved by centrifugal force to the side of the disc and on the reactor wall. The liquid is moved down by gravity and collects at the bottom of the reactor.

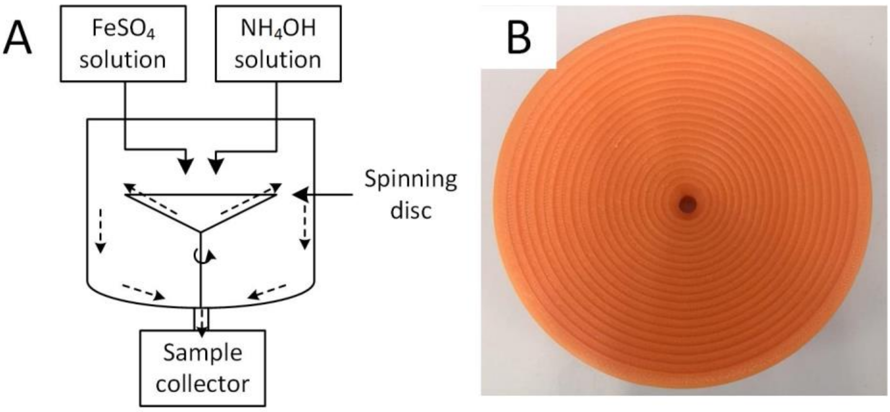

Figure 37. A - The scheme of the spinning disc reactor and the principle of its action; B – photo of the spinning disc.

After collection the solution was stirred for 1 hour. Then the particles were separated from the products of reaction using a magnet and washed 3 times with RO water. The obtained particles were then dried in the oven overnight at 50 ^{o}C.

2.3.2 Composite particles synthesis

- **Calculation of the concentration of precursors**

The initial idea was to create core-shell nanoparticles by Ag reduction in the presence of Fe_3O_4. Calculations were made in order to estimate the amount of Ag required to cover the Fe_3O_4 nanoparticles. These calculations were made with the following assumptions:

- Iron oxide nanoparticles are spherical particles
- The radius of iron oxide is equal to the average calculated radius of particles obtained from TEM;
- Iron oxide nanoparticles are well dispersed so all of the surface is accessible for the reaction;
- The yield of the Ag reduction reaction is 100%;
- All silver is reduced on the Fe_3O_4 particles surface and is distributed evenly across the surface.

Based on the radius of the particles the volume of one particle can be calculated:

$$V = \frac{4\pi r^3}{3} \tag{40}$$

From the volume of the particle and density (the density of Fe_3O_4 is $\rho = 5.17\ g/cm^3$), the mass of one particle can be obtained:

$$m = V\rho \tag{41}$$

The overall mass of the particles can be varied and determined, therefore the number of Fe_3O_4 particles can be calculated using the following equation:

$$N = \frac{m_{overall}}{m_{1\,particle}} \tag{42}$$

The surface area of Fe_3O_4 nanoparticles can be determined with the equation for the surface area of sphere:

$$S_{1\,particle} = 4\pi r^2 \tag{43}$$

Then the overall surface area of all Fe_3O_4 particles will be:

$$S_{overall} = S_{1\,particle} * N \tag{44}$$

The mass of the reduced silver can be calculated from following equation, considering the mass of $AgNO_3$ is known and 100% of Ag ions are reduced in the following reaction:

$$2AgNO_3 + 2NaBH_4 \rightarrow 2Ag^0 + H_2 + B_2H_6 + 2NaNO_3 \tag{45}$$

The amount of reacting $AgNO_3$ in moles will be:

$$n = \frac{m\ (AgNO_3)}{M\ (AgNO_3)} \tag{46}$$

According to reaction (45) the mole amount of reacting $AgNO_3$ is equal to the mole amount of obtained Ag so the mass of Ag can be calculated:

$$m(Ag) = n * M(Ag) \tag{47}$$

Next, the volume of the obtained silver can be calculated:

$$V = \frac{m}{\rho} \tag{48}$$

Finally, the thickness of the deposited Ag layer can be obtained:

$$h = \frac{V}{S} \tag{49}$$

Therefore the silver layer thickness depends on the mass of Fe_3O_4 and $AgNO_3$ and also on the size of the Fe_3O_4 nanoparticles and can be described by the equation:

$$h = 0.164\frac{m(AgNO_3) * r(Fe_3O_4)}{m(Fe_3O_4)} \tag{50}$$

By following the previously described calculations, the synthesis procedures were established as shown in Table 13.

For the S2 composites S2 – 3 and S2 - 4 the concentrations were used as for S1 - 3 and S1 - 4 synthesis respectively. The schematic representation of the composite synthesis is shown at Figure 38.

Table 13. The parameters of performed syntheses and calculated "shell" thickness of the core-shell particles formed.

Synthesis code name	Amount of Fe_3O_4, g	Radius of Fe_3O_4, nm	Amount of $AgNO_3$, g	Thickness of the silver shell, nm
S1 – 1	0.6	31.5	0.17	1.5
S1 – 2	0.3	31.5	0.17	3.0
S1 – 3	0.1	31.5	0.17	8.8
S1 – 4	0.1	31.5	1.70	87.9
S2 – 3	0.1	11.0	0.17	3.1
S2 – 4	0.1	11.0	1.70	30.7

- **Synthesis procedure of the S1 and S2 based composites.**

This procedure is a modified synthesis from a previous work [114]. The Fe_3O_4 nanoparticles were dispersed by magnetic stirring in 300 ml of RO water for 10 min. Then, 100 ml of $AgNO_3$ (99.9 %. Alfa Aesar) solution was added. After the mixing, 30 ml of 0.1 M $NaBH_4$ (98 %, Sigma Aldrich) solution was added dropwise. The solution was then left to stir for 10 min. Afterwards, the nanoparticles were separated by a magnetic field and washed 3 times with RO water. The particles were dried overnight in the oven at 45 °C.

- **Synthesis procedure of S3 composite**

$FeSO_4 \cdot 7\ H_2O$ (99%, Fisher scientific) and $FeCl_3 \cdot 6\ H_2O$ (99% ACROS Organics) in amounts of 0.5 g and 0.16 g respectively were dissolved in 20 ml RO water. Then, 0.1 g of polyvinylpyrrolidone (MW=40000, ACROS Organics) was added and stirred until dissolved. NaOH (Extra Pure, Fisher Chemical) solution in amount 10 ml of concentration 0.01 M was then added dropwise. Then the mixture was stirred for 30 min at 40 ^oC after which 15 ml of $[Ag(NH_3)_2]NO_3$ solution was added. After stirring, 20 ml of 0.83 M $NaBH_4$ solution was then added dropwise. The solution was left to react for 1 h at 40 ^oC.

Fresh $[Ag(NH_3)_2]NO_3$ was prepared by dissolving 15 mg of $AgNO_3$ in 2 ml RO water, then 10 % NH_4OH was added dropwise during vigorous stirring. At first, a brown precipitate formed (Ag_2O) which was diluted with further addition of NH_4OH. When the precipitate completely dissolved the addition of NH_4OH was stopped. The volume of solution was then made up to 15 ml by addition of RO water.

After the reaction completed, nanoparticles were separated by a magnet from the dispersion and washed with RO water. Washing was repeated 3 times. Then the particles were dried at 45 ^oC in the oven overnight.

- **Synthesis procedure of S4 composite**

In RO water (250 ml) were dissolved $FeSO_4 \cdot 7\ H_2O$ (1.39 g) and arginine (99%, Sigma Aldrich) (5g). The solution was stirred for 1 h at 70 ^oC. $AgNO_3$ (0.85 g) and arginine (5 g) were dissolved in 250 ml RO water and added to the first solution. The mixture was left to stir for 8 h at 70 ^oC.

After that, nanoparticles were separated with a magnet and washed in RO water 3 times. The particles were dried at 45 ^oC overnight.

- **Synthesis procedure of S5 composite**

Fe_3O_4 (0.05 g), synthesised as described in procedure S1, was dispersed in 100 ml methanol (Extra Pure, Fisher Chemical) and 10 ml 25% NH_4OH mixture by ultrasonication for 10 min. Then 0.02 ml of tetraethyl orthosilicate (98%, ACROS Organics) was added and the dispersion was ultrasonicated for a further 2 h. After that, particles were separated by a magnet and washed 3 times in methanol. Then, particles were re-dispersed in 50 ml solution of 0.6 g $SnCl_2$ (pure, Fisher Chemical) and 0.01 M HCl (Fisher Chemical) by ultrasonication for 30 min. The particles were washed in RO water and re-dispersed in 50 ml 0.13 M $[Ag(NH_3)]NO_3$ by ultrasonication for 1 h.

Then the obtained particles were magnetically separated, washed in RO water 3 times and dried overnight at 45 °C.

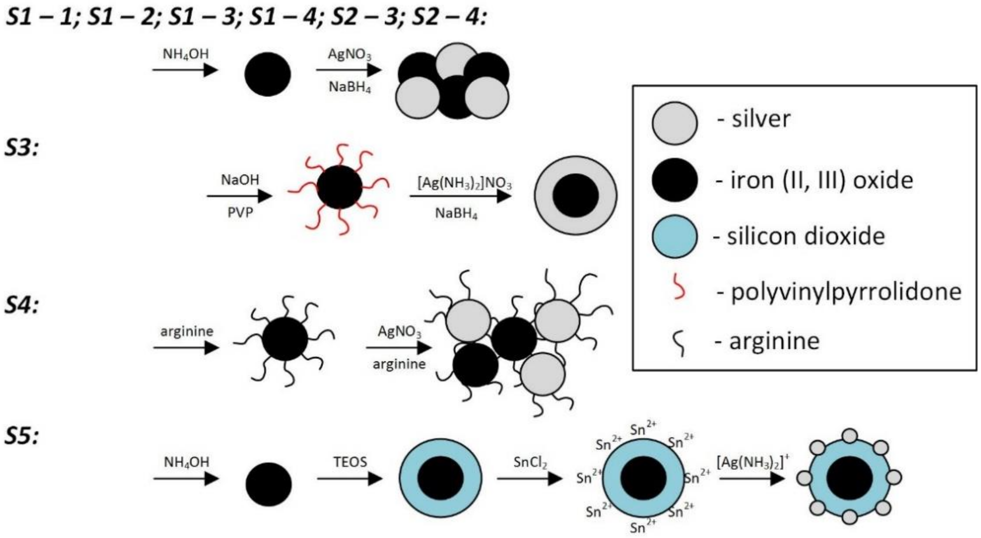

Figure 38. Schematic representation of the composite nanoparticle synthesis.

The nanoparticles were characterised by the following methods:

1) Size and chemical composition were determined by SEM, EDX, TEM and ICP
2) The crystal structure was determined by x-ray diffractometry (XRD).
3) The magnetic properties were first evaluated by a preliminary test (placing the magnet near the vial with particles to see if they were attracted) and later by vibrating sample magnetometry.
4) The catalytic activity was characterised by CV and confirmed by actual plating.

2.4 Catalyst dispersion

- **Ultrasonication equipment**

A Langford 575 ultrasonication cleaning unit was used with an operating frequency of 40 kHz, applied ultrasonic power of 300 W and a volume of 3.6 L. The operating power of the ultrasonication bath was estimated by the calorimetry method [160], with change of temperature over 20 min of bath operation being measured. The experiment was repeated 3 times. Then the power was calculated by using equation 51.

$$P = \frac{dT}{dt} C_p m, \tag{51}$$

where P – is power of the ultrasonication, $\frac{dT}{dt}$ – the change of temperature over time, C_p – heat capacity of the solvent, m – the mass of solvent.

The calculated power of the ultrasonication in 100 ml of water is 1.4 W.

The positioning of the beaker in the ultrasonication bath is depicted in Figure 39.

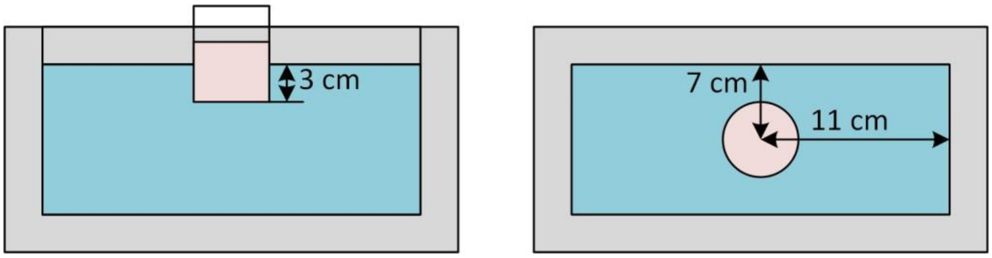

Figure 39. The position of the beaker in the ultrasonication equipment side view (left) and top view (right).

- **Dispersion preparation**

Dried synthesised nanoparticles (0.25 g) obtained by procedure 1 (S1) were placed in 100 ml RO water (or 0.01 M HCl for S4 pH2 sample) in a 150 ml glass beaker. The beaker then was placed in the ultrasonication bath and ultrasonicated for 5 or 30 min (Figure 40).

Often ultrasonication can cause significant heating of the water in both the bath and beaker. This was not usually observed after 30 min ultrasonication. However, if ultrasonication was performed in immediate succession heating of the dispersion up to 40 °C was observed. The change in temperature affects the magnetic properties of the materials [161]. Therefore, the experiments were conducted after at least 15 min equipment rest time.

- **Filtration**

After ultrasonication some of the dispersions were filtered. Moistened qualitative filter paper QL 120 Fisherbrand (pore size is 6 μm) was placed in a Buchner funnel. Vacuum filtration was used. The collected filtrate was placed in a 250 ml beaker in order to conduct further depositions.

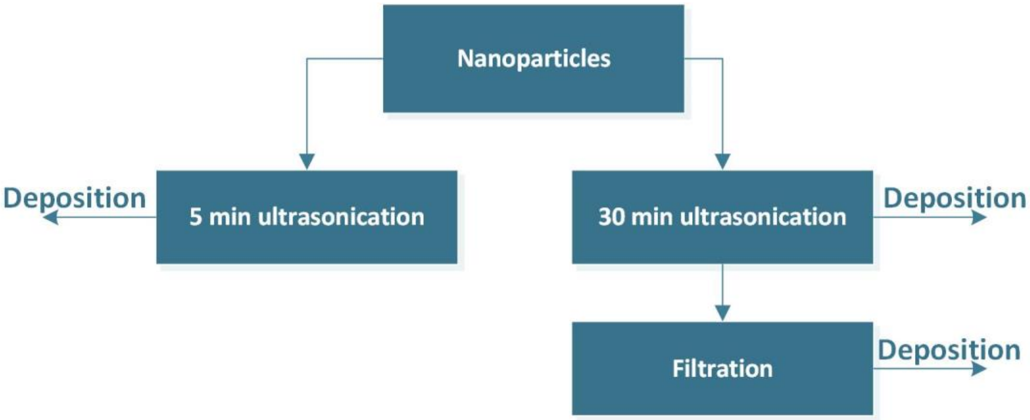

Figure 40. Schematic flow chart of the experiments on the dispersion of nanoparticles.

2.5 Gradient magnetic field application during electroless Cu plating

Two set-ups of magnet and substrate arrangement were used in order to apply the magnetic field to the substrate surface:

- **Set-up 1**

This set-up was used for 3 mm thick laminate substrate (Chapter 5). A Ni-Cu-Ni plated NdFeB N42 (N refers to Neodymium while 42 is the strength of the magnet in MGOe) magnet with dimensions 10 x 5 x 2 mm was used (the north and south pole are on opposite 10 mm x 5 mm faces). The magnet was attached to one side of the substrate by tape (Figure 41). The opposite side was a working side where the plating was expected to be obtained.

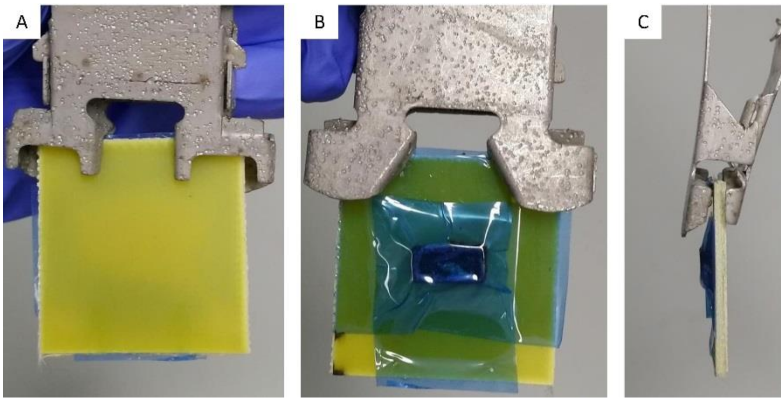

Figure 41. The set-up for the magnetic field application to the substrate. A – the working side of the substrate, B – the side with the magnet attached, C – side view of the substrate.

Subsequently, the substrate was subjected to the procedure described in section 2.2 of methodology with minor modifications:

- The catalyst dispersion was not stirred and used straight after preparation.
- Electroless Cu plating solution (80 ml) was used per sample. The solution was not stirred during deposition – magnetic stirring was not possible due to the interaction between the stirrer and attached magnet.
- Mechanical stirring was not used for the same reasons – in order to avoid disruption resulting from movement of the blades. Another method of dispersion is ultrasonication. However, due to weak interactions between the magnetic field and the catalyst particles, the catalyst particles were displaced by ultrasonication.

❖ **Set-up 2**

The second set-up included use of the template and holder (Chapter 7).

1) Simulation of the magnetic template

The magnetic template was developed in order to “pattern” the magnetic field. First, 2D simulations of the magnetic flux density distribution across the substrate surface were performed using Finite Element Method Magnetics (FEMM) software.

A schematic representation of the simulation is shown in Figure 42. The parameters of the simulated cases are presented in Table 14. More details and results of simulations are described in Chapter 6.

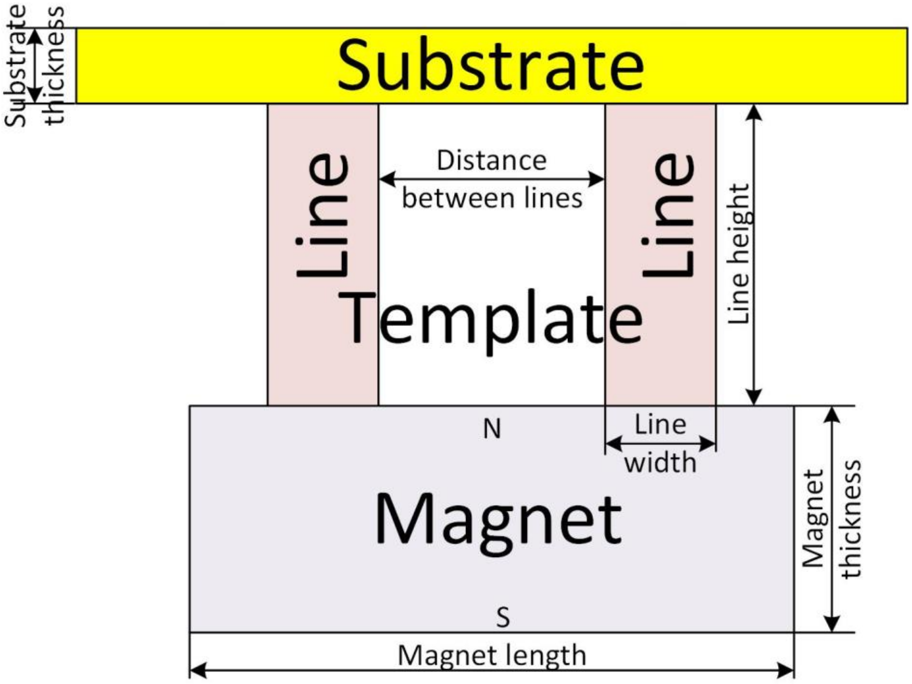

Figure 42. The scheme of the simulated set up with the terminology used. Template consisted of “lines” – the metallic parts of the template which provide the gradient magnetic field.

Table 14. The parameters of the magnetic template simulations.

Number	**Line width, mm**	**Line height, mm**	**Distance between lines, mm**	**Magnet length, mm**	**Magnet thickness, mm**	**Number of lines**	**Magnet orientation towards substrate surface**	**Substrate thickness, mm**
1	0.5	1	0.5	10	2	10	Perpendicular	3
2	0.5	1	0.5	10	2	10	Perpendicular	0.41
3	0.5	2	0.5	10	2	10	Perpendicular	0.41
4	0.5	3	0.5	10	2	10	Perpendicular	0.41
5	0.5	4	0.5	10	2	10	Perpendicular	0.41
6	0.5	5	0.5	10	2	10	Perpendicular	0.41
7	0.5	6	0.5	10	2	10	Perpendicular	0.41
8	0.5	7	0.5	10	2	10	Perpendicular	0.41
9	0.5	8	0.5	10	2	10	Perpendicular	0.41
10	0.5	9	0.5	10	2	10	Perpendicular	0.41
11	0.5	10	0.5	10	2	10	Perpendicular	0.41
12	0.5	15	0.5	10	2	10	Perpendicular	0.41
13	0.5	20	0.5	10	2	10	Perpendicular	0.41
14	0.5	25	0.5	10	2	10	Perpendicular	0.41
15	0.5	30	0.5	10	2	10	Perpendicular	0.41
16	0.5	35	0.5	10	2	10	Perpendicular	0.41
17	0.5	40	0.5	10	2	10	Perpendicular	0.41
18	0.5	45	0.5	10	2	10	Perpendicular	0.41
19	0.5	50	0.5	10	2	10	Perpendicular	0.41
20	0.5	60	0.5	10	2	10	Perpendicular	0.41
21	0.5	70	0.5	10	2	10	Perpendicular	0.41
22	0.5	80	0.5	10	2	10	Perpendicular	0.41
23	0.5	90	0.5	10	2	10	Perpendicular	0.41
24	0.5	100	0.5	10	2	10	Perpendicular	0.41
25	0.5	1	0.5	2	2	10	Perpendicular	0.41
26	0.5	1	0.5	6	2	10	Perpendicular	0.41
27	0.5	1	0.5	10	2	10	Perpendicular	0.41
28	0.5	1	0.5	14	2	10	Perpendicular	0.41
29	0.5	1	0.5	18	2	10	Perpendicular	0.41
30	0.5	1	0.5	10	1	10	Perpendicular	0.41

Table 14 (continued).

31	0.5	1	0.5	10	2	10	Perpendicular	0.41
32	0.5	1	0.5	10	3	10	Perpendicular	0.41
33	0.5	1	0.5	10	4	10	Perpendicular	0.41
34	0.5	1	0.5	10	5	10	Perpendicular	0.41
35	0.5	1	0.5	10	10	10	Perpendicular	0.41
36	0.5	1	0.25	10	2	10	Perpendicular	0.41
37	0.5	1	0.75	10	2	10	Perpendicular	0.41
38	0.5	20	0.75	20	10	16	Perpendicular	0.41
39	0.5	20	0.75	20	10	16	Parallel*	0.41

*Typically for patterning purposes the magnet was placed perpendicular to the substrate surface. Therefore the perpendicular orientation was most often simulated.

2) Template fabrication

The dimensions of the template were in accordance with simulation number 38 and it was made from 080A15 steel cut into the desired shape by a wire-cut electrical discharge machine. The scheme of the template is shown in Figure 43. The photo of the template is shown at Figure 44, A.

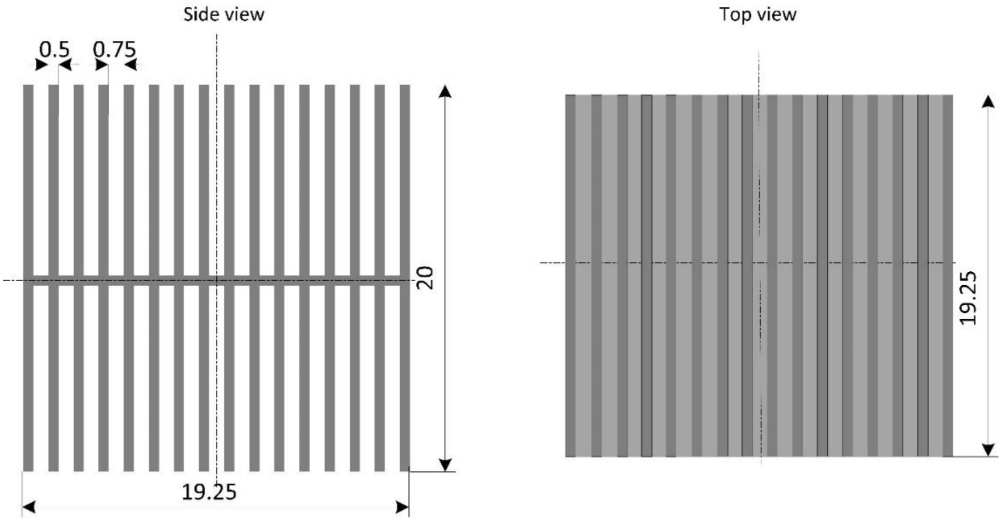

Figure 43. The scheme of the magnetic steel template side (left) and top view (right). The dimensions are in mm.

3) Holder fabrication

A holder was made in order to secure the sample, template and magnet as well as protect them from the electroless plating solution. The set-up of the magnet, template and substrate and how it was positioned in the holder are presented at Figure 44, B. The scheme of the holder (Figure 44, C) is presented at Figure 45. A polyether ether ketone (PEEK) holder and screws were used. PEEK is resistant to reaction with the formaldehyde and NaOH solutions at elevated temperatures [162]. The o-rings were made from ethylene propylene diene monomer rubber which also has excellent resistance to reaction with the formaldehyde and NaOH solutions [163].

After the experiments the holder was etched using a mixture of 3% H_2SO_4 and 3% H_2O_2 solutions until the Cu was entirely removed. The holder was then washed by RO water and dried in the air.

The holder was positioned in the solution according to Figure 44, D. Agitation was provided via mechanical stirring.

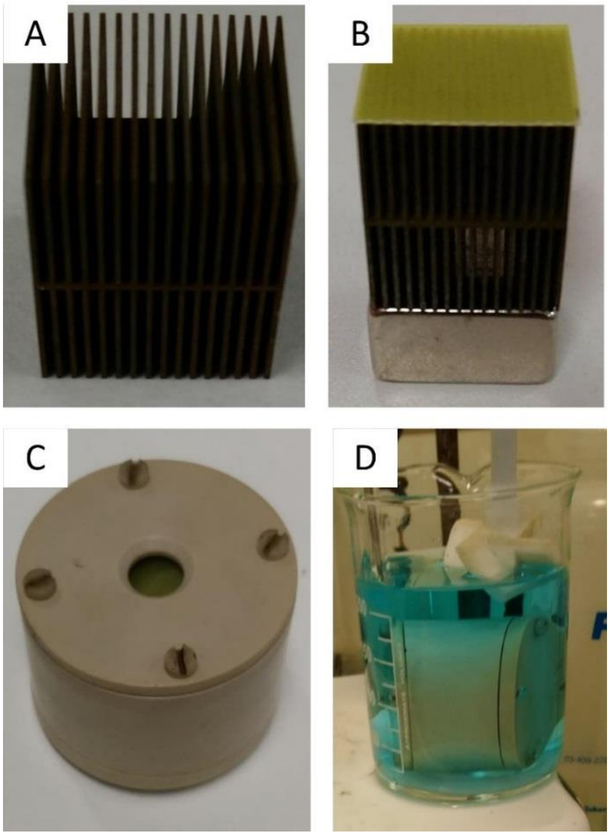

Figure 44. Photographs of A – magnetic template, B – magnet, magnetic template and substrate assembled together, C – the holder with magnet, magnetic template and substrate inside, D - the electroless plating set-up with holder placed inside.

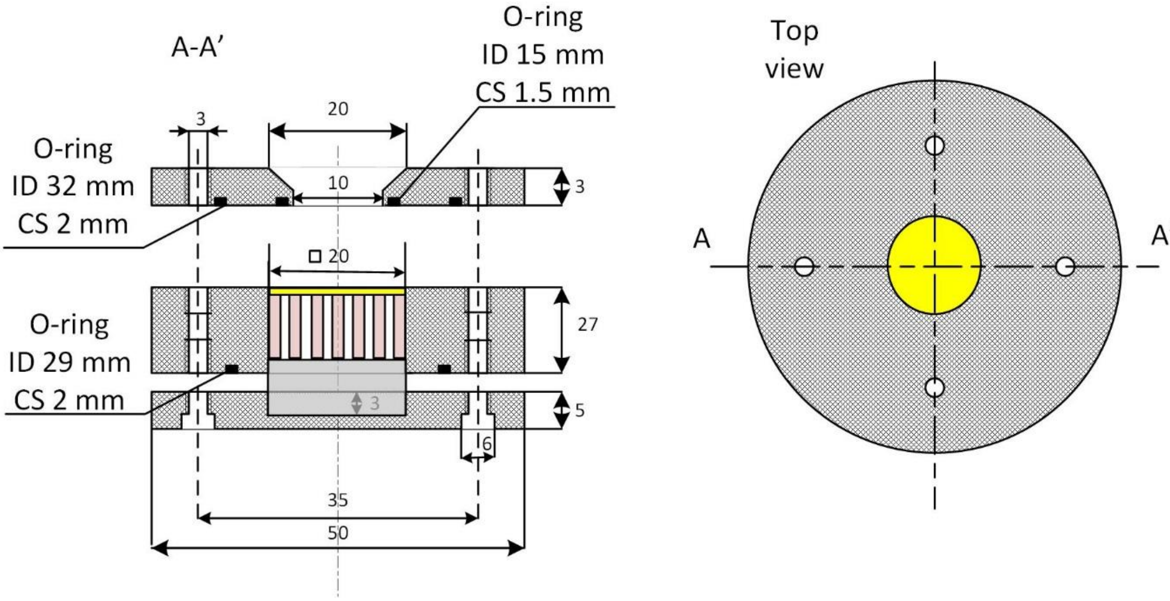

Figure 45. Drawing of the holder from the side (left) and from top (right). The set-up of magnet, template and the substrate depicted inside the holder.

4) Substrate pre-treatment

In order to pre-treat the laminate surface the ‘swell-and etch’ approach was used. First, the substrate was placed in ethylene glycol pre-heated to 80 °C for 10 min. Ethylene glycol softened the polymer so the substrate is “swelled”. After rinsing in water for 2 min, the substrate was then placed in 80 °C 75 g/dm^3 $KMnO_4$ and 40 g/dm^3 NaOH solution for 20 min. The potassium permanganate selectively etched the surface. Subsequently, the substrate was placed in a solution containing 3% by volume of both 98% H_2SO_4 and 37% H_2O_2 in order to neutralise the $KMnO_4$ on the substrate surface. Then, the substrates were rinsed in RO water for 5 min and dried in the air.

2.6 Selective electroless plating under the magnetic field influence

First the experiments were performed using the single magnet configuration (Figure 41). All obtained catalysts were tested after 5 min ultrasonication, 30 min ultrasonication and 30 min ultrasonication with subsequent filtration. The experiment plan including catalyst deposition time is shown in Figure 46.

The catalysts which showed the best performance (where Cu plating was obtained) were tested by using the second configuration, with the magnetic template. The choice of ultrasonication treatment applied to the catalysts was based on previous performance. S5 catalyst was ultrasonicated for 30 min with subsequent filtration while the S4-based catalysts were simply ultrasonicated for 30 min. Catalyst S4 was also dispersed in a solution with pH2 (in 0.01 M HCl solution) for 30 min without filtration. S1-3 catalyst was ultrasonicated for 5 min before deposition.

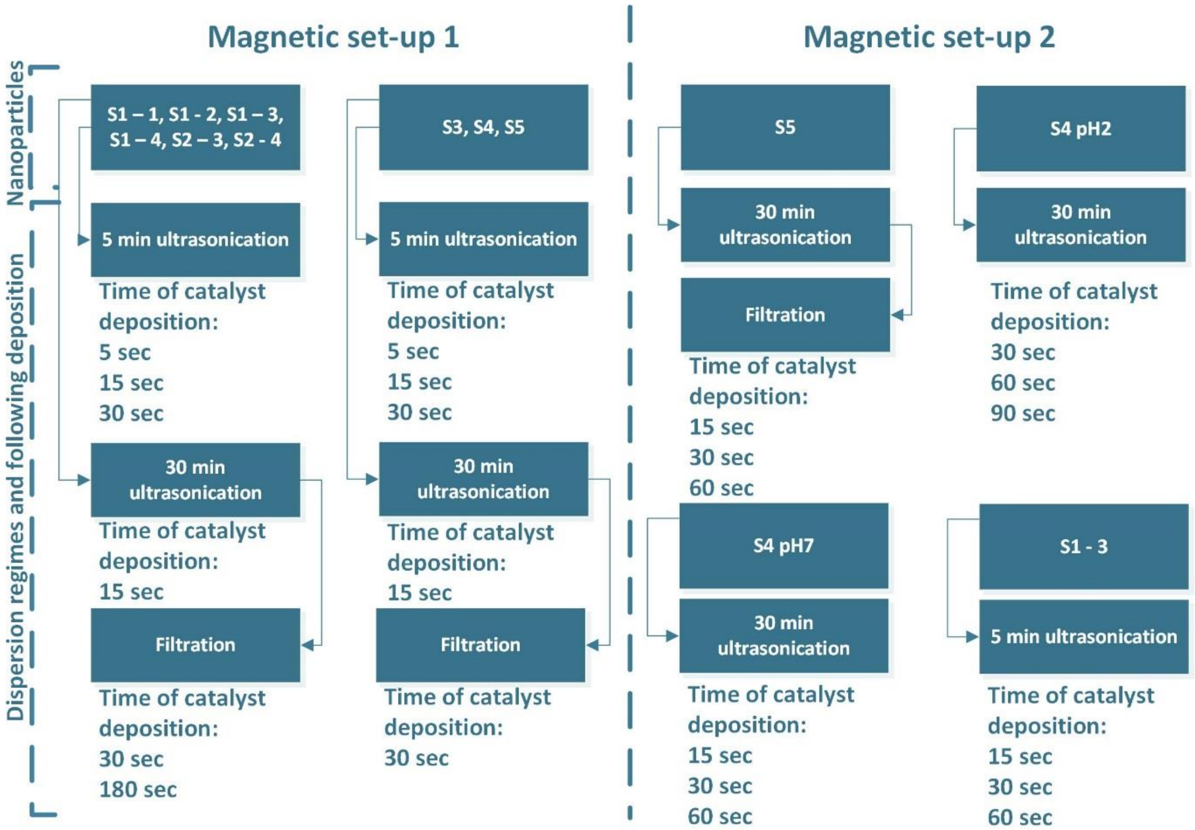

Figure 46. The scheme of the experiments performed on catalyst dispersion and catalyst deposition. The magnetic set-ups correspond to the set-ups described in section 2.5 of the current Chapter.

2.7 Characterisation

- **Scanning electron microscopy and energy-dispersive X-Ray spectroscopy**

1) Analysis of nanoparticle size and composition

A Sigma 500 VP scanning electron microscope with an X-MaxN 80 Oxford Instruments silicon drift detector fitted in the SEM (EDX) were used to characterise the size and composition of the synthesised magnetic catalyst nanoparticles respectively. The SEM was operated by using a secondary electron (SE2) detector in order to collect the element distribution information prior to EDX analysis. The EDX operated in the mapping regime in order to obtain the element distribution across samples. The EDX was performed at an accelerating voltage of 10 V and a working distance 10 mm.

The samples were prepared according to the following procedure:

Analysed material in the amount 0.005 g was dispersed in 10 ml RO water by ultrasonication for 5 min. Then, 2 drops of obtained solution were dropped onto the carbon tape attached to the aluminium stub and left to dry overnight in an oven at 50 °C. After drying, the sample was inserted into the SEM and analysed.

The obtained images from SEM were evaluated using ImageJ software in order to calculate the average particle size and distribution. The diameter of 100 particles was measured per image, with at least 5 different images evaluated per sample. Then the average diameter and standard deviation were calculated.

2) Analysis of distribution of the catalyst deposited on epoxy substrate and morphology of electroless plated Cu film on the epoxy substrate.

The epoxy substrate with deposited catalyst and electroless Cu were analysed after deposition with magnet alone or with template and magnet. In some cases, the samples were not entirely conductive and the deposited particles and Cu layer sometimes had low adhesion to the substrate. Therefore, the following procedure was performed for sample preparation.

First, both sides of the samples were sputter-coated with Au/Pd target 80/20 ratio by using a SC7640 Sputter coater, Polaron at a current of 15 mA for 60 sec to ensure conductivity to the samples. Then, the substrate was placed on the pin stub with attached carbon tape. Before analysis, and to ensure the adhesion of the particles to the substrate, all samples were blown with compressed air using an Air Duster.

- **Transmission electron microscopy**

TEM was used to image the Fe_3O_4 nanoparticles. This equipment allows for higher resolution analysis of samples of nanometer size.

A JEM-2100 Plus Electron microscope was used to conduct the measurements. Analysed particles (0.001 g) were dispersed in 2 ml ethanol by ultrasonication for 5 min. The dispersion was dropped on a Holey Carbon grid, 200 µm mesh, (Agar scientific) and allowed to dry. Then the sample was analysed.

- **X-Ray diffractometry**

PANalytical X-Ray Diffractometer was used in order to confirm the crystal structure of the synthesised nanoparticles. Nanoparticles were thoroughly ground by pestle and mortar and placed in the sample holder and analysed. The measurement angle (2Θ) was from 10 to 80 °. The scan was collected at the step 0.02 °.

- **Magnetic properties evaluation**

First, the ability of the nanoparticles to be attracted by the magnet was evaluated by placing the magnet near the vial with nanoparticles. Magnetic nanoparticles attract to the magnet as shown in Figure 47.

Figure 47. Test of the magnetic properties of nanoparticles, A – tested particles as stored in a vial, B – tested particles attracted to the magnet placed near the vial.

If the particles were attracted to the magnet, then they were further evaluated by vibrating sample magnetometry (VSM). A sample of known mass was placed in the sample holder (silicon capsule) and measured on a MicroSence Vibrating Sample magnetometer at the following magnetic field -20000 Oe to +20000 Oe with steps: 500 (from 20000 to 2000 and from -2000 to -20000); 50 (from -2000 to -200 and from 200 to 2000) and 10 (from -200 to 200).

The obtained results were normalized per gram of sample.

- **Cyclic voltammetry (CV)**

The catalytic activity of obtained material toward formaldehyde oxidation is can be characterised by CV. In order to determine whether the chosen material is catalytic, a working electrode composed of the catalytic material is used [26,32,40]. If nanoparticles are investigated then the inert electrode needs to be functionalized [46,64,65]. In this study, the particles could not be deposited by dip-coating because they did not have any adhesion to the surface.

Attraction of the particles by the magnetic force to the electrode surface also was not possible as the magnetic field interacts with the electric field and the technique is based on current flow measurement so the magnetic field might interfere with results. Therefore, the drop coating approach was chosen. In order to secure particles in place, Nafion is often used [49,65,164,165] which polymerizes on the surface and immobilizes the particles. However, Nafion can affect the measurements – it can reduce conductivity [166]. This could result in particles, which by electroless Cu plating experiments would show catalytic activity, showing a very low current for formaldehyde oxidation. Therefore, it was decided to conduct the experiments without Nafion.

In order to achieve reproducibility further factors were controlled:

- The concentration of the particles in dispersion (g/l).
- The volume of the dispersion dropped onto the electrode and the area covered by the drop.
- The duration of the dispersion of the particles by ultrasonication was the same for all samples.
- Freshly dispersed samples were always used.

The experiment was performed using an Analytic radiometer PST050, VoltaLab potentiometer. A three electrode set-up was used: the reference electrode was Ag/AgCl; the counter electrode – platinum 1 cm^2 sheet and the working electrode glassy carbon 0.07 cm^2. The measurements were performed at the sweep rate 50 mV/sec.

The working electrode was modified by previously synthesised nanoparticles:

Analysed nanoparticles in the amount 0.005 g were dispersed in 1.5 ml water (S3; S4; S5) or isopropanol (S1 and S2 based composites) by 30 sec ultrasonication. Then, 5 µl of dispersion was dropped onto the carbon surface in such a way that the drop covered the entire surface of the carbon but did not spread onto the plastic part of the electrode. Then the electrode was dried in air (if isopropanol dispersion was used) or in the oven at 40 ^oC until dry (if water dispersion was used). Then the measurements were conducted.

The electrolytes used for the measurements were: 3.33 g/l NaOH solution - in order to obtain the background current and 3.33 g/l NaOH and 0.1 M formaldehyde solution for measurements of formaldehyde oxidation. The measurements were conducted at room temperature.

- **Dynamic light scattering (DLS)**

The hydrodynamic particle size was characterised using a Zetasizer Nano S, Malvern Panalytical. Disposable polymethyl methacrylate cuvettes with a path length of 10 mm. An aliquot of freshly prepared dispersion was placed in the cuvette and analysed at 25 ^{o}C. Each measurement was repeated 5 times.

- **Stability characterisation**

Dispersions of 0.025 g nanoparticles in 100 ml RO water were made by 30 min ultrasonication and subsequent filtration. Then the beaker was covered by Parafilm and left untouched. Digital photos of the dispersions were made as follows: as prepared, after 10 min, 30 min, 60 min and 24 hours.

- **Magnetic strength measurements**

The distribution of the magnetic flux density across the substrate surface was measured by a Hirst GM07 gaussmeter. The tip was placed at the surface of the substrate perpendicular to the surface and the value of B_z (magnetic flux density component) was recorded.

- **White light interferometry**

In order to estimate the effect of the magnetic field on the deposited film thickness and roughness, a ContourGT, Bruker white light interferometer was used. Samples with no magnetic influence were measured at 3 different spots in order to estimate the area roughness. The samples with an applied gradient magnetic field were measured 3 times each at the area with maximum magnetic field influence and at the area with minimum magnetic field influence. The measurements were made at a magnification of 20 X with a measuring speed of 1 X.

- **Optical microscopy**

A Leica Microsystems S6D Stereozoom Microscope and Omnimet software was used to make images at magnification 2x and 4x.

- **Resistance**

In order to check whether deposited film was conductive an ISO-tech IDM91E digital multimeter was used. Test leads were placed at opposite edges of the deposit (10 mm distance between each other) and resistance was measured.

- **Adhesion testing**

The adhesion of the deposited copper layer was tested using the cross cut adhesion test kit CC2000. A cutter with 1 mm spacing SP 1702 was used. The cutting was done in two directions perpendicular to each other. Then the adhesion tape was placed on the cut region and pulled after 1 min.

- **Inductively coupled plasma optical emission spectrometry**

This technique was used to identify the overall composition of the synthesised magnetic nanoparticles. An Optima 8300, PerkinElmer optical emission spectroscope was used for the measurements. The particles (0.002 g) were mixed with 10 ml of concentrated HNO_3 (70%), ACS grade. The mixture was ultrasonicated for 5 min to allow quicker particles dissolution. The sample was left for 1-2 days until completely clear, which indicates that the particles entirely dissolved. Then the solution volume was made up to 100 ml by mixing with RO water.

In addition, ICP was used for analysis of metal concentration in dispersions. The dispersion (0.5 ml) was collected and mixed with 1 ml 70% HNO_3. The dispersion was ultrasonicated and left until dissolved. Then the solution was made up to 10 ml with RO water.

The standard solution was made in 7% HNO_3 in order to match the analysed samples. The concentration of the metals in the analysed samples was calculated as 2 mg/100 ml (i.e. 20 ppm). Therefore, the following Ag and Fe concentration standards were made: blank, 1 ppm, 5 ppm, 10 ppm, 15 ppm, 20 ppm (Figure 48).

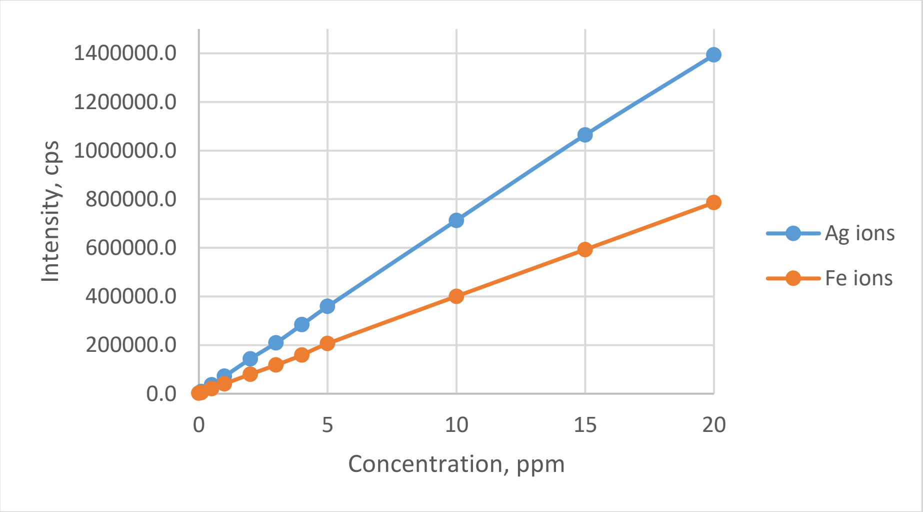

Figure 48. The standard curves of Ag and Fe ions for ICP analysis.

2.8 Conclusion

In order to achieve selective metallisation by applying a gradient magnetic field, the following changes were made to the standard process of electroless Cu plating (Figure 49):

- The 3 mm substrate was replaced by a thinner 0.41 mm substrate;
- The template and holder were made. The substrate was placed in the holder with the template and magnet prior to the catalyst deposition;
- A novel magnetic catalyst was synthesised and dispersed in water by ultrasonication. The catalyst dispersion was filtered before deposition.

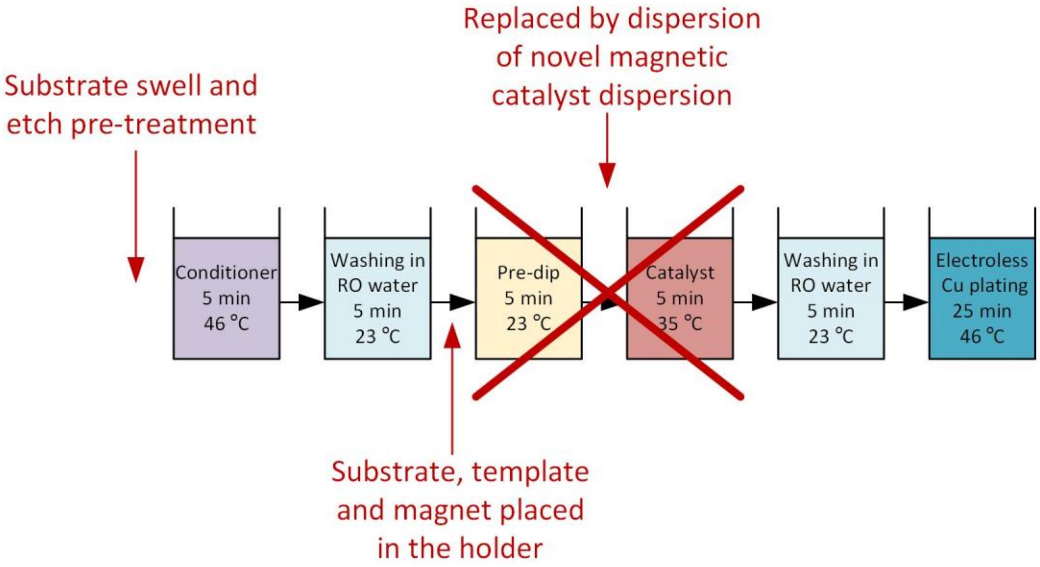

Figure 49. The scheme of the process of the selective metallisation by applying the magnetic field.

Chapter 3. Preliminary study: the effect of a gradient magnetic field on Pd/Sn catalyst deposition and electroless copper plating processes

3.1 Introduction

Electroless deposition in a magnetic field has been investigated by several research groups [81,83–85,167–169]. The magnetic field affected layer roughness, morphology, density and thickness. These works were mainly performed in electrolytes containing magnetic species such as Ni and Co.

A number of groups achieved patterned deposits by electrochemical plating under application of a gradient magnetic field [79,86,97,99,103–105]. However, similar work has not been performed during electroless plating, as was discussed earlier in the literature review.

In the present Chapter, the effect of a gradient magnetic field on catalyst deposition and electroless plating was investigated. Electroless Cu baths from basic solutions were studied. The choice of the electroless copper plating bath was based on the following considerations [22]:

1) Electroless copper plating is widely used in industry, mainly in electronics;

2) Often, selective electroless copper plating is required, hence the patterning of it during deposition has potential applications;

The choice of substrate was carefully considered. Electroless copper plating is usually used for metallisation of non-conductive material, e.g. plastic and fabrics, which cannot be magnetised. Non-conductive substrates require catalyst deposition prior to the electroless metal plating [6]. The catalyst activates the reaction of formaldehyde oxidation.

$$2HCHO + 4OH^- \rightarrow 2HCOO^- + H_2 + 2H_2O + 2e^- \qquad (51)$$

The electrons released during this reaction interact with Cu^{2+} ion and Cu^0 deposits onto the substrate.

$$Cu^{2+} + 2e^- \rightarrow Cu^0 \qquad (52)$$

Pd/Sn catalyst is commonly used to initiate electroless copper plating in industry. Both Pd and Sn have low magnetic susceptibility and cannot be attracted by a magnetic field [88].

The gradient magnetic field was achieved by placing the magnet behind the substrate. The side of the magnet with dimensions of 10x10 mm was placed on the substrate side. The substrate itself has dimensions of 30x30 mm, so the magnetic field was not evenly distributed across the substrate surface and a gradient magnetic field was achieved.

The main goal of this chapter was to investigate the possibility of patterning of the electroless deposition by applying a gradient magnetic field and to study the effect of the gradient magnetic field on deposit parameters such as roughness and morphology.

3.2 Deposition of electroless copper on epoxy substrate with and without magnetic field application

The magnetic field across the substrate surface was measured by a magnetometer as described in the Methodology chapter. The following distribution of the magnetic flux density was obtained according to the measurements (Figure 50):

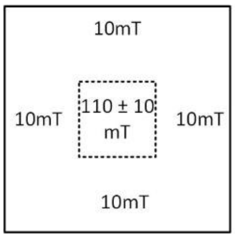

Figure 50. Distribution of the magnetic flux density across the substrate surface. The dotted area is where the magnet was placed behind the substrate.

It is clear from this that the magnetic flux density is not uniform across the sample surface and a gradient of magnetic field influence was achieved.

In order to investigate the effect of a gradient magnetic field on the electroless copper plating process, depositions with and without the attached magnet were performed. Both experiments were performed following a commercially developed procedure as detailed in the Methodology chapter. The surface was examined by eye, and no visible patterning effect resulting from the gradient magnetic field was observed (Figure 51, A, Figure 52, A).

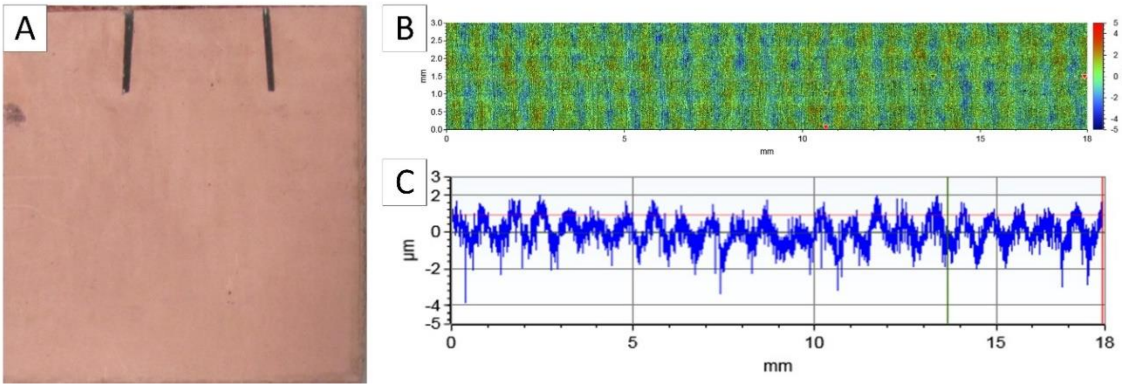

Figure 51. The electroless Cu deposit obtained without magnetic field application. A – the digital photo of the deposit surface; white-light interferometry measurements result: B – surface map; C - profile of the surface.

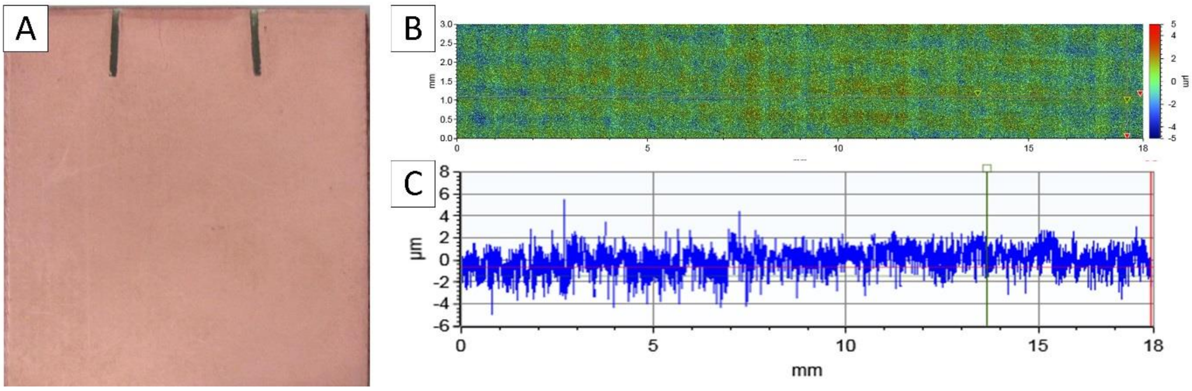

Figure 52. The electroless Cu deposit obtained during magnetic field application. A – digital photo of the deposit surface; white-light interferometry measurements result: B – surface map; C - profile of the surface.

White-light interferometry was conducted on the samples in order to investigate changes in the thickness of the deposited layer. Neither the profile of the surface nor the surface map showed any difference in the layer thickness between the centre of the substrate and the substrate sides for both studied depositions.

3.3 Discussion

The goal of the preliminary study was to determine whether the magnetic field has a patterning effect on the electroless Cu plating process. The obtained plating was continuous after both depositions with and without the magnetic field.

According to previously reported work [84] electroless plating can be suppressed in strong magnetic fields (5 T). In the present work, no effect of magnetic field on the Cu plating was observed though the rate of the reaction was not measured as it was not a goal of the study. The applied magnetic field was weaker than in the previously reported work [84] and the maximum measured value of the flux density on the substrate surface was 120 mT.

Patterned Cu deposition through application of a gradient magnetic field was achieved during the electrodeposition process in previously reported works [86,96]. In addition, convection was improved by the magnetic field application during immersion plating of Cu. The observed effects in both types of experiment were due to interaction of Cu^{2+} ions with the magnetic field. However, in electroless plating solutions the Cu ions exists mainly in the complexed form, and therefore they do not have unpaired electrons like Cu^{2+}. This explains why the gradient magnetic field had no visible effect on the electroless Cu plating.

During the copper reduction reaction in electroless plating Cu[EDTA] complexes decomplex and Cu^{2+} ions are present in the electrolyte. Therefore, potential effects of a gradient magnetic field on electroless plating cannot be entirely ruled out, though stronger magnetic fields should be applied in order for the effects to be observed.

This research is different from previous work [84] in that plating on non-conductive material was investigated, which required catalyst deposition before electroless Cu deposition. The magnetic field was applied during both the catalyst deposition and electroless Cu plating stages. There has been no work published investigating the influence of a gradient magnetic field on Pd/Sn catalyst deposition.

The works which investigated the methods of selective electroless Cu plating showed that selective deposition of catalyst leads to the selective deposition of Cu. In the present work, electroless Cu deposited across the whole substrate surface. Therefore, it can be concluded that the deposited Pd/Sn covered the whole substrate surface and that there is no patterning effect by a gradient magnetic field on Pd/Sn catalyst deposition.

The absence of the patterning effect is due to the low values of magnetic susceptibility of all involved species: Cu, Pd and Sn. Significant effects of the magnet on the electroless plating process were previously observed only when plating involved ferromagnetic species like Ni or Co, although these did not result in selective metallisation.

Thus, the gradient magnetic field with a maximum magnetic flux density 120 mT does not have an effect on the patterning of Pd/Sn deposition and subsequent electroless Cu plating. In order to achieve this effect, either a stronger magnetic field or ferromagnetic species should be investigated.

Chapter 4. Synthesis and characterisation of a magnetic catalyst

4.1 Introduction

According to the results obtained in Chapter 3, copper cannot be deposited selectively by application of a gradient magnetic field in the electroless process due to the absence of ferromagnetic species in the electrolyte and catalyst solutions. Therefore, modifications of the electroless plating or pre-treatment processes are required.

Modification of the electroless plating electrolyte was not considered feasible. It would require introduction of ferromagnetic species to the electrolyte, which can cause changes in the reaction mechanism and also co-deposition of introduced species. This could potentially alter the properties of the deposited layer which has been avoided in the present work.

The catalyst deposition procedure prior to the electroless plating process was considered for modification. The catalyst can be in the ionic [170] or nanoparticle [14] form. The interaction of the ions with the magnetic field is negligible unless an electron current is involved in the process [87].The nanoparticles have much stronger interaction with the magnetic field because they consist of several atoms and the interaction with the magnetic field involves all the unpaired electrons in the atoms. Some works have shown that ferromagnetic nanoparticles can be deposited in patterns by using a gradient magnetic field [109,111,112,171,172]. Therefore, nanoparticle catalysts were considered.

The most investigated nanoparticle catalysts for electroless Cu plating are Pd, Ag, Cu, Au and none of them are ferromagnetic. The ferromagnetic metals Fe, Co and Ni [173] also can be the catalysts for formaldehyde oxidation, however there has been minimal research in this area. Ohno [29] showed that formaldehyde oxidation starts on Ni and Co at higher potentials than for precious metals. This means that the system needs higher energy to start the deposition process. Also Fe, Ni and Co are oxidised in the air and have an oxide layer on the surface which can supress the catalytic activity of the particles. If these metals are used for catalysing formaldehyde oxidation then they should be used immediately after formation.

Another challenge is that the Fe, Ni and Co are more reactive than Cu according to the metal activity series. According to Bindra, Cu is present in the electroless plating solution in the non-complexed form and therefore can potentially immersion plate Fe, Co and Ni surfaces [174].

In order to avoid degradation of catalytic properties and immersion plating, composite materials were considered as the possible catalyst for the electroless Cu plating process. Composite nanoparticles consist of two or more materials, the properties of which combine in the final composite. Composite nanoparticles can consist of material with magnetic properties and material with catalytic properties so the composite particles will possess both. Numerous combinations of Fe, Co, Ni and their oxides and alloys with Cu, Ag, Au, Pt, Pd and their alloys can be investigated as potential catalysts with magnetic properties for electroless plating. In the present work the combination of Fe_3O_4 and Ag as a possible magnetic catalyst for electroless plating was chosen.

Magnetite (Fe_3O_4) is a commonly used magnetic material. There are a range of synthesis methods of these nanoparticles, some of which are relatively simple and are conducted at room temperature and normal atmospheric pressure. These particles have a relatively high magnetisation saturation value (93 emu/g).

Silver (Ag) is often considered as a cheaper alternative to the Pd catalyst for formaldehyde oxidation and a range of works are dedicated to possible synthesis methods and catalytic activity investigation [41,46,62,64,68,175,176]. Also there are a range of syntheses of Ag nanoparticle reported that are simple and cheap.

The methods of Fe_3O_4-Ag composite nanoparticles synthesis were also reported previously and range from a “green” synthesis (e.g. with the use of an amino acid at room temperature) to high temperature high pressure methods with use of toxic organic compounds.

The method of synthesis was limited by the following criteria:

1) The amount of toxic reagents used should be minimised in keeping with one aim of this research which is to develop a more environmentally-friendly alternative to existing patterning methods, which includes a decrease in hazardous waste;
2) The procedure should allow high yield and be economically viable; this implies the restriction of use of organic solvents. The temperature of the synthesis should be relatively low and the pressure preferably atmospheric in order to decrease the cost of production. Therefore the choice was limited to water-based low temperature synthesis procedures;
3) The synthesised particles should have both catalytic and magnetic properties. There are a number of water-based synthesis routes of Fe_3O_4 – Ag composite particles, most of which involve the use of the surfactants or stabilizers [177], which bind to the particle

surface of the obtained composite material. However, this has been reported to affect the catalytic properties of the composite in the electroless copper plating process [178].

Most of the composite nanoparticles were synthesised by reduction of the shell precursor in the presence of the formed core particles [177]. The chosen method is based on the synthesis described in works [124,132]. In the chosen procedure the Fe_3O_4 nanoparticles were synthesised first by the modified Massaart method as described in Chapter 2.3. After synthesis the particles were washed, dried and re-dispersed in water. Then, Ag was reduced in the presence of Fe_3O_4 by $NaBH_4$.

The Fe_3O_4 synthesis was chosen without $FeCl_3$ atoms in order to eliminate Cl presence to avoid possible interaction of Cl^- ions with Ag^+. However, particles synthesised with only the $FeSO_4$ precursor are usually reported [72] to have a larger size than the those synthesised from mix of Fe^{2+} and Fe^{3+} ions. Therefore, synthesis on the spinning disc reactor was used in order to reduce the particle size without the use of surface functionalisation.

4.2 Synthesis of iron oxide nanoparticles

4.2.1. Synthesis procedure

Two procedures were used for the iron oxide nanoparticle synthesis:

1. The precursors were mixed in the beaker by magnetic stirrer; the base solution (25% NH_4OH) supplied by dropwise addition; particles were allowed to grow for 1 h. (**S1**)
2. The precursors were mixed on the spinning disc; the base solution was supplied by continuous pumping on the disc; particles were allowed to grow for 1 h. (**S2**)

During both syntheses the solutions turned dark green straight after NH_4OH addition and turned black after 10 min of mixing (Figure 53).

After the synthesis, particles were separated by a magnet placed on the bottom of the beaker and washed several times. After filtration and drying, particles were ground and collected. S1 particles had a black colour whilst S2 particles turned brown after grinding.

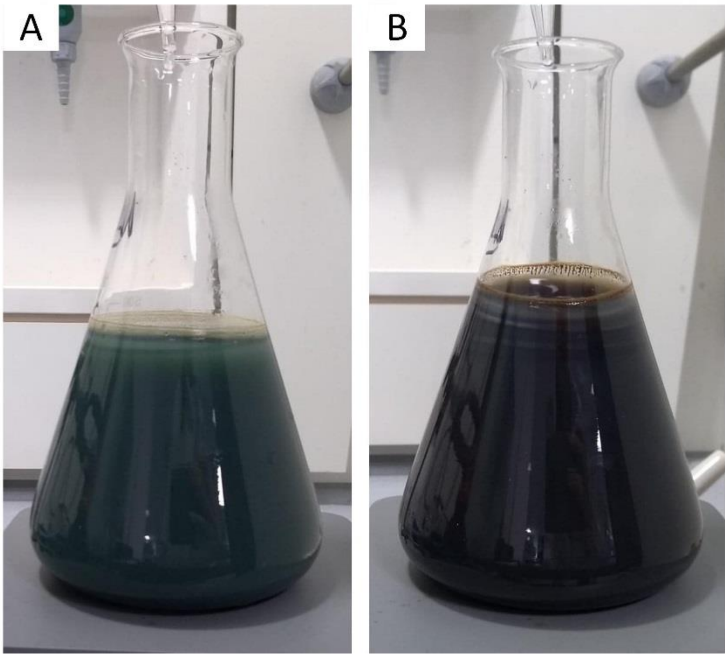

Figure 53. Digital image of the beaker during synthesis S1. A – 30 sec after base solution addition, B – 10 min after base solution addition.

4.2.2 Particle size

Images of the synthesised iron oxide particles were obtained by TEM (Figure 54). The S1 particles were larger with a higher size distribution, with an average particle diameter of 63 ± 23 nm. The S2 particles had a narrower size distribution and a smaller particle diameter of 11 ± 6 nm.

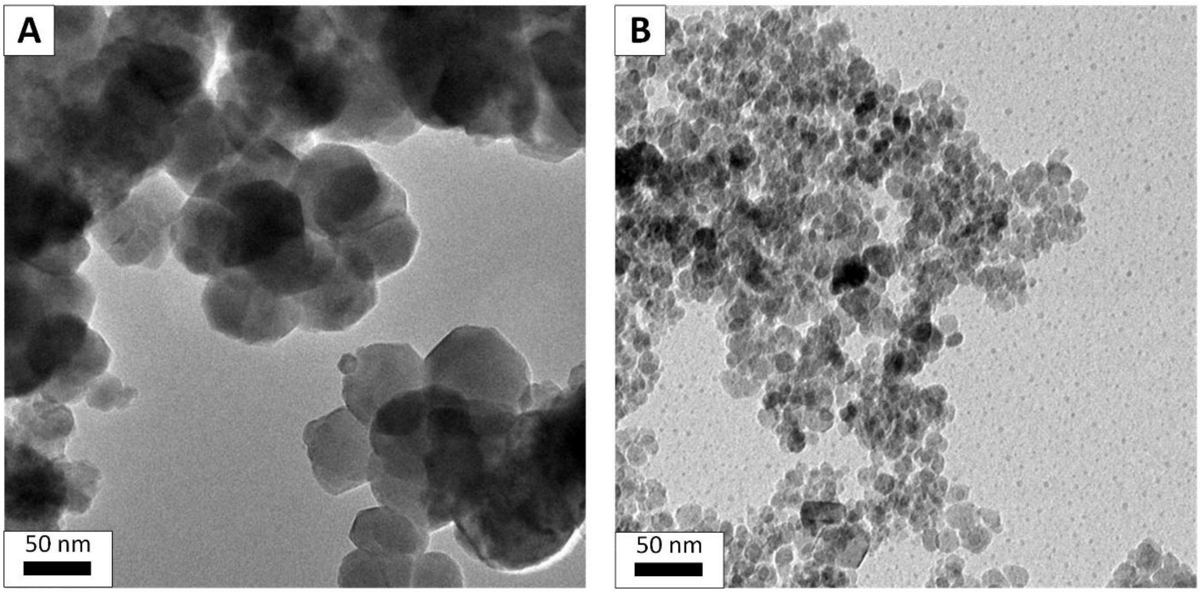

Figure 54. TEM images of synthesised iron oxide particles: A – S1, B – S2.

4.2.3 Particle structure

The crystal structure of the particles was analysed by XRD (Figure 55). Peaks at 2Θ = 18.333, 30.158, 35.522, 43.173, 53.563, 57.1, 62.704 ° were observed for both S1 and S2 particles and were attributed to magnetite Fe_3O_4 formation (ref. code Fe_3O_4: 01-088-0315).

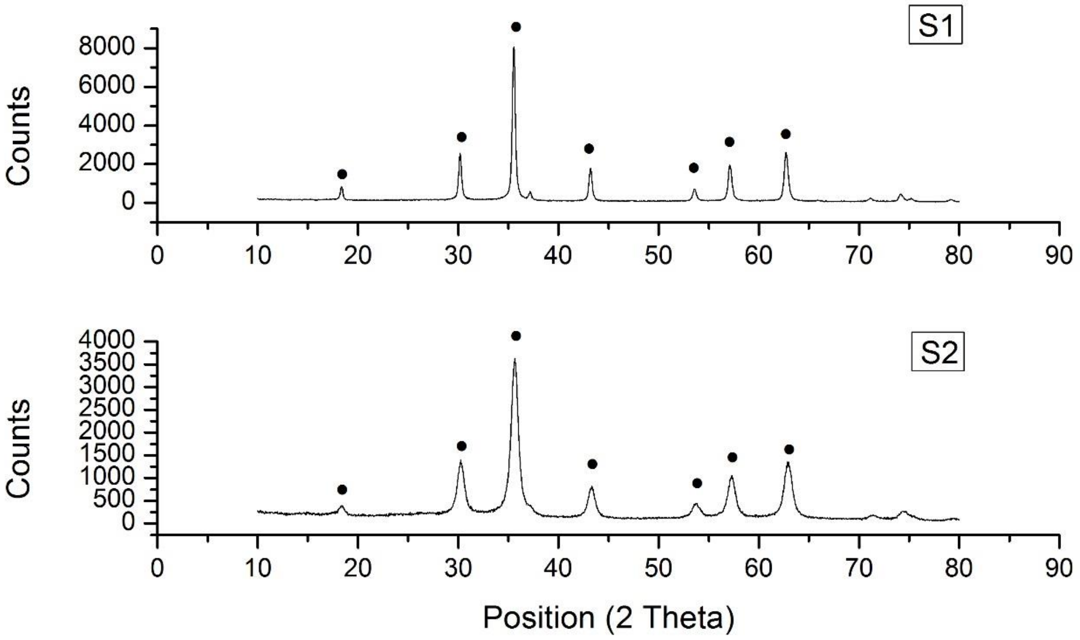

Figure 55. XRD spectrum of iron oxide nanoparticles synthesised by different procedures: S1 (top) and S2 (bottom).

4.2.4 Magnetic properties

Preliminary tests were performed in order to prove that the synthesised particles were magnetic by the placing the magnet close to the vial with the nanoparticles. All particles were attracted by the magnet.

Vibrating magnetometry was used for measurement of the magnetic properties of the particles (Figure 56). The magnetic saturation values were 75 emu/g (S1) and 68 emu/g (S2) (Figure 56, A). Both particles showed a ferromagnetic-type response. According to Figure 56, B, material S1 has a hysteresis loop of 88 Oe, while the S2 hysteresis loop is 5 Oe. This indicated that the S1 nanoparticles are ferromagnetic and can maintain magnetisation, while the S2 particles are superparamagnetic.

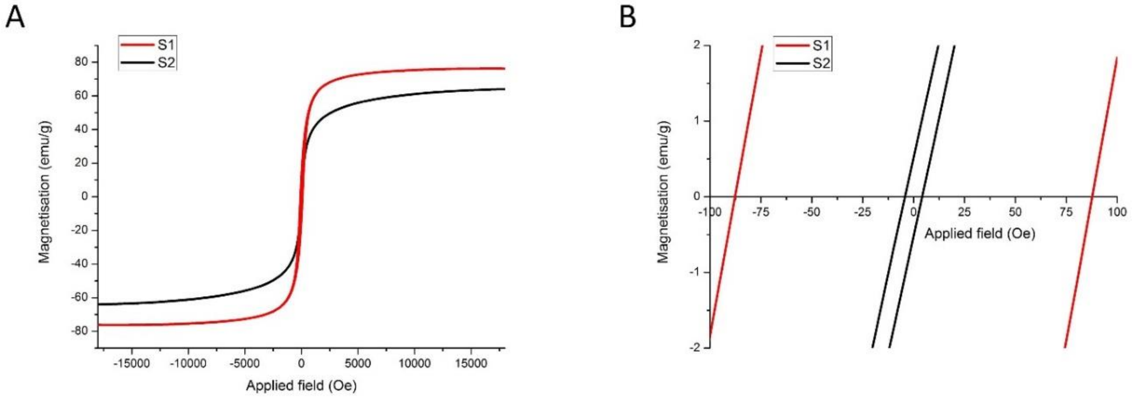

Figure 56. Vibrating sample magnetometry (VSM) measurements of iron oxide nanoparticles S1 and S2. A – magnetisation curve, B – hysteresis loop of the magnetization curve.

4.2.5 Catalytic properties

Catalytic activity towards formaldehyde oxidation was evaluated by CV. The scan started at -700 mV and the potential was increased up to 200 mV, then the scan continued in the opposite direction until -700 mV was reached again.

CV measurements of the S1 and S2 nanoparticles did not reveal any rise in oxidation current between -700 mV and 200 mV, where the typical oxidation peak is observed for the majority of metals that are able to catalyse formaldehyde oxidation (Figure 57). In addition, no reduction peak was observed.

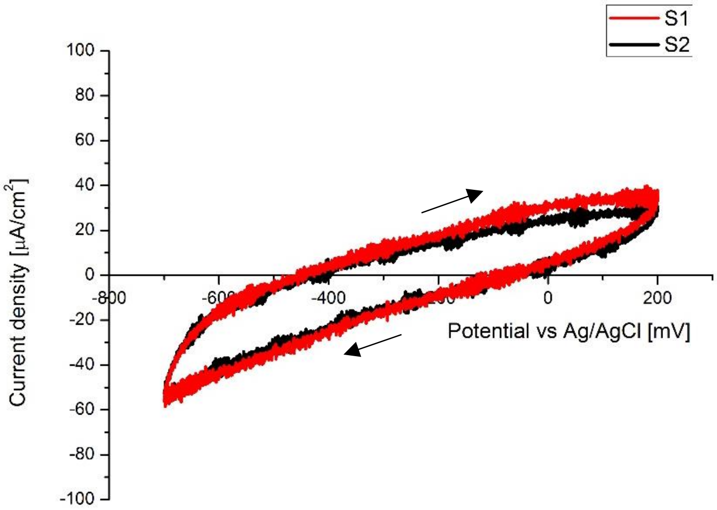

Figure 57. CV measurements of synthesised iron oxides in formaldehyde solution at room temperature.

4.2.6 Discussion

Both kinds of obtained iron oxide nanoparticles showed the ability to be attracted by the magnetic field, which is one of the two main properties required. The particles have similar crystal structure to Fe_3O_4 according to the XRD results but did not show any catalytic activity towards formaldehyde oxidation according to the CV measurements. However, the size of the nanoparticles and their magnetic behaviour is different.

Both synthesis procedures were based on the same chemical reaction of $FeSO_4$ and NH_4OH, the suggested mechanism of which is [118,119]:

$$Fe^{2+} + 2OH^- \rightarrow Fe(OH)_2 \tag{52}$$

$$3Fe(OH)_2 + \frac{1}{2}O_2 \rightarrow Fe(OH)_2 + 2FeOOH + H_2O \tag{53}$$

$$Fe(OH)_2 + 2FeOOH \rightarrow Fe_3O_4 + 2H_2O \tag{54}$$

Synthesis of Fe_3O_4 from Fe^{2+} ions proceeds through intermediates $Fe(OH)_2$ and FeOOH formation, which can explain the green colour of solution after base addition [72,179]. The reaction of Fe_3O_4 formation proceeds at a basic pH. However the hydrolysis and oxidation of the Fe^{2+} ions causes H^+ formation which decreases the pH of the solution and the rate of reaction [114]:

$$4Fe^{2+} + H_2O + O_2 \rightarrow 4FeOOH + 8H^+ \tag{55}$$

In order to ensure Fe_3O_4 formation, continuous base supply was provided by dropwise addition of base to the Fe salt solution (S1) and by the continuous pumping of the ammonium solution and the iron salt on the spinning disc (S2). If an insufficient amount of base is provided the product of the reaction will consist of non-magnetic species such as $Fe(OH)_2$ (“green rust”) and γ-FeOOH (lepidocrocite)[179,180].

When Fe^{2+} and Fe^{3+} precursor salts are used for synthesis, the procedure should be conducted in a N_2 atmosphere to avoid oxidation of Fe^{2+} to Fe^{3+} and formation of maghemite [114,179–182]. In the present work both syntheses were conducted in the air. As the only precursor salt used was Fe^{2+}, further oxidation of part of the Fe^{2+} to Fe^{3+} was required and was achieved by oxygen dissolved from the air (55).

Magnetite can oxidise in the presence of oxygen to the maghemite (γ-Fe_2O_3). Because maghemite has ferromagnetic properties similar to magnetite [179], the oxidation of the particles is not critical for the current work. Also, annealing for 2 hours at 250 °C is required in order to achieve full transformation of the magnetite to maghemite when the rate of oxidation in the air is relatively small. Therefore, the particles were dried on the air and were stored without atmosphere control.

The synthesised S1 and S2 iron oxide particles showed a difference in particles size such that the particles obtained by spinning disc have a much smaller diameter (Figure 54). The main difference between the two synthesis procedures is the method of reagent mixing. Dropwise addition of base causes inhomogeneity in the pH of the bulk solution. First, in the region of high pH $Fe(OH)_2$ is formed, then the pH decreases due to solution stirring and lepidocrocite (FeOOH) is formed [180]. Due to interaction between FeOOH and Fe^{2+} ions magnetite is formed. Small magnetite particles then recrystallise to form larger crystals [179,183].

When the spinning disc reaction is used the mixing intensifies, with the solution forming a thin film on the surface of the spinning disc [147,184]. This technique allows maintenance of a constant ratio of reacting species through simultaneous separate supply of Fe^{2+} and NH_4OH solutions, which avoids inhomogeneity in the pH of the solution. Moreover, the supply of oxygen is intensified due to larger surface exposure to the air. Oxygen is one of the reactants which allows Fe_3O_4 formation and when the supply of oxygen is intensified smaller particles are usually formed [183].

A similar particle size could be also achieved by using different Fe salts (e.g. mixture of the $FeCl_3$ and $FeCl_2$ instead of $FeSO_4$ [72,185–187]), bases (e.g. NaOH or ethylene glycol [72,188]), or by using stabilizers which will supress particle growth [185,188]. However, a change of the reaction precursors not only affects the particle size but also the zeta potential, magnetic properties and crystallinity [114,179]. For this reason, only the method of solution agitation was varied.

In order to confirm the crystal structure of the obtained iron oxides, XRD analysis was conducted. According to the results (Figure 55), both of the obtained oxides had a magnetite structure. It should be noted that the crystal structure of magnetite and maghemite are very similar and as a result the X-Ray diffraction peak pattern is also very similar [114,179].

The typical colour of Fe_3O_4 is black, whilst a brown colour is observed in Fe_2O_3 particles [114,179]. S1 nanoparticles did not change from a black colour even after storage for several months, while S2 nanoparticles changed to brown straight after grinding. The surface of S2 particles could have been oxidised in the air to Fe_2O_3, however due to the presence of both crystal structures and their similar XRD patterns the presence of Fe_2O_3 was not discernible.

According to the XRD measurements (Figure 55), S2 particles had a broader peak than S1, which usually indicates lower crystallinity of the sample which could be caused by excessive oxygen supply [183].

Both S1 and S2 particles were attracted by the magnet as expected. There are only two iron oxides which have ferromagnetic properties – maghemite and magnetite [179]. Therefore, this indicates that one of those oxides was obtained. The magnetic properties of the particles varied (Figure 56). S1 had a higher magnetisation (75 emu/g) compared to S2 (65 emu/g), though both materials show similar values to those reported previously [114,179,189–191]. Magnetisation of nanoparticles depends significantly on the size of the particles - the more domains that are oriented in the same direction the stronger the interaction with the magnetic field will be. Therefore smaller particles show smaller magnetisation values compared to larger particles with similar composition [191]. Also S1 particles had a hysteresis loop which is typically seen in Fe_3O_4 particles of similar size and indicates the ability to maintain magnetisation. S2 particles had a much narrower hysteresis loop and show almost superferromagnetic behaviour, which can again be attributed to the small particle size [114,179]. At later stages of the experiments the particles will be subjected to a static permanent magnetic field therefore the ability to maintain the magnetisation is not expected to have an effect on the experimental results.

Catalytic activity of the particles was evaluated by CV experiments (Figure 57). Neither S1 nor S2 particles showed any activity towards formaldehyde oxidation. Usually noble metals [2,53,54,62,68] or Cu [59,192,193] can act as the catalyst for electroless copper plating and it was reported that oxide film formation on the surfaces of non-noble metals can supress their catalytic properties [31].

Thus, two types of magnetic nanoparticle for a novel catalyst were obtained with an average size of 63 and 11 nm for S1 and S2, respectively. Both particles types showed ferromagnetic properties and had no catalytic activity, meaning further modifications are required in order to obtain catalytic properties towards formaldehyde oxidation.

4.3 Composite particle formation with S1 magnetite nanoparticles

4.3.1 Introduction

First, the synthesis of composite Fe_3O_4-Ag nanoparticles was attempted with larger magnetic nanoparticles from S1. The idea behind this synthesis was to deposit Ag in the presence of Fe_3O_4. A Ag precursor was used at low concentrations in order to prevent formation of large particles. Ideally, formation of a core-shell structure is preferable for the present research in order for the surface of the particles to be formed of only Ag, as it is Ag that catalyses formaldehyde oxidation. However, the formation of core-shell particles is usually achieved by particle surface functionalization, which will not be a part of the present section of this chapter. Nevertheless, calculations were made for the ideal situation of Ag being reduced on the surface of Fe_3O_4 particles (Chapter 2.3.2).

In short, the following equation was derived (repeated here for convenience):

$$h = 0.164\frac{m(AgNO_3) * r(Fe_3O_4)}{m(Fe_3O_4)} \tag{50}$$

According to the equation (50), a 1.46 nm thick shell of Ag can be obtained if 0.6 g of Fe_3O_4 nanoparticles with radius 31.5 nm are used for synthesis and 0.17 g of $AgNO_3$ is reduced on the surface of the Fe_3O_4 nanoparticles (Table 15).

In order to improve the catalytic properties of the particles, the amount of Ag per gram of synthesised material was increased by a) decreasing the amount of Fe_3O_4 in the synthesis (S1 – 2 and S1 – 3) or b) increasing the $AgNO_3$ concentration in the synthesis (S1 – 4) (Table 15).

Alternative composite nanoparticles were synthesised with smaller Fe_3O_4 nanoparticles from S2 synthesised by using the spinning disc reactor (Table 15). For comparison the same precursor ratios used in S1 – 3 and S1 – 4 were used.

Table 15. The parameters of performed syntheses and calculated "shell" thickness of the core-shell particles formed.

Synthesis code name	**Amount of Fe_3O_4, g**	**Amount of $AgNO_3$, g**
S1 – 1	0.6	0.17
S1 – 2	0.3	0.17
S1 – 3	0.1	0.17
S1 – 4	0.1	1.70
S2 – 3	0.1	0.17
S2 – 4	0.1	1.70

There was a possibility of obtaining Ag particles which did not form a composite with Fe_3O_4. Therefore, the washing procedure was modified. Usually centrifugation is used for separation of synthesised nanoparticles from solution. In the present work magnetic separation was used which also helped to remove possible non-magnetic parts of the material. However, this did not help to remove Fe_3O_4 particles which did not form composites with Ag.

4.3.2 Particles size and composition

The distribution of Fe and Ag in the composite material was analysed by SEM/EDX (Figure 58). All composites showed unequal distribution of Ag across the material. According to the images, the brighter particles on the SEM correspond to the silver component.

The average diameters of Ag particles in the composite measured from the SEM images by using ImageJ software are presented in Table 16. The average size of the Ag particles increases with an increase in the Ag:Fe_3O_4 ratio.

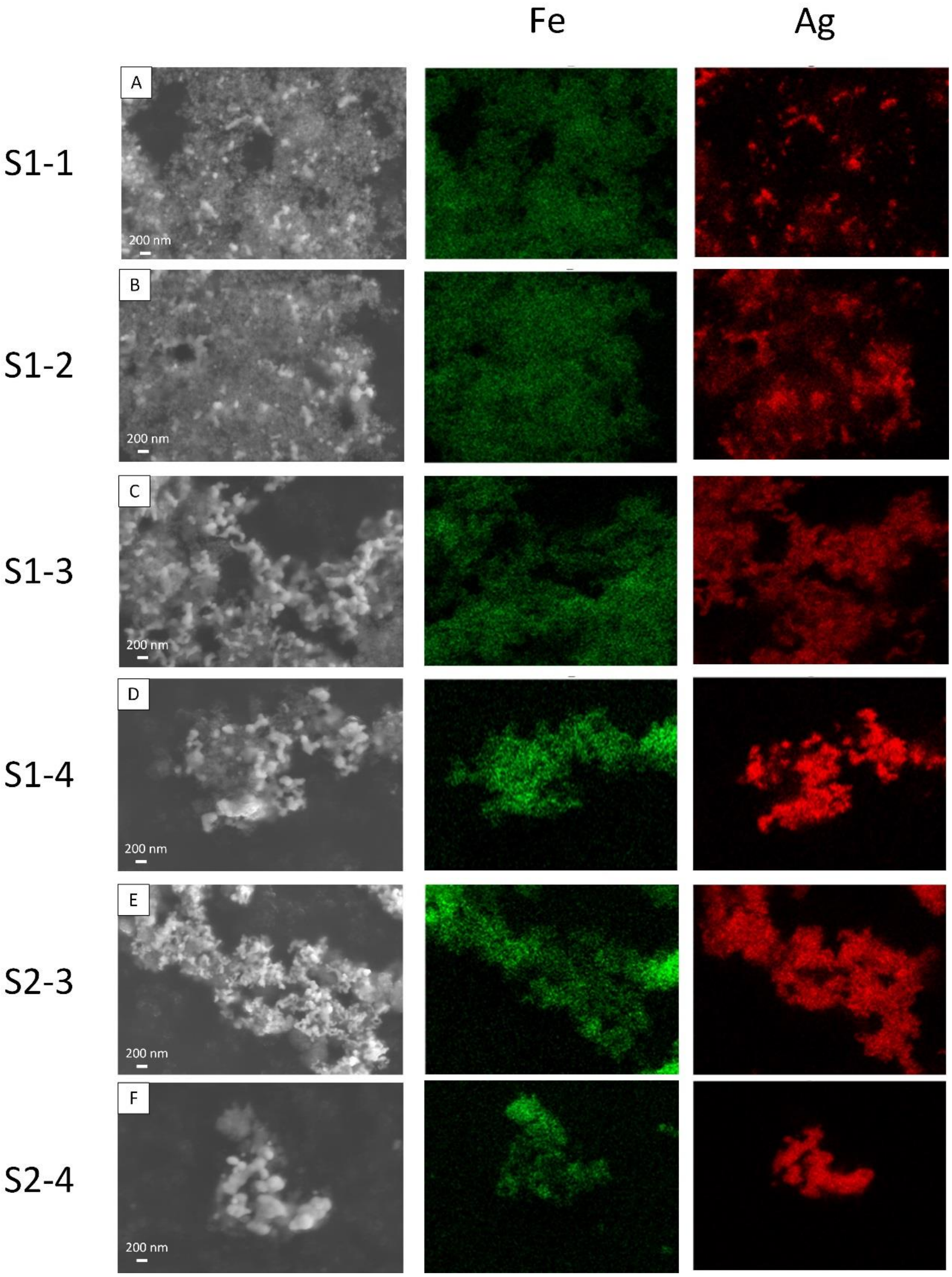

Figure 58. The results of SEM/EDX analysis of composite Fe_3O_4-Ag nanoparticles and the distribution of Fe and Ag across the analysed samples.

Table 16. The average diameter of Ag nanoparticles in the synthesised composites nanoparticle.

Synthesis procedure	S1 - 1	S1 - 2	S1 - 3	S1 – 4	S2 - 3	S2 - 4
Size, nm	81 ± 23	89 ± 29	92 ± 28	136 ± 52	82±22	139 ± 61

According to the SEM analysis (Figure 58), the size of the Ag nanoparticles is slightly different for the S2-based composites compared to the S1-based composites with similar precursor loading (Table 16). Larger Ag particles were formed at the higher Ag concentration and finer particles at the smaller concentration compared with similar syntheses from S1-3 and S1-4 (Table 16).

The amount of the Ag in synthesised nanoparticles was evaluated by ICP analysis. The nanoparticles were completely dissolved in acid, then ICP analysis was conducted which allows for determination of the concentration of the dissolved ions in the solution. The weight percent (*w*) of Ag in the sample per overall mass of all metal ions (Fe and Ag) was calculated by using the following equation (56) and presented in Figure 59:

$$w(Ag) = \frac{m(Ag)}{m(Ag) + m(Fe)} \tag{56}$$

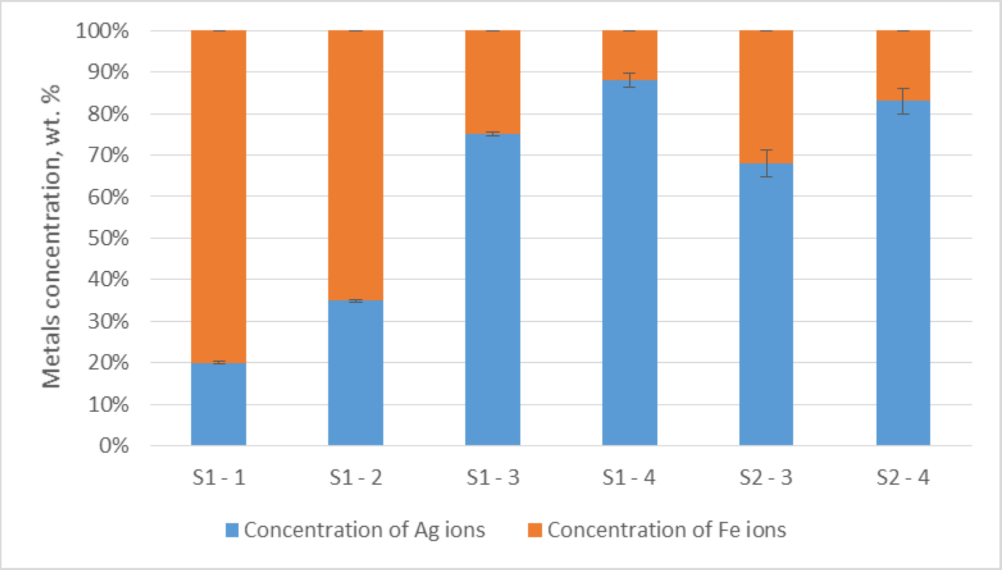

Figure 59. The weight percent of Ag/Fe in the synthesised composite nanoparticles as determined by ICP.

The amount of Ag increases with an increased ratio of $AgNO_3$:Fe_3O_4 precursor for composite nanoparticle synthesis. The values of Ag in S2 based composites are similar to the ones obtained for S1 based composites and vary by less than 10%.

4.3.4 Crystal structure of composite

The structure of the obtained material was analysed by XRD (Figures 60). Analysis of the structure of the composite material revealed separate formation of Fe_3O_4 and Ag (Ref. Code Ag: 01-087-0717). There is no evidence of the presence of $AgNO_3$ (19.585°, 21.679°, 24.265°, 29.645°, 32.766°, ref. Code $AgNO_3$: 00-043-0649) or $AgFeO_2$ (28.791°, 5.418°, 39.309°, 52.489° ref. Code $AgFeO_2$: 01-075-2147).

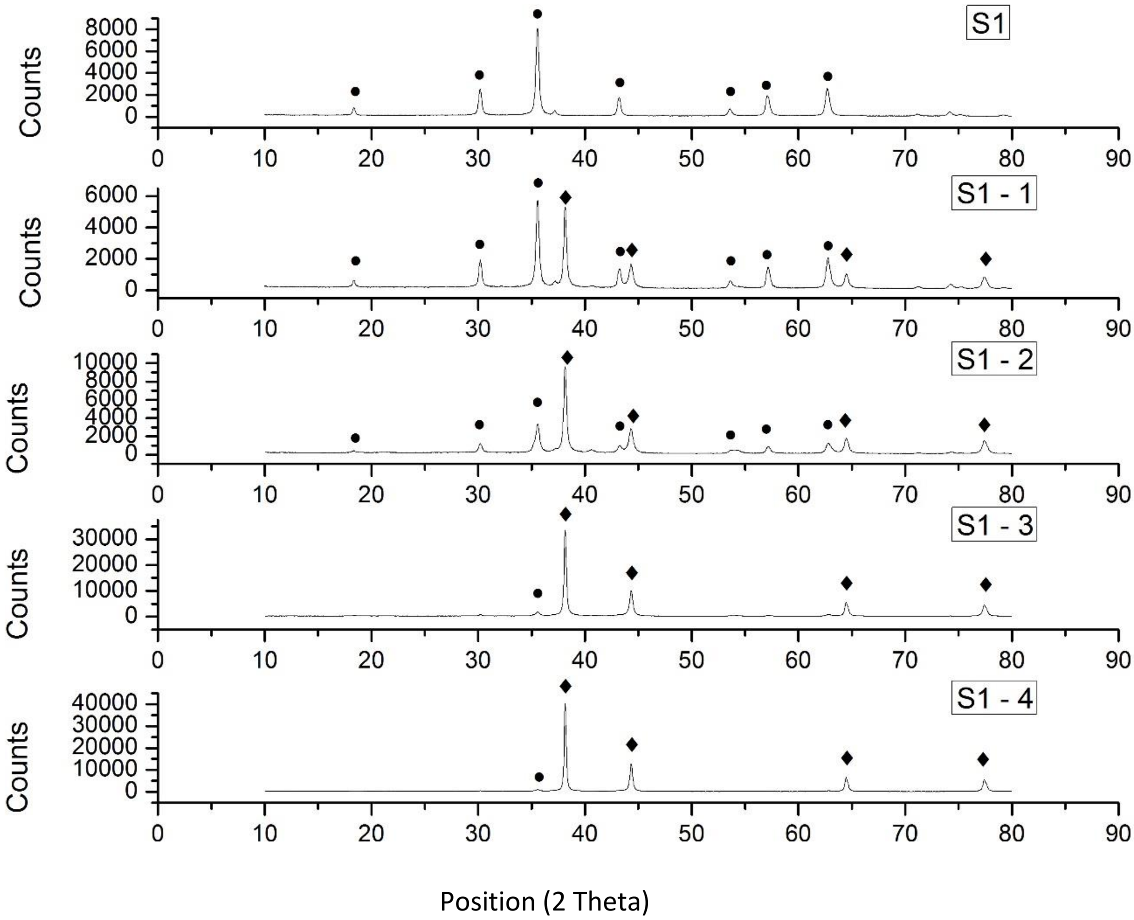

Figure 60. XRD spectra of synthesised Fe_3O_4 (S1) and composite Fe_3O_4-Ag (S1 – 1, S1 – 2, S1 – 3 and S1 – 4) nanoparticles. Circles indicate the peaks of Fe_3O_4 structure and rhombi indicate the peaks of Ag structure.

The intensity of Ag peaks (at 2Θ=38.119°, 44.305°, 64.452°, 77.409°) increases between the S1-1 and S1-4 composites, while the peaks for Fe_3O_4 are less noticeable though they are still present on the spectrum.

The S2-based composite nanoparticles are similar and showed the formation of both Fe_3O_4 and Ag (Figure 61).

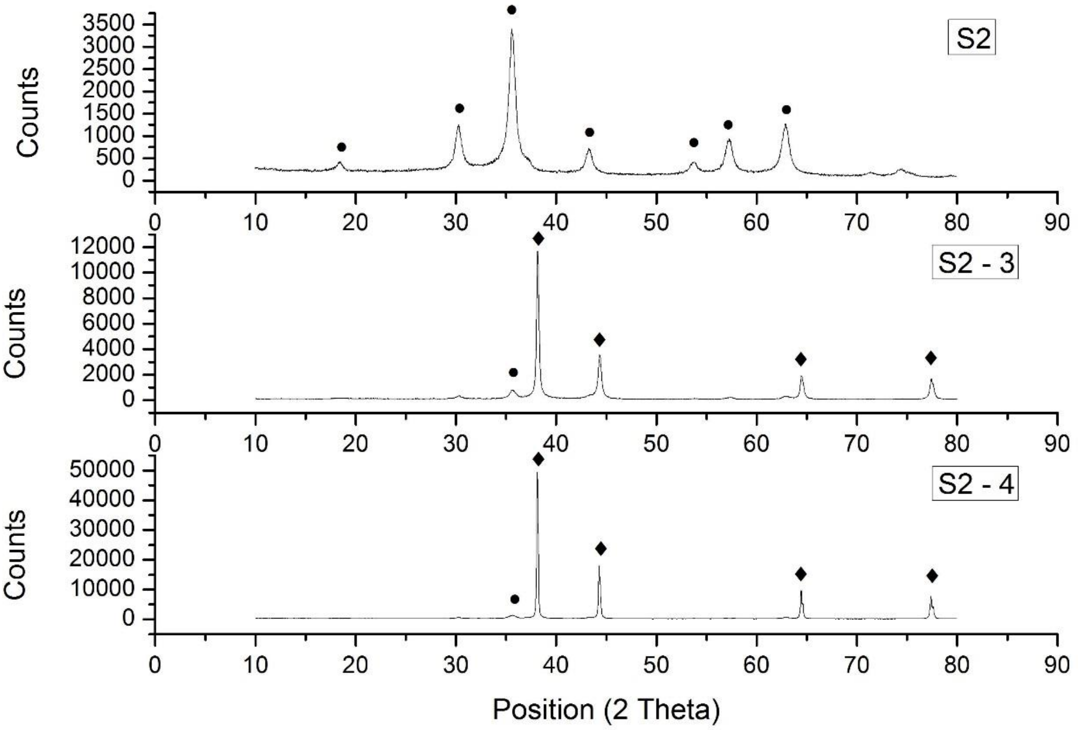

Figure 61. XRD spectra of synthesised Fe_3O_4 (S2) and composite Fe_3O_4-Ag (S2 – 3 and S2 – 4) nanoparticles. Circles indicate the peaks of Fe_3O_4 structure and rhombi indicate the peaks of Ag structure.

4.3.5 Magnetic properties

The preliminary tests were performed according to section 2.5. All particles were attracted by the magnet.

The magnetic properties of the Fe_3O_4 and Fe_3O_4 – Ag composites were measured by VSM (Figure 62). The saturation magnetization values of all composites are lower than the one obtained for their respective precursor Fe_3O_4 particles and decrease with increasing $AgNO_3$:Fe_3O_4 precursor ratio.

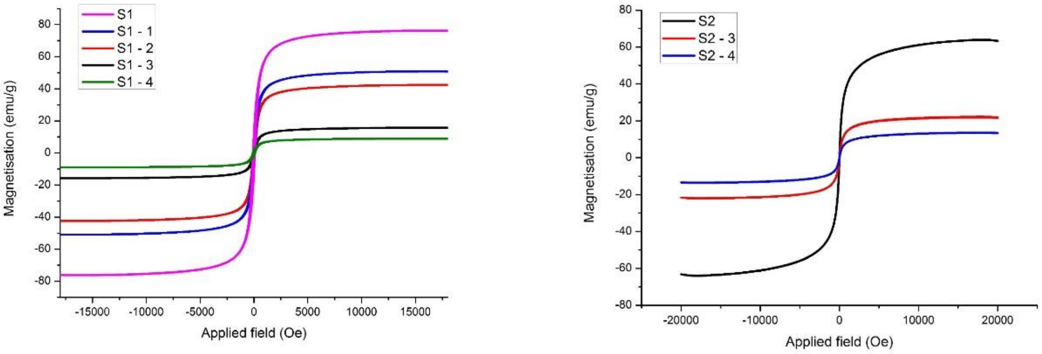

Figure 62. The magnetization curves of Fe_3O_4 nanoparticles and Fe_3O_4-Ag composite nanoparticles obtained by VSM measurements: S1 based composite (left) and S2 based composite (right).

4.3.6 Catalytic properties

The catalytic activity of the particles was investigated by CV. A vitreous carbon electrode was used as a working electrode and it was modified prior to the measurement. For a full description of the approach see Methodology 2.7, but briefly, a known amount of particles were dispersed in isopropanol by ultrasonication. A known volume of nanoparticle dispersion was dropped onto the surface of the vitreous carbon and allowed to dry in the air. Immediately after, the measurements were conducted. A solution of 0.1 M formaldehyde and 1 M sodium hydroxide was used as an electrolyte, which mimics the copper plating solution, however neither EDTA nor Cu salt was placed in the solution. All measurements were set up at room temperature similar to the measurements performed in the literature [26,29,32]. The measurements were conducted at the 50 mV/s scan rates. The measurements started at open circuit potential and increased up to 200 mV, then the scan continued in the opposite direction until the open circuit potential was reached.

Firstly, the measurements were conducted only in sodium hydroxide solution in order to prove the absence of any redox reaction present between the tested composites and sodium hydroxide. There were no oxidation peaks detected by the described method (Figure 63, Figure 64).

The results of the CV measurements in the sodium hydroxide and formaldehyde solution of composites particles are shown in Figures 63 and 64. The peak with highest intensity (7.5 mA/cm^2) was observed for the S1 – 4 composite. This is significantly higher than the next highest peak observed, which occurred in S1 – 3 (2 mA). Moreover, the observed peaks for the mentioned composites are at different potentials -100 and 100 mV for S1 – 3 and S1 – 4 respectively.

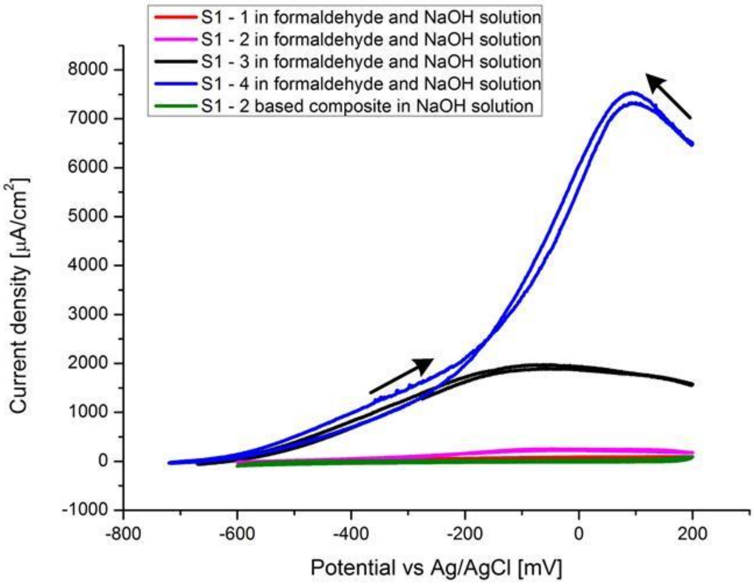

Figure 63. The results of the CV measurements of the composites of Fe_3O_4-Ag in sodium hydroxide and formaldehyde solution. The scan started at the open circuit potential.

Other composites investigated showed much lower peak intensities (90 µA for S1 - 1 and 250 µA for S1 – 2).

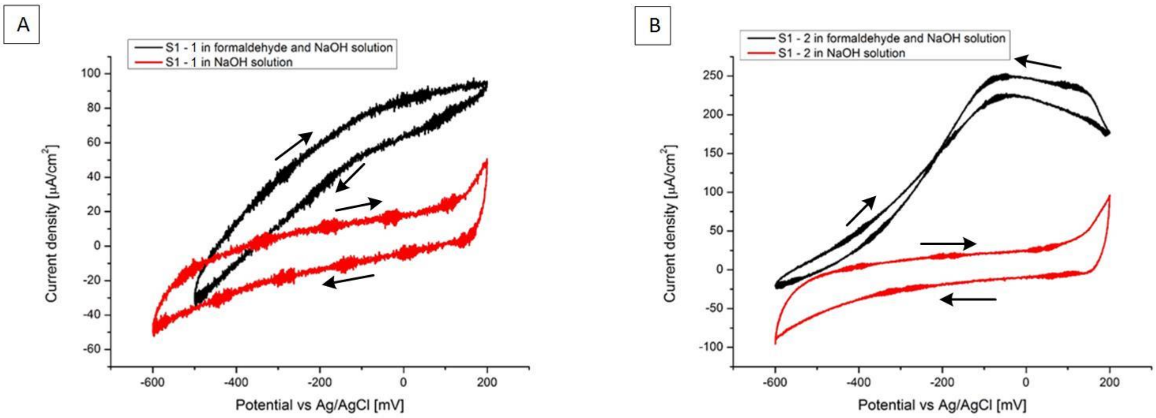

Figure 64. The results of the CV measurements of composites Fe_3O_4-Ag S1-1 (A) and S1-2 (B) in NaOH solution (red) and in a solution of formaldehyde and NaOH (black).

The oxidation current of the both S2 based composites are similar to S1 – 4 composite, the peaks are also positioned at a similar potential (Figure 65).

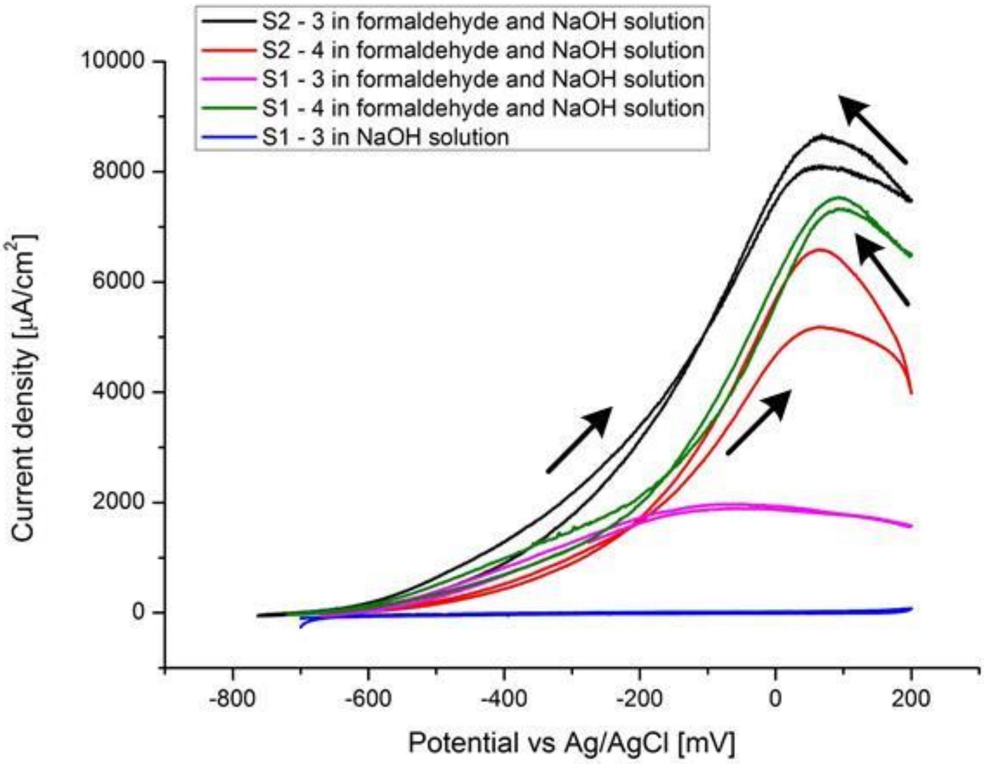

Figure 65. CV measurements of the S2 and S1 based composites in formaldehyde solution.

4.3.7 Discussion

The Fe_3O_4/$AgNO_3$ precursor ratio in these experiments was chosen in order to maintain the concentration of $AgNO_3$ solution low. It was expected that a low concentration of $AgNO_3$ would allow formation of smaller sized Ag nanoparticles and avoid the generation of larger particles. When the concentration of $AgNO_3$ solution was increased (S1 – 4, S2 - 4) the average diameter of the Ag particles also significantly increased (from 92 nm for S1 – 3 composite to 136 nm for the S1 – 4 composite; from 82 nm for S2 - 3 to 139 nm for S2 - 4) (Figure 58, Table 16), which corresponds to results obtained by other research groups for Fe_3O_4 - Ag composite synthesis [135,194]. During experiments S1 - 1, S1 – 2 and S1 – 3, in order to increase the amount of Ag in the composite, the amount of Fe_3O_4 precursors was decreased. According to the particle size measurements the average diameter of Ag particles increased by 10 nm.

The surface of the Fe_3O_4 particles is thought to act as the site for Ag nucleation, which is thermodynamically more favourable than creation of new sites in the bulk solution [177]. When the amount of Fe_3O_4 nanoparticles decreased in the solution, less nucleation sites become available to the Ag deposition. From the same amount of Ag precursor larger amount of smaller particles can be formed. This explains the smaller Ag particles diameter for the S2 – 3 composite compared to S1 – 3, where only the size of precursor Fe_3O_4 is different.

The overall concentration of Ag was estimated by ICP (Figure 59). The concentration of Ag increases with the $AgNO_3$:Fe_3O_4 ratio from S1 – 1 to S1 – 4 and from S2 – 3 to S2 - 4. The particles were washed by using magnetic separation, so Ag which did not form a magnetic composite was removed from the sample during washing. High values of remaining Ag can indicate that composite Fe_3O_4-Ag nanoparticles were successfully formed.

XRD analysis showed that both Fe_3O_4 and Ag particles were present in the composite material (Figure 60, Figure 61). According to the ICP results, the intensity of Ag peaks increased with increasing Ag content. The peaks corresponding to Fe_3O_4 are almost not present in the spectra of S1 – 3, S1 – 4, S2 – 3 and S2 - 4 composites. This can be explained by the significant rise in intensity of the Ag peaks (40000 count) which make peaks for Fe_3O_4 (2000 counts) less noticeable.

The magnetization saturation values of the composites seem to be strongly dependant on the concentration of Fe_3O_4 in the sample (Figure 62). All magnetization saturation values of composites are lower than the ones obtained for the Fe_3O_4 which is in agreement with the literature [133,195–197] and can be explained by the decrease in concentration of the magnetic material in the sample. This is especially noticeable when samples S1 - 2 and S1 - 3 are compared. Those samples have the largest difference in the amount of Fe ions determined (65% and 25% respectively) and also have the largest difference in saturation magnetization values – (40 emu/g and 15 emu/g). The samples with the highest determined Ag content (S1 – 4 and S2 – 4) and therefore the lowest Fe content also had the lowest saturation magnetization value (12 emu/g). However, these samples were still attracted by the magnetic field so they meet the criteria for magnetic properties in further experiments.

In order to compare the catalytic activity of the particles, the potentials of the oxidation current (Figure 63, Figure 64, Figure 65) at 10^{-4} A/cm^2 were compared, similar to work by Ohno (Figure 66).

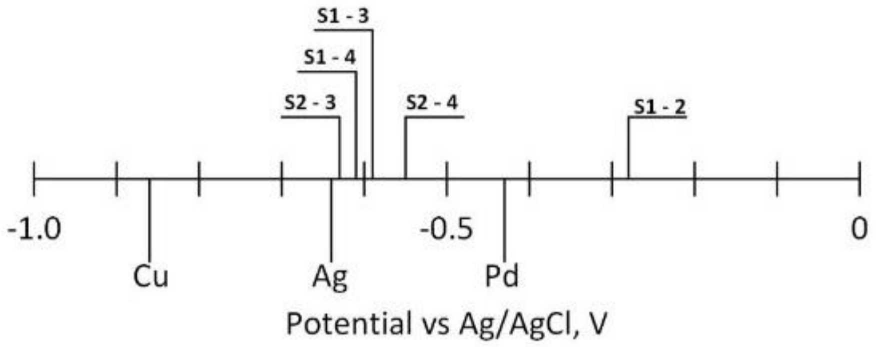

Figure 66. Summary of the potentials of formaldehyde oxidation at current density of 10^{-4}A/cm^2 for the synthesised Fe_3O_4-Ag composites.

The values of potential of the Cu, Ag and Pd electrodes were taken from work by Ohno [29]. The oxidation current density of formaldehyde in the S1 – 1 composite did not reach 10^{-4} A/cm^2 and therefore was not plotted. All recorded potentials are lower than for pure Ag recorded by Ohno. This can be explained by the fact that composites contain non-catalytic Fe_3O_4 particles which reduces the activity per cm^2 of deposited sample. The composites with larger Ag concentration (S1 - 3, S1 – 4, S2 – 3 and S2 -4) have significantly lower potentials of formaldehyde oxidation compared to the S1 – 2, which can also be explained by the higher concentration of Ag per sample. However, the sample with largest Ag concentration (S1 – 4, 88 % Ag) had a potential higher than sample S2 -3 (75% Ag). The size of Ag is different between the samples: 136 nm for S1 – 4 and 82 nm for S2 – 3. The smaller particles have a larger surface area which increases their catalytic activity. However, the potentials for S1 – 3, S1 – 4, S2 – 3 and S2 – 4 are very similar and lower than those recorded for Pd which is typically used as a catalyst for formaldehyde oxidation and therefore electroless plating.

Despite the similar composition of Fe_3O_4-Ag composites the oxidation peaks vary from -100 mV to 100 mV for different composites. This could possibly be attributed to the difference in Ag particle size [198,199]. Also, the shape of the Ag particles was not controlled during the experiments which can also affect the position of the oxidation peak [46,65].

Thus, Fe_3O_4-Ag composite nanoparticles were obtained with different concentrations of Ag, which affected magnetic and catalytic properties of the material. All synthesised composites showed catalytic activity towards formaldehyde oxidation and were attracted by a magnetic field meaning they are potential novel magnetic catalysts for selective copper deposition. The catalysts with the highest catalytic activity S1 -3, S1 -4, S2 – 3 and S2 -4 were further tested for selective electroless plating.

4.4 Synthesis of composite nanoparticles with the use of stabilizers

4.4.1 Introduction

There are two types of stabilization of nanoparticles in dispersion: electrostatic and steric. Electrostatic stabilization can be achieved by modifying the charge on the particle surface so that attractive forces (Van der Waals) are compensated for by the repulsion of the charges (coulomb forces). In order to achieve this, the particle surface can be functionalised via addition of a charged molecule [200–202]. In addition, the pH of the dispersion can be altered in order to achieve positive or negative charge on the required nanoparticles.

Steric stabilization is usually achieved by functionalisation of the surface with large molecules of non-ionic surfactant so that the particles are separated at a distance large enough to prevent creation of Van-der Waals forces [200,203]. If the polymers used have a charge, then both steric and electrostatic interaction take place and electrosteric stabilization occurs.

In order to achieve a stable dispersion of Fe_3O_4-Ag, the following stabilizers can be used; PVP [126,133], arginine [135], tartaric acid [138], cetrimonium bromide (CTAB) [204], trisodium citrate[205] etc. The stabilizers are usually introduced during or before synthesis. Often stabilizers can also act as reducing agents for Ag^+ ions [206]. If the stabilizers are only present on the core particles then a shell Ag layer forms. If the stabilizers are also present in the solution then the reduction of Ag will also happen in the solution and composite particles will be obtained. However, it was reported that functionalisation of catalyst particles reduced their catalytic properties [178]. Functionalisation can affect the magnetic properties of the nanoparticles and reduce their magnetic susceptibility.

Often, particles used for catalysis are synthesised without any further separation and washing [43,47,55]. The advantage of this approach is better dispersion of the particles in colloid dispersions i.e. particles could form agglomerates during drying which would require re-dispersion by grinding or ultrasonication. Particles can change during storage due to absorption of impurities, oxidation or interaction with light. One disadvantage of this approach is that the products of reaction are still present in the solution and their effect on the following reactions should be considered. In addition, the concentration of the synthesised nanoparticles cannot be precisely controlled.

The main criteria for the choice of synthesis procedure was to have a stabilizer on the nanoparticle surface, which had been previously reported in the literature to not hinder catalytic activity towards formaldehyde oxidation.

The procedures used were as follows:

1) (S3) In the first procedure [133] polyvinylpyrrolidone (PVP) was used as a stabilizing agent. Despite some studies that suggest that PVP decreases catalytic activity, PVP is still often used to stabilize the catalyst for electroless plating [44,55]. There are a range of synthesis procedures published in which PVP is used as stabilizer during nanoparticle synthesis. PVP is expected to act as a steric stabilizer.
2) (S4) The second procedure [135] used arginine as a stabilizer. Arginine was previously reported to stabilize the catalyst for electroless deposition [178]. Arginine adsorbed on the composite nanoparticles surface and acts as an electrostatic stabilizer.
3) (S5) Sn is the most commonly used stabilizer for the catalyst in electroless plating. The third chosen procedure [159] used Sn^{2+} as a reducing agent for Ag nanoparticles and enabled Ag deposition on the previously obtained Fe_3O_4-SiO_2 nanocomposites. Sn^{2+} also acts as a stabilizer due to electrostatic repulsion of ions.

4.4.2 Particle size, composition and structure

The particles obtained from the 3 different preparation methods were analysed by SEM and EDX (Figure 67). The EDX data for Ag and Fe distribution shows that in samples S3 and S4 independent Fe_3O_4 and Ag nanoparticles formed, while sample S5 had uniformly distributed Ag across the composite material.

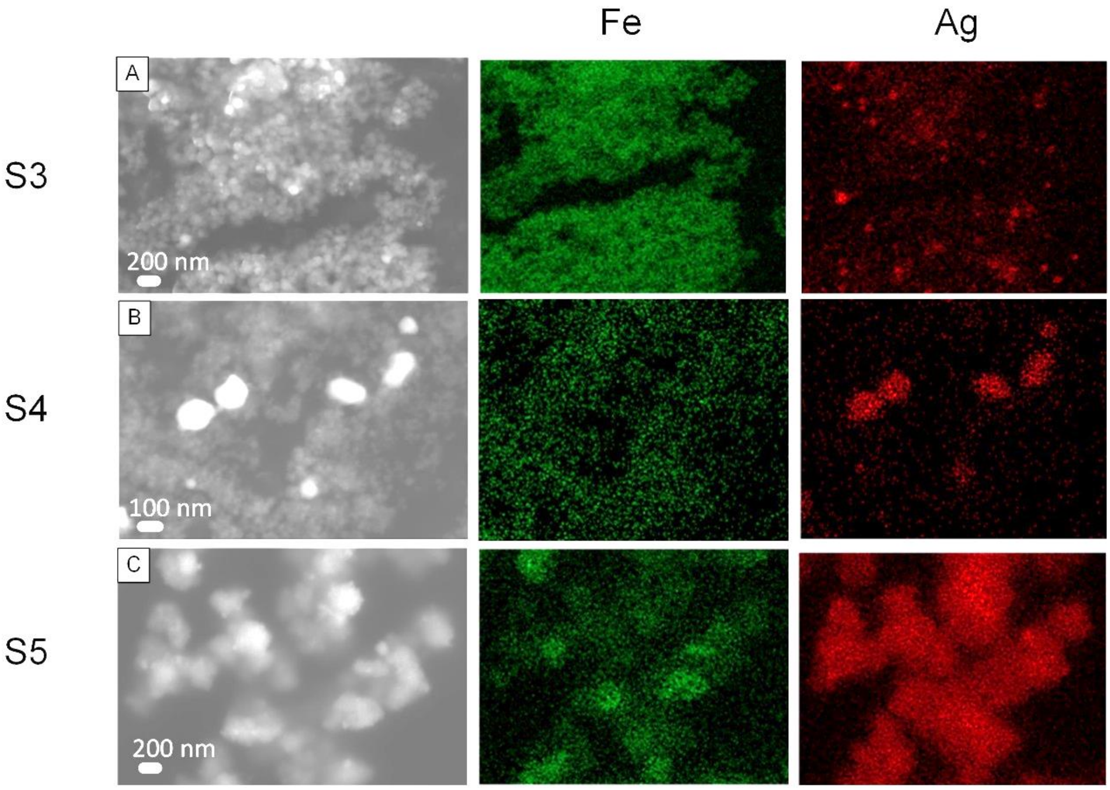

Figure 67. The results of SEM and EDX analysis of particles S3 – A, S4 – B, S5 – C.

ICP analysis was performed on the samples in order to analyse the amount of Ag and Fe in the samples (Figure 68). The Ag content between samples S3 and S5 increased from 13% to almost 50% respectively.

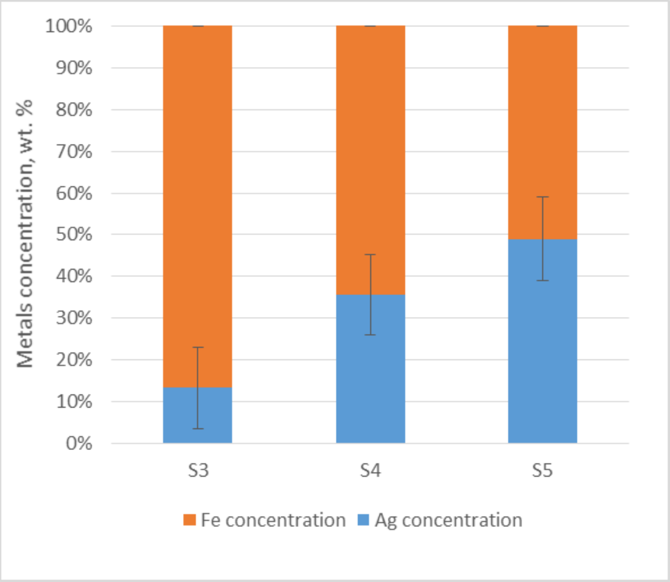

Figure 68. Plot of mass percentage of Ag and Fe in the samples analysed by ICP.

4.4.3 Crystal structure of composites

The crystal structure of the particles was identified by XRD and presented at Figure 69. All particles have a distinctive structure of Fe_3O_4 (Ref. code Fe_3O_4: 01-088-0315) and Ag (Ref. Code Ag: 01-087-0717).

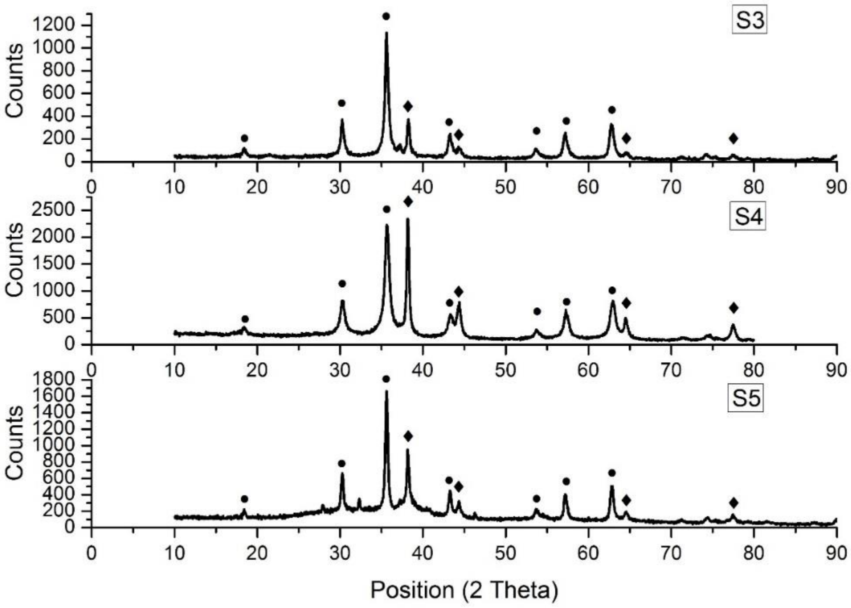

Figure 69. XRD spectra of synthesised composite Fe_3O_4-Ag nanoparticles. Circles indicate the peaks of Fe_3O_4 structure and rhombi indicate the peaks of Ag structure.

4.4.3 Magnetic properties

The preliminary tests were performed according to section 2.5. All particles were attracted by the magnet.

The magnetisation saturation values of the particles lies between 35 emu/g and 57 emu/g (Figure 70). The highest magnetisation saturation was obtained for the PVP-stabilized nanoparticles. The value is higher than that reported from the respective article (20 emu/g) [133]. In the respective articles for synthesis of S4 and S5 nanocomposites the magnetic saturation values were not measured.

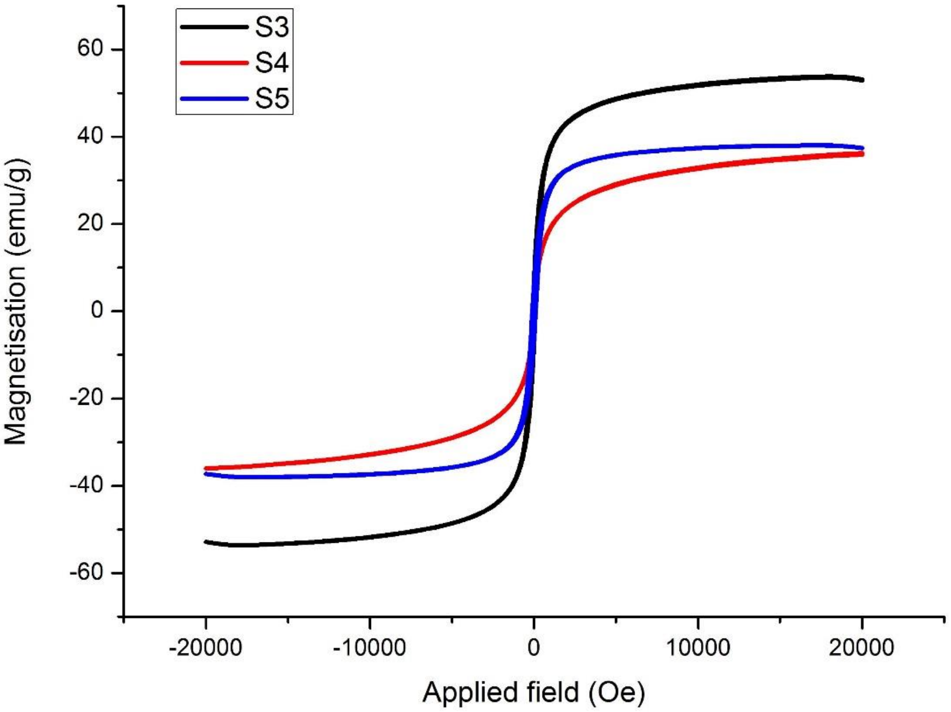

Figure 70. The magnetisation curves of Fe_3O_4-Ag composite nanoparticles S3, S4 and S5 obtained by VSM measurements.

4.4.4 Catalytic properties

The catalytic properties of the particles were evaluated in a procedure similar to that described for the S1 and S2-based nanoparticles.

Particles were dispersed in water or isopropanol before dropping onto the surface of the glassy carbon electrode. Particles dispersed in water had much higher oxidation current densities (especially S3 and S4) than those dispersed in isopropanol. No oxidation peak was observed when CV measurements were performed in the absence of formaldehyde. All peaks were observed at a potential of approximately 50 mV (Figure 71).

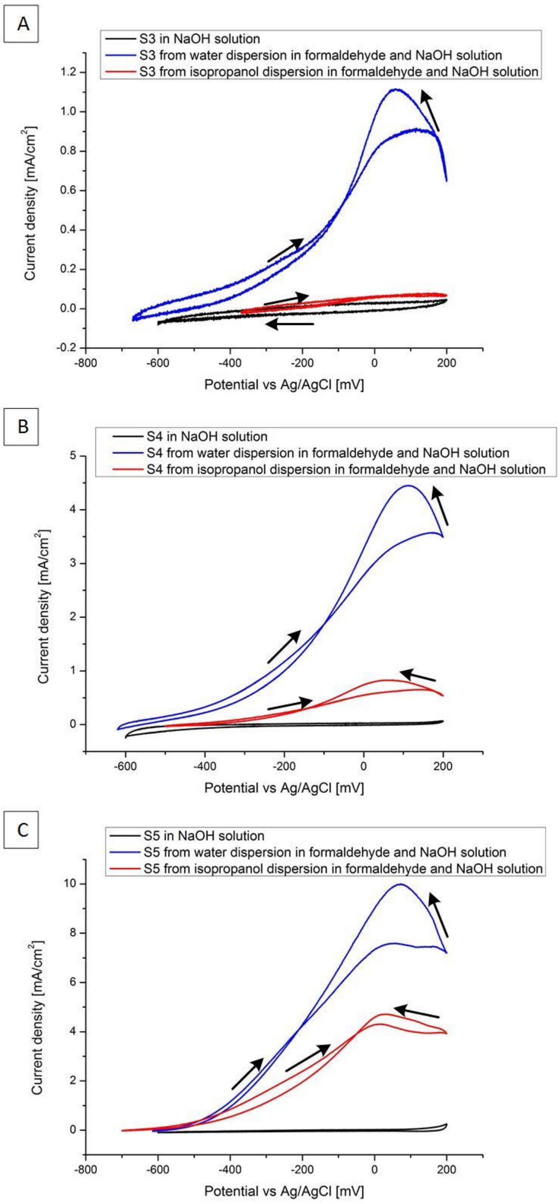

Figure 71. The results of the CV measurements of Fe_3O_4-Ag composites in a NaOH and formaldehyde solution: A – S3, B – S4, C – S5.

4.5 Discussion

The mechanisms behind the nanoparticle synthesis procedures are varied.

First, the S3 composite was synthesised in the presence of PVP. Polyvinylpyrrolidone (PVP) is a polymer which is often used in nanoparticle synthesis (including Fe_3O_4 and Ag) as a capping agent [42,44,47,53,55,204,207]. Monomers of PVP consist of 5 membered lactam and vinyl groups (Figure 72, A). The synthesis procedure for Fe_3O_4 was different to the one used in the previous chapter: both Fe^{2+} and Fe^{3+} ions salts were used as a precursor, therefore the reaction mechanism was [114]:

$$Fe^{2+} + 2Fe^{3+} + 8OH^{-} \rightarrow Fe_3O_4 + 4H_2O \tag{57}$$

PVP molecules bind with the Fe_3O_4 surface during the synthesis which prevents particle agglomeration and allows smaller particles to be obtained. According to the reported results of FTIR and XPS analysis [207], PVP binds to the Fe_3O_4 surface via the carbonyl group.

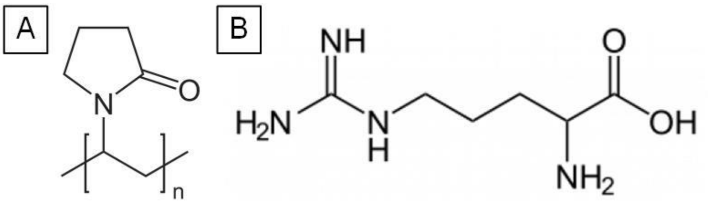

Figure 72. The chemical structure of A – PVP, B – arginine.

Subsequently, the ammoniacal silver was reduced by $NaBH_4$ in the presence of Fe_3O_4 by the following reaction:

$$8Ag^{+} + BH_4^{-} + 8OH^{-} \rightarrow 8Ag + H_2BO_3^{-} + 5H_2O \tag{58}$$

Several works have reported synthesis of Ag nanoparticles in the presence of PVP [206,208,209]. All works also suggest that the binding between PVP and the Ag surface occurs through the carbonyl group. The configuration of both the PVP polymer and the Ag and Fe_3O_4 composites is unclear, as both nanoparticles are supposed to bind to the polymer through the carbonyl group. Some research suggests that there are several layers of PVP obtained, some of which bind to the Fe_3O_4 surface and others do not, so this may potentially allow binding to the reduced Ag nanoparticles.

In the present work, Ag did not deposit uniformly across the sample. The reduction of Ag^+ ions by $NaBH_4$ is instantaneous which often leads to a broad size distribution and large particle formation. PVP is supposed to control the growth of the Ag nanoparticles in the present synthesis procedure. However, as it was added before Fe_3O_4 formation the amount of PVP that is not attached to the Fe_3O_4 surface is not controlled and can be insufficient for full Ag nanoparticle functionalization. The effect of the products of Fe_3O_4 synthesis on Ag nanoparticle formation is also unclear.

The second synthesis (S4) was performed by using arginine as a capping and reducing agent. Arginine is a basic amino acid and has a structure as depicted at Figure 72, B – It has an aliphatic carbon chain with a guanidinium group (pKa = 12.5) at one end and the alpha-nitric group (pKa = 9.0) and carboxyl group (pKa = 2.1) at the other end. Arginine acts as a source of OH^- groups in the Fe_3O_4 synthesis [210]. As a source of iron, only Fe^{2+} ions were used, so the possible mechanism of the reaction is [72]:

$$Fe^{2+} + 2OH^- \rightarrow Fe(OH)_2 \tag{59}$$

$$3Fe(OH)_2 + \frac{1}{2}O_2 \rightarrow Fe(OH)_2 + 2FeOOH + H_2O \tag{60}$$

$$Fe(OH)_2 + 2FeOOH \rightarrow Fe_3O_4 + 2H_2O \tag{61}$$

One study also suggest a possible protonation of Fe^{2+} to Fe^{3+} by arginine’s amino group [210].

Arginine binds to the surface of the formed particles. The majority of the literature suggests that arginine binds to the Fe_3O_4 surface via the carboxyl group which is supported by FTIR and XPS data [210–212]. However, one research group [213] suggested that the guanidinium group binds to the Fe_3O_4 surface, while the carboxyl and alpha-amino groups remain “free”. They observed that the particles were better dispersed in an acidic pH when compared to a basic pH, so they concluded that the carboxyl and alpha-amino groups create hydrogen bonds at basic pH which causes agglomeration, while at acidic pH the groups are charged which prevents agglomeration. However, the guanidinium group also gains a charge at acidic pH values and can hinder particle attraction, therefore there is not enough evidence to confirm binding of the guanidinium group to the Fe_3O_4 surface. It should be noted that as the discussed Fe_3O_4-arginine structures were obtained by different synthesis methods, this could potentially result in different mechanisms of surface functionalization.

After formation of Fe_3O_4 particles, $AgNO_3$ and additional arginine were placed in the beaker. The arginine carboxyl group donates electrons for Ag^+ ion reduction and binds to the Ag nanoparticle surface [214,215]. The formation of core-shell structure is unlikely as both Fe_3O_4 and Ag bind to the arginine through the same functional group.

In the third synthesis procedure, Sn^{2+} was used as a reducing agent. First, Fe_3O_4, obtained as discussed in Chapter 2, was covered with SiO_2 by the following reaction [216]:

$$Si(OC_2H_5)_4 + 2H_2O \rightarrow SiO_2 + 4C_2H_5OH \tag{62}$$

Then the SiO_2 surface was seeded by Sn^{2+}. This process is analogous to the activation of non-conductive substrates prior to Pd catalysation used in electroless plating. After, the Ag was reduced by the following reaction [159]:

$$Sn^{2+} + 2[Ag(NH_3)_2]^{2+} \rightarrow Sn^{4+} + 2Ag + 2NH_3 \tag{63}$$

The obtained particles had a core-shell structure as the Ag was clearly present around the Fe_3O_4 nanoparticle (Figure 67). This structure was obtained because the reducing agent – Sn^{2+} ions were exclusively present on the surface of the Fe_3O_4-SiO_2 nanoparticles. Unreacted Sn^{2+} was removed from solution by washing of the particles between synthesis stages. This was achieved by washing the nanoparticles between the Sn seeding step and Ag deposition. Unreacted Sn^{2+} was removed and only absorbed species were left.

The crystal structure of the S3, S4 and S5 (Figure 69) nanoparticles is similar to the composites obtained in synthesis S2 and S1 in the previous chapter. XRD showed that all of the particles are composites of Fe_3O_4 and Ag. According to the ICP analysis (Figure 68) the obtained particles have different Ag:Fe ratios - 1:6.7 (S3), 1:1.85 (S4), 1:1.04 (S5). This difference can be explained by different loading of the precursors for the synthesis. Also, a larger standard deviation of Ag concentration in functionalized nanoparticles (S3, S4, S5) compared to non-functionalized particles (S1 and S2) was calculated. This indicates lower batch to batch consistency in the syntheses. Issues with reproducibility of nanoparticle synthesis have been reported [151,154] and discussed [152] in the literature. The nanoparticles have a large surface area which can easily be subjected to adventitious adsorption of impurities, which makes consistent surface functionalization difficult to obtain.

All obtained composites were attracted by a magnet and were able to be used further as magnetic catalysts. The values of magnetic saturation of the functionalised composite nanoparticles are similar: S3 – 57 emu/g, S4 – 38 emu/g and S5 – 35 emu/g. These values are below the saturation magnetisation of Fe_3O_4 nanoparticles S1 (75 emu/g) and S2 (68 emu/g), but exceed the values of composite nanoparticles with large Ag content (S1 - 3, S1 - 4, S2 - 3, S2 - 4), which are below 20 emu/g. The obtained values correlate with the data obtained in ICP analysis (Figure 68) – the larger the concentration of Ag in the samples the smaller the magnetic saturation value.

The CV results showed that all of the obtained composites in this Chapter can catalyse formaldehyde oxidation.

The potentials of the oxidation were measured at 10^{-4} A/cm^2, the same as those discussed in Chapter 4.2.5.

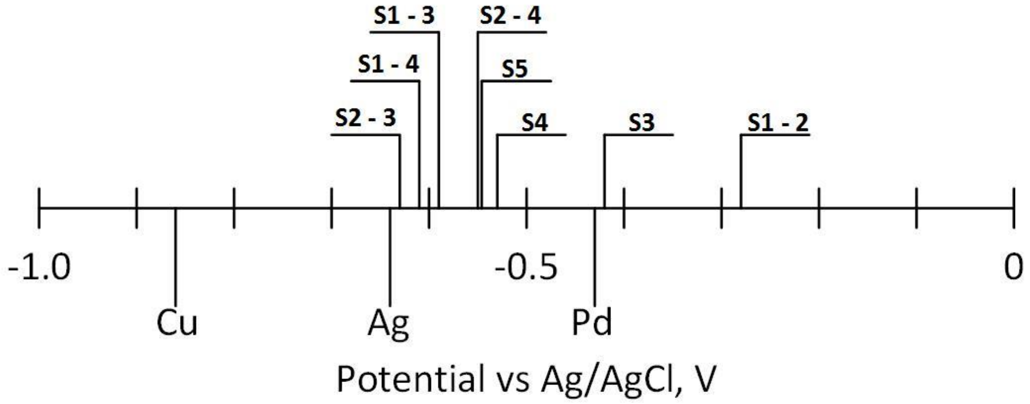

Figure 73. Summary of the potentials of formaldehyde oxidation at current density of 10^{-4}A/cm^2 for the synthesised Fe_3O_4-Ag composites.

The stabilized particles have higher potentials than the particles synthesised without the use of stabilizers (Figure 73). It was discussed earlier that functionalisation of the particles can hinder their catalytic activity. The increase in the potential corresponds with the decrease of Ag concentration for the stabilized particles. S5 has the lowest potential amongst the particles synthesised in the chapter and the highest Ag concentration.

The values of peak current density are varied, however as was discussed earlier, current density cannot quantitatively characterise the catalyst nanoparticle performance because other factors also influence this. For example, two procedures of working electrode preparation were tested. Examined nanoparticles were dispersed in isopropanol or water prior to drop-coating of the electrode. After, the electrode was dried, CV was conducted. Higher current densities were observed when particles from the water dispersion were measured. This could possibly be due to the evaporation rate of solvent, which influences the particle distribution across the electrode

[217]. The prepared dispersions are not stable and the particles sediment within 2-3 minutes. In freshly prepared dispersions, particles are well distributed across the sample and during drying the particles are driven by liquid flow. Because of the high rate of isopropanol evaporation, the particles do not have sufficient time to redistribute and this results in particle agglomeration. When the particles were deposited from water dispersion the water evaporated much slower than isopropanol. In this case the particles sediment uniformly across the sample which resulted in a larger surface area and higher current density measurements.

In summary, composite particles containing Fe_3O_4 and Ag were synthesised using PVP, arginine and Sn^{2+} as stabilizers. The S5 particles have a core-shell structure. All particles have catalytic activity towards formaldehyde oxidation and will be further examined as magnetic catalysts for electroless Cu plating.

Chapter 5. Electroless copper catalyst deposition under the influence of a magnetic field

5.1 The dispersion and deposition of non-functionalised magnetic catalyst by applying a gradient magnetic field

5.1.1 Introduction

The catalyst should be deposited on the non-conductive material prior to electroless copper plating [6]. Usually a Pd/Sn colloid or solution is used as a catalyst. Deposition from solution is one of the lowest cost techniques as it does not require expensive equipment and confers reproducibility. However, cheaper alternative catalysts are being investigated [43,44,47,55,59,62,64,192,218,219].

During synthesis, the particles are stabilized by substances such as PVP [44,47,53,55,218], SDS [43], PDA [68], amino acids [178] etc. Often, catalysts used as synthesised from the same solution contain the products of the synthesis reaction. In some works the particles were washed and dried after synthesis and then re-dispersed. Litchfield et al. published work in which they dispersed commercial copper nanopowder and then stabilized by ultrasonication in a solution with a stabilizing agent [192]. The method was only attempted on the Cu nanoparticles but not on the composite material as obtained in the current work. Ultrasonication can damage composites and destroy their structure [220,221]. Also it has been reported that some stabilizers can hinder catalytic activity of particles and prevent electroless copper plating from occurring [178,192].

Another technique which can be used for the formation of a stable colloid is changing the pH of the solution in order to achieve a high charge on the particle surface [202]. However, this technique was not considered as the composite material consists of 2 different nanoparticles: Fe_3O_4 and Ag and by obtaining the extra charge on the particle surface, the composite particles may repel or if the opposite charge is attained Fe_3O_4 and Ag surfaces may excessively agglomerate.

Some particles used in the current work (S1 and S2-based composites) were synthesised without any stabilizers so it was expected that the solutions will not have significant stability. Also the magnetic particles tend to agglomerate especially when the magnetic field is applied [181], which is difficult to prevent. Therefore, it was decided to conduct experiments without introducing stabilizers and conduct deposition on the freshly dispersed particles in order to achieve reproducible results.

The method of particle dispersion was considered. Continuous stirring by magnetic or overhead stirrers is often used. The magnetic stirrers can attract the catalyst and influence the solution stability. In addition, the catalyst used in the current work was dried after synthesis which causes the agglomeration of particles. Therefore, ideally the used dispersion method should be able to destroy agglomerates. Some of the possible techniques are – ultrasonication by bath or horn, ball milling or high pressure treatment. Ultrasonication was chosen as the most economically favourable. A bath was chosen in order to avoid complete destruction of the composite structure and also to avoid contact of the solution with equipment such as the horn.

Another approach to eliminate agglomerates from the colloid solution is to remove them using filtration which was used in the present work. In order to measure the concentration of the catalyst in the dispersion after the filtration the dispersions were analysed by ICP.

Usually the catalyst for electroless plating is characterised in the colloid form and by evaluating the obtained electroless Cu plating [41,59,62,176]. The majority of the catalyst for electroless plating deposits on the surface due to adsorbtion [52,62,178]. In the present work the magnetic field was applied during catalyst deposition. The magnetic particles can agglomerate in the magnetic field [108,113]. Therefore, the characterisation of particle distribution after deposition on the surface was also evaluated by SEM analysis.

The analysis of quantity of the deposited copper was considered. The change in weight is commonly used in order to characterise the amount of deposited material. However, in the present case, a significantly smaller surface is subjected to the deposition, which makes it difficult to record the change in weight. Also any change does not reflect parameters of the deposited layer such as adhesion and uniformity.

Another technique which was considered was ICP analysis of the deposited catalyst. This would help to evaluate the amount of particles deposited and the ratio of Ag to Fe ions. However, this would not reflect the distribution of particles across the sample and the degree of their agglomeration.

Therefore, it was decided that low magnification SEM should be used to evaluate how the catalyst is distributed across the sample as well as the morphology of the obtained electroless copper deposit.

5.1.2 Catalyst deposition after 5 min ultrasonication

In this section the catalysts synthesised without any functionalisation and stabilization were investigated: S1 – 3, S1 – 4, S2 – 3 and S2 - 4. The catalyst were simply dispersed in water by ultrasonication. DLS analysis was attempted on the dispersions. However, due to the low stability the obtained results did not meet the required quality for reliable analysis.

In the first experiments, the catalyst deposition time was varied: 5 sec, 15 sec and 30 sec.

Particles S1 – 3 in amount 0.025 g were ultrasonicated in 100 ml of water for 5 min. Straight after, the substrate with the attached magnet behind it was placed in the dispersion and removed after 5, 15 or 30 sec. Longer catalyst depositions were also tested. However, the surface was overloaded with catalyst and the resulting Cu plating did not have any adhesion to the surface and was removed after washing the substrate.

A dark deposit appeared at the area opposite the substrate surface where the magnetic field was applied (Figure 74, A). Subsequently, the substrate was washed in RO water and placed in the electroless copper bath for 25 min with the magnet still attached. The procedure is described in more details in sections 2.5 and 2.6.

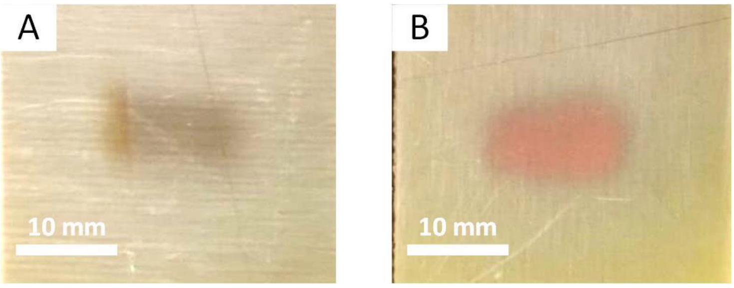

Figure 74. Digital images of substrate after A – catalyst deposition stage, B – after electroless copper plating stage.

SEM images were obtained after the catalyst deposition and copper deposition stages (Figure 75). A more continuous layer of deposited copper was obtained when more catalyst was deposited on the substrate.

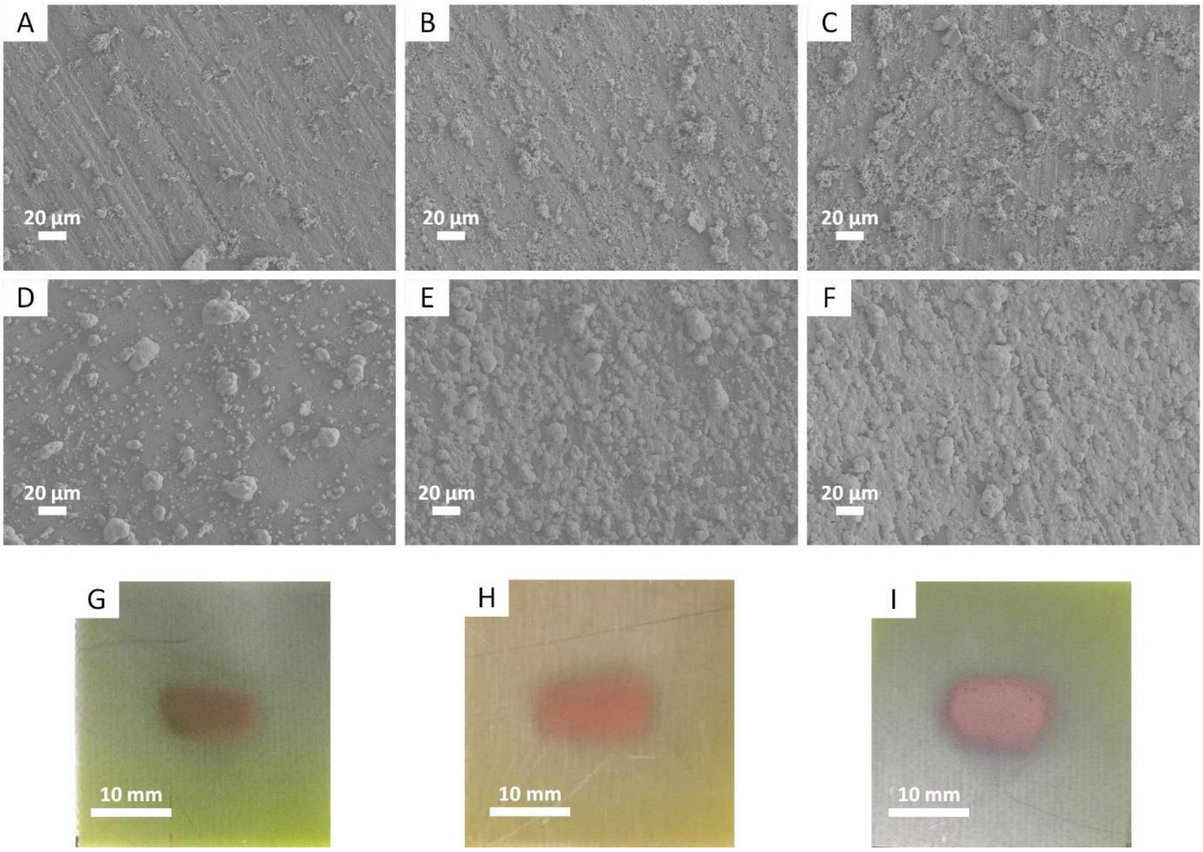

Figure 75. SEM images of the deposited catalyst S1-3 (A-C) and electroless copper (D-F), and digital images of obtained copper plating (G-I) at different catalyst deposition times: 5 sec (A, D, G), 15 sec (B, E, H) and 30 sec (C, F, I).

The same procedure was repeated with the same deposition times for catalysts S1 – 4, S2 - 3 and S2 – 4. Typical SEM images of the deposited catalyst and digital images of the substrate after the electroless copper plating stage are presented in Figure 76. The substrates have significantly less deposition compared to the one obtained in catalyst S1 - 3. According to the SEM images, catalysts S2 - 3 and S2 – 4 have a large amount of agglomerates.

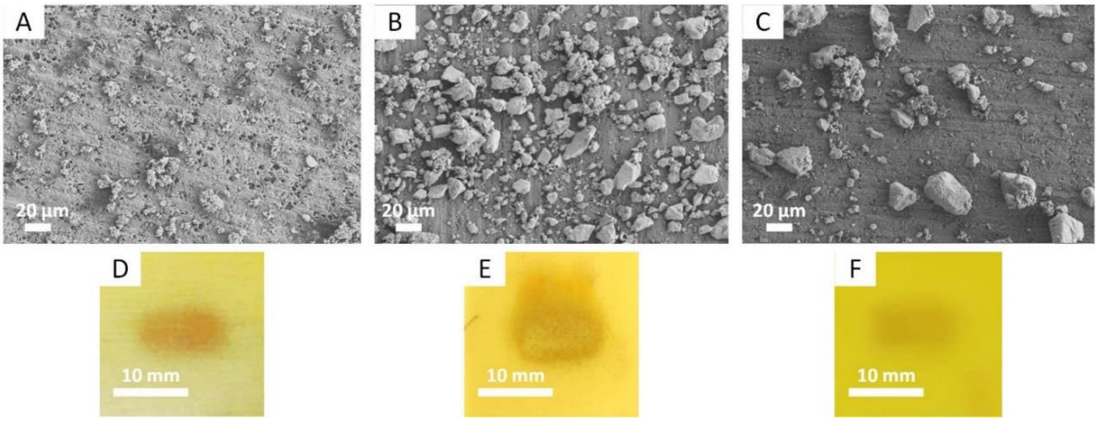

Figure 76. SEM images of the deposited catalyst layer (A-C) and digital images (D-F) of the substrates after the electroless copper plating stage. The catalysts S1 – 4 (A, D), S2- 3 (B, E) and S2 – 4 (C, F) were used.

5.1.3 Catalyst deposition after 30 min ultrasonication

In order to break down the agglomerate, catalysts of the same concentration were ultrasonicated for 30 min. First the catalysts were deposited for 30 sec as this was determined as the optimal time of catalyst deposition for S1- 3. However, overloading of the surface with catalyst was observed for all samples, as could be observed from the absence of adhesion of the deposited electroless copper. Therefore, the catalysts were deposited for 15 sec in order to compare with previous results. The SEM images of the deposited catalysts and the digital photographs of the substrates after electroless copper plating are presented in Figure 77. Longer ultrasonication does not improve the quality of the S1 - 4, S2 - 3 and S2 - 4 deposits as very low amounts of copper plating were observed. The plating obtained with the S1-3 catalyst was not continuous and had the presence of needle-like structures at the substrate centre. The deposit displacement was observed on the sample catalysed by S2 – 3 particle. In addition, according to the SEM images (Figure 77, C, D) the S2 - 3 and S2 - 4 catalysts still have large agglomerates on the surface. Therefore, solutions were filtrated after 30 min of ultrasonication.

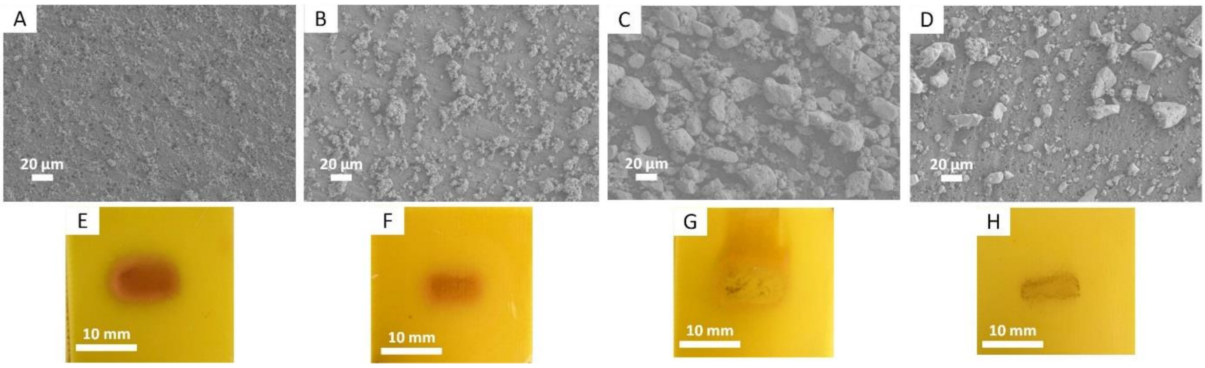

Figure 77. SEM images of the deposited catalyst layer (A-D) and digital images (E-H) of the substrates after the electroless copper plating stage. The catalysts S1 – 3 (A, E), S1 – 4 (B, F), S2- 3 (C, G) and S2 – 4 (D, H) were used.

5.1.4 Catalyst deposition after 30 min ultrasonication and filtration

The concentration of Ag and Fe ions in the catalyst particle dispersions was measured by ICP analysis (Figure 78).

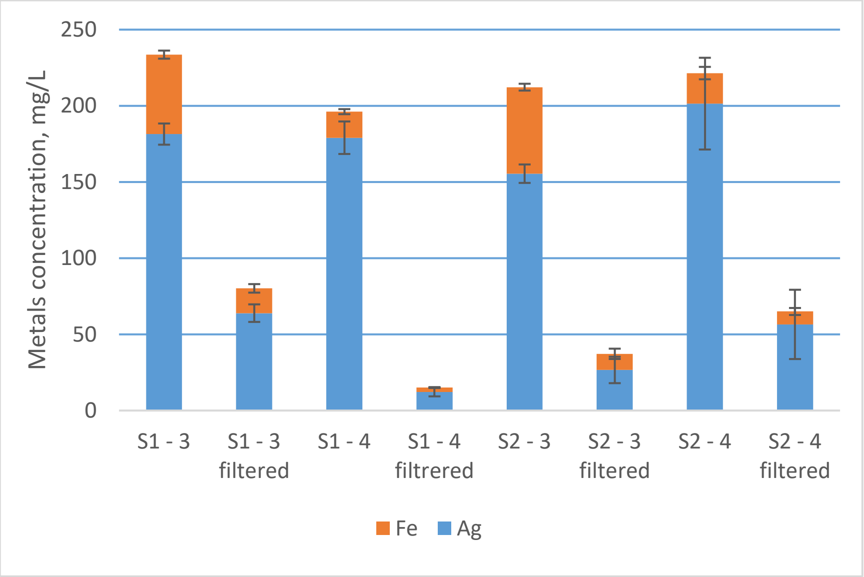

Figure 78. The ICP analysis of Fe and Ag concentration in the dispersions of the Fe_3O_4-Ag nanoparticles before and after filtration.

According to the obtained data the concentration of the ions significantly decreased after the filtration because some particles remained on the filter. Therefore, longer immersion times in the catalyst were tested: 30 sec and 3 min.

The S1 - 3 catalyst deposited in a needle-like structure at the centre of the magnetic field influence, especially when the catalyst was deposited for 3 min (Figure 79).

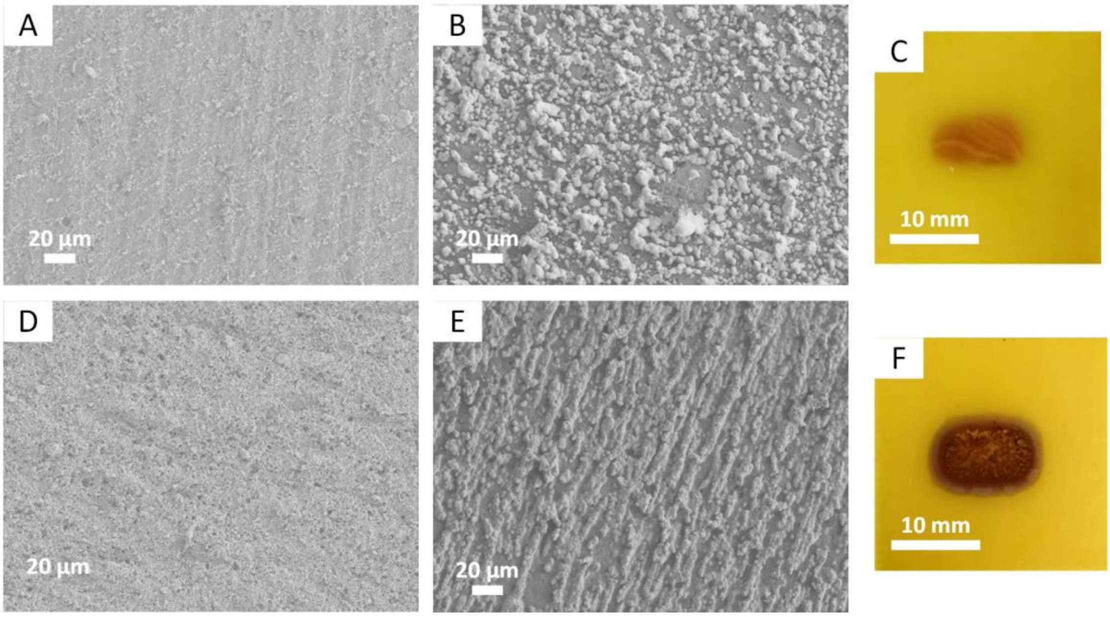

Figure 79. SEM images of the deposited catalyst layer (A, D) and electroless copper plating (B, E), and digital images (C, F) of the substrates after electroless copper plating stage. Catalyst S1 – 3 was deposited for 30s (A - C) and 3 min (D – F).

S1 – 4 and S2 - 4 catalysts had similar performance. Both catalysts deposited with large amount of agglomerates (Figure 80, Figure 81) and continuous film formation was not achieved.

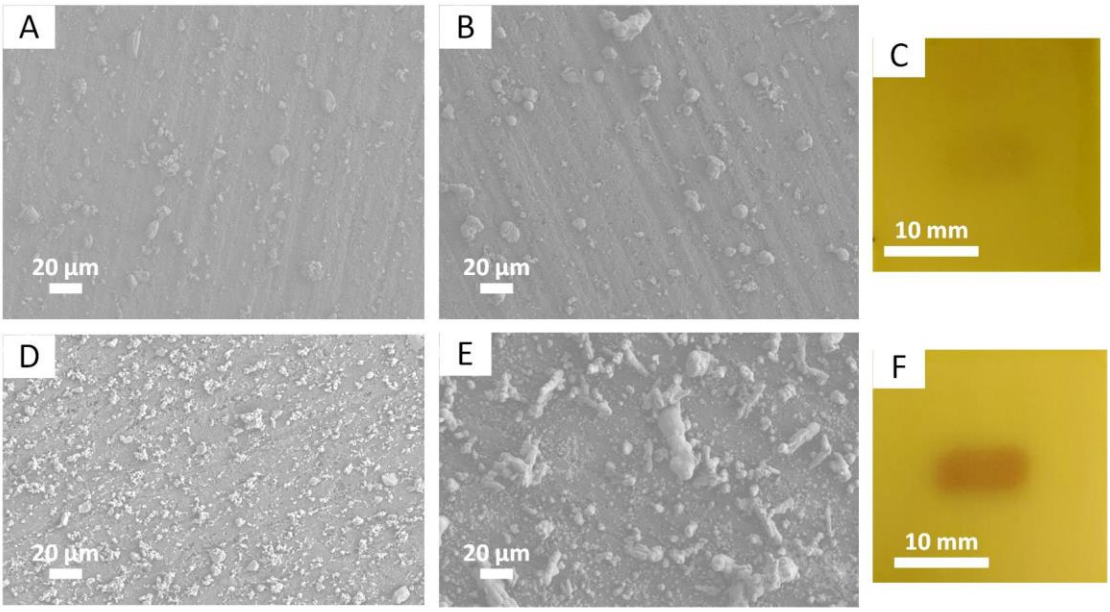

Figure 80. SEM images of the deposited catalyst layer (A, D) and electroless copper plating (B, E), and digital images (C, F) of the substrates after the electroless copper plating stage. The catalyst S2 – 4 was deposited for 30 sec (A - C) and 3 min (D – F).

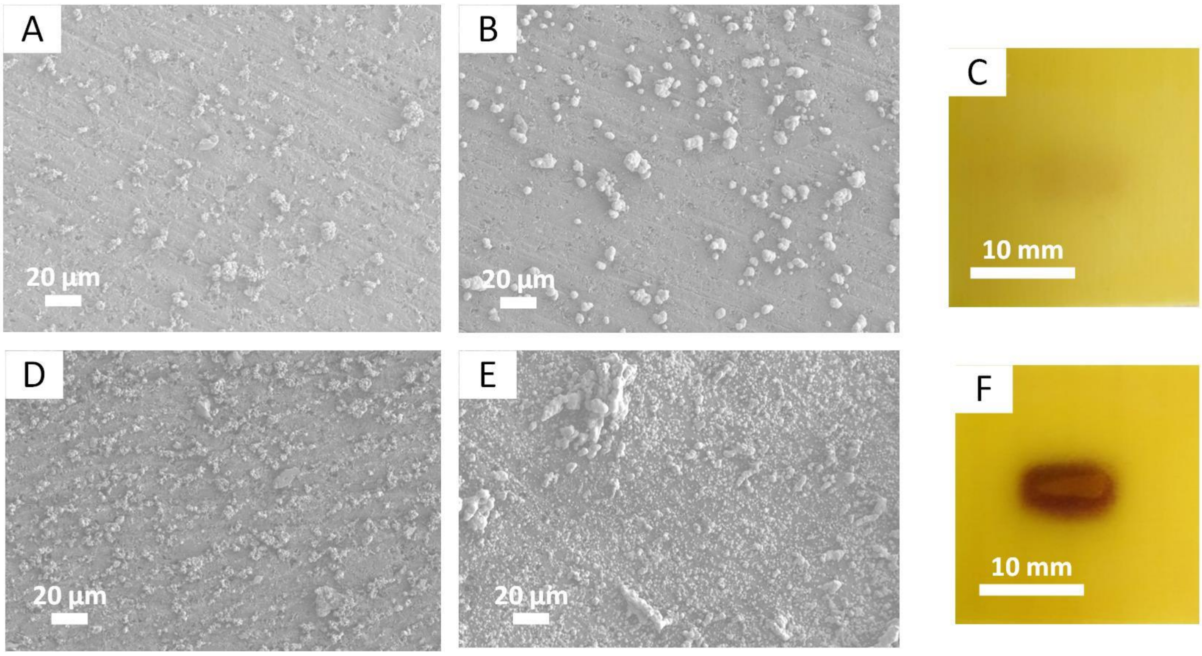

Figure 81. SEM images of the deposited catalyst layer (A, D) and electroless copper plating (B, E), and digital images (C, F) of the substrates after the electroless copper plating stage. The catalyst S1 – 4 was deposited for 30 sec (A - C) and 3 min (D – F).

The S2 - 3 catalyst showed significantly improved performance after filtration and a much brighter deposit was obtained (Figure 82). Also, during longer exposure to the catalyst, needle-like structures were observed at the centre of the substrate (Figure 82 F, H). It should be noted that a continuous deposit was observed at the area located higher than the magnetically influenced area. This happened during all depositions performed with the S2 - 3 catalyst, but never occurred with any other catalysts tested. It should be noted that no catalyst displacement was observed prior to electroless plating.

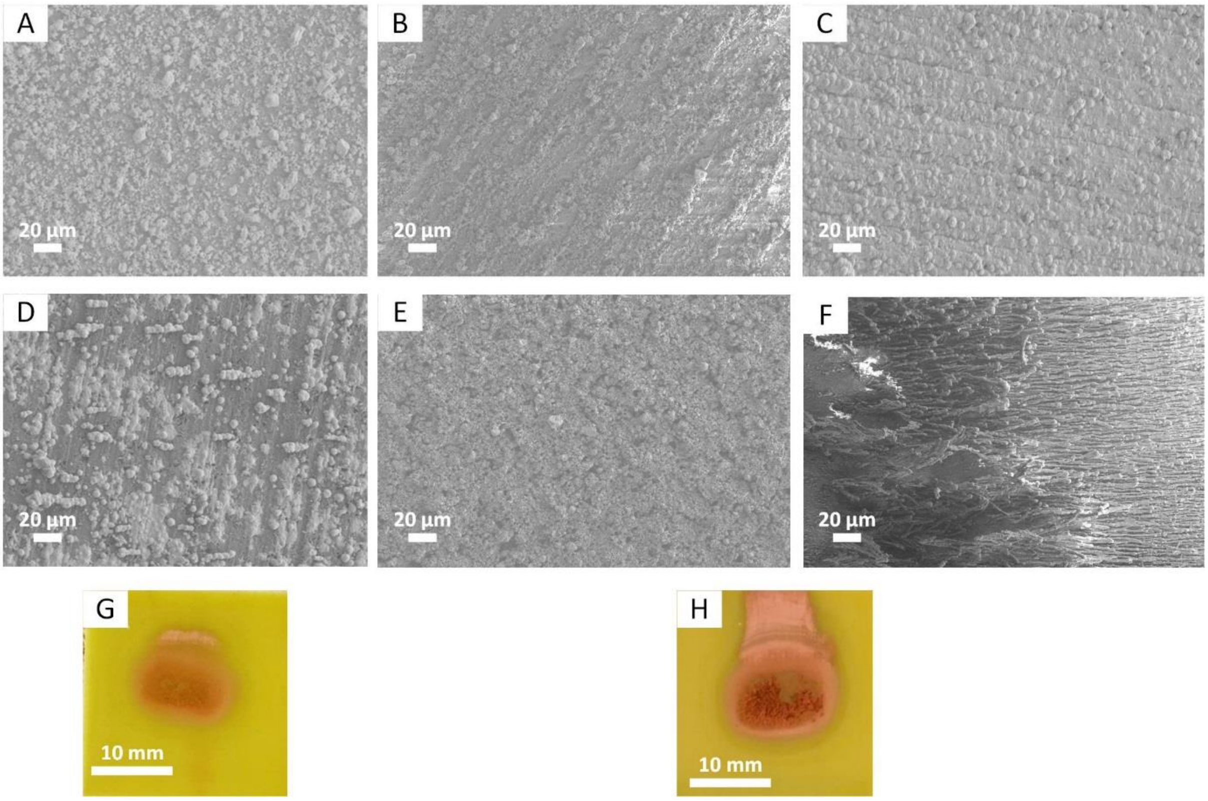

Figure 82. SEM images of the deposited catalyst layer (A-C) and electroless copper plating (D-F), and digital images (G, H) of the substrates after electroless copper plating stage. The catalyst S2 – 3 was deposited for 30 sec (A, D, G) and 3 min (B, C, E, F, H). B, C – the images were taken at the top part of the continuous deposit, E, F – the images were taken at the centre part of the deposit.

5.1.5 Discussion

The correlation between the distribution of the deposited catalyst on the substrate surface and the resulting copper deposit was investigated.

The first deposits were obtained after 5 min of ultrasonication of catalyst colloid. The shorter time of ultrasonication was chosen in order to prevent destruction of the composite nanoparticles.

All catalysts employed had a similar composition and size however the performance was different. The most effective catalyst was S1 - 3, as distinctive copper plating was achieved (Figure 75). Compared to the other deposited catalysts (Figure 76), S1 – 3 had better distribution across the sample and did not have the large agglomerates seen in the S2 based catalysts. A more evenly distributed catalyst across the surface will have a larger surface area and will result in higher catalytic activity [222].

Catalysts S2 – 3 and S2 – 4 had significantly lower performance and almost no copper plating was achieved (Figure 76). Both catalysts were made with Fe_3O_4 obtained on a SDR. In addition to the small particles which were shown in section 4.2, large particles were also formed. It can be attributed to the synthesis procedure – the solutions of Fe salts and base were first mixed on a spinning disc and were afterwards collected using a continuously stirring vessel. However, there was no stirring when the solutions were transported through the pipe from the spinning disc to the vessel. The reaction of the Fe_3O_4 formation is not immediate and continues while solutions are transported from the spinning disc reactor which may result in large particle formation.

In order to decrease the amount of agglomerates, longer ultrasonication was performed. Both catalysts S1 - 3 and S1 – 4 resulted in copper layer formation (Figure 77, E, F), however in both cases the central part of the deposit remained not entirely plated and had a dark coloration due to the presence of catalyst. This indicates non-uniform distribution of the catalyst around the area where the magnetic field was applied and non-uniform distribution of the magnetic field around the area. Secondly the deposit had a needle-like structure at the central part of deposit (observed during visual examination) which is due to catalyst nanoparticle alignment in the magnetic field [113].

Longer ultrasonication of S2 based particles did not result in copper plating formation (Figure 77, G, H) and agglomerates were still present when the deposited catalyst was analysed (Figure 77, C, D). This indicate either strong agglomerate formation or the presence of large particles in solution. In order to eliminate the agglomerates and large particles, filtration was used. There are a range of filters that can be used with various pore sizes. Intuitively the filter with smaller pore size should be chosen. However, due to the presence of agglomerates, filtration with a fine pore size will result in a low concentration of particles in the dispersion. Even after filtration with a filter with pore size 6 µm the concentration decreased more than 3-fold according to the ICP analysis (Figure 78).

The filtration did not significantly improve the performance of S1 - 3 and S1 – 4 (Figure 80, Figure 82). A filter with pore size 6 µm was used, and less agglomerates of this size were observed in both catalysts. It is possible that a filter with a finer pore size should be used in order to achieve improvement in the aforementioned catalysts.

The performance of the S2-based catalysts was improved with filtration (Figure 80, Figure 82). Using the S2 – 3 catalyst resulted in formation of a uniform copper layer at the edges of the magnetic field influence and at the area located higher than the magnetically influenced region. The plating at that area can be explained by the displacement of the catalyst particles. The displacement only occurred towards the top area of the substrate so it cannot be caused by gravitational forces as they would result in the displacement of the catalyst to the bottom part of the substrate [103]. Another theory was that some part of the particles have less magnetic attraction than others and are therefore being removed during rinsing stages, although this would likely also result in displacement in the other directions. Displacement of the catalyst prior to electroless plating was not observed. Therefore, this can only occur during the electroless plating process. This may be occurring as a result of hydrogen evolution reaction which proceeds during formaldehyde oxidation [6]. Hydrogen bubbles move towards the solution surface during the electroless plating process, along the surface of the top part of the substrate. Hydrogen bubbles also possibly transport less magnetic parts of the catalyst - the parts with the higher silver and lower Fe_3O_4 content. The presence of more Ag particles results in more uniform Cu plating.

The obtained results may be contrary to the CV measurements made in the previous chapter – the best performing catalyst S1 – 3 had a higher potential compared to S2 - 3 and S1 – 4 nanoparticles (Figure 66). Possible reasons for this include the following:

First of all, sample preparation for CV measurements and for electroless plating are different. For CV, the solution is drop-coated onto the electrode surface and no magnetic field is applied. Therefore, particles are not influenced by any external force that could cause agglomeration. Also for CV the probe was taken from the middle of the vial and there was no preferential intake of particles of any certain size. When the magnetic field was applied, larger particles are more likely to be attracted as they have larger magnetic susceptibility, while smaller particles will also agglomerate [114]. For this reason, the particles evaluated by CV will not experience the same high level of agglomeration as the ones deposited under the magnetic field influence. Therefore, the probe used for the CV analysis will contain less agglomerates and particles of smaller size. This will significantly improve the performance of the catalysts in which large agglomerates are present after the deposition in the magnetic field (S1 – 4, S2 – 3 and S2 – 4).

Overall, the obtained deposits do not show high uniformity and the quality of the deposit differs at the centre and outside part around the magnet. Therefore, further investigation of the magnetic field properties are required.

The most uniform copper plating was obtained when S1 – 3 was deposited for 30 s after 5 min ultrasonication (Figure 75). Further treatment of the catalyst resulted in needle-like structure formation, which was also observed when S2 – 3 catalyst was used after filtration. It is possible that the smaller particles tend to align with the magnetic field, while if bigger particles are used the performance of the catalyst decreases.

The typical electroless copper plating appearance observed in the present work can be categorised as shown in Table 17.

Table 17. Digital photographs of typical categories of obtained electroless copper plating during applying permanent magnet and respective SEM images of catalyst distribution and electroless copper layer.

Digital photographs of obtained Cu plating	**SEM images of deposited catalyst**	**SEM images of electroless Cu**
	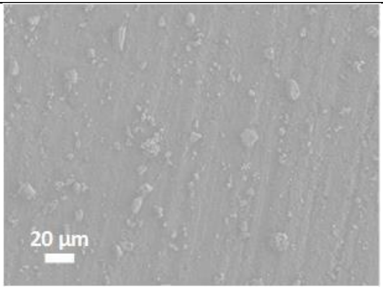	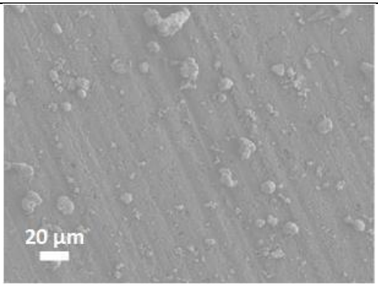
No visible plating	Agglomerates of catalyst mainly deposited	Barely any Cu deposit
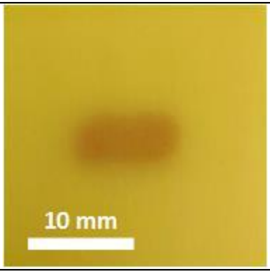	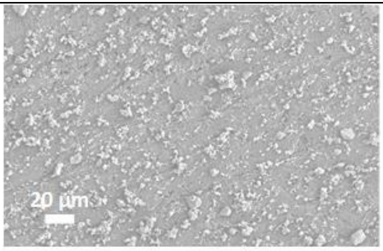	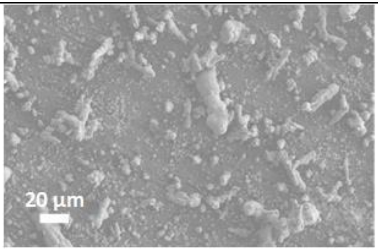
Light pink coloration	Catalyst still has lots of agglomerates but they are spread around the substrate	Non-uniform Cu deposit
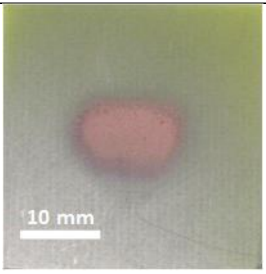	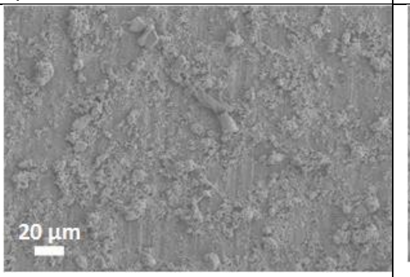	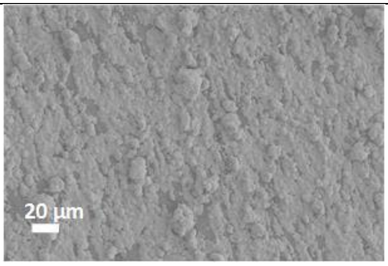
Bright pink layer	Smaller catalyst agglomerates spread around the substrate surface	Electroless Cu film was formed
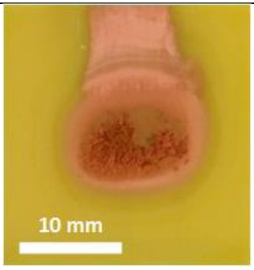	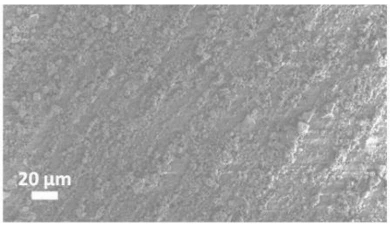	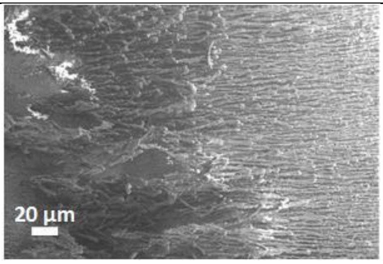
Needle-like deposit	Small catalyst particles aligned in the magnetic field	Low adhesion and needle-like Cu layer obtained

5.2 The dispersion and deposition of the functionalised magnetic catalyst by applying a gradient magnetic field

5.2.1 Introduction

The catalytic activity of the particles is highly dependent on their surface area. In order to maintain high surface area of the catalyst, the particles should be well dispersed in the colloid and uniformly deposited on the substrate surface.

The nanoparticles obtained in the previous chapter were first dried after synthesis. During drying, the particles can make chemical bonds and form agglomerates [223,224]. The functionalization of the particles with steric stabilizers helps to prevent agglomeration during drying [224]. However, if stabilizers do not bind to the whole surface of the particles, agglomerates can still be formed [225]. In order to break the agglomerates and disperse the particles in water, ultrasonication was used. Some work showed that even after relatively short treatment (30-60 min), the size of agglomerates significantly decreased [59,226] . Therefore, 30 min ultrasonication treatment was used.

The dispersions are often analysed by dynamic light scattering analysis (DLS). This shows the distribution of the particle size in a dispersion. However, DLS has certain limitations. Firstly, only stable dispersions can be analysed because the measurement is relatively long and changes in the dispersions (including agglomeration and sedimentation) affect the results. In addition, it has limitations for analysis of dispersions with particles of different sizes. The technique is based on analysis of intensity of scattered light. Larger particles give a stronger signal than smaller ones. The scattering power of particles is proportional to their diameter to the sixth power [227]. Therefore often the signal from particles of smaller diameters can be masked by signals from larger particles [228,229]. This was observed during the experiments on bimodal dispersions (where the proportion of particles diameters is 2:1 or larger) and the particle with smaller diameter were not detected by DLS at all.

In the present Chapter, similar to Chapter 5.1, the dispersion of the nanoparticles in water, the distribution of the particles after deposition by applying a magnetic field and subsequent electroless Cu plating were all evaluated.

The following particles were studied in this Chapter: particles stabilized by PVP (S3), arginine (S4) and Sn ions (S5). The S4 particles were also dispersed in a 0.01 M HCl at pH2 because the charge of arginine depends on the pH and more stable dispersions obtained at acidic pH were previously reported [213].

5.2.2 Colloid dispersions of the magnetic catalyst nanoparticles

The nanoparticles obtained in Chapter 4.4 were dispersed in water for 30 min by ultrasonication and analysed by ICP and DLS. The same catalyst dispersions were filtered after ultrasonication in order to eliminate the agglomerates and large particles and analysed again.

The results of ICP analysis are presented in Figure 83. The concentration of Ag and Fe ions were measured. The concentration of both detected metals from non-filtered dispersions is similar for all samples and varies from 134 to 163 mg/l. After filtration, the overall concentration of metals significantly decreased in the S3 and S4 dispersions by 6.7 and 9 times respectively. The concentration of metals from filtered dispersions S4 pH 2 and S5 also decreased but only by 1.6 and 1.3 times respectively. The concentration of Ag decreased proportionally with the overall metals concentration for most of the samples except S4 pH 2.

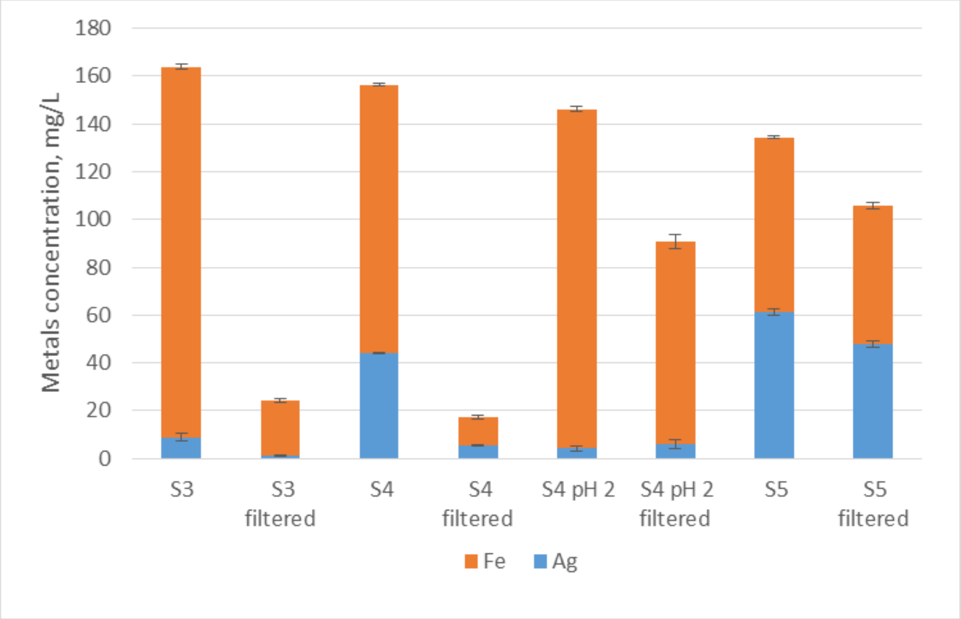

Figure 83. The concentration of Ag (blue) and Fe (orange) ions determined by ICP analysis in magnetic nanoparticle dispersions S3, S4, S4 pH 2, and S5 before and after filtration.

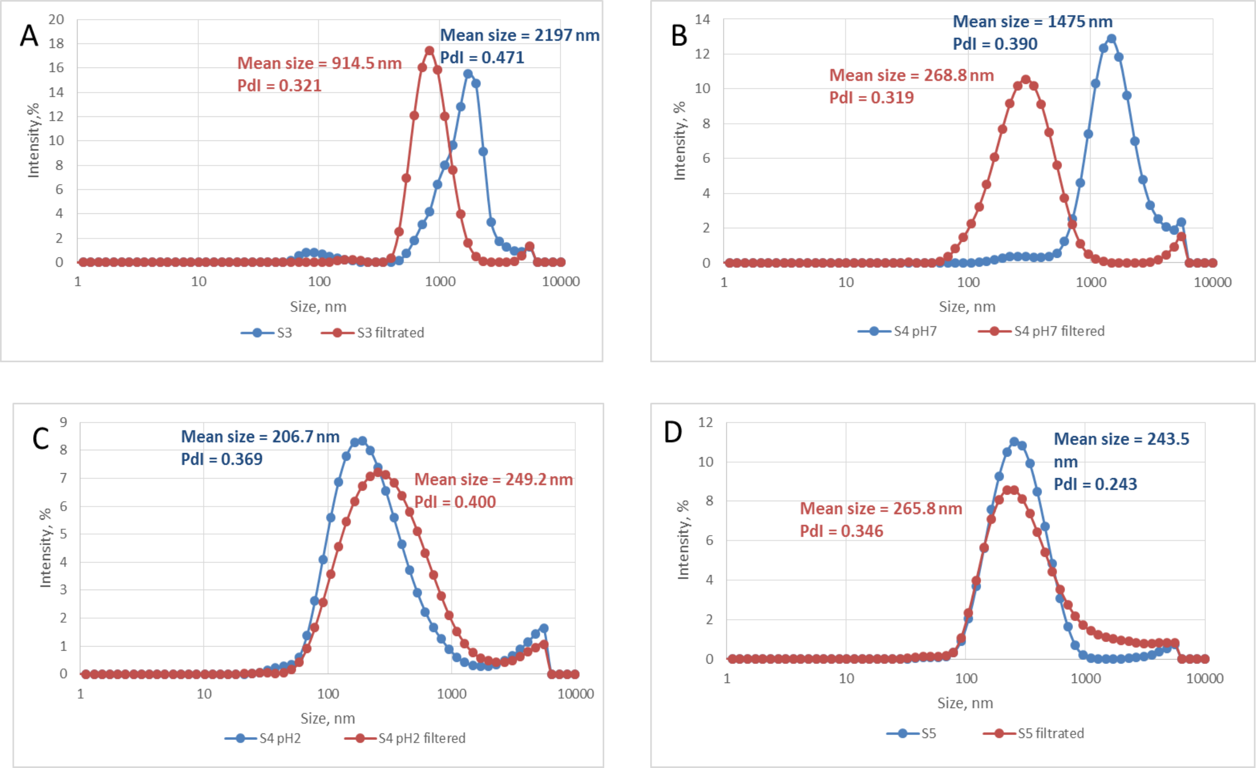

Figure 84. Particle size distribution determined by DLS analysis for catalyst nanoparticle dispersions before and after filtration: A – S3, B – S4, C – S4 pH 2, D – S5.

The results of the DLS analysis are presented in Figure 84. The mean size of the S3 and S4 dispersed particles significantly decreased after the filtration by 1282.5 nm and 1206.5 nm respectively. The polydispersity index (PdI) also decreased for both (by 0.15 and 0.07 respectively). Opposite trends were observed in the other two dispersions (S4 pH 2 and S5), as the mean size increased after the filtration by 42.5 nm in the S4 pH 2 dispersion and 22.3 nm in the S5 dispersion. The PdI also increased by 0.031 and 0.103 respectively.

5.2.3 Deposition of catalyst by applying a magnetic field and subsequent electroless copper plating

The catalyst was deposited on the substrate by applying a magnetic field as described in the methodology Chapter. Briefly, the magnetic catalyst particles were dispersed by ultrasonication for 30 min in 100 ml RO water. Then the substrate, with a magnet attached to one side of it, was placed in the freshly prepared dispersion for 15 sec. The SEM images of catalyst deposited on the substrate and photographs of corresponding electroless plating are presented in Figure 85.

The S3 catalyst had a film-like continuous morphology when deposited on the substrate while the other catalysts did not. All catalyst depositions resulted in distinctive electroless copper plating, however none of the Cu deposits were continuous. Electroless deposited Cu is more “packed” (but still not continuous) for samples obtained from S3 and S5 catalysts compared to the others. The electroless copper layer obtained from S4 and S5 catalysts had low adhesion at the central part of the deposit.

In order to remove large undispersed agglomerates, the catalyst dispersions were filtered before being deposited on the substrate surface (Figure 86). The deposition time was increased to 30 sec because the catalyst concentration decreased due to agglomerates remaining on the filter, which was also confirmed by ICP analysis (Figure 83).

Electroless Cu plating was observed on the deposits obtained from the S5 catalyst although the central part is dark and has low adhesion to the substrate. Other samples show no or very little evidence of electroless copper being plated according to the SEM analysis.

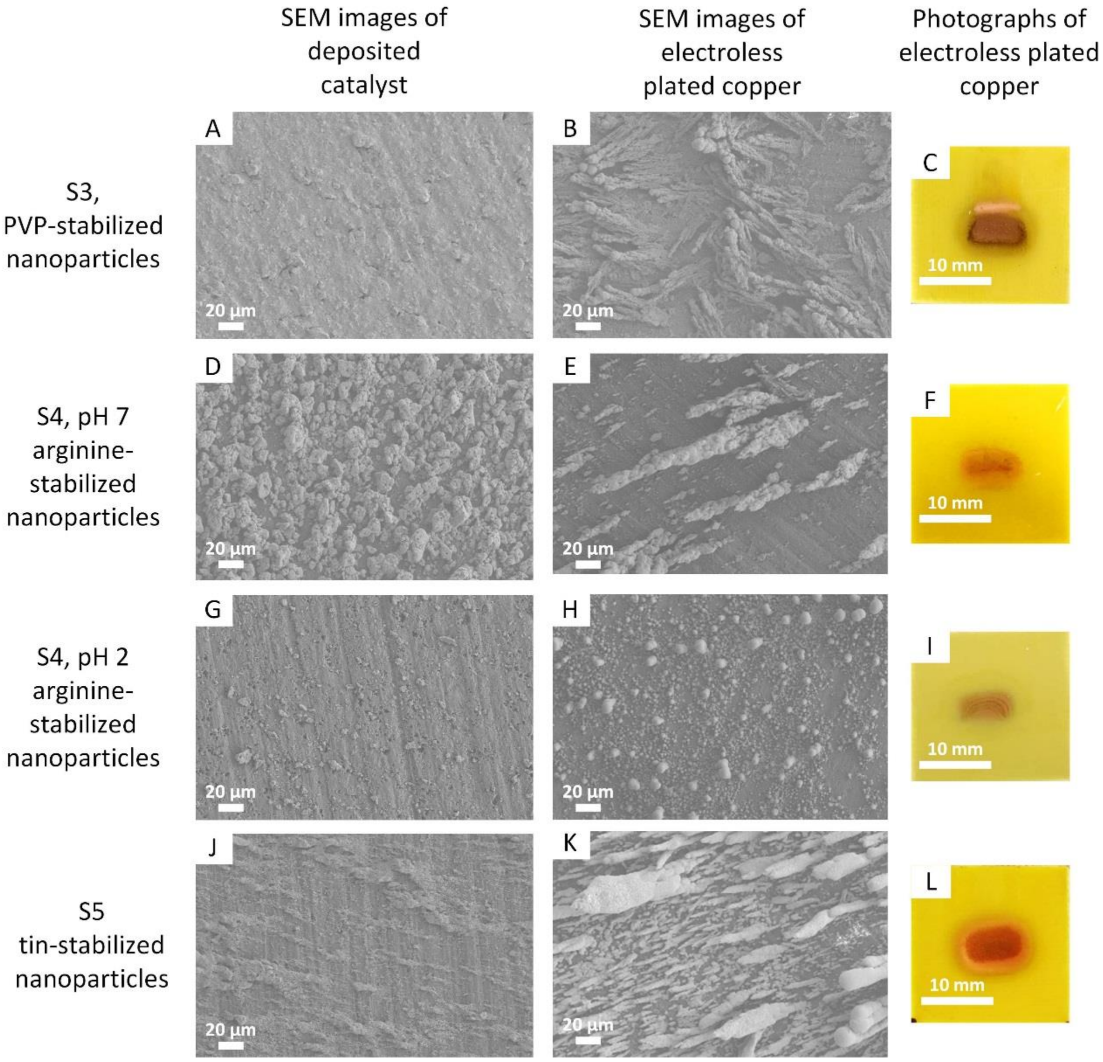

Figure 85. The SEM images of catalysts deposited for 15 sec on epoxy substrate after 30 min ultrasonication by applying a magnetic field and corresponding digital photographs of substrates after the subsequent electroless copper plating stage.

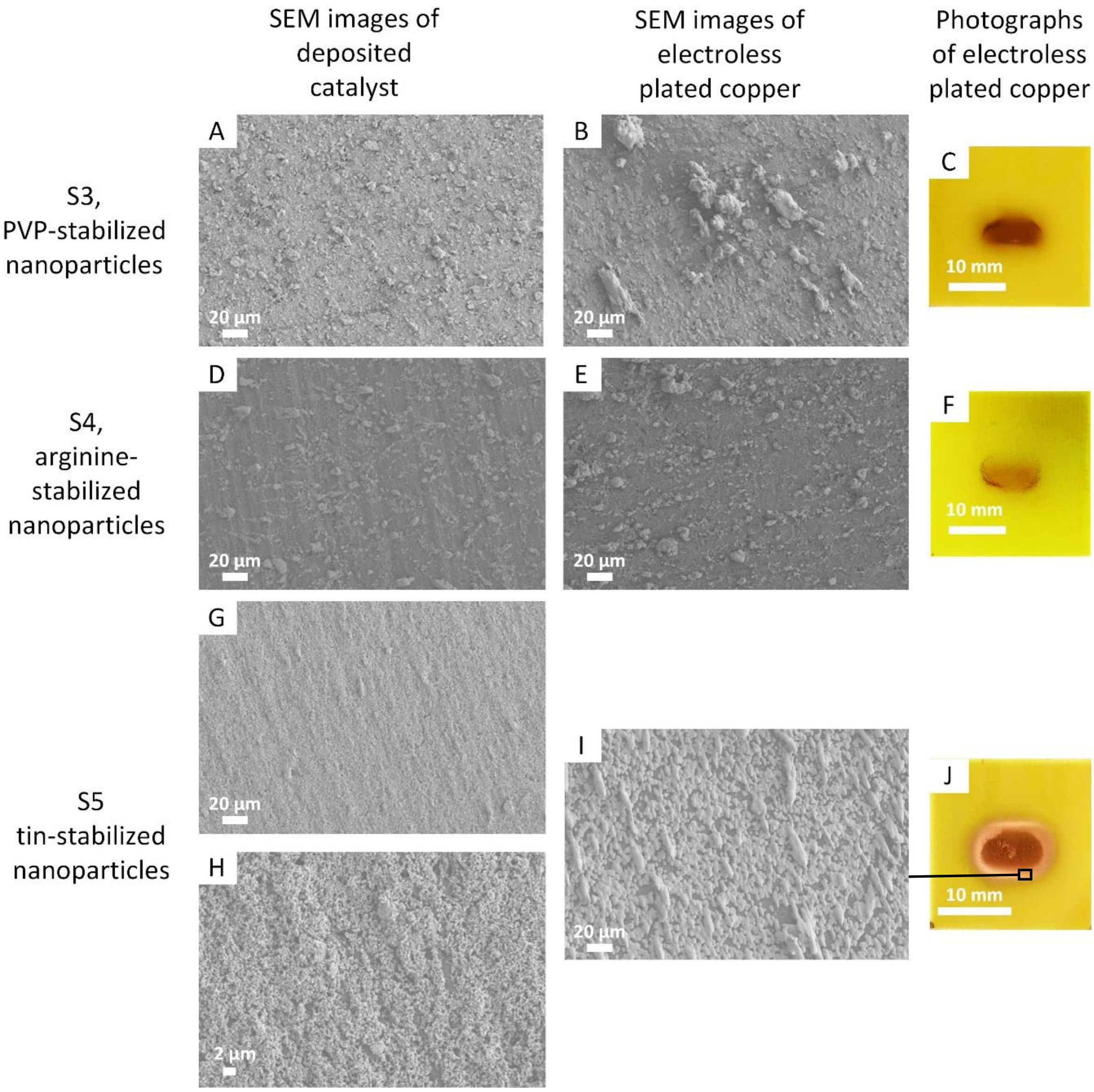

Figure 86. The SEM images of catalysts deposited for 30 sec on epoxy substrate after 30 min ultrasonication and filtration by applying a magnetic field and corresponding digital photographs of substrates after the subsequent electroless copper plating stage.

The S4 pH 2 catalyst deposition was not consistent. The catalyst was often displaced prior to the sample being placed in the electroless Cu bath (Figure 87). Electroless Cu plating was not performed on these samples.

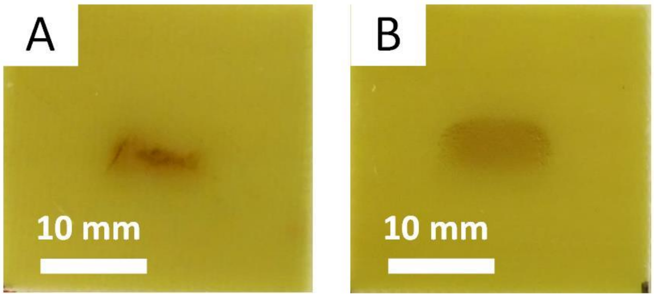

Figure 87. The digital photographs of substrate with S4 pH 2 catalyst deposit after 30 min ultrasonication and filtration. The catalyst was deposited for 30 sec in both cases.

5.2.4 Discussion

According to the ICP data (Figure 83), some dispersions had a higher overall metal concentration than others. For example the S3 dispersion had 163 mg/L of Fe and Ag ions together while S5 had only 143 mg/L. Both dispersions were made with an equal amount of nanoparticles. S3 had the largest concentration and S5 had the lowest. The difference in the concentration was due to the different molar mass of the particles resulting from the difference in particle composition – S3 was functionalized with PVP while S5 contained SiO_2 and Sn ions layers.

It should be noted that the standard deviation for ICP measurements was quite low and did not exceed 2 % of the measured value. The repeats for each substance were from the same batch of synthesised nanoparticles. The previous Chapter 4 highlighted the repeatability issues with nanoparticle synthesis. The purpose of using material from the same bath was to indicate whether any reproducibility problems will arise due to the ultrasonication and filtration stages. The low standard deviation values indicated that the process was reproducible.

A much lower concentration of Ag was determined by ICP when the S4 pH 2 sample was analysed compared to the S4 sample. The pH was adjusted with 0.01 M HCl. Ag cannot be dissolved in dilute HCl and the rate of Fe_3O_4 dissolution is relatively low at this concentration [230]. However, the presence of HCl strongly affected the ICP measurements of Ag. Nitric acid was used to prepare all samples for analysis. Ag dissolved in nitric acid reacts even with trace amount of HCl and forms insoluble AgCl which cannot be determined by ICP [231]. Therefore, the results for the S4 pH 2 solution can be disregarded.

Agglomerates were observed on the substrate surface after particle deposition. The dispersions subject to 5 min ultrasonication showed low stability and the samples did not meet the quality criteria for the DLS analysis. Samples subject to 30 min ultrasonication were analysed by DLS – a large amount of agglomerates exceeding 1 µm were observed in samples S3 and S4 (Figure 84 A, B). After filtration, the mean size of the particles significantly decreased for both dispersions. According to the ICP analysis (Figure 83) the overall concentration of both Fe and Ag ions also significantly decreased in the dispersion after filtration. This showed that more than 50% of dispersions were agglomerated and remained on the filter.

The S4 pH 2 and S5 dispersions had a much lower particle size even before filtration according to the DLS analysis (Figure 84 C, D). For both materials, the mean size even slightly increased after the filtration process, which indicated that the dispersions were not stable and have a tendency to agglomerate over time. ICP (Figure 83) shows the decrease in Fe and Ag concentration of the particles after filtration, however this was not as significant as for the S3 and S4 dispersions. This means that a lower amount of material was agglomerated after ultrasonication.

S3 particles were synthesised using PVP, which is expected to functionalise the particle surface and prevent agglomeration [223]. Some works show that the amount of PVP should be optimised [225,232,233]. A low concentration of PVP can lead to inadequate surface functionalisation and results in the agglomeration of non-functionalised surfaces and chemical bond formation during drying. Excessive amounts of PVP also lead to agglomeration. Therefore, further work should aim to optimise the concentration of PVP to prevent agglomerate formation.

The S4 sample was synthesised using arginine. The charge of arginine depends on the pH and affects the agglomeration of the particles. It was previously reported [213] that particles functionalised with arginine were better dispersed in acidic conditions and indeed in the present work the particles showed less agglomerates when dispersed at pH 2.

The S5 composite particles did not have any steric stabilising layer. However, stabilisation did occur due to electrostatic repulsion of Sn^{4+} ions. The S5 dispersion showed the smallest Fe and Ag loss after the filtration which means that the particles were the best dispersed. However, some agglomerates were still present. The main difference between particle syntheses was that S5 was subject to continuous ultrasonication which prevented particle agglomeration during synthesis. Samples S3 and S4 were magnetically stirred during synthesis, however due to the magnetic properties of the particles themselves, some were attracted by the magnetic stirrer and remained attached to it during synthesis, which resulted in agglomerate formation.

The catalysts dispersed for 30 min were deposited by applying a magnetic field. The substrates were then electroless copper plated. All analysed nanoparticles deposited at the area with magnetic field influence and all resulted in copper plating (Figure 85). The S3 catalyst formed a film when deposited (Figure 85, C), due to PVP polymerisation. However, electroless Cu deposition was obtained although the adhesion was low. This is due to overloading of the catalyst on the substrate surface. The catalyst remained on the substrate surface by magnetic forces. The deposited copper bonded with the catalyst without forming bonds to the substrate. So when the magnet was removed there were no magnetic forces to keep the catalyst at the substrate surface and both the catalyst and the electroless copper were not bonded to the surface.

When the S3 was deposited after the filtration, the catalyst did not form a film (Figure 86, A), due to low loading of the catalyst. The concentration of particles significantly decreased after filtration according to the ICP analysis (Figure 83), which explains the observation that less catalyst was deposited. Some electroless copper was plated but did not form a continuous film. In this case the catalyst distribution resulted in an "island" of copper plating which did not overlap with each other during growth to form a continuous film. This explains the low loading of catalyst on the surface. Similar results were obtained for the S4 dispersion before and after filtration and the S4 pH 2 dispersion before filtration. It should be noted that the presence of agglomerates still resulted in electroless Cu plating (Figure 85, D, F).

The S4 pH 2 sample showed displacement of the catalyst at the depositions after filtration (Figure 87), so no reproducible results were obtained. The S4 catalyst had a small size of Fe_3O_4 particles. The interaction between the magnetic field and magnetic nanoparticles is proportional to the particle size [190]. Therefore, when magnets of low strength were used the attraction between particles and magnet was too low to maintain the presence of particles and during the process they moved. When the pH of the dispersion was not adjusted the particles formed agglomerates which were of micron size (Figure 85, D) and therefore had a stronger interaction with the magnetic field and therefore no displacement occurred.

The S5 catalyst resulted in electroless copper plating both before and after filtration (Figure 85, L, Figure 86, J respectively). The plating occurred mainly at the contour of the pattern. This was due to the uniformity of the magnetic field distribution on the surface when the magnetic field was applied. So higher values of magnetic flux density at the centre of the magnet resulted in catalyst overloading at the central part of the patterned area.

The main goal of the present chapter was to establish the trends in catalyst quality and distribution across the sample and the quality of the obtained electroless copper plating. The following conclusions were made:

1) Agglomerates.

Electroless Cu plating was obtained when agglomerates were either present or absent, so the proposed decrease in catalytic activity and the decrease in surface area does not affect the ability to obtain electroless copper plating.

2) Functionalisation.

At the current stage of the research, functionalisation itself does not affect the ability to plate with magnetic nanoparticles. However, functionalisation should not result in the formation of continuous catalyst layers when the particles are deposited which would affect the adhesion.

3) The particles distribution on the surface.

The particles should uniformly distribute across the catalyst surface without making either a continuous catalyst film, or an overpopulated surface in order to maintain the layer adhesion. Also there should be enough catalyst to form a continuous Cu plating.

4) The size of the catalyst.

If weak magnetic fields are used, the size of the magnetic portion of the catalyst should be optimised. The interaction between particle and magnetic field depends on the particle size. Smaller particles can be displaced.

Chapter 6. Development of the magnetic template

6.1 Introduction

The patterning of ferromagnetic material using a gradient magnetic field is a technique used in various fields, from biomedical applications [109–111,171] to the patterning of electrochemical deposition [79,97,99,103–105]. In this process, magnetic materials such as iron or steel were used as the templates. The shape and dimensions of the templates may vary depending on the application.

In order to achieve a gradient magnetic field distribution on the surface of the substrate, the thickness of the substrate should be taken into consideration. With an increase in the substrate thickness the influence of the magnetic field dramatically falls [111].

If magnetic material is used as a template, it should be placed under the influence of a uniform magnetic field in order to be magnetized. The strength of the field affects the distribution of the gradient magnetic field on the substrate surface. A permanent magnet or electromagnet can be used as a source of a uniform magnetic field. Due to construction and economic considerations, a permanent magnet was chosen as the source of the uniform magnetic field in the present research. The size and weight of the magnet is also restricted by the application – it should be possible to attach it to the substrate during the electroless plating process.

Therefore the main limitations are:

- Technological simplicity: e.g. the introduction of a large, strong magnet can increase the risk and complicate the process;
- The thickness of the substrate – thicker substrates will require the use of a stronger magnetic field.

Selective electroless plating is required in a number of patterns. The majority of the research groups investigate selective line deposition [14,54,66–68,170,219,234,235] however some works demonstrate more complex forms including circular lines [54,67], squares [66–68] and circles [66]. The main goal of selective plating is the precise reproduction of the pattern with the smallest possible element size (e.g. line width) and the smallest spacing between neighbouring elements. In addition, the overlapping of the elements should be strictly avoided because in electronics these can cause a short circuit.

In order to simulate the magnetic field distribution FEMM software was used. This allows simulation of the magnetic field distribution and can also be used to calculate the strength of the magnetic field on the substrate surface. The simulation was run using on a permanent magnet field distribution and a template consisting of parallel lines.

6.2 Permanent magnet

At first, the magnetic influence of the permanent magnet on the substrate was simulated (Figure 88, A). A distribution of magnetic flux density across the substrate surface was obtained (Figure 88, B).

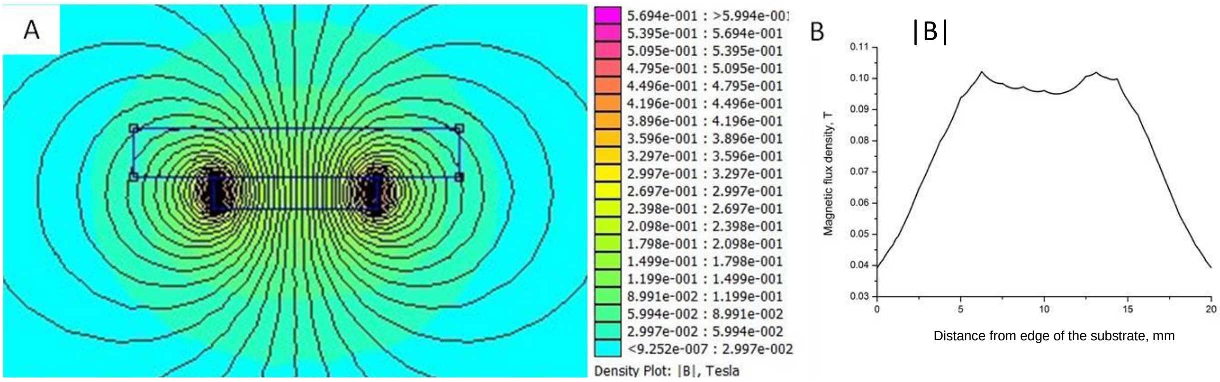

Figure 88. Magnetic field distribution simulated by FEMM for the permanent magnet A – cross section of the set up; B – magnitude of magnetic flux density distribution on the substrate surface.

The normal magnetic flux density (the flux density component perpendicular to the substrate surface, B_z) was obtained during simulation (Figure 89, A) and its gradient ($\frac{dB_z}{\mathrm{dx}}$) across the substrate surface was calculated (Figure 89, B). The highest gradient was obtained near the magnet edges, while at the centre the gradient was almost 0.

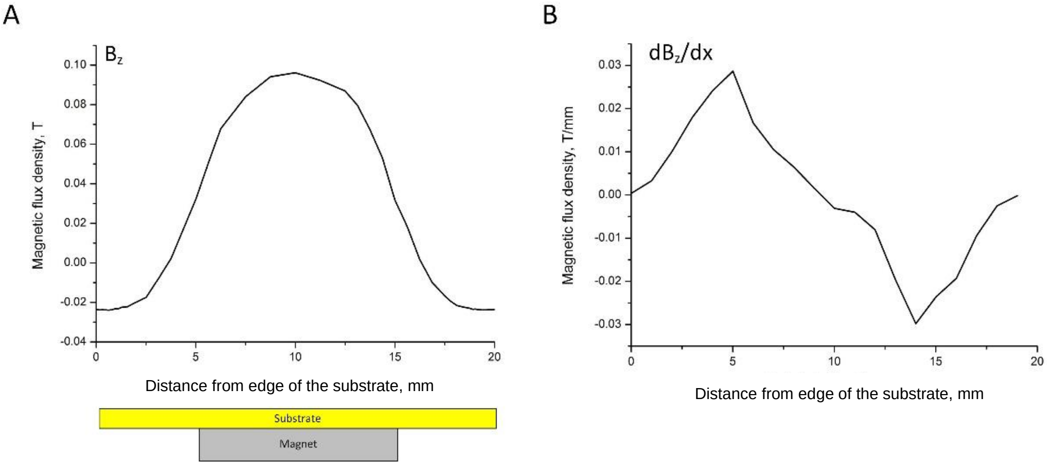

Figure 89. A – normal magnetic flux density distribution across substrate surface, B – gradient of the normal magnetic flux density across the substrate surface.

6.3 Template fabrication

In order to estimate the main tendencies of the magnetic field distribution, a cross section of the template of parallel lines made from steel 1010 was modelled. First, the following system was simulated (the yellow colour indicates the parameters which were altered):

Table 18. The parameters of the simulated system with changing thickness of the substrate.

Line width, mm	Line height, mm	Distance between lines, mm	Magnet length, mm	Magnet thickness, mm	Amount of lines	Magnet orientation towards substrate surface	Substrate thickness, mm
0.5	1	0.5	10	2	10	Perpendicular	3
							0.41

The thickness of the substrate was varied in order to obtain patterning of the magnetic flux density across the substrate surface. According to Figure 90, when a 3 mm thick substrate was used no patterning effect of magnetic flux density occurred. When a 0.41 mm substrate was used a repetitive wave pattern was obtained. However, the peak and the trough of the wave at the edges of the template corresponded to larger magnetic flux density values compared to the centre of the template.

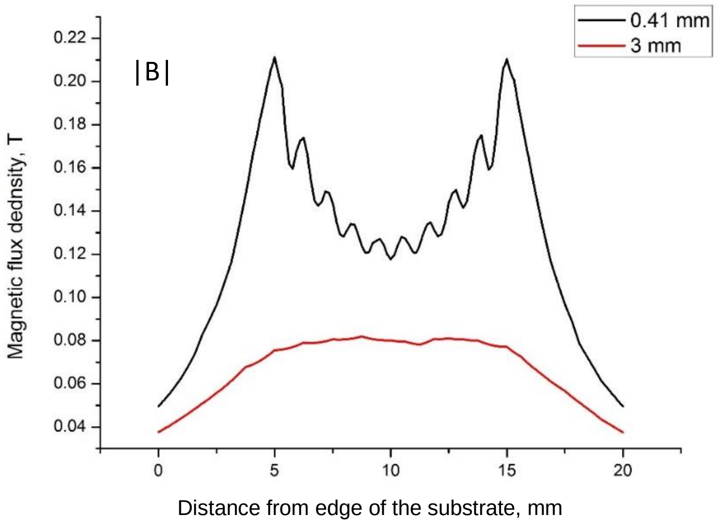

Figure 90. Magnitude of the magnetic flux density distribution across the substrate surface for 0.41 mm and 3 mm thick substrates.

The gradient of the normal magnetic flux density was also simulated (Figure 91). Higher gradient values were obtained at the edge of the template.

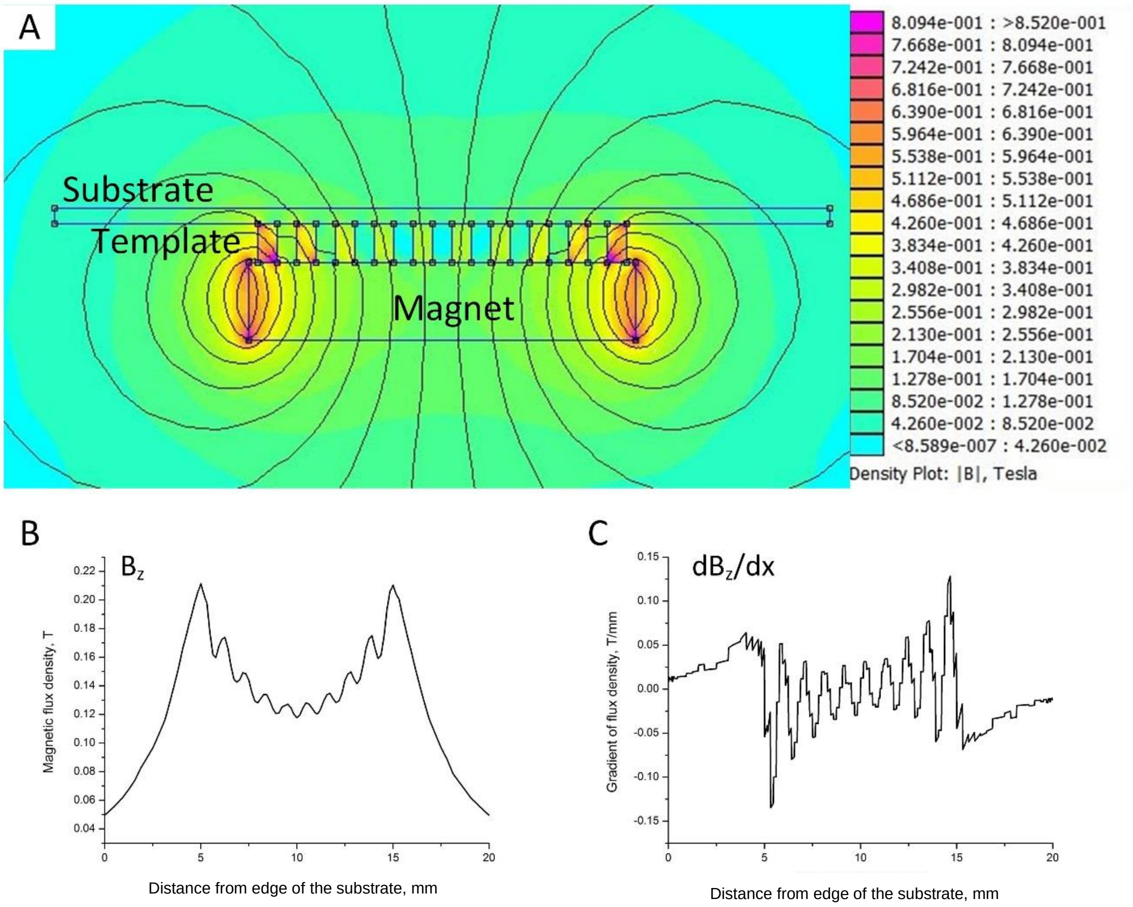

Figure 91. Magnetic field distribution simulated by FEMM for the permanent magnet and template A – cross section of the set up; B – normal magnetic flux density distribution on the substrate surface, C – gradient of the normal magnetic flux density distribution across sample surface.

The aims of the following optimisation are:

- To decrease the “edge” effect – make the peaks of all “waves” have the same value of magnetic flux density
- To keep the amplitude of the waves as high as possible
- To get the magnetic flux density value at the wave peak comparable with the value obtained when a single magnet is placed

The influence of the height of the template line on the patterning effect of the magnetic flux density was evaluated. The systems were simulated as shown in Table 19 and the flux density distribution for the systems are presented at Figure 92.

Table 19. The parameters of the simulated system with changing template line height.

Line width, mm	Line height, mm	Distance between lines, mm	Magnet length, mm	Magnet thickness, mm	Amount of lines	Magnet orientation towards substrate surface	Substrate thickness, mm
0.5	1 to 10 step 1	0.5	10	2	10	Perpendicular	0.41
	10 to 50 step 5						
	50 to 100 step 10						

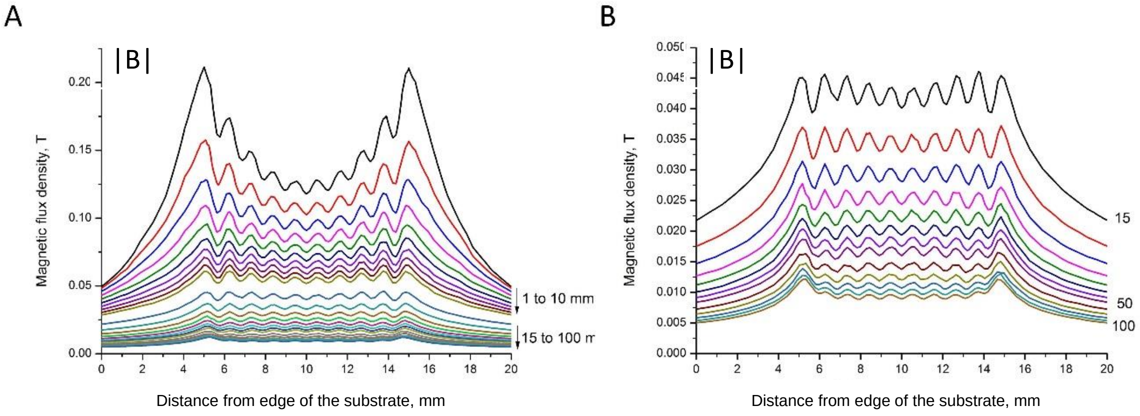

Figure 92. Magnetic flux density distribution across the substrate surface for the template with lines height from A - 1 to 100 mm, B – 15 to 100 mm.

The difference between flux density values of the peaks located at the edge of the template and the central part became almost negligible for lines with a height 15 mm and higher (Figure 93, A). However, it also decreased the maximum achieved magnetic flux density value (Figure 93, B). The distance between the wave peaks and troughs also decrease with increasing height of the line (Figure 93, C).

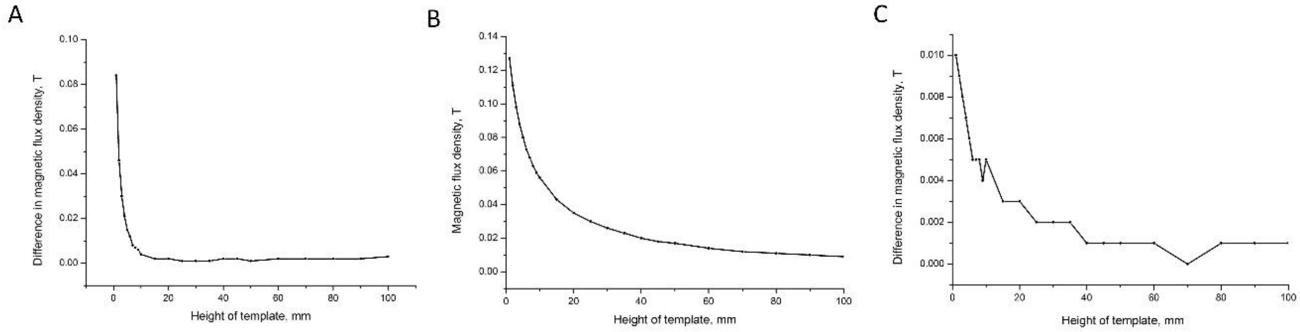

Figure 93. A – The difference in magnetic flux density between the edge and centre of the template as a function of template height; B – the change in the maximum magnetic flux density obtained per simulation as a function of template height; C – The change in the amplitude of the magnetic flux density waves as a function of template height.

The influence of the magnet length was also evaluated (Table 20, Figure 94). The main observed effect was a shift of the position of the "edge effect" to the magnet edge – the templates lines at the locations opposite to the magnet edges produce the highest magnetic flux density at the substrate surface.

Table 20. The parameters of the simulated system with changing magnet length.

Line width, mm	Line height, mm	Distance between lines, mm	Magnet length, mm	Magnet thickness, mm	Amount of lines	Magnet orientation towards substrate surface	Substrate thickness, mm
0.5	1.0	0.5	2.0 6.0 10.0 14.0 18.0	2.0	10	Perpendicular	0.41

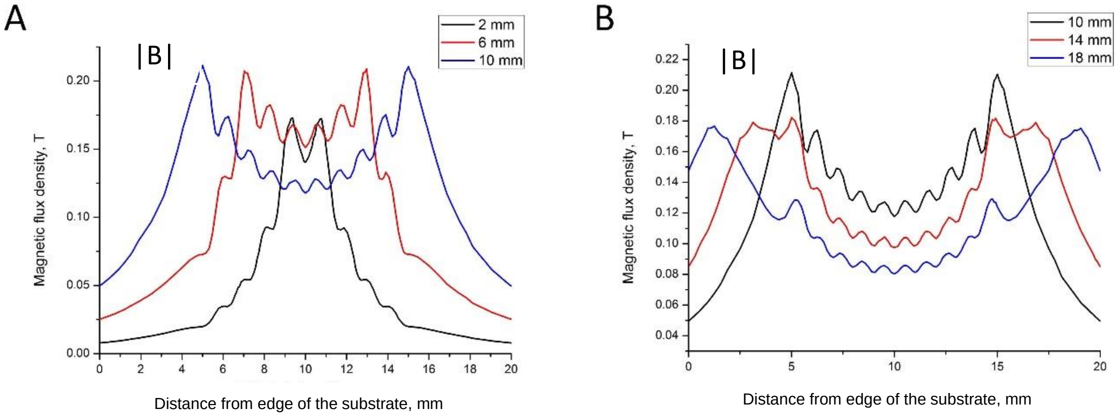

Figure 94. Magnetic flux density distribution across the sample surface for the system with magnet length A – 2, 6 and 10 mm; B – 10, 14 and 18 mm.

The effect of the thickness of the magnet on the magnetic flux density across the sample was evaluated (Table 21, Figure 95, A). Using a thicker magnet results in higher maximum values of magnetic flux density and a higher distance between "wave" peak and trough.

Table 21. The parameters of the simulated system with changing magnet thickness.

Line width, mm	Line height, mm	Distance between lines, mm	Magnet length, mm	Magnet thickness, mm	Amount of lines	Magnet orientation towards substrate surface	Substrate thickness, mm
0.5	1.0	0.5	10.0	1 to 5 Step 1	10	Perpendicular	0.41
				10			

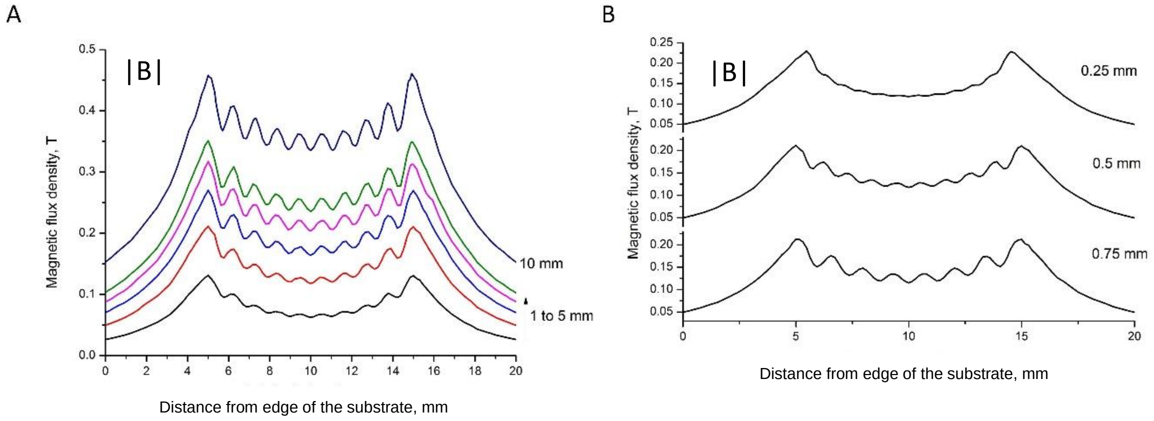

Figure 95. Magnetic flux density distribution across the sample surface for the system with changing A – magnet thickness, B – distance between template lines.

Changing the parameter of distance between template lines (Table 22) leads to a greater difference between the peak and trough of the "wave" of magnetic flux density (Figure 95, B).

Table 22. The parameters of the simulated system with changing distance between template lines.

Line width, mm	**Line height, mm**	**Distance between lines, mm**	**Magnet length, mm**	**Magnet thickness, mm**	**Amount of lines**	**Magnet orientation towards substrate surface**	**Substrate thickness, mm**
0.5	1.0	0.25	10.0	2.0	10	Perpendicular	0.41
		0.50					
		0.75					

Considering the previously discussed parameters the following system was simulated (Table 23):

Table 23. The parameters of the simulated system with changing magnet orientation.

Line width, mm	Line height, mm	Distance between lines, mm	Magnet length, mm	Magnet thickness, mm	Amount of lines	Magnet orientation towards substrate surface	Substrate thickness, mm
0.5	20	0.75	20	10	16	Perpendicular	0.41
						Parallel	

When the magnetisation of the magnet is perpendicular to the substrate surface the magnetic lines on the substrate surface centre are also perpendicular to the substrate (Figure 96, A). The distribution of the patterned magnetic flux density (Figure 96, B) on the substrate surface was improved by the modifications mentioned in this chapter – the edge effect significantly decreased while the distance between "wave" peaks and troughs remained relatively large - 0.02 T. The maximum achieved magnetic flux density of 0.14 T is comparable to the one obtained in the single magnet simulation (0.1 T). The gradient of the normal magnetic flux density was also patterned (Figure 96, C).

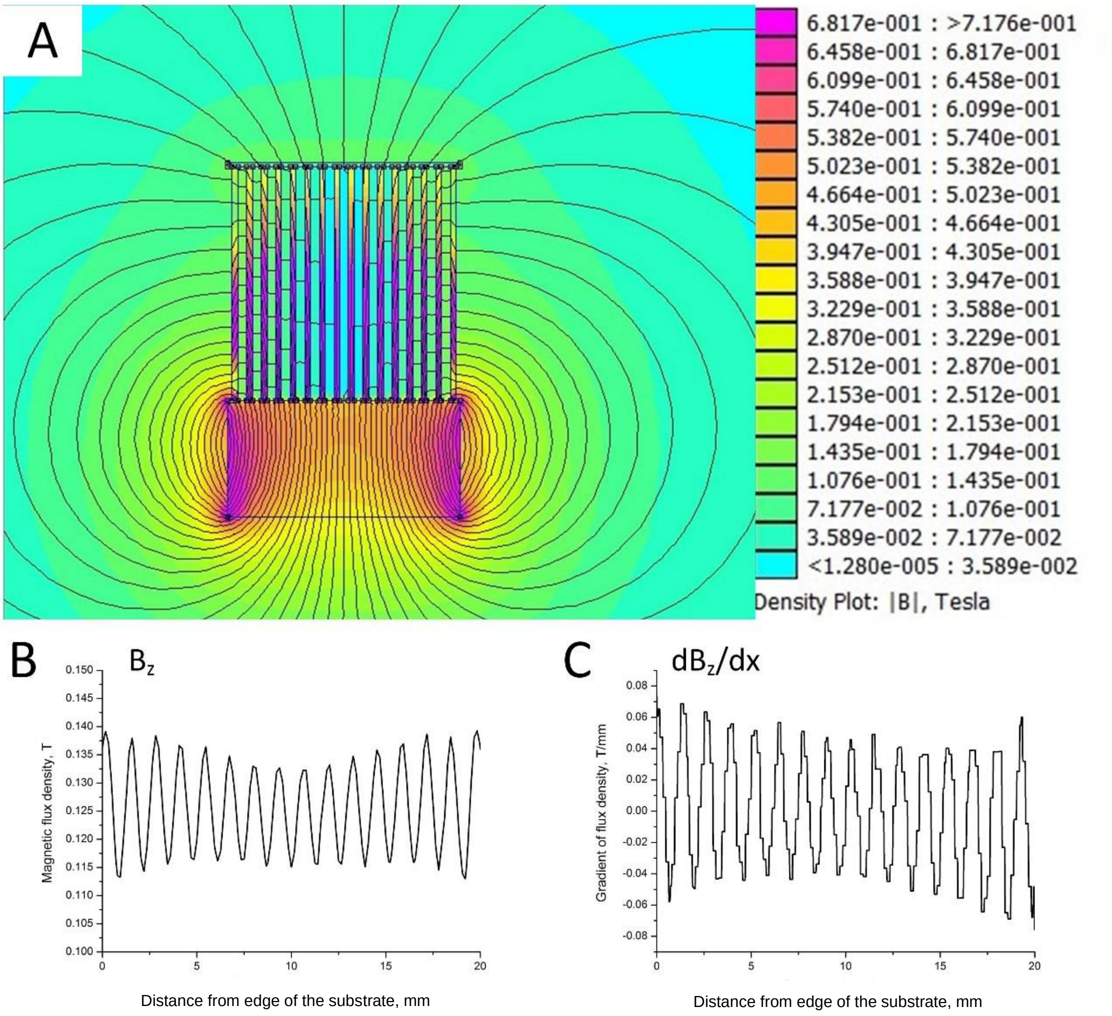

Figure 96. Magnetic field distribution simulated by FEMM for the permanent magnet and template oriented perpendicular to the substrate surface. A – cross section of the set up; B – magnetic flux density distribution on the substrate surface, C – gradient of the normal magnetic flux density distribution across the sample surface.

Next, the same template, substrate and magnet were simulated but the direction of magnetization was changed by 90^O, making it parallel to the substrate surface. The magnetic lines on the substrate surface become more parallel to the surface, especially at the central part of the substrate (Figure 97, A). The magnetic flux density distribution still has a significant edge effect (Figure 97, B), however the gradient of normal magnetic flux density does not (Figure 97, C). In addition, the amount of peaks in the magnetic flux density distribution plot is 15 when a 16-lined template being simulated. This indicate that peaks correspond to the areas between template lines due to the geometry of the magnetic lines distribution.

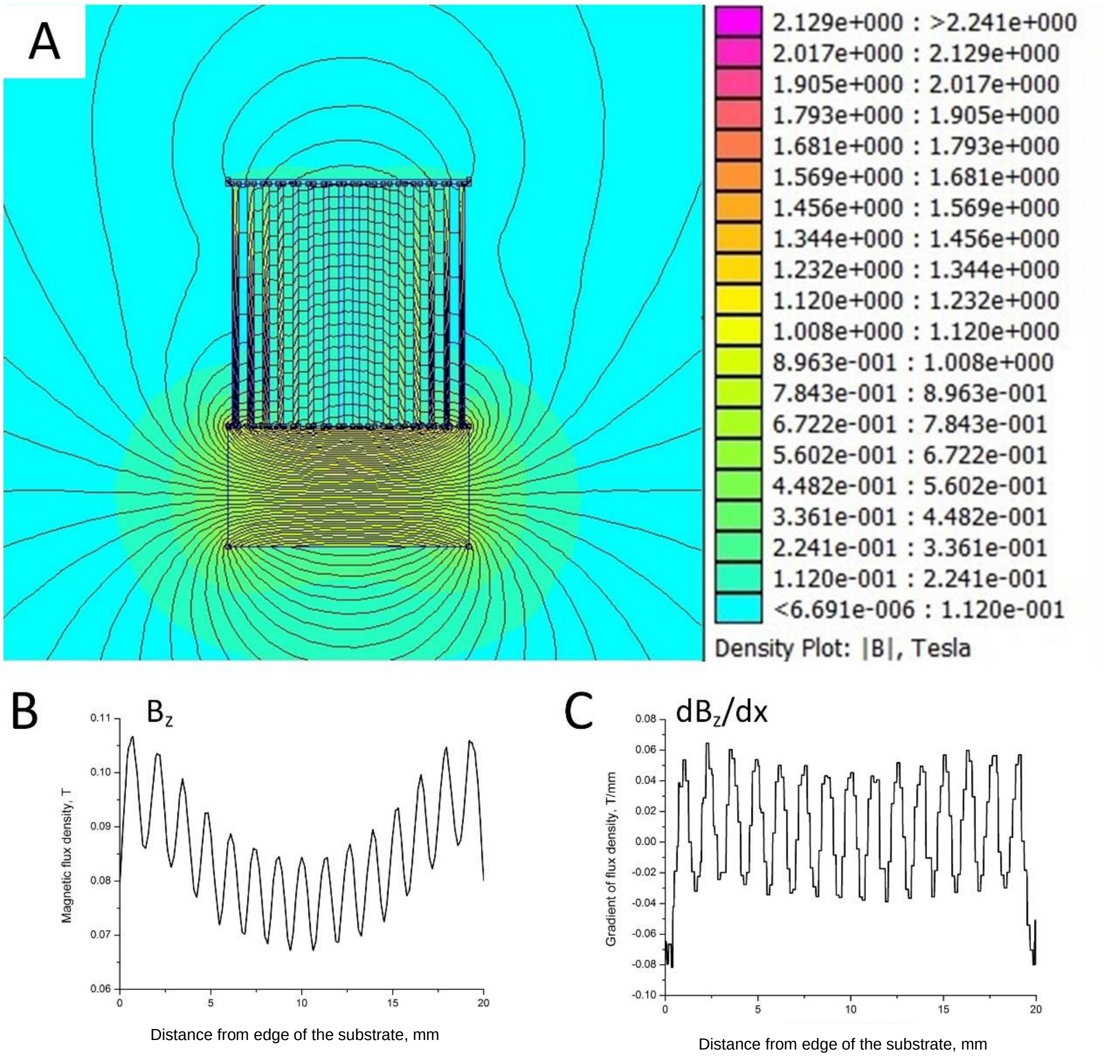

Figure 97. Magnetic field distribution simulated by FEMM for the permanent magnet and template oriented parallel to the substrate surface A – cross section of the set up; B – magnetic flux density distribution on the substrate surface, C – gradient of the normal magnetic flux density distribution across the sample surface.

6.4 Discussion

Analysis of the results of this chapter revealed that the distribution of the magnetic field across the sample was variable. As discussed in various works, the interaction between magnetic nanoparticles and magnetic fields is proportional to the $B\nabla B$ parameter[97], though the majority of works operate with only the ∇B parameter[109,112,171,236]. According to the simulation, the magnitude of the magnetic flux density is uniform at the central part of the substrate and decreases at the sides, while the gradient of the normal magnetic flux density is significantly higher at the sides of the magnetic field influence (Figure 88). If the particles were attracted only to the place with the highest gradient, plating would occur only on the outline of the magnet, however as shown in the previous chapter there are particles located at the centre where the gradient is quite low (Figure 75).

In the Chapters 5.1 and 5.2 depositions with a needle-like morphology were often obtained, which results from magnetic nanoparticles aligning with the magnetic field lines. According to the simulation the magnetic field lines are perpendicular to the surface of the central part of the substrate, while more acute angles are observed at the areas corresponding the edge of the magnet (Figure 88, A). This also explains why better quality deposits were obtained at the edge: the catalyst particles were spreading along magnetic field lines that were almost parallel to the substrate surface [113]. Therefore, not only the magnetic flux density should be considered but also the direction of the magnetic field lines. However, multiple works used a magnet with magnetization perpendicular to the substrate surface and did not report any needle-like arrangement of particles[109,111,112]. The importance of the alignment of magnetic field lines in respect to the position of the substrate to the current work should be further investigated.

Next, the template for patterning the magnetic field was simulated and optimised. Many of the observed effects are due to the increased distance between the magnet and the substrate surface (Figure 92, Figure 93):

- The patterning effect of the magnetic template decreased
- The “edge” effect of the magnet decreased
- The amplitude of the pattern wave decreased
- The maximum magnetic flux density decreased

All the effects are attributed to the loss of the magnetic field strength with the distance from the source of the magnetic field.

The length of magnet changed mainly the edge effect (Figure 94) - higher flux density is observed at the points corresponding to the magnet position. Previously, some works mentioned that a higher gradient of magnetic field occurs at the sides of the magnet [79,103]. One of the approaches to decrease the influence of the edges on the template is to significantly increase the size (width and length) of the magnet compared to the size of the template. However, larger magnets can cause more health and safety issues and make the experiment set-up more complex.

The thickness of the magnet was also varied (Figure 95, A). The strength of the magnetic field increases with thickness of magnet, so the effect of the field on the surface also increased. In general, this has the opposite effect to increasing distance from the magnet.

The distance between template’s lines was also simulated (Figure 95, B). Larger distances led to a more discrete pattern being obtained. The magnetic fields of the template lines overlap if positioned too close and superimpose on each other.

The final simulated template was 20 mm in height in order to decrease the effect of magnet edges on the pattern (Figure 96). A longer height would significantly decrease the magnitude of the flux density. A larger magnet, a bigger space between lines and a thin substrate were all chosen in order to achieve a pattern with a large amplitude. A wave-shaped pattern was achieved for both magnetic flux density and the normal flux density gradient. The only concern was that the perpendicular position of the magnetic lines as mentioned earlier caused needle-like magnetic nanoparticle deposition. Therefore, it was decided to change the direction of the magnet magnetization to that which was parallel to the substrate (Figure 97). This position of the magnet kept the same magnitude of magnetic flux density and gradient of the normal magnetic flux density. However, more distinguishable effects on the “edges” are expected.

Chapter 7. Selective metallisation by applying a gradient magnetic field

7.1 Introduction

Often, selective electroless plating is achieved by selective surface activation by laser irradiation [66,237,238] or selective catalyst deposition [13–15,54,239]. The distribution of the catalyst across the substrate surface affects the quality of the subsequent electroless Cu plated layer.

According to the literature search (Chapter 1.1.10) the requirements for the catalyst when it is selectively deposited are:

1) The initialized areas should be located close enough to each other in order to obtain continuous plating [54,66].
2) In order to form a copper track on an insulating substrate copper needs to be plated evenly in the required pattern. Therefore the catalyst should be distributed equally across the required surface [18].
3) The catalyst nanoparticles should have narrow size distribution, especially when selective metallisation is required. The electroless Cu grows isotropically, so large catalyst particles will result in large Cu growth which can compromise the pattern [170,240]. Catalyst agglomerates can also lead to higher roughness of the deposited layer [68].

In the present work catalyst distribution was also affected by the magnetic field. The magnetic field causes particle agglomeration [113,241]. Also, the attracted particles can form 3D structures on the surface due to the nature of the attractive forces [108]. The magnetic field can also affect the even distribution of the catalyst across the surface.

The magnetic template was simulated and made as described in Chapter 6.3. The following catalysts were studied:

S1-3 – the Fe_3O_4-Ag nanocomposite was synthesised without surface functionalization (Chapter 4.2).The particles were dispersed in water for 30 min and filtered.

S3 – Fe_3O_4-Ag composite was functionalized with PVP (Chapter 4.3). The particles were dispersed for 30 min in water by ultrasonication.

S4 – Fe_3O_4-Ag composite was functionalized with arginine (Chapter 4.3). The particles were dispersed for 30 min in water (S4) or 0.01M HCl solution (S4 pH2) by ultrasonication.

S5 – Fe_3O_4-SiO_2-Sn-Ag composites (Chapter 4.3). The particles were dispersed for 30 min in water by ultrasonication and filtered.

According to the results obtained in Chapter 6 a 0.4 mm thick substrate is required in order to obtain a gradient magnetic field on the substrate surface. An unclad laminate of required thickness was used in the current chapter.

The condition of the substrate surface is important for the adhesion of the electroless Cu plating layer. The adhesion of the deposited layer is a result of chemical and mechanical interactions [175]. Chemical interactions arise from the electrochemical and covalent bonding of substrate with depositing metal and catalyst. The mechanical interactions appear due to the increased surface area of contact between the laminate and metal as well as interlocking of the catalyst and deposited metal in the substrate cavities.

When the unclad epoxy laminate was used as a substrate, a pre-treatment was required in order to increase surface roughness [175,242,243]. The treatment of the substrate was conducted according described in the Chapter 2.5.

In order to place the magnetic template and magnet behind the substrate, a cell was made (Chapter 2.5). The purpose of the cell was:

1) To protect the template and the magnet from the electroless Cu plating solution. Cu plating solution operates at basic pH and elevated temperature (46 ^{o}C) which causes steel corrosion.
2) To secure the substrate-template locations. In order to accurately replicate the pattern on the substrate, the template and magnet should not move during the catalyst deposition, washing and electroless plating stages. The cell restricts the movement of the magnet and ensures consistent patterning.

An issue arose from agitation of the electroless plating solution. Agitation is required in order to remove the products of the reaction from the reactive sites and supply the unreacted species. Agitation affects the speed of deposition and the quality of the deposit [6]. In a laboratory setting, magnetic stirring is used in order to provide agitation to the solution. However, due to the use of a magnet it is not possible to use magnetic agitation. This could potentially move the substrate and the magnet as well as attract the stirrer to magnet.

Another way to induce agitation is to use overhead stirring, whereby the stirring is initiated by the movement of the blades. First the cell was placed in an orientation such that the substrate working side was facing up. However, it was observed that due to intensive stirring the catalyst was often displaced from the substrate. Therefore, the cell position was changed in such a way that the working side of the substrate was perpendicular to the movement of the stirring blades Figure 98.

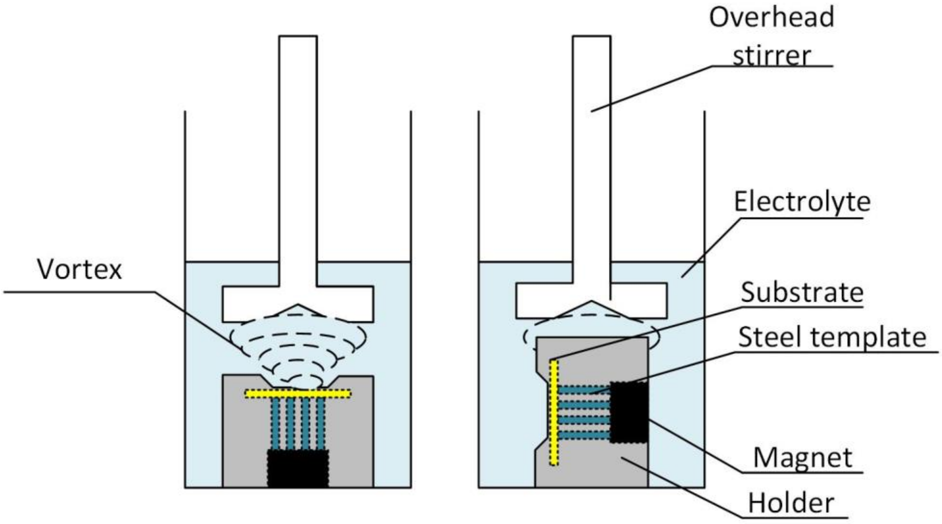

Figure 98. Schematic presentation of the cell position in the solution. The substrate positioned horizontally up-face (left) or vertically (right).

7.2 Substrate preparation

The unclad epoxy laminates as received or after swell-and-etch treatment were analysed by SEM. According to the images, the morphology of the laminate changed after the treatment. The cavities were made on the substrate surface after swell and etch treatment (Figure 99, A, C).

The electroless copper was deposited on the laminate as received or after the treatment. The Pd/Sn catalyst was used prior to the electroless metal plating. The deposited electroless copper film had better adhesion to the treated substrate than the untreated one (Figure 99, B, D). However, even when deposition was conducted after the treatment, deposited copper film had blisters.

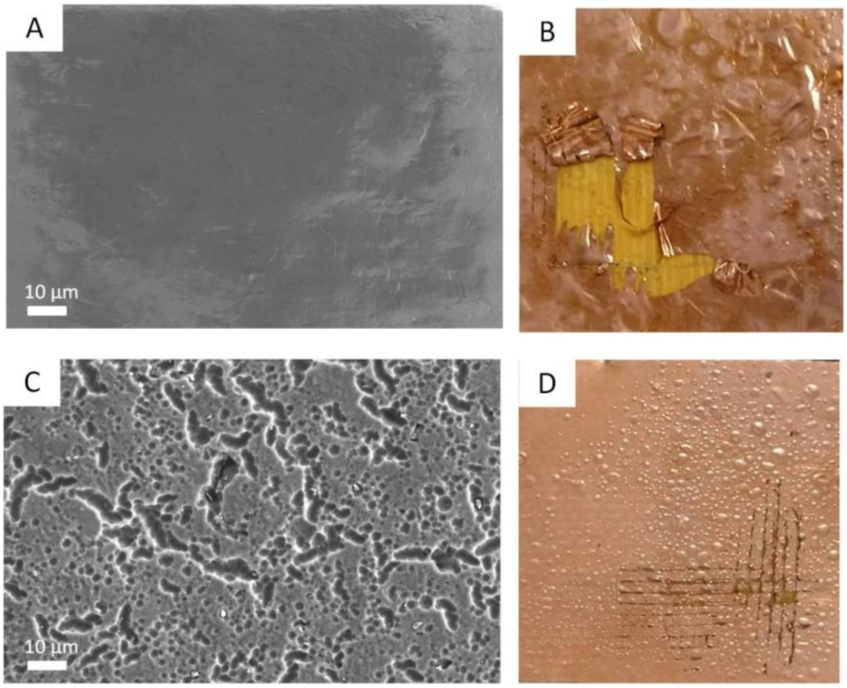

Figure 99. A, C - SEM images of unclad laminate; B, D – photographs of laminate after the adhesion testing of electroless Cu plating; A, B - the unclad laminate as received; C, D – the unclad laminate after swell-and-etch treatment.

7.3 Catalyst patterning

As was described in Chapter 6, the parallel arrangement of the magnet to the substrate was tested. However, no particle attraction was observed at the central part of the substrate therefore all following experiments were performed with a perpendicular arrangement of the magnet – the template was placed on the north or south pole of the magnet.

An image of a typical substrate after catalyst deposition is shown at Figure 100, A. All of the tested catalysts deposited in straight parallel line patterns (Figure 101, A-D), which followed the magnetic flux density distribution defined by the magnetic template Figure 100, B. The visible circular features on the substrate are the substrate glass fibres exposed due to the swell-and-etch substrate pre-treatment. The width of the lines differed within each sample – the lines going through the centre were narrower than those located near the substrate edge. However, no significant change in the width was observed along the length of the line. The observed effect is due to the edge effect of the magnetic field, which results in the magnetic flux density being higher at the edges than the centre of the template. The larger magnetic flux density results in thicker patterned lines at the edge. The presence of the agglomerates is clear for the deposited catalysts S3 and S4 pH7. Less agglomerates appeared when the S4 pH2 catalyst was deposited and almost none appeared when catalyst S5 was deposited.

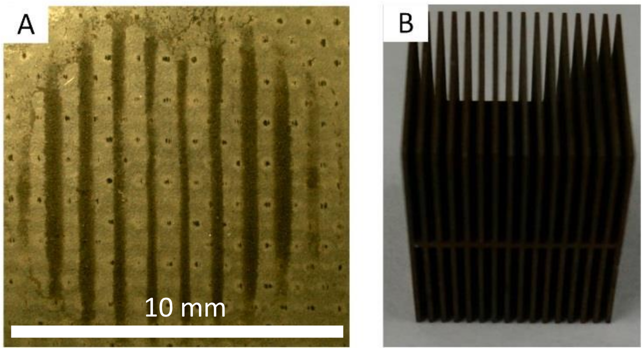

Figure 100. Photographs of A - a typical substrate with deposited magnetic catalyst in the shape of parallel lines; B – a steel template for patterning of the magnetic field.

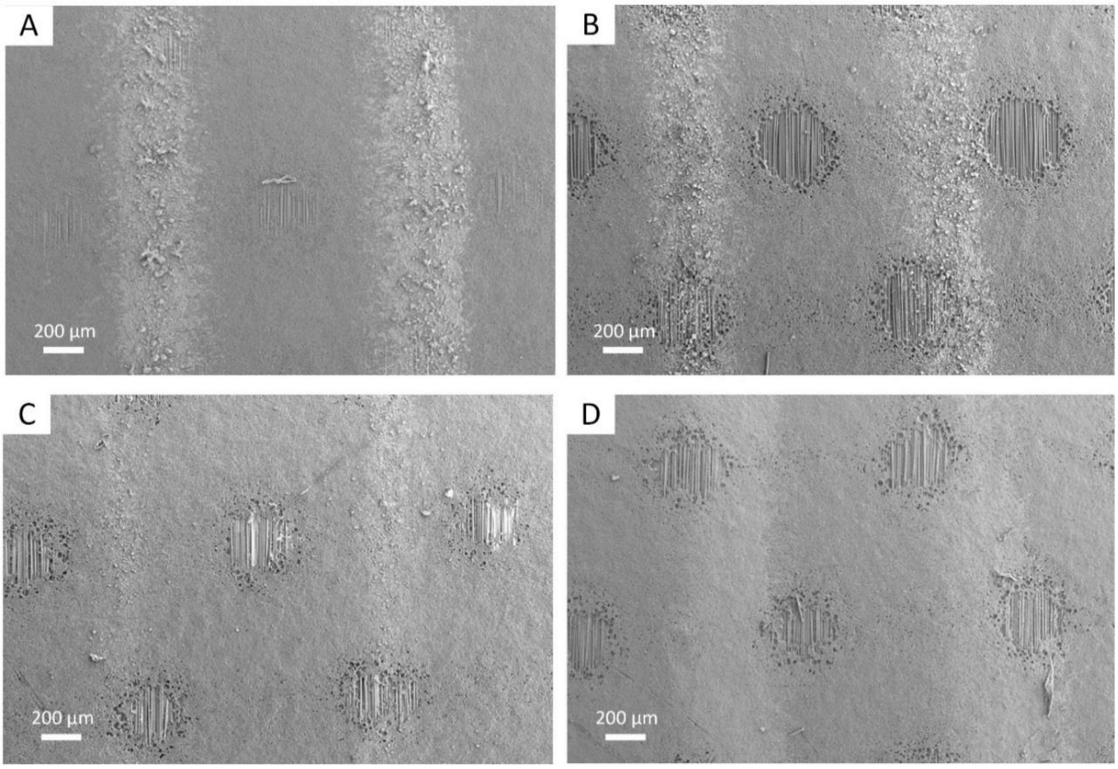

Figure 101. SEM images of the deposited catalyst A – S3; B – S4 pH7; C – S4 pH2, D – S5

7.4 Selective electroless Cu plating with catalyst S1-3

The electroless plating which followed the substrate activation by the S1-3 catalyst was not reproducible. The repeats are shown in Figure 102. Using the same experiment conditions, resultant electroless plating varied from no plating to finely-deposited copper lines. This was due to the low stability of the colloid which was discussed in Chapter 5. This meant that during deposition the processes of sedimentation and agglomeration occurred within the dispersion, which affected the reproducibility of the experiment. This resulted in differential catalyst distribution on the substrate surface from sample to sample and affected the subsequent electroless plating. Due to the low reproducibility the catalyst was not investigated further.

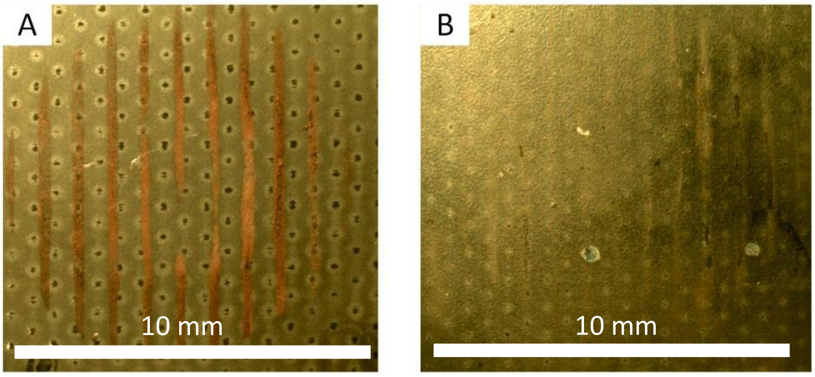

Figure 102. Electroless Cu deposited after surface activation with catalyst S1-3; A and B samples represent repeats of the same procedure.

7.5 Selective electroless Cu plating obtained after surface activation with catalyst S3

The catalyst first was deposited for 15, 30 and 60 sec and analysed by SEM (Figure 103, A-C). Large agglomerates were present in all cases of deposition. Bare substrate surface is visible after 15 sec catalyst deposition, while at 30 and 60 sec deposition the substrate seems entirely covered.

Electroless plating was carried out after the catalyst depositions (Figure 103, D-F). There was no plating obtained at the centre of the substrate when the substrate was activated by catalyst S3 for 15 (Figure 103, D) and 30 sec (Figure 103, E). The 60 sec activation resulted in plating at the central part of the substrate, although the plating was non-continuous (Figure 103, F, G). According to the SEM images the surface coverage with catalyst increased with longer time of catalyst deposition.

As was shown previously the nanoparticles contained a low amount of the catalytic component (Ag). This lead to an absence of copper plating when a short time of catalyst deposition was used.

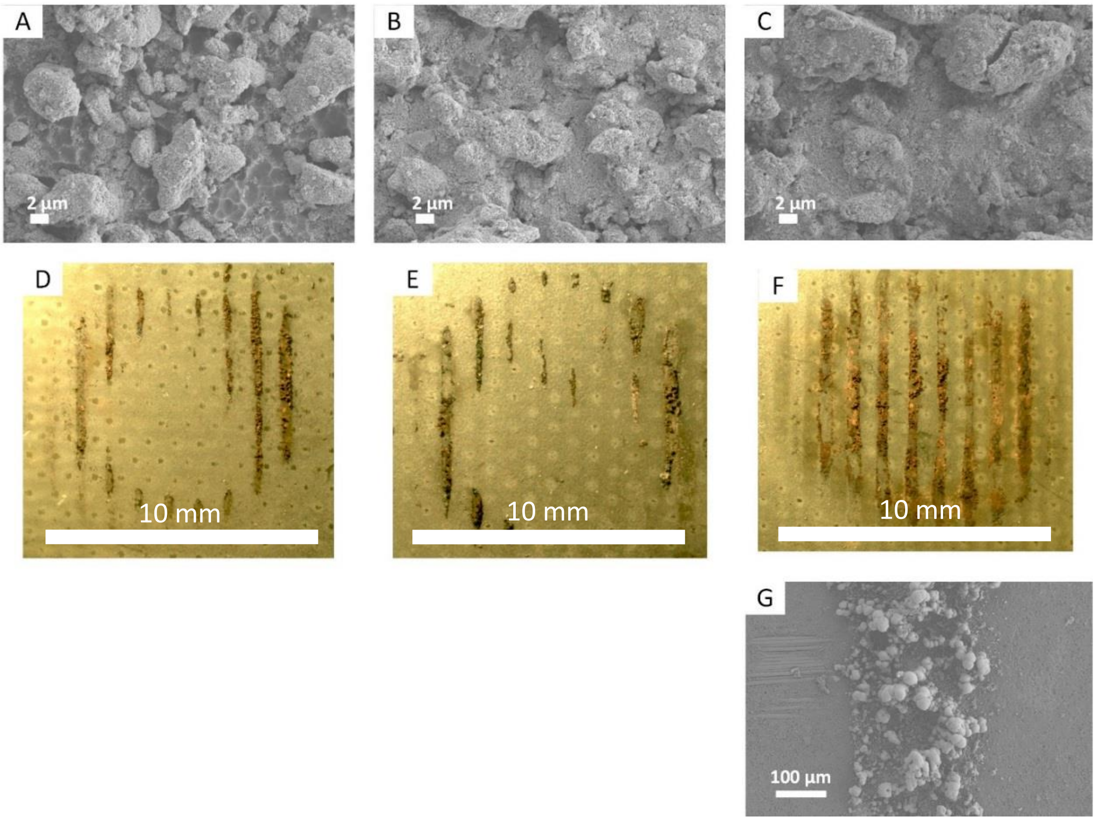

Figure 103. A-C – SEM images of substrate with deposited S3 catalyst for A – 15 sec, B – 30 sec, C – 60 sec; D-F – photographs of substrate with deposited catalyst in line pattern for D – 15 sec, E – 30 sec, F – 60 sec; G – electroless Cu plated after 60 sec surface activation with S3 catalyst.

7.6 Selective electroless Cu plating with catalyst S4

The S4 catalyst deposited for 15 sec did not cover the surface entirely (Figure 104, A), though both large agglomerates (above 4 µm) and small particles (below 1 µm) were clearly present on the surface. After the longer catalyst deposition time for 30 (Figure 104, B) and 60 sec (Figure 104, C) more catalyst was observed on the substrate surface and more agglomerates were present.

Selective metallisation was achieved in the samples activated for 15 (Figure 104, D) and 30 sec (Figure 104, E). Almost no deposit was achieved when samples were catalysed for 60 sec (Figure 104, F). The deposit in first two cases was not continuous, which is similar to the results obtained when catalyst S3 was used.

The presence of large agglomerates of catalyst caused non-continuous Cu plating in the case of both S3 and S4. The effect of the agglomerate on the Cu plating is schematically presented in Figure 105. Larger catalyst particles cannot be trapped by surface cavities, while plated Cu usually does not contact with the substrate surface which results in low adhesion of the layer and its removal during washing.

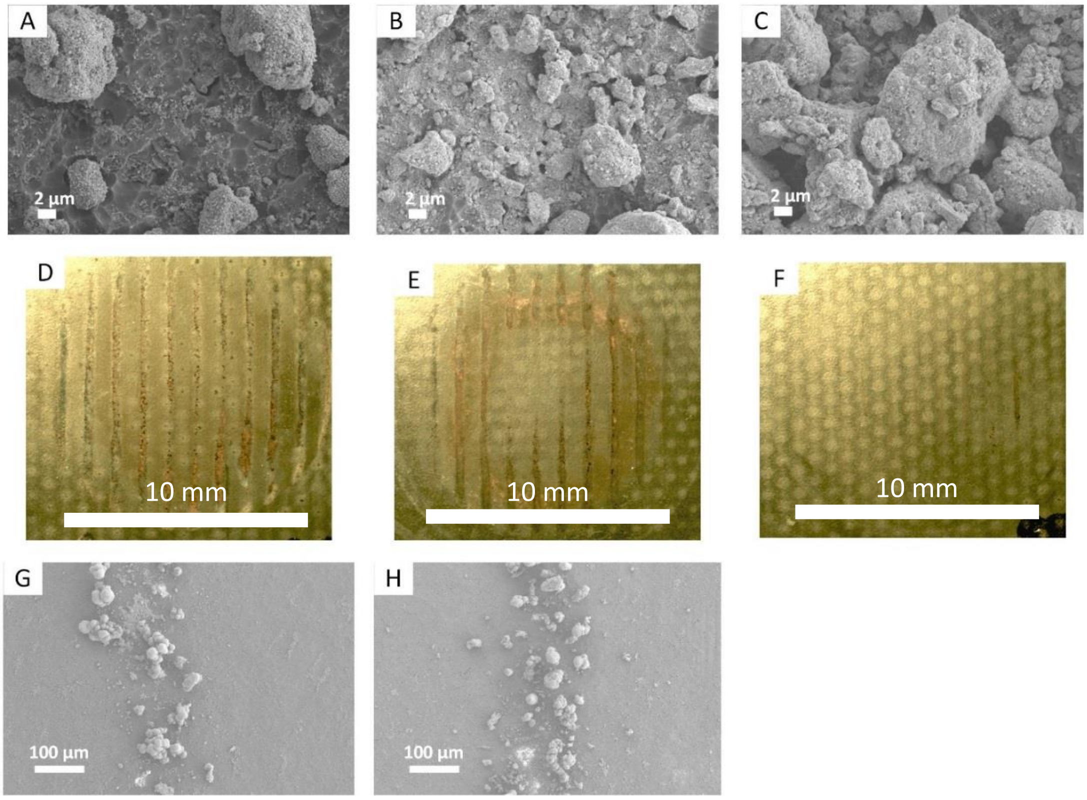

Figure 104. A-C – SEM images of substrate with deposited S4 catalyst for A – 15 sec, B – 30 sec, C – 60 sec; D-F – photographs of substrate with deposited catalyst in a line pattern for D – 15 sec, E – 30 sec, F – 60 sec; SEM images of electroless Cu plated after surface initialization with S4 catalyst for G – 15 sec, H – 30 sec.

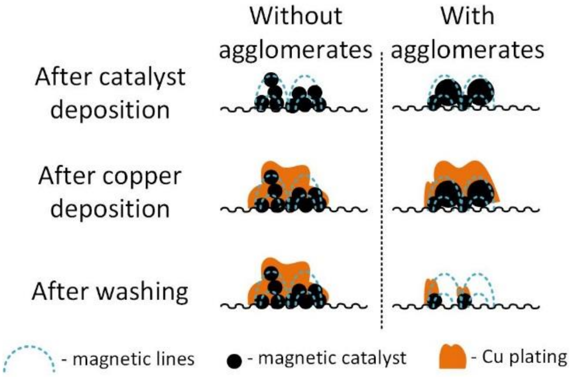

Figure 105. Schematic representation of electroless Cu plating after surface activation with monodisperse catalysts (left) and agglomerates of catalyst (right) to show a possible mechanism for a non-continuous copper deposition.

7.7 Selective electroless Cu plating with catalyst S4 pH2

More continuous electroless plated Cu lines were obtained when using the S4 pH2 catalyst. According to the SEM images (Figure 106, A-C), the catalyst deposited on the surface had less agglomerates which improved the quality of the deposited Cu layer. The agglomerates were observed on the surface only after 60 sec catalyst deposition (Figure 106, C).

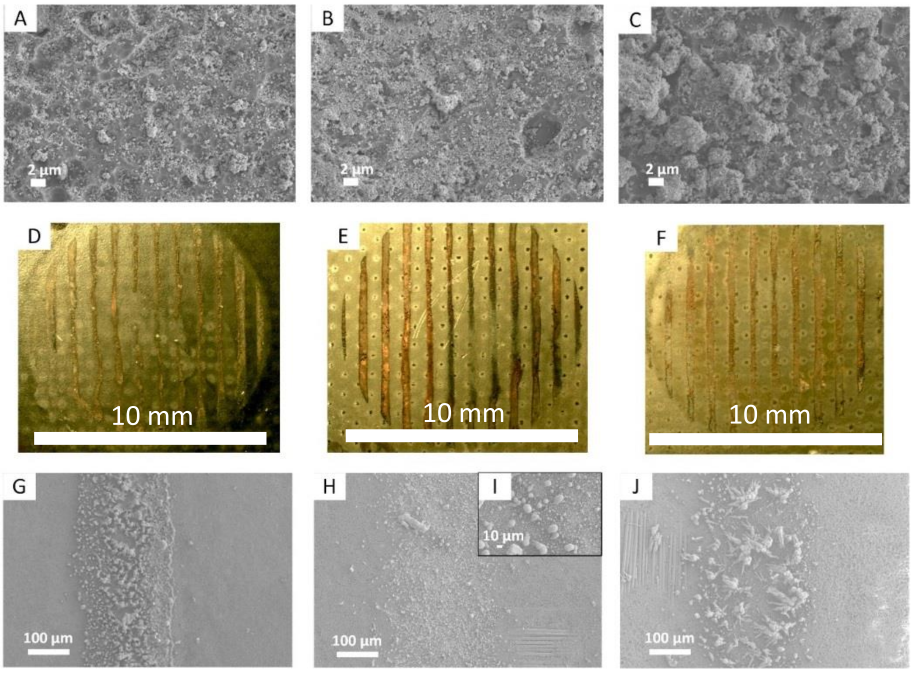

Figure 106. A-C – SEM images of substrate with deposited S4 pH2 catalyst for A – 30 sec, B – 60 sec, C – 90 sec; D-F – photographs of substrate with deposited catalyst in a line pattern for D – 30 sec, E – 60 sec, F – 90 sec; SEM images of electroless Cu plated after surface activation with S4 pH2 catalyst for G – 30 sec, H – 60 sec, I – magnified image H, J - 90 sec.

The photographs of subsequent selective electroless copper deposits are presented at Figure 106, D-F. The electroless copper deposited after 30 sec of surface catalyst deposition was not continuous and island-like plating was obtained (Figure 106, D, G). Continuous lines were obtained with a deposition of time of 30 sec (Figure 106, E, H, I) at the edge of the substrate where the flux density was higher. It was expected that increasing the time of catalyst deposition would have the same effect as increasing the magnetic flux density. However, when the time of catalyst deposition was increased, catalyst agglomerates were deposited which lead to non-continuous plating (Figure 106, F, J). The longer the particles were exposed to the magnetic field the more agglomerates formed [241], which resulted in the presence of more agglomerates when catalyst was deposited for 90 sec.

7.8 Selective electroless Cu plating with catalyst S5

Catalyst S5 was deposited on the substrate surface without forming agglomerates larger than 2 microns (Figure 107, A-C). There was no deposit obtained after 15 sec surface activation (Figure

107, D). Electroless Cu plating was obtained after 30 sec (Figure 107, E, G) and 60 sec (Figure 107, F, H) surface activation. A continuous Cu layer was obtained after 60 sec activation.

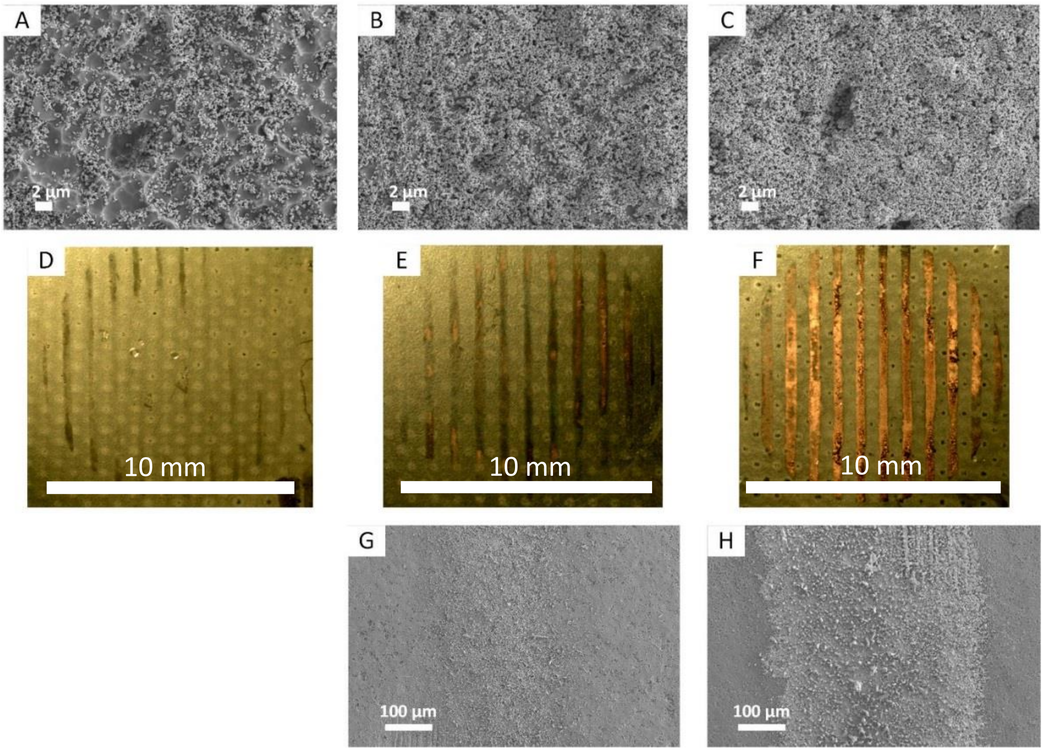

Figure 107. A-C – SEM images of substrate with deposited S5 catalyst for A – 15 sec, B – 30 sec, C – 60 sec; D-F – photographs of substrate with deposited catalyst in line pattern for D – 15 sec, E – 30 sec, F – 60 sec; SEM images of electroless Cu plated after surface activation for G - 30 sec, H – 60 sec.

The quality of the deposit varies across the sample. The electroless Cu plating differed from line to line (Figure 108) and within one line (Figure 109). This was due to the differences in magnetic flux density from line to line and across one line – the flux density increased closer to the substrate edge. For example, the line thickness is 700 µm for the line at Figure 108, C and the thickness of the line at Figure 108, F is only 400 µm. The resistance of the lines depicted in Figure 108, F, E was measured by multimeter and found to be 0.04 Ω, which is comparable with that reported by other works [158].

The lines located near the edge of the magnetic template have a needle-like deposit at the edges of the line and non-continuous deposit at the centre (Figure 108, A-C). This corresponds to case 3 in Figure 110. Due to high magnetic flux density, the catalyst overloaded the central part of the line. Therefore, deposited Cu had low adhesion and was removed during washing. The lines located closer to the centre had a needle-like structure at the middle of the line (Figure 108, D, E; Figure 109, A, B, D). The area is still overloaded with catalyst but this is not as extreme as at the edges and resulted in needle-like Cu deposition (Figure 110, case 2). Closer to the centre, smooth continuous lines were obtained (Figure 109, E, Figure 110, case 1).

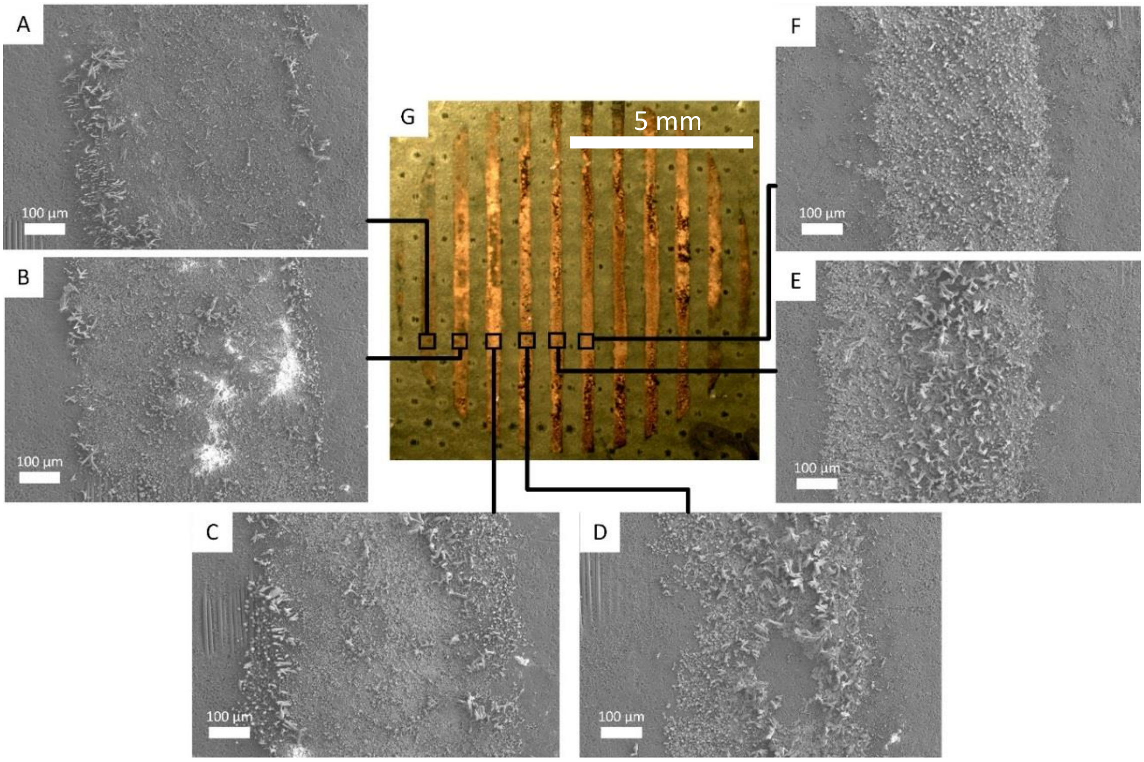

Figure 108. A-F – SEM images of the deposited Cu plated lines corresponding to the places depicted in image G – the photo of the substrate with selectively deposited Cu.

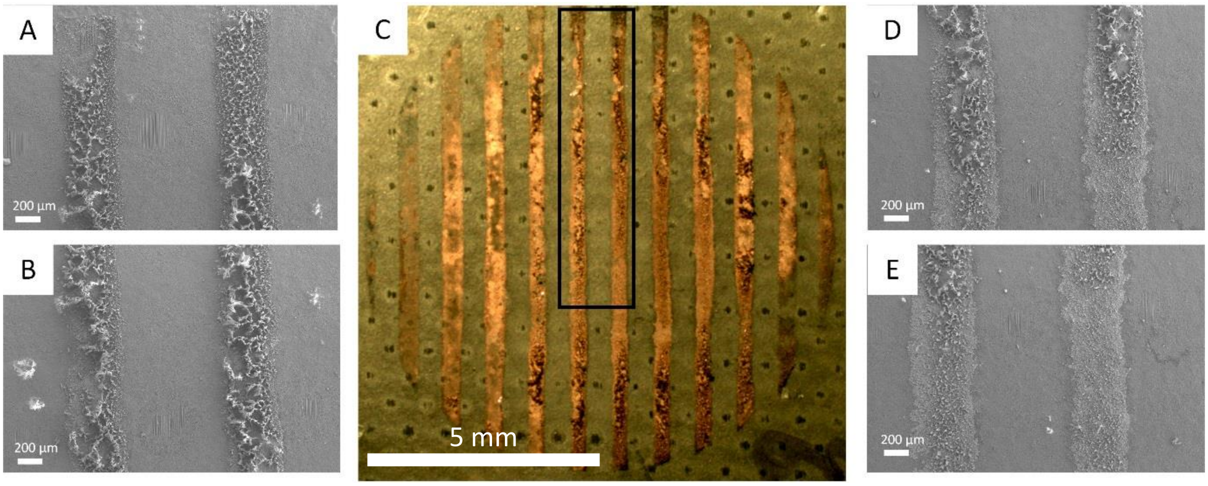

Figure 109. A, B, D, E –SEM images of the Cu plated lines corresponding to the area highlighted at image C from top to bottom respectively, C – photo of the selectively deposited electroless Cu.

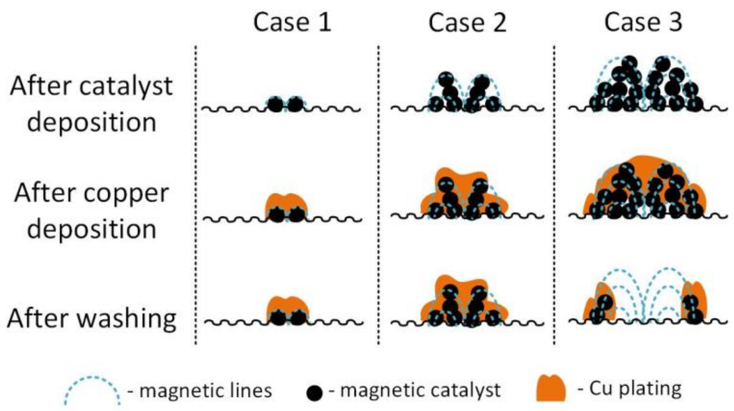

Figure 110. Schematic representation of electroless Cu plating after surface activation with differing magnetic field influence.

7.9 Discussion

All tested catalysts were patterned in the shape of parallel lines (Figure 101), however the quality of subsequent electroless Cu plating was significantly different across the samples.

The deposition of S1-3 catalyst was not reproducible (Figure 102) which is probably due to the absence of any functional layer on the particle surface that leads to non-stabilized particles in dispersion.

Use of both the S3 (Figure 103) and S4 (Figure 104) catalysts resulted in non-continuous Cu plating which was due to the presence of catalyst particle agglomerates. The agglomerates affected the continuity of the plating and island-like plating (i.e. a non-continuous film) was obtained. Both S3 and S4 catalysts were not filtered which resulted in large amounts of agglomerates.

The use of both the S4 pH2 (Figure 106) and S5 (Figure 107) catalysts resulted in formation of continuous lines. When the S4 pH2 catalyst was used, continuous lines were obtained at the edges of the substrate where the magnetic flux density was higher than at the centre. Both catalysts were deposited for 60 sec and did not have large agglomerates.

The 2D simulation of the distribution of magnetic flux density on the substrate surface showed that at magnetized areas, the flux density was of similar strength (Figure 96). However, in practice, the flux density varied enough to affect the quality of the catalyst deposition and subsequent electroless Cu plating.

The best selective deposition was obtained by using S5 catalyst which has a structure: Fe_3O_4-SiO_2-Sn-Ag. The catalyst was stabilized due to Sn^{2+} ion repulsion which occurs as a result of electrostatic forces. Amongst all functionalised catalyst particles obtained in the present work, the S5 catalyst had the lowest potential of formaldehyde oxidation which was investigated in Chapter 4.4. The main distinction from other investigated catalysts is that the S5 did not form large agglomerates when deposited (Figure 101), which resulted in the subsequent continuous plating. The thickness of the line at the centre of the pattern was 400 µm. The line plating is still not entirely homogeneous - large copper grains can be observed on the surface (figure 108, F). These could possibly be attributed to the unequal distribution of catalyst on the surface, which should be avoided. The lines located further from the template centre had more defects including growth of needle-like structures and non-continuous plating (Figure 108, Figure 109).

Regardless of the type of deposited catalyst particles, a common trend was observed between samples. The quality of the electroless copper was dependent upon the catalyst distribution across substrate surface. Firstly, when the distance between catalyst particles was too large, the plated copper did not form a continuous film (Figure 104, A, G, Figure 106, A, G). This was also previously reported in the literature and was discussed in the Chapter 1.1.10. Secondly, the electroless copper often lacked adhesion to the substrate. This was observed when agglomerates of the catalyst nanoparticles or excess catalyst was deposited. Usually, electroless deposited copper has either chemical or mechanical adhesion to the substrate surface. Chemical adhesion can be achieved by surface functionalisation, which was not investigated in this work. Mechanical adhesion is usually enhanced by the roughness of the surface so the deposited film can be mechanically interlocked. It was demonstrated in Figure 99 that electroless copper deposited by the standard procedure had weak adhesion to the non-treated laminate, which enhanced after swell-and etch pre-treatment of the substrate. When excess catalyst or catalyst agglomerates were deposited on the substrate, the subsequent electroless copper deposited only on the top layer of the catalyst. The copper did not grow enough to make contact with the surface of the substrate. The catalyst was held on the substrate due to the attraction to the magnetic field. When the magnetic field was removed neither catalyst nor deposited copper had any adhesion to the substrate and therefore both were removed from the substrate surface during washing (Figure 103, C, F, G, Figure 104, C, F).

Finally, needle-like plating was also obtained in some samples (Figure 106, Figure 108). The needles formed due to the aggregation of catalyst along the magnetic field lines. Formation of needles was absent at the areas with weaker magnetic field strength.

In order to improve the quality of the pattern, the magnetic steel template should be modified to provide equal field gradients at the required parts of the substrate. The agglomerates should be removed from the catalyst nanoparticle dispersion. In addition, the parameters of catalyst deposition should be investigated and optimised by varying the concentration of the catalyst, time of catalyst dispersion in water and the time of catalyst deposition on the substrate surface.

Chapter 8. Conclusion and future work

The present work showed that it is possible to obtain selective electroless Cu plating by applying a gradient magnetic field if a magnetic catalyst is used instead of the standard Pd/Sn catalyst. The proposed approach to selective metallisation does not require the photolithography process. The desired pattern can be obtained during the electroless plating process. A comparison of photolithography and selective metallisation by magnetic field application is presented at Figure 111.

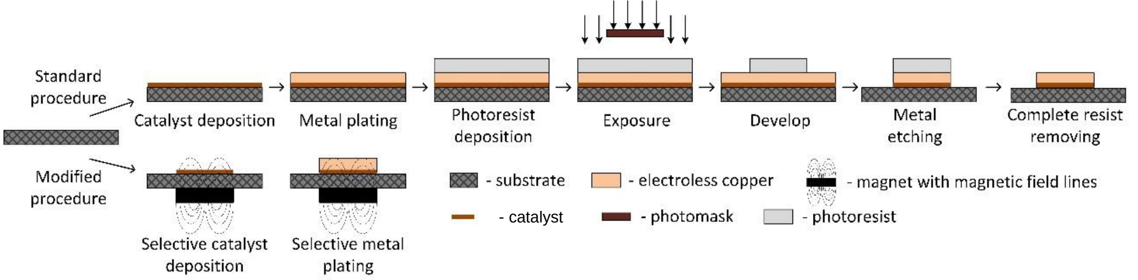

Figure 111. A comparison of the photolithography process with selective metallisation obtained by a application of a gradient magnetic field.

In this research the following aspects were investigated:

- Catalysts consisting of Fe_3O_4 magnetic nanoparticles and Ag catalytic nanoparticles for electroless plating process were studied. All particles were synthesised from aqueous solutions at a temperature below 100 ^oC and normal pressure. The following nanoparticles were obtained: non-functionalised Fe_3O_4-Ag, PVP-functionalised Fe_3O_4-Ag, arginine-functionalised Fe_3O_4-Ag and Fe_3O_4-SiO_2-Sn-Ag. All obtained particles had magnetic properties – they can be attracted by a magnet and are also catalytic towards formaldehyde oxidation according to the CV analysis.
- Possible ways of achieving a gradient magnetic field on the substrate surface were investigated. The gradient magnetic field was introduced by placing a single magnet and by securing the magnet with a steel template. Subsequently, the magnetic field distribution was simulated by using FEMM software and the corresponding template with simulated dimensions was fabricated. In addition, the holder for magnet, steel template and substrate was fabricated in order to protect the magnet and steel template from solution exposure.
- The synthesised magnetic catalyst was deposited selectively by using a single magnet with the steel template. It was found that if the catalyst deposited for a certain time

(depending on the type of the catalyst), needle-like agglomerates of the catalyst particles formed which followed the pattern of the magnetic field lines. Also loosely-adherent catalysts can be displaced from the areas where the magnetic field is applied during the electroless copper plating process. It was found that due to the magnetic field “edge” effect, the distribution of the catalyst was not uniform across the whole area where the magnetic field was applied.

- Copper deposition experiments were performed using the magnetic field template. Defects in the copper selectively deposited in the magnetic field were further discussed and attributed to excess deposited catalyst (low adhesion) and the presence of agglomerates (low adhesion, non-continuous plating). Needle-like plating was also observed at the areas with higher magnetic intensities, as was also observed with use of a single magnet.
- Selective electroless copper plating was obtained by applying a gradient magnetic field and by using magnetic catalyst particles. Continuous lines with width 400 µm were obtained by using the Fe_3O_4-SiO_2-Sn-Ag catalyst particles. The resistance of the lines was measured as 0.04 Ω.

In order to improve the quality of the deposited electroless copper, reduce the feature size of the deposited pattern and enable deposition of more complicated patterns, the following work should be performed:

- Continue investigation on the magnetic catalyst. The catalysts obtained in the present work did not have a narrow size distribution and/or had a composite structure, which makes the properties of the particles vary within each sample. Particles with core-shell structures and narrow size distribution should be tested for selective electroless plating applications. In addition, the composition of the particles was not varied in the present work. First of all composites with palladium instead of silver nanoparticles should be tested as palladium is usually reported to have higher catalytic activity for electroless Cu plating process than silver. In addition, the magnetic material can be changed in order to tune the magnetic properties of the particles and make them more or less responsive to the applied magnetic field.
- Improve stability of dispersed catalysts. The catalysts that were studied in this work had some agglomerates still present after dispersion. This affected the quality of the deposited electroless copper. Therefore, more work should be done to improve particle

dispersion. Other methods of particle dispersion could be studied for example ball milling and high pressure homogenization. There has been little work done on the optimisation of dispersion preparation parameters. The time of ultrasonication, concentration of the particles in the dispersion and temperature can all be varied. Also, additives can be used to stabilize the particles. Particle deposition from as-synthesised dispersions of nanoparticle should also be attempted.

- The method of gradient magnetic field application should be also studied. Gradient magnetic fields can be achieved by using, for example, magnet arrays but this was not attempted in the present work. The simulation of the magnetic field distribution across the sample surface should be studied in 3D. More simulations should be performed in order to attempt creation of more complex magnetic field patterns on the substrate surface.

Also the developed approach of selective electroless metal deposition should be tested on other non-conductive materials (e.g. glass, ceramics, fabric) and with other metals deposited from electroless baths e.g. Pt, Pd and Ag. In the case of Ni-P, Ni-B, Co and Fe electroless plating, the effect of a magnetic field on the quality of the electroless plating should be studied first.

References

[1] J.S.H. Cho, H.Ky. Kang, S. Simon, W. Wong, Y. Shacham-Diamand, Electroless Cu for VLSI, MRS Bull. 18 (1993) 31–38. https://doi.org/10.1557/S0883769400047308.

[2] Y. Shacham-Diamand, T. Osaka, Y. Okinaka, A. Sugiyama, V. Dubin, 30 Years of electroless plating for semiconductor and polymer micro-systems, Microelectron. Eng. 132 (2015) 35–45. https://doi.org/10.1016/j.mee.2014.09.003.

[3] E.K. Choi, J. Park, B.S. Kim, D. Lee, Fabrication of Electrodes and Near-Field Communication Tags based on Screen Printing of Silver Seed Patterns and Copper Electroless Plating, 16 (2015) 2199–2204. https://doi.org/10.1007/s12541-015-0283-y.

[4] Y.S. Rosen, Y. Lidor, R. Baiter, A. Szeskin, A. Awadallah, Y. Shacham-Diamand, S. Magdassi, Copper interconnections and antennas fabricated by hot-pressing printed copper formate, Flex. Print. Electron. 2 (2017). https://doi.org/10.1088/2058-8585/aa89bb.

[5] J.J. Chen, Y.L. Guo, Y. Wang, J. Zhang, H.J. Li, Z.S. Feng, Selective metallization of alumina ceramics by inkjet printing combined with electroless copper plating, J. Mater. Chem. C. 4 (2016) 10240–10245. https://doi.org/10.1039/c6tc03315f.

[6] G. Mallory, Electroless Plating: Fundamentals and Applications, AESF, 1991.

[7] S.Z. Qiao, J. Liu, G.Q. Max Lu, Synthetic Chemistry of Nanomaterials, Elsevier B.V., 2017. https://doi.org/10.1016/B978-0-444-63591-4.00021-5.

[8] R.A. Lawes, Manufacturing costs for microsystems/MEMS using high aspect ratio microfabrication techniques, Microsyst. Technol. 13 (2007) 85–95. https://doi.org/10.1007/s00542-006-0252-6.

[9] Y.. Liu, H.S. Cole, Laser surface modification for copper deposition on polyimide, Chem. Heterocycl. Compd. 129 (1989) 579–584.

[10] J. Xu, Y. Liao, H. Zeng, Z. Zhou, H. Sun, J. Song, X. Wang, Y. Cheng, Z. Xu, K. Sugioka, K. Midorikawa, Selective metallization on insulator surfaces with femtosecond laser pulses, Opt. Express. 15 (2007) 12743. https://doi.org/10.1364/oe.15.012743.

[11] N.S. Dellas, K. Meinert, S.E. Mohney, Laser-enhanced electroless plating of silver seed layers for selective electroless copper deposition, J. Laser Appl. 20 (2008) 218–223. https://doi.org/10.2351/1.2995767.

[12] H.S. Cole, Y.S. Liu, J.W. Rose, R. Guida, Laser-induced selective copper deposition on polyimide, Appl. Phys. Lett. 53 (1988) 2111–2113. https://doi.org/10.1063/1.100292.

[13] B.K. Park, D. Kim, S. Jeong, J. Moon, J.S. Kim, Direct writing of copper conductive patterns by ink-jet printing, Thin Solid Films. 515 (2007) 7706–7711. https://doi.org/10.1016/j.tsf.2006.11.142.

[14] C.C. Tseng, Y.H. Lin, Y.Y. Shu, C.J. Chen, M. Der Ger, Synthesis of vinyl acetate/Pd nanocomposites as activator ink for ink-jet printing technology and electroless copper plating, J. Taiwan Inst. Chem. Eng. 42 (2011) 989–995. https://doi.org/10.1016/j.jtice.2011.05.002.

[15] C.-Y. Kao, K.-S. Chou, Electroless Copper Plating onto Printed Lines of Nanosized Silver Seeds, Electrochem. Solid-State Lett. 10 (2007) D32. https://doi.org/10.1149/1.2431241.

[16] Y. Wang, Y. Wang, J. ju Chen, H. Guo, K. Liang, K. Marcus, Q. ling Peng, J. Zhang, Z. sheng Feng, A facile process combined with inkjet printing, surface modification and electroless deposition to fabricate adhesion-enhanced copper patterns on flexible polymer substrates for functional flexible electronics, Electrochim. Acta. 218 (2016) 24–31. https://doi.org/10.1016/j.electacta.2016.08.143.

[17] P.C. Hidber, W. Helbig, E. Kim, G.M. Whitesides, Microcontact Printing of Palladium Colloids: Micron-Scale Patterning by Electroless Deposition of Copper, Langmuir. (1996). https://doi.org/10.1021/la9507500.

[18] S.C. Huang, T.C. Tsao, L.J. Chen, Selective electroless copper plating on poly(ethylene terephthalate) surfaces by microcontact printing, J. Electrochem. Soc. 157 (2010) 222–227. https://doi.org/10.1149/1.3306136.

[19] P.C. Hidber, P.F. Nealey, W. Helbig, G.M. Whitesides, New strategy for controlling the size and shape of metallic features formed by electroless deposition of copper: Microcontact printing of catalysts on oriented polymers, followed by thermal shrinkage, Langmuir. 12(21) (1996) 5209–5215. https://doi.org/Doi 10.1021/La960238u.

[20] A. Equbal, N.K. Dixit, A.K. Sood, Electroless Plating on Plastic, Int. J. Sci. Eng. Res. 4 (2013).

[21] J. Duffy, L. Pearson, M. Paunovic, The Effect of pH on Electroless Copper Deposition, J. Electrochem. Soc. 130 (1983) 876–880. https://doi.org/10.1149/1.2119847.

[22] M.A. Y. Shacham-Diamand, V. Dubin, Electroless copper deposition for ULSI, Thin Solid Film. 262 (1995) 93–103.

[23] V.M. Dubin, Y. Shacham-Diamand, B. Zhoo, P.K. Vasudev, C.H. Ting, Selective and blanket electroless copper deposition for ultralarge scale integration, J. Electrochem. Soc. 144 (1997) 898–908. https://doi.org/10.1149/1.1837505.

[24] P. Bindra, J. Tweedie, Mechanisms of Electroless Metal Plating: I. Application of the Mixed Potential Theory, J. Electrochem. Soc. 130 (1983) 1112–1114. https://doi.org/10.1149/1.2119895.

[25] M. Paunovic, Electroless Deposition of Copper, Mod. Electroplat. Fifth Ed. 1 (2011) 433–446. https://doi.org/10.1002/9780470602638.ch17.

[26] J.E.A.M. Van Den Meerakker, On the mechanism of electroless plating. I. Oxidation of formaldehyde at different electrode surfaces, J. Appl. Electrochem. 11 (1981) 387–393. https://doi.org/10.1007/BF00613959.

[27] H. Wiese, K.G. Weil, On the Mechanism of Electroless Copper Deposition, Berichte Der Bunsengesellschaft Für Phys. Chemie. 91 (1987) 619–626.

[28] I. Ohno, Electrochemistry of electroless plating, Mater. Sci. Eng. A. 146 (1991) 33–49. https://doi.org/10.1016/0921-5093(91)90266-P.

[29] I. Ohno, O. Wakabayashi, S. Haruyama, Anodic Oxidation of Reductants in Electroless Plating, J. Electrochem. Soc. 132 (1985) 2323. https://doi.org/10.1149/1.2113572.

[30] M. Paunovic, Ligand Effects in Electroless Copper Deposition, J. Electrochem. Soc. Electrochem. Sci. Technol. 124 (1977) 349–354.

[31] J. Dumesic, J. a. Koutsky, T.W. Chapman, The Rate of Electroless Copper Deposition by Formaldehyde Reduction, J. Electrochem. Soc. 121 (1974) 1405. https://doi.org/10.1149/1.2401698.

[32] P. Bindra, J. Roldan, Mechanisms of Electroless Metal Plating II. Formaldehyde Oxidation, J. Electrochem. Soc. 132 (1985) 2581–2589. https://doi.org/10.1149/1.2119895.

[33] F.M. Donahue, Kinetics of Electroless Copper Plating, J. Electrochem. Soc. 127 (1980) 51. https://doi.org/10.1149/1.2129638.

[34] R. Schumacher, J.J. Pesek, O.R. Melroy, Kinetic analysis of electroless deposition of copper, J. Phys. Chem. 89 (1985) 4338–4342. https://doi.org/10.1021/j100266a037.

[35] V.N. Kuznetsov, R.G. Golovtshanskaya, S.S. Kruglikov, Electrochemical study of the electroless copper plating process, Surf. Coatings Technol. 28 (1986) 151–160. https://doi.org/10.1016/0257-8972(86)90054-X.

[36] T. Osaka, H. Takematsu, K. Nihei, A Study on Activation and Acceleration by Mixed PdCl2/SnCl2 Catalysts for Electroless Metal Deposition A Study on Activation and Acceleration by Mixed PdClJSnCI Catalysts for Electroless Metal Deposition, Electrochem. Sci. Technol. 127 (1980) 1021–1029. https://doi.org/10.1149/1.2129810.

[37] P.L. Djokic, Stojan S. ; Cavalloti, Electrodeposition: Theory and Practice, 2010. https://doi.org/10.1007/978-1-4419-5589-0.

[38] A. Capon, R. Parsons, The oxidation of formic acid on noble metal electrodes. II. A comparison of the behaviour of pure electrodes, J. Electroanal. Chem. 44 (1973) 239–254. https://doi.org/10.1016/S0022-0728(73)80250-5.

[39] J.E.A.M. Van Den Meerakker, On the mechanism of electroless plating. II. One mechanism for different reductants, J. Appl. Electrochem. 11 (1981) 395–400. https://doi.org/10.1007/BF00613960.

[40] E. Steinhäuser, Potential low-cost palladium-alternatives for activating electroless copper deposition, Circuit World. 36 (2010) 4–8. https://doi.org/10.1108/03056121011066279.

[41] Z.C. Liu, Q.G. He, P. Hou, P.F. Xiao, N.Y. He, Z.H. Lu, Electroless plating of copper through successive pretreatment with silane and colloidal silver, Colloids Surfaces A Physicochem. Eng. Asp. 257–258 (2005) 283–286. https://doi.org/10.1016/j.colsurfa.2004.10.036.

[42] C.-C. Yang, Y.-Y. Wang, C.-C. Wan, Synthesis and Characterization of PVP Stabilized Ag/Pd Nanoparticles and Its Potential as an Activator for Electroless Copper Deposition, J. Electrochem. Soc. 152 (2005) C96. https://doi.org/10.1149/1.1850379.

[43] C.C. Yang, C.C. Wan, Y.Y. Wang, Synthesis of Ag/Pd nanoparticles via reactive micelles as templates and its application to electroless copper deposition, J. Colloid Interface Sci. 279 (2004) 433–439. https://doi.org/10.1016/j.jcis.2004.06.098.

[44] C. Peng, S.H.Y. Lo, C.C. Wan, Y.Y. Wang, Study of the adsorptive behavior of Pd/PVP nanoparticles and its interaction with conditioner in electroless copper deposition, Colloids Surfaces A Physicochem. Eng. Asp. 308 (2007) 93–99. https://doi.org/10.1016/j.colsurfa.2007.05.058.

[45] J.-L. Lan, C.-C. Wan, Y.-Y. Wang, Mechanistic Study of Ag/Pd-PVP Nanoparticles and Their Functions as Catalyst for Electroless Copper Deposition, J. Electrochem. Soc. 155 (2008) K77–K83. https://doi.org/10.1149/1.2838908.

[46] C.L. Lee, Y.L. Tsai, C.W. Chen, Specific and mass activity of silver nanocube and nanoparticle-based catalysts for electroless copper deposition, Electrochim. Acta. 104 (2013) 185–190. https://doi.org/10.1016/j.electacta.2013.04.116.

[47] J.-L. Lan, C.-C. Wan, Y.-Y. Wang, Mechanistic Study of Ag/Pd-PVP Nanoparticles and Their Functions as Catalyst for Electroless Copper Deposition, J. Electrochem. Soc. 155 (2008) K77. https://doi.org/10.1149/1.2838908.

[48] J. Horkans, C. Sambucetti, V. Markovich, Initiation of electroless Cu plating on nonmetallic surfaces, IBM J. Res. Dev. 28 (1984) 690–696. https://doi.org/10.1147/rd.286.0690.

[49] C.-H. Chen, H.-L. Yang, H.-R. Chen, C.-L. Lee, Activity on Electrochemical Surface Area: Silver Nanoplates as New Catalysts for Electroless Copper Deposition, J. Electrochem. Soc. 159 (2012) D507–D511. https://doi.org/10.1149/2.025209jes.

[50] A. Safavi, S. Momeni, M. Tohidi, Silver-Palladium Nanoalloys Modified Carbon Ionic Liquid Electrode with Enhanced Electrocatalytic Activity Towards Formaldehyde Oxidation, Electroanalysis. 24 (2012) 1981–1988. https://doi.org/10.1002/elan.201200257.

[51] E. Matijević, A.M. Poskanzer, P. Zuman, The Characterization of the Stannous Chloride/ Palladium Chloride Catalysts for Electroless Plating, NASF Surf. Technol. White Pap. 61 (2016) 958–965.

[52] X. Cui, D.A. Hutt, D.J. Scurr, P.P. Conway, The Evolution of Pd⁄Sn Catalytic Surfaces in Electroless Copper Deposition, J. Electrochem. Soc. 158 (2011) D172–D177. https://doi.org/10.1149/1.3536543.

[53] L.J. Chen, C.C. Wan, Y.Y. Wang, Chemical preparation of Pd nanoparticles in room temperature ethylene glycol system and its application to electroless copper deposition,

J. Colloid Interface Sci. 297 (2006) 143–150. https://doi.org/10.1016/j.jcis.2005.10.029.

[54] M.W. Wang, T.Y. Liu, D.C. Pang, J.C. Hung, C.C. Tseng, Inkjet printing of a pH sensitive palladium catalyst patterns of ITO glass for electroless copper, Surf. Coatings Technol. 259 (2014) 340–345. https://doi.org/10.1016/j.surfcoat.2014.02.031.

[55] S.H.Y. Lo, Y.Y. Wang, C.C. Wan, Synthesis of PVP stabilized Cu/Pd nanoparticles with citrate complexing agent and its application as an activator for electroless copper deposition, J. Colloid Interface Sci. 310 (2007) 190–195. https://doi.org/10.1016/j.jcis.2007.01.057.

[56] C.C. Yang, C.C. Wan, Y.Y. Wang, The role of poly (N-vinyl-2-pyrrollidone) in Ag/Pd nanoparticles formation and its application to electroless deposition, J. Electrochem. Soc. 153 (2006) 27–31. https://doi.org/10.1149/1.2176917.

[57] C.L. Lee, C.M. Tseng, R.B. Wu, S.C. Syu, Synthesis of highly active Ag/Pd nanorings for activating electroless copper deposition, J. Electrochem. Soc. 156 (2009) 348–350. https://doi.org/10.1149/1.3156687.

[58] A.J. Cobley, D.J. Comeskey, L. Paniwnyk, T.J. Mason, Through hole plating of printed circuit boards using ultrasonically dispersed copper nanoparticles, Circuit World. 36 (2010) 9–13. https://doi.org/10.1108/03056121011066288.

[59] J.E. Graves, M. Sugden, R.E. Litchfield, D.A. Hutt, T.J. Mason, A.J. Cobley, Ultrasound assisted dispersal of a copper nanopowder for electroless copper activation, Ultrason. Sonochem. 29 (2016) 428–438. https://doi.org/10.1016/j.ultsonch.2015.10.016.

[60] Y. Fujiwara, A. Koishikawa, Y. Kobayashi, S. Ikeda, T. Sugaya, Y. Hoshiyama, H. Miyake, Initial stage of electroless Cu deposition on epoxy substrate catalyzed with ag nanoparticles, J. Electrochem. Soc. 161 (2014) 546–551. https://doi.org/10.1149/2.0891410jes.

[61] Y. Fujiwara, Y. Kobayashi, T. Sugaya, A. Koishikawa, Y. Hoshiyama, H. Miyake, Adsorption promotion of Ag nanoparticle using cationic surfactants and polyelectrolytes for electroless Cu plating catalysts, J. Electrochem. Soc. 157 (2010) 211–216. https://doi.org/10.1149/1.3306025.

[62] Y. Fujiwara, Y. Kobayashi, K. Kita, R. Kakehashi, M. Noro, J. Katayama, K. Otsuka, Ag Nanoparticle Catalyst for Electroless Cu Deposition and Promotion of Its Adsorption onto

Epoxy Substrate, J. Electrochem. Soc. 155 (2008) D377. https://doi.org/10.1149/1.2890288.

[63] C.L. Lee, C.M. Tseng, S.C. Wu, R.B. Wu, Activator for electrolessly depositing copper from triangular AgPd nanoshells, Electrochem. Solid-State Lett. 11 (2008) 2007–2009. https://doi.org/10.1149/1.2820903.

[64] A. Vaskelis, A. Jagminiene, L. Tamasauskaite-Tamasiunaite, R. Juskenas, Silver nanostructured catalyst for modification of dielectrics surface, Electrochim. Acta. 50 (2005) 4586–4591. https://doi.org/10.1016/j.electacta.2004.10.093.

[65] J. Geng, Y. Bi, G. Lu, Morphology-dependent activity of silver nanostructures towards the electro-oxidation of formaldehyde, Electrochem. Commun. 11 (2009) 1255–1258. https://doi.org/10.1016/j.elecom.2009.04.014.

[66] D. Chen, Q. Lu, Y. Zhao, Laser-induced site-selective silver seeding on polyimide for electroless copper plating, Appl. Surf. Sci. 253 (2006) 1573–1580. https://doi.org/10.1016/j.apsusc.2006.02.039.

[67] J.H. Byeon, K.Y. Yoon, Y.K. Jung, J. Hwang, Thermophoretic deposition of palladium aerosol nanoparticles for electroless micropatterning of copper, Electrochem. Commun. 10 (2008) 1272–1275. https://doi.org/10.1016/j.elecom.2008.06.025.

[68] Y. Wang, N. Li, D. Li, S. Yu, C. Wang, A bio-inspired method to inkjet-printing copper pattern on polyimide substrate, Mater. Lett. 140 (2015) 127–130. https://doi.org/10.1016/j.matlet.2014.11.006.

[69] S. Blundell, Magnetism in Condensed Matter, Oxford University Press Inc, New York, 2001. https://doi.org/10.1119/1.1522704.

[70] P. Beckley, Magnetism in Solids: Hysteresis, Encycl. Mater. Sci. Technol. (2001) 5032–5035. https://doi.org/10.1016/b0-08-043152-6/00873-1.

[71] A. Gupta, D. Yan, Mineral Processing Design and Operations, Second Edi, Elsevier B.V, Amsterdam, 2016. https://doi.org/10.1016/b978-0-444-63589-1.00017-4.

[72] H. Iida, K. Takayanagi, T. Nakanishi, T. Osaka, Synthesis of Fe3O4 nanoparticles with various sizes and magnetic properties by controlled hydrolysis, J. Colloid Interface Sci. 314 (2007) 274–280. https://doi.org/10.1016/j.jcis.2007.05.047.

[73] S.I.U. Madrid, U. Pal, F.S.-D. Jesus, Controlling size and magnetic properties of Fe_3O_4 clusters in solvothermal process, Adv. Nano Res. 2 (2014) 187–198. https://doi.org/10.12989/anr.2014.2.4.187.

[74] X. Liang, H. Shi, X. Jia, Y. Yang, X. Liu, Dispersibility, Shape and Magnetic Properties of Nano-Fe_3O_4 Particles, Mater. Sci. Appl. 02 (2011) 1644–1653. https://doi.org/10.4236/msa.2011.211219.

[75] G.F. Goya, T.S. Berquó, F.C. Fonseca, M.P. Morales, Static and dynamic magnetic properties of spherical magnetite nanoparticles, J. Appl. Phys. 94 (2003) 3520–3528. https://doi.org/10.1063/1.1599959.

[76] S. Upadhyay, K. Parekh, B. Pandey, Influence of crystallite size on the magnetic properties of Fe_3O_4 nanoparticles, J. Alloys Compd. 678 (2016) 478–485. https://doi.org/10.1016/j.jallcom.2016.03.279.

[77] L.M.A. Monzon, J.M.D. Coey, Magnetic fields in electrochemistry: The Lorentz force. A mini-review, Electrochem. Commun. 42 (2014) 38–41. https://doi.org/10.1016/j.elecom.2014.02.006.

[78] T.Z. Fahidy, Magnetoelectrolysis, J. Appl. Electrochem. 13 (1983) 553–563. https://doi.org/10.1007/BF00617811.

[79] M. Uhlemann, K. Tschulik, A. Gebert, G. Mutschke, J. Fröhlich, A. Bund, X. Yang, K. Eckert, Structured electrodeposition in magnetic gradient fields, Eur. Phys. J. Spec. Top. 220 (2013) 287–302. https://doi.org/10.1140/epjst/e2013-01814-3.

[80] Y.D. Yu, Z.L. Song, H.L. Ge, G.Y. Wei, Influence of magnetic fields on cobalt electrodeposition, Surf. Eng. 30 (2014) 83–88. https://doi.org/10.1179/1743294413Y.0000000229.

[81] X. Lu, D. Li, Q. Wang, G. Li, Y. Cao, J. He, Ni-P electroless deposition with different complexing agent under uniform and gradient high magnetic fields, Magnetohydrodynamics. 48 (2012) 1–6.

[82] Y. Yu, G. Wei, X. Hu, H. Ge, Z. Yu, The effect of magnetic fields on the electroless deposition of Co-W-P film, Surf. Coatings Technol. 204 (2010) 2669–2676. https://doi.org/10.1016/j.surfcoat.2010.02.020.

[83] L. Chia-Chien, T.-C.C. Chou, Effects of magnetic field on the reaction kinetics of electroless nickel deposition, Electrochim. Acta. 40 (1995) 965–970. https://doi.org/10.1016/0013-4686(95)00007-2.

[84] Y. Oshikiri, M. Sato, A. Yamada, R. Aogaki, Gravity Field Effect on Copper-Electroless Plating –Comparison with the Magnetic Field Effect, Jpn. J. Appl. Phys. 43 (2004) 3596–3604. https://doi.org/10.1143/JJAP.43.3596.

[85] N. Hirota, S. Hara, H. Uetake, H. Nakamura, K. Kitazawa, In situ microscopic observations of an electroless silver deposition process under high magnetic fields, J. Cryst. Growth. 286 (2006) 465–469. https://doi.org/10.1016/j.jcrysgro.2005.10.122.

[86] G. Hinds, F.E. Spada, J.M.D. Coey, T.R. Ni Mhiochain, M.E.G. Lyons, Magnetic Field Effects on Copper Electrolysis, J. Phys. Chem. B. 105 (2001) 9487–9502. https://doi.org/10.1021/jp010581u.

[87] L.M.A. Monzon, J.M.D. Coey, Magnetic fields in electrochemistry: The Kelvin force. A mini-review, Electrochem. Commun. 42 (2014) 42–45. https://doi.org/10.1016/j.elecom.2014.02.005.

[88] D.R. Lide, Handbook of Chemistry and Physics, National Institute of Standards and Technology, 2003.

[89] D.J. Griffiths, Introduction to Electrodynamics, Cambridge University Press, 2017. https://doi.org/10.1017/9781108333511.

[90] A.F. Demirors, P.P. Pillai, B. Kowalczyk, B.A. Grzybowski, Colloidal assembly directed by virtual magnetic moulds, Nature. 503 (2013) 99–103. https://doi.org/10.1038/nature12591.

[91] T. Okada, N.I. Wakayama, L. Wang, H. Shingu, J.I. Okano, T. Ozawa, The effect of magnetic field on the oxygen reduction reaction and its application in polymer electrolyte fuel cells, Electrochim. Acta. 48 (2003) 531–539. https://doi.org/10.1016/S0013-4686(02)00720-X.

[92] N.B. Chaure, F.M.F. Rhen, J. Hilton, J.M.D. Coey, Design and application of a magnetic field gradient electrode, Electrochem. Commun. 9 (2007) 155–158. https://doi.org/10.1016/j.elecom.2006.08.059.

[93] L.M.A. Monzon, K. Rode, M. Venkatesan, J.M.D. Coey, Electrosynthesis of iron, cobalt,

and zinc microcrystals and magnetic enhancement of the oxygen reduction reaction, Chem. Mater. 24 (2012) 3878–3885. https://doi.org/10.1021/cm301766s.

[94] J.M.D. Coey, R. Aogaki, F. Byrne, P. Stamenov, Magnetic stabilization and vorticity in submillimeter paramagnetic liquid tubes, Proc. Natl. Acad. Sci. U. S. A. 106 (2009) 8811–8817. https://doi.org/10.1073/pnas.0900561106.

[95] P. Dunne, L. Mazza, J.M.D. Coey, Magnetic structuring of electrodeposits, Phys. Rev. Lett. 107 (2011) 2–5. https://doi.org/10.1103/PhysRevLett.107.024501.

[96] P. Dunne, R. Soucaille, K. Ackland, J.M.D. Coey, Magnetic structuring of linear copper electrodeposits, J. Appl. Phys. 111 (2012) 2012–2015. https://doi.org/10.1063/1.3678295.

[97] K. Tschulik, J.A. Koza, M. Uhlemann, A. Gebert, L. Schultz, Effects of well-defined magnetic field gradients on the electrodeposition of copper and bismuth, Electrochem. Commun. (2009). https://doi.org/10.1016/j.elecom.2009.09.041.

[98] O.Y. Gorobets, V.Y. Gorobets, D.O. Derecha, O.M. Brukva, Nickel electrodeposition under influence of constant homogeneous and high-gradient magnetic field, J. Phys. Chem. C. 112 (2008) 3373–3375. https://doi.org/10.1021/jp0762572.

[99] F. Karnbach, M. Uhlemann, A. Gebert, J. Eckert, K. Tschulik, Magnetic field templated patterning of the soft magnetic alloy CoFe, Electrochim. Acta. 123 (2014) 477–484. https://doi.org/10.1016/j.electacta.2014.01.055.

[100] M. Uhlemann, A. Krause, J.P. Chopart, A. Gebert, Electrochemical deposition of co under the influence of high magnetic fields, J. Electrochem. Soc. 152 (2005) 817–826. https://doi.org/10.1149/1.2073167.

[101] J.A. Koza, S. Muhlenhoff, P. Zabinski, P.A. Nikrityuk, K. Eckert, M. Uhlemann, A. Gebert, T. Weier, L. Schultz, S. Odenbach, Hydrogen evolution under the influence of a magnetic field, Electrochim. Acta. 56 (2011) 2665–2675. https://doi.org/10.1016/j.electacta.2010.12.031.

[102] J.A. Koza, S. Muhlenhoff, M. Uhlemann, K. Eckert, A. Gebert, L. Schultz, Desorption of hydrogen from an electrode surface under influence of an external magnetic field - In-situ microscopic observations, Electrochem. Commun. 11 (2009) 425–429. https://doi.org/10.1016/j.elecom.2008.12.010.

[103] P. Dunne, J.M.D. Coey, Patterning metallic electrodeposits with magnet arrays, Phys. Rev. B - Condens. Matter Mater. Phys. 85 (2012) 1–21. https://doi.org/10.1103/PhysRevB.85.224411.

[104] K. Tschulik, R. Sueptitz, J. Koza, M. Uhlemann, G. Mutschke, T. Weier, A. Gebert, L. Schultz, Studies on the patterning effect of copper deposits in magnetic gradient fields, Electrochim. Acta. 56 (2010) 297–304. https://doi.org/10.1016/j.electacta.2010.08.080.

[105] K. Tschulik, X. Yang, G. Mutschke, M. Uhlemann, K. Eckert, R. Sueptitz, L. Schultz, A. Gebert, How to obtain structured metal deposits from diamagnetic ions in magnetic gradient fields?, Electrochem. Commun. 13 (2011) 946–950. https://doi.org/10.1016/j.elecom.2011.06.007.

[106] M. Subramanian, A. Miaskowski, S.I. Jenkins, J. Lim, Remote manipulation of magnetic nanoparticles using magnetic field gradient to promote cancer cell death, Appl. Phys. A. 125 (2019). https://doi.org/doi:10.1007/s00339-019-2510-3.

[107] V.H.B. Ho, K.H. Müller, N.J. Darton, D.C. Darling, F. Farzaneh, N.K.H. Slater, Simple magnetic cell patterning using streptavidin paramagnetic particles, Exp. Biol. Med. 234 (2009) 332–341. https://doi.org/10.3181/0809-RM-273.

[108] G. Frasca, F. Gazeau, C. Wilhelm, Formation of a Three-Dimensional Multicellular Assembly Using Magnetic Patterning, Langmuir. 25 (2009) 2348–2354.

[109] H. Akiyama, A. Ito, Y. Kawabe, M. Kamihira, Fabrication of complex three-dimensional tissue architectures using a magnetic force-based cell patterning technique, Biomed. Microdevices. 11 (2009) 713–721. https://doi.org/10.1007/s10544-009-9284-x.

[110] K. Ino, A. Ito, H. Honda, Cell patterning using Magnetite Nanoparticles and Magnetic force, Biotechnol. Bioeng. 97 (1996) 503–505. https://doi.org/10.1002/bit.

[111] K. Ino, M. Okochi, N. Konishi, M. Nakatochi, R. Imai, M. Shikida, A. Ito, H. Honda, Cell culture arrays using magnetic force-based cell patterning for dynamic single cell analysis, Lab Chip. 8 (2008) 134–142. https://doi.org/10.1039/B712330B.

[112] Z. Yang, J. Wei, K. Gizynski, M.G. Song, B.A. Grzybowski, Interference-like patterns of static magnetic fields imprinted into polymer/nanoparticle composites, Nat. Commun. 8 (2017) 1–8. https://doi.org/10.1038/s41467-017-01861-1.

[113] Q. Cao, Z. Wang, B. Zhang, Y. Feng, S. Zhang, X. Han, L. Li, Targeting Behavior of Magnetic Particles Under Gradient Magnetic Fields Produced by Two Types of Permanent Magnets, IEEE Trans. Appl. Supercond. 26 (2016).

[114] U. Schwertmann, R.M. Cornell, Iron Oxides in the Laboratory, Second edi, WILEY-VCH, 1992. https://doi.org/10.1180/minmag.1992.056.383.20.

[115] A.S. Teja, P.Y. Koh, Synthesis, properties, and applications of magnetic iron oxide nanoparticles, Prog. Cryst. Growth Charact. Mater. 55 (2009) 22–45. https://doi.org/10.1016/j.pcrysgrow.2008.08.003.

[116] M. Su, C. He, K. Shih, Facile synthesis of morphology and size-controlled α-Fe_2O_3 and Fe_3O_4 nano-and microstructures by hydrothermal/solvothermal process: The roles of reaction medium and urea dose, Ceram. Int. 42 (2016) 14793–14804. https://doi.org/10.1016/j.ceramint.2016.06.111.

[117] W. Wu, Q. He, C. Jiang, Magnetic iron oxide nanoparticles: Synthesis and surface functionalization strategies, Nanoscale Res. Lett. 3 (2008) 397–415. https://doi.org/10.1007/s11671-008-9174-9.

[118] A.. Olowe, J.M.. Génin, The mechanism of oxidation of ferrous hydroxide in sulphated aqueous media: Importance of the initial ratio of the reactants, Corros. Sci. 32 (1991) 965–984. https://doi.org/10.1016/0010-938X(91)90016-I.

[119] P. Refait, J.-M.. Génin, The oxidation of ferrous hydroxide in chloride-containing aqueous media and pourbaix diagrams of green rust one, Corros. Sci. 34 (1993) 797–819. https://doi.org/10.1016/0010-938X(93)90101-L.

[120] P. Gong, H. Li, X. He, K. Wang, J. Hu, W. Tan, S. Zhang, X. Yang, Preparation and antibacterial activity of Fe_3O_4@Ag nanoparticles, Nanotechnology. 18 (2007). https://doi.org/10.1088/0957-4484/18/28/285604.

[121] X. Zhang, W. Jiang, X. Gong, Z. Zhang, Sonochemical synthesis and characterization of magnetic separable Fe_3O_4/ Ag composites and its catalytic properties, J. Alloys Compd. 508 (2010) 400–405. https://doi.org/10.1016/j.jallcom.2010.08.070.

[122] J. Du, C. Jing, Preparation of Fe_3O_4@Ag SERS substrate and its application in environmental Cr(VI) analysis, J. Colloid Interface Sci. 358 (2011) 54–61. https://doi.org/10.1016/j.jcis.2011.02.044.

[123] L.M. Tung, N.X. Cong, L.T. Huy, N.T. Lan, V.N. Phan, N.Q. Hoa, L.K. Vinh, N.V. Thinh, L.T. Tai, D. Ngo, Synthesis, Characterizations of Superparamagnetic Fe_3O_4–Ag Hybrid Nanoparticles and Their Application for Highly Effective Bacteria Inactivation, J. Nanosci. Nanotechnol. 16 (2016) 5902–5912. https://doi.org/10.1166/jnn.2016.11029.

[124] A. Benvidi, S. Jahanbani, Self-assembled monolayer of SH-DNA strand on a magnetic bar carbon paste electrode modified with Fe_3O_4@Ag nanoparticles for detection of breast cancer mutation, J. Electroanal. Chem. 768 (2016) 47–54. https://doi.org/10.1016/j.jelechem.2016.02.038.

[125] Z. Kozakova, I. Kuritka, N.E. Kazantseva, V. Babayan, M. Pastorek, M. Machovsky, P. Bazant, P. Saha, The formation mechanism of iron oxide nanoparticles within the microwave-assisted solvothermal synthesis and its correlation with the structural and magnetic properties, Dalt. Trans. 44 (2015) 21099–21108. https://doi.org/10.1039/c5dt03518j.

[126] Y. Chi, Q. Yuan, Y. Li, J. Tu, L. Zhao, N. Li, X. Li, Synthesis of Fe_3O_4@SiO_2-Ag magnetic nanocomposite based on small-sized and highly dispersed silver nanoparticles for catalytic reduction of 4-nitrophenol, J. Colloid Interface Sci. 383 (2012) 96–102. https://doi.org/10.1016/j.jcis.2012.06.027.

[127] K. Choi, S. Park, B. Joo, J. Jung, Recyclable Ag-coated Fe_3O_4@TiO_2 for efficient photocatalytic oxidation of chlorophenol, Surf. Coat. Technol. 320 (2017) 240–245. https://doi.org/10.1016/j.surfcoat.2017.01.029.

[128] R.F. Egerton, Physical principles of electron microscopy, Second, Springer, Edmonton, Canada, 2016.

[129] D. Hao, S. Cheng-Min, H. Chao, X. Zhi-Chuan, L. Chen, T. Yuan, S. Xue-Zhao, G. Hong-Jun, Synthesis and properties of Au-Fe_3O_4 and Ag-Fe_3O_4 heterodimeric nanoparticles, Chinese Phys. B. 19 (2010) 066102.

[130] L. Zhang, Y. Dou, H. Gu, Synthesis of Ag – Fe_3O_4 heterodimeric nanoparticles, J. Colloid Interface Sci. 297 (2006) 660–664. https://doi.org/10.1016/j.jcis.2005.11.009.

[131] S.D. Solomon, M. Bahadory, A. V. Jeyarajasingam, S.A. Rutkowsky, C. Boritz, L. Mulfinger, Synthesis and study of silver nanoparticles, J. Chem. Educ. 84 (2007) 322–325. https://doi.org/10.1021/ed084p322.

[132] E. Tahmasebi, Y. Yamini, Facile synthesis of new nano sorbent for magnetic solid-phase extraction by self assembling of bis-(2,4,4-trimethyl pentyl)-dithiophosphinic acid on Fe_3O_4@Ag core@shell nanoparticles: Characterization and application, Anal. Chim. Acta. 756 (2012) 13–22. https://doi.org/10.1016/j.aca.2012.10.040.

[133] Y. Sun, Y. Tian, M. He, Q. Zhao, C. Chen, C. Hu, Y. Liu, Controlled synthesis of Fe_3O_4/Ag core-shell composite nanoparticles with high electrical conductivity, J. Electron. Mater. 41 (2012) 519–523. https://doi.org/10.1007/s11664-011-1800-0.

[134] S. Zhu, C. Fan, J. Wang, J. He, E. Liang, M. Chao, Realization of high sensitive SERS substrates with one-pot fabrication of Ag – Fe_3O_4 nanocomposites, J. Colloid Interface Sci. 438 (2015) 116–121. https://doi.org/10.1016/j.jcis.2014.09.015.

[135] J.R. Chiou, B.H. Lai, K.C. Hsu, D.H. Chen, One-pot green synthesis of silver/iron oxide composite nanoparticles for 4-nitrophenol reduction, J. Hazard. Mater. 248–249 (2013) 394–400. https://doi.org/10.1016/j.jhazmat.2013.01.030.

[136] B. Chudasama, A.K. Vala, N. Andhariya, R. V. Upadhyay, R. V. Mehta, Antifungal activity of multifunctional Fe_3O_4-Ag nanocolloids, J. Magn. Magn. Mater. 323 (2011) 1233–1237. https://doi.org/10.1016/j.jmmm.2010.11.012.

[137] D. Tang, R. Yuan, Y. Chai, Magnetic core-shell Fe_3O_4@Ag nanoparticles coated carbon paste interface for studies of carcinoembryonic antigen in clinical immunoassay, J. Phys. Chem. B. 110 (2006) 11640–11646. https://doi.org/10.1021/jp060950s.

[138] C.H. Liu, Z.D. Zhou, X. Yu, B.Q. Lv, J.F. Mao, D. Xiao, Preparation and characterization of Fe_3O_4/Ag composite magnetic nanoparticles, Inorg. Mater. 44 (2008) 291–295. https://doi.org/10.1007/s10789-008-3014-2.

[139] S. Venkateswarlu, B. Natesh Kumar, B. Prathima, K. Anitha, N.V. V Jyothi, A novel green synthesis of Fe_3O_4-Ag core shell recyclable nanoparticles using Vitis vinifera stem extract and its enhanced antibacterial performance, Phys. B Condens. Matter. 457 (2015) 30–35. https://doi.org/10.1016/j.physb.2014.09.007.

[140] A.R. Shahverdi, A. Fakhimi, H.R. Shahverdi, S. Minaian, Synthesis and effect of silver nanoparticles on the antibacterial activity of different antibiotics against Staphylococcus aureus and Escherichia coli, Nanomedicine Nanotechnology, Biol. Med. 3 (2007) 168–171. https://doi.org/10.1016/j.nano.2007.02.001.

[141] G.A. Martínez-Castañón, N. Niño-Martínez, F. Martínez-Gutierrez, J.R. Martínez-Mendoza, F. Ruiz, Synthesis and antibacterial activity of silver nanoparticles with different sizes, J. Nanoparticle Res. 10 (2008) 1343–1348. https://doi.org/10.1007/s11051-008-9428-6.

[142] V.K. Sharma, R.A. Yngard, Y. Lin, Silver nanoparticles: Green synthesis and their antimicrobial activities, Adv. Colloid Interface Sci. 145 (2009) 83–96. https://doi.org/10.1016/j.cis.2008.09.002.

[143] L. Zhang, Z. Wu, L. Chen, L. Zhang, X. Li, H. Xu, H. Wang, G. Zhu, Preparation of magnetic Fe_3O_4/TiO_2/Ag composite microspheres with enhanced photocatalytic activity, Solid State Sci. 52 (2016) 42–48. https://doi.org/10.1016/j.solidstatesciences.2015.12.006.

[144] H. Liang, H. Niu, P. Li, Z. Tao, C. Mao, J. Song, S. Zhang, Multifunctional Fe_3O_4@C@Ag hybrid nanoparticles : Aqueous solution preparation , characterization and photocatalytic activity, Mater. Res. Bull. 48 (2013) 2415–2419. https://doi.org/10.1016/j.materresbull.2013.02.066.

[145] J. Chen, Z. Guo, H. Wang, M. Gong, X. Kong, P. Xia, Q. Chen, Biomaterials Multifunctional Fe_3O_4@C@Ag hybrid nanoparticles as dual modal imaging probes and near-infrared light-responsive drug delivery platform, Biomaterials. 34 (2013) 571–581. https://doi.org/10.1016/j.biomaterials.2012.10.002.

[146] Y. Chi, Q. Yuan, Y. Li, L. Zhao, N. Li, X. Li, W. Yan, Magnetically separable Fe_3O_4@SiO_2@TiO_2-Ag microspheres with well-designed nanostructure and enhanced photocatalytic activity, J. Hazard. Mater. (2013). https://doi.org/10.1016/j.jhazmat.2013.08.077.

[147] R.G. Moharir, P.R. Gogate, V.K. Rathod, Process intensification of synthesis of magnetite using spinning disc reactor, Can. J. Chem. Eng. 90 (2012) 996–1005. https://doi.org/10.1002/cjce.20600.

[148] A.F. D'Intino, B. de Caprariis, M.L. Santarelli, N. Verdone, A. Chianese, Best operating conditions to produce hydroxyapatite nanoparticles by means of a spinning disc reactor, Front. Chem. Sci. Eng. 8 (2014) 156–160. https://doi.org/10.1007/s11705-014-1427-9.

[149] N. Smith, C.L. Raston, M. Saunders, R. Woodward, Synthesis of magnetic nanoparticles using spinning disc processing, 2006 NSTI Nanotechnol. Conf. Trade Show - NSTI

Nanotech 2006 Tech. Proc. 1 (2006) 343–346.

[150] L. Kvítek, J. Soukupova, Comment on “Preparation and antibacterial activity of Fe_3O_4@Ag nanoparticles,” Nanotechnology. 20 (2009) 18–20. https://doi.org/10.1088/0957-4484/20/2/028001.

[151] L.K. Mireles, E. Sacher, L. Yahia, S. Laurent, D. Stanicki, A comparative physicochemical, morphological and magnetic study of silane-functionalized superparamagnetic iron oxide nanoparticles prepared by alkaline coprecipitation, Int. J. Biochem. Cell Biol. 75 (2016) 203–211. https://doi.org/10.1016/j.biocel.2015.12.002.

[152] D.R. Baer, The Chameleon effect: Characterization challenges due to the variability of nanoparticles and their surfaces, Front. Chem. 6 (2018) 1–7. https://doi.org/10.3389/fchem.2018.00145.

[153] D.R. Baer, M.H. Engelhard, G.E. Johnson, J. Laskin, J. Lai, K. Mueller, P. Munusamy, S. Thevuthasan, H. Wang, N. Washton, A. Elder, B.L. Baisch, A. Karakoti, S.V.N.T. Kuchibhatla, D. Moon, Surface characterization of nanomaterials and nanoparticles: Important needs and challenging opportunities, J. Vac. Sci. Technol. A Vacuum, Surfaces, Film. 31 (2013) 050820. https://doi.org/10.1116/1.4818423.

[154] R. França, X.F. Zhang, T. Veres, L. Yahia, E. Sacher, Core-shell nanoparticles as prodrugs: Possible cytotoxicological and biomedical impacts of batch-to-batch inconsistencies, J. Colloid Interface Sci. 389 (2013) 292–297. https://doi.org/10.1016/j.jcis.2012.08.065.

[155] A.S. Karakoti, P. Munusamy, K. Hostetler, V. Kodali, S. Kuchibhatla, G. Orr, J.G. Pounds, J.G. Teeguarden, B.D. Thrall, D.R. Baer, Preparation and characterization challenges to understanding environmental and biological impacts of ceria nanoparticles, Surf. Interface Anal. 44 (2012) 882–889. https://doi.org/10.1002/sia.5006.

[156] J. Bratby, Coagulation and Flocculation in Water and Wastewater Treatment, Third, IWA Publishing, 2016.

[157] T.F. Tadros, Topics in Colloid and Interface Science Colloids in Agrochemicals Self-Organized Surfactant Structures Emulsion Science and Technology Rheology of Dispersions Colloids in Cosmetics and Personal Care Colloids in Paints, 2012.

[158] W. Sha, X. Wu, K.G. Keong, Electroless copper and nickel-phosphorus plating, Woodhead Publishing Limited, Cambridge, 2011.

[159] B. Lv, Y. Xu, H. Tian, D. Wu, Y. Sun, Synthesis of $Fe_3O_4SiO_2Ag$ nanoparticles and its application in surface-enhanced Raman scattering, J. Solid State Chem. 183 (2010) 2968–2973. https://doi.org/10.1016/j.jssc.2010.10.001.

[160] T. Kikuchi, T. Uchida, Calorimetric method for measuring high ultrasonic power using water as a heating material, J. Phys. Conf. Ser. 279 (2011). https://doi.org/10.1088/1742-6596/279/1/012012.

[161] M. Faraji, Y. Yamini, M. Rezaee, Magnetic nanoparticles: Synthesis, stabilization, functionalization, characterization, and applications, J. Iran. Chem. Soc. 7 (2010) 1–37. https://doi.org/10.1007/BF03245856.

[162] W.A. Woishnis, S. Ebnesajjad, Chemical Resistance of Specialty Thermoplastics, 2012. https://doi.org/10.1016/b978-1-4557-3110-7.00021-x.

[163] Chemical resistance guide, Chemline Plast. (2008). www.chemline.com.

[164] J. Suntivich, H.A. Gasteiger, N. Yabuuchi, Y. Shao-Horn, Electrocatalytic Measurement Methodology of Oxide Catalysts Using a Thin-Film Rotating Disk Electrode, J. Electrochem. Soc. 157 (2010) B1263. https://doi.org/10.1149/1.3456630.

[165] G.Y. Gao, D.J. Guo, H.L. Li, Electrocatalytic oxidation of formaldehyde on palladium nanoparticles supported on multi-walled carbon nanotubes, J. Power Sources. 162 (2006) 1094–1098. https://doi.org/10.1016/j.jpowsour.2006.07.057.

[166] G. V. Zhutaeva, M.R. Tarasevich, M. V. Radina, I.S. Chernyshova, Composites based on phenyl substituted cobalt porphyrins with Nafion as catalysts for oxygen electroreduction, Russ. J. Electrochem. 45 (2009) 1080–1088. https://doi.org/10.1134/S1023193509090146.

[167] Y. Yu, G. Wei, X. Hu, H. Ge, Z. Yu, The effect of magnetic fields on the electroless deposition of Co–W–P film, Surf. Coatings Technol. 204 (2010) 2669–2676. https://doi.org/10.1016/j.surfcoat.2010.02.020.

[168] T. Xuan, L. Zhang, Q. Huang, Crystallization behavior of electroless Co-Ni-B alloy plated in magnetic field in presence of cerium, Trans. Nonferrous Met. Soc. China. 16 (2006) 363–367. https://doi.org/10.1016/S1003-6326(06)60062-9.

[169] C.C. Lee, T.C. Chou, Effects of magnetic field on the electroless nickel/cobalt deposition,

Ind. Eng. Chem. Res. 37 (1998) 1815–1820. https://doi.org/10.1021/ie970706a.

[170] S. L. Brandow, M.-S. Chen, T. Wanq, C.S. Dulcey, J.M. Caivert, J.F. Bohland, G.S. Calcthrese, W. Dressick, Size-Controlled Colloidal Pd(II) Catalysts for Electroless Ni Deposition in Nanolithography Applications, J. Electrochem. Soc. 144 (1997) 3425–3434.

[171] X. Xue, E.P. Furlani, Template-assisted nano-patterning of magnetic core-shell particles in gradient fields, Phys. Chem. Chem. Phys. 16 (2014) 13306–13317. https://doi.org/10.1039/c4cp01563k.

[172] C.H. Chang, C.W. Tan, J. Miao, G. Barbastathis, Self-assembled ferrofluid lithography: Patterning micro and nanostructures by controlling magnetic nanoparticles, Nanotechnology. 20 (2009). https://doi.org/10.1088/0957-4484/20/49/495301.

[173] A. Goldman, Handbook of Modern Magnetic Ferromagnetic Materials, Springer Science & Business Media, 1999.

[174] Y. Ren, B. Lai, Comparative study on the characteristics, operational life and reactivity of Fe/Cu bimetallic particles prepared by electroless and displacement plating process, RSC Adv. 6 (2016) 58302–58314. https://doi.org/10.1039/c6ra11255b.

[175] N. Fritz, H.-C. Koo, Z. Wilson, E. Uzunlar, Z. Wen, X. Yeow, S.A. Bidstrup Allen, P.A. Kohl, Electroless Deposition of Copper on Organic and Inorganic Substrates Using a Sn⁄Ag Catalyst, J. Electrochem. Soc. 159 (2012) D386–D392. https://doi.org/10.1149/2.099206jes.

[176] R.H. Guo, S.Q. Jiang, C.W.M. Yuen, M.C.F. Ng, An alternative process for electroless copper plating on polyester fabric, J. Mater. Sci. Mater. Electron. 20 (2009) 33–38. https://doi.org/10.1007/s10854-008-9594-4.

[177] R. Ghosh Chaudhuri, S. Paria, Core/shell nanoparticles: classes, properties, synthesis mechanisms, characterization, and applications., Chem. Rev. 112 (2012) 2373–433. https://doi.org/10.1021/cr100449n.

[178] M. Kohtoku, H. Honma, O. Takai, Electroless Plating Catalyst Performance of a Cationic Moiety Bearing Palladium Complex, J. Electrochem. Soc. 161 (2014) D806–D812. https://doi.org/10.1149/2.0861414jes.

[179] R.M. Cornell, U. Schwertmann, The iron oxides: structure, properties, reactions,

occurrences and uses: second ed., 2003. https://doi.org/10.1002/3527602097.

[180] T. Ahn, J.H. Kim, H.M. Yang, J.W. Lee, J.D. Kim, Formation pathways of magnetite nanoparticles by coprecipitation method, J. Phys. Chem. C. 116 (2012) 6069–6076. https://doi.org/10.1021/jp211843g.

[181] D.K. Kim, Y. Zhang, W. Voit, K. V Rao, M. Muhammed, Synthesis and characterization of surfactant-coated superparamagnetic monodispersed iron oxide nanoparticles, 225 (2001) 30–36.

[182] M. Aliahmad, N. Nasiri Moghaddam, Synthesis of maghemite (γ-Fe_2O_3) nanoparticles by thermal-decomposition of magnetite (Fe_3O_4) nanoparticles, Mater. Sci. Pol. 31 (2013) 264–268. https://doi.org/10.2478/s13536-012-0100-6.

[183] O.P. Perez, Y. Umetsu, ORP-monitored magnetite formation from aqueous solutions at low temperatures, Hydrometallurgy. 55 (2000) 35–56.

[184] C.M. Ng, P.C. Chen, S. Manickam, Green High-Gravitational Synthesis of Silver Nanoparticles Using a Rotating Packed Bed Reactor (RPBR), Ind. Eng. Chem. Res. 51 (2012) 5375–5381.

[185] J. Sun, S. Zhou, P. Hou, Y. Yang, J. Weng, L. Xiaohong, M. Li, Synthesis and characterization of biocompatible Fe_3O_4 nanoparticles, J. Biomed. Mater. Res. Part A. 80 (2006) 333–341. https://doi.org/10.1002/jbm.a.

[186] L. Fu, V.P. Dravid, D.L. Johnson, Self-assembled (SA) bilayer molecular coating on magnetic nanoparticles, Appl. Surf. Sci. 181 (2001) 173–178.

[187] I. Martínez-Mera, M.E. Espinosa-Pesqueira, R. Pérez-Hernández, J. Arenas-Alatorre, Synthesis of magnetite (Fe_3O_4) nanoparticles without surfactants at room temperature, Mater. Lett. 61 (2007) 4447–4451. https://doi.org/10.1016/j.matlet.2007.02.018.

[188] Y. Wei, B. Han, X. Hu, Y. Lin, X. Wang, X. Deng, Synthesis of Fe_3O_4 nanoparticles and their magnetic properties, Procedia Eng. 27 (2012) 632–637. https://doi.org/10.1016/j.proeng.2011.12.498.

[189] J. Lu, X. Jiao, D. Chen, W. Li, Solvothermal Synthesis and Characterization of Fe_3O_4 and gamma-Fe_2O_3 nanoplates, J. Phys. Chem. C. 113 (2009) 4012–4017. https://doi.org/10.3788/cjl201643.0106006.

[190] Q. Li, C.W. Kartikowati, S. Horie, T. Ogi, T. Iwaki, K. Okuyama, Correlation between particle size/domain structure and magnetic properties of highly crystalline Fe_3O_4 nanoparticles, Sci. Rep. 7 (2017) 1–4. https://doi.org/10.1038/s41598-017-09897-5.

[191] D. Cao, H. Li, L. Pan, J. Li, X. Wang, P. Jing, X. Cheng, W. Wang, J. Wang, Q. Liu, High saturation magnetization of γ-Fe_2O_3 nano-particles by a facile one-step synthesis approach, Sci. Rep. 6 (2016) 1–9. https://doi.org/10.1038/srep32360.

[192] R.E. Litchfield, J. Graves, M. Sugden, D.A. Hutt, A. Cobley, Functionalised copper nanoparticles as catalysts for electroless plating, Proc. 16th Electron. Packag. Technol. Conf. EPTC 2014. (2014) 235–240. https://doi.org/10.1109/EPTC.2014.7028381.

[193] K.A. Wills, K. Krzyzak, J. Bush, J.E. Graves, C. Hunt, Additive process for patterned metallized conductive tracks on cotton with applications in smart textiles, J. Text. Inst. 5000 (2018) 0. https://doi.org/10.1080/00405000.2017.1340822.

[194] A. Amarjargal, L.D. Tijing, I.T. Im, C.S. Kim, Simultaneous preparation of Ag/Fe_3O_4 core-shell nanocomposites with enhanced magnetic moment and strong antibacterial and catalytic properties, Chem. Eng. J. 226 (2013) 243–254. https://doi.org/10.1016/j.cej.2013.04.054.

[195] T. Ugur, Y. Gundogdu, I.H. Boyaci, K. Pekmez, Synthesis of magnetic core – shell Fe_3O_4 – Au nanoparticle for biomolecule immobilization and detection, J. Nanoparticle Res. 12 (2010) 1187–1196. https://doi.org/10.1007/s11051-009-9749-0.

[196] L. Wang, J. Luo, Q. Fan, M. Suzuki, I.S. Suzuki, M.H. Engelhard, Y. Lin, N. Kim, J.Q. Wang, C.J. Zhong, Monodispersed core-shell Fe_3O_4@Au nanoparticles, J. Phys. Chem. B. 109 (2005) 21593–21601. https://doi.org/10.1021/jp0543429.

[197] B. Chudasama, A.K. Vala, N. Andhariya, R. V. Upadhyay, R. V. Mehta, Enhanced antibacterial activity of bifunctional Fe_3O_4-Ag core-shell nanostructures, Nano Res. 2 (2009) 955–965. https://doi.org/10.1007/s12274-009-9098-4.

[198] Y. Takasu, T. Iwazaki, W. Sugimoto, Y. Murakami, Size effects of platinum particles on the electro-oxidation of methanol in an aqueous solution of HClO4, Electrochem. Commun. 2 (2000) 671–674. https://doi.org/10.1016/S1388-2481(00)00101-6.

[199] W. Zhou, J.Y. Lee, Particle size effects in Pd-catalyzed electrooxidation of formic acid, J. Phys. Chem. C. 112 (2008) 3789–3793. https://doi.org/10.1021/jp077068m.

[200] A.H. Lu, E.L. Salabas, F. Schuth, Magnetic nanoparticles: Synthesis, protection, functionalization, and application, Angew. Chemie - Int. Ed. 46 (2007) 1222–1244. https://doi.org/10.1002/anie.200602866.

[201] F. Muller, W. Peukert, R. Polke, F. Stenger, Dispersing nanoparticles in liquids, Int. J. Miner. Process. 74 (2004) 31–41. https://doi.org/10.1016/j.minpro.2004.07.023.

[202] Y. Hwang, J.K. Lee, J.K. Lee, Y.M. Jeong, S. ir Cheong, Y.C. Ahn, S.H. Kim, Production and dispersion stability of nanoparticles in nanofluids, Powder Technol. 186 (2008) 145–153. https://doi.org/10.1016/j.powtec.2007.11.020.

[203] J.H. Fendler, Colloid Chemical Approach to Nanotechnology, Korean J. Chem. Eng. 18 (2001) 1–13. https://doi.org/10.1007/BF02707191.

[204] B. Zhao, Z. Nan, Enhancement of electric conductivity by incorporation of Ag into core/shell structure of Fe_3O_4/Ag/PPy NPs, Mater. Sci. Eng. C. 32 (2012) 804–810. https://doi.org/10.1016/j.msec.2012.01.030.

[205] K.J. Carroll, D.M. Hudgins, S. Spurgeon, K.M. Kemner, B. Mishra, M.I. Boyanov, L.W. Brown, M.L. Taheri, E.E. Carpenter, One-pot aqueous synthesis of Fe and Ag core/shell nanoparticles, Chem. Mater. 22 (2010) 6291–6296. https://doi.org/10.1021/cm101996u.

[206] C. Wu, B.P. Mosher, K. Lyons, T. Zeng, Reducing ability and mechanism for polyvinylpyrrolidone (PVP) in silver nanoparticles synthesis, J. Nanosci. Nanotechnol. 10 (2010) 2342–2347. https://doi.org/10.1166/jnn.2010.1915.

[207] Y. Zhang, J.Y. Liu, S. Ma, Y.J. Zhang, X. Zhao, X.D. Zhang, Z.D. Zhang, Synthesis of PVP-coated ultra-small Fe3O4 nanoparticles as a MRI contrast agent, J. Mater. Sci. Mater. Med. 21 (2010) 1205–1210. https://doi.org/10.1007/s10856-009-3881-3.

[208] Y. Gao, P. Jiang, D.F. Liu, H.J. Yuan, X.Q. Yan, Z.P. Zhou, J.X. Wang, L. Song, L.F. Liu, W.Y. Zhou, G. Wang, C.Y. Wang, S.S. Xie, Evidence for the Monolayer Assembly of Poly(vinylpyrrolidone) on the Surfaces of Silver Nanowires, J. Phys. Chem. B. 108 (2004) 12877–12881.

[209] C.L. Lee, C.C. Syu, Ag nanoparticle as a new activator for catalyzing electroless copper bath with 2,2′-bipyridyl, Electrochim. Acta. 56 (2011) 8880–8883. https://doi.org/10.1016/j.electacta.2011.07.110.

[210] Z. Wang, H. Zhu, X. Wang, F. Yang, X. Yang, One-pot green synthesis of biocompatible arginine-stabilized magnetic nanoparticles, Nanotechnology. 20 (2009). https://doi.org/10.1088/0957-4484/20/46/465606.

[211] A. Dalvand, R. Nabizadeh, M. Reza, M. Khoobi, Modeling of Reactive Blue 19 azo dye removal from colored textile wastewater using L-arginine-functionalized Fe_3O_4 nanoparticles: Optimization , reusability , kinetic and equilibrium studies, J. Magn. Magn. Mater. 404 (2016) 179–189. https://doi.org/10.1016/j.jmmm.2015.12.040.

[212] A. Ebrahiminezhad, Y. Ghasemi, S. Rasoul-Amini, J. Barar, S. Davaran, Impact of amino-acid coating on the synthesis and characteristics of iron-oxide nanoparticles (IONs), Bull. Korean Chem. Soc. 33 (2012) 3957–3962. https://doi.org/10.5012/bkcs.2012.33.12.3957.

[213] Y. Lai, W. Yin, J. Liu, R. Xi, J. Zhan, One-pot green synthesis and bioapplication of l-arginine-capped superparamagnetic Fe_3O_4 nanoparticles, Nanoscale Res. Lett. 5 (2010) 302–307. https://doi.org/10.1007/s11671-009-9480-x.

[214] F. Wu, D. Liu, T. Wang, W. Li, X. Zhou, Different surface properties of l-arginine functionalized silver nanoparticles and their influence on the conductive and adhesive properties of nanosilver films, J. Mater. Sci. Mater. Electron. 26 (2015) 6781–6786. https://doi.org/10.1007/s10854-015-3289-4.

[215] B. Hu, S.B. Wang, K. Wang, M. Zhang, S.H. Yu, Microwave-assisted rapid facile “green” synthesis of uniform silver nanoparticles: Self-assembly into multilayered films and their optical properties, J. Phys. Chem. C. 112 (2008) 11169–11174. https://doi.org/10.1021/jp801267j.

[216] D.L. Green, S. Jayasundara, Y.F. Lam, M.T. Harris, Chemical reaction kinetics leading to the first Stober silica nanoparticles - NMR and SAXS investigation, J. Non. Cryst. Solids. 315 (2003) 166–179. https://doi.org/10.1016/S0022-3093(02)01577-6.

[217] Y. Wei, W. Deng, R.H. Chen, Effects of insoluble nano-particles on nanofluid droplet evaporation, Int. J. Heat Mass Transf. 97 (2016) 725–734. https://doi.org/10.1016/j.ijheatmasstransfer.2016.02.052.

[218] S. Magdassi, M. Grouchko, A. Kamyshny, Copper nanoparticles for printed electronics: Routes towards achieving oxidation stability, Materials (Basel). 3 (2010) 4626–4638.

https://doi.org/10.3390/ma3094626.

[219] Y. Li, Q. Lu, X. Qian, Z. Zhu, J. Yin, Preparation of surface bound silver nanoparticles on polyimide by surface modification method and its application on electroless metal deposition, Appl. Surf. Sci. 233 (2004) 299–306. https://doi.org/10.1016/j.apsusc.2004.03.235.

[220] Q. Fang, S. Xuan, W. Jiang, X. Gong, Yolk-like micro/nanoparticles with superparamagnetic iron oxide cores and hierarchical nickel silicate shells, Adv. Funct. Mater. 21 (2011) 1902–1909. https://doi.org/10.1002/adfm.201002191.

[221] A.G. Skirtach, B.G. De Geest, A. Mamedov, A.A. Antipov, N.A. Kotov, G.B. Sukhorukov, Ultrasound stimulated release and catalysis using polyelectrolyte multilayer capsules, J. Mater. Chem. 17 (2007) 1050–1054. https://doi.org/10.1039/b609934c.

[222] S. Ozkar, Enhancement of catalytic activity by increasing surface area in heterogeneous catalysis, Appl. Surf. Sci. 256 (2009) 1272–1277. https://doi.org/10.1016/j.apsusc.2009.10.036.

[223] B. Wang, W. Zhang, W. Zhang, C. Yu, G. Wang, L. Huang, A.S. Mujumdar, Influence of drying processes on agglomeration and grain diameters of magnesium oxide nanoparticles, Dry. Technol. 25 (2007) 715–721. https://doi.org/10.1080/07373930701291108.

[224] H. Urch, M. Vallet-Regi, L. Ruiz, J.M. Gonzalez-Calbet, M. Epple, Calcium phosphate nanoparticles with adjustable dispersability and crystallinity, J. Mater. Chem. 19 (2009) 2166–2171. https://doi.org/10.1039/b810026h.

[225] G. Ghosh, M. Kanti Naskar, A. Patra, M. Chatterjee, Synthesis and characterization of PVP-encapsulated ZnS nanoparticles, Opt. Mater. (Amst). 28 (2006) 1047–1053. https://doi.org/10.1016/j.optmat.2005.06.003.

[226] I.M. Mahbubul, R. Saidur, M.A. Amalina, E.B. Elcioglu, T. Okutucu-ozyurt, Effective ultrasonication process for better colloidal dispersion of nanofluid, Ultrason. Sonochem. 26 (2015) 361–369. https://doi.org/10.1016/j.ultsonch.2015.01.005.

[227] D. Mahl, J. Diendorf, W. Meyer-zaika, M. Epple, Possibilities and limitations of different analytical methods for the size determination of a bimodal dispersion of metallic nanoparticles, Colloids Surfaces A Physicochem. Eng. Asp. 377 (2011) 386–392.

https://doi.org/10.1016/j.colsurfa.2011.01.031.

[228] C.M. Hoo, N. Starostin, P. West, M.L. Mecartney, A comparison of atomic force microscopy (AFM) and dynamic light scattering (DLS) methods to characterize nanoparticle size distributions, J. Nanoparticle Res. 10 (2008) 89–96. https://doi.org/10.1007/s11051-008-9435-7.

[229] G. Bryant, J.C. Thomas, Improved Particle Size Distribution Measurements Using Multiangle Dynamic Light Scattering, Langmuir. 11 (1995) 2480–2485. https://doi.org/10.1021/la00007a028.

[230] P.S. Sidhu, R.J. Gilkes, R.M. Cornell, A.M. Posner, J.P. Quirk, Dissolution of iron oxides and oxyhydroxides in hydrochloric and perchloric acids, Clays Clay Miner. 29 (1981) 269–276. https://doi.org/10.1346/CCMN.1981.0290404.

[231] P.R. Gaines, ICP Operations Guide A Guide for using ICP-OES and ICP-MS, Inorg. Ventur. (2011) 44.

[232] N.V. Long, C.M. Thi, M. Nogami, M. Ohtaki, Novel issues of morphology, size, and structure of Pt nanoparticles in chemical engineering: Surface attachment, aggregation or agglomeration, assembly, and structural changes, New J. Chem. 36 (2012) 1320–1334. https://doi.org/10.1039/c2nj40027h.

[233] X.S. Shen, G.Z. Wang, X. Hong, W. Zhu, Nanospheres of silver nanoparticles: agglomeration, surface morphology control and application as SERS substrates, Phys. Chem. Chem. Phys. 11 (2009) 7348–7349. https://doi.org/10.1039/b913171j.

[234] J. Perelaer, C.E. Hendriks, A.W.M. De Laat, U.S. Schubert, One-step inkjet printing of conductive silver tracks on polymer substrates, Nanotechnology. 20 (2009) 165303. https://doi.org/10.1088/0957-4484/20/16/165303.

[235] W.J. Dressick, C.S. Dulcey, J.H. Georger, G.S. Calabrese, J.M. Calvert, Covalent Binding of Pd Catalysts to Ligating Self-Assembled Monolayer Films for Selective Electroless Metal Deposition, J. Electrochem. Soc. 141 (1994) 210–220. https://doi.org/10.1149/1.2054686.

[236] S. Palacin, P.C. Hidber, J.P. Bourgoin, C. Miramond, C. Fermon, G.M. Whitesides, Patterning with magnetic materials at the micron scale, Chem. Mater. 8 (1996) 1316–1325. https://doi.org/10.1021/cm950587u.

[237] J. Zhang, T. Zhou, Y. Xie, L. Wen, Exposing Metal Oxide with Intrinsic Catalytic Activity by Near-Infrared Pulsed Laser: Laser-Induced Selective Metallization on Polymer Materials, Adv. Mater. Interfaces. 4 (2017) 1–10. https://doi.org/10.1002/admi.201700937.

[238] W.J. Dressick, C.S. Dulcey, J.H. Georger, G.S. Calabrese, J.M. Calvert, Covalent Binding of Pd Catalysts to Ligating Self-Assembled Monolayer Films for Selective Electroless Metal Deposition, Electrochem. Soc. Electron Microsc. N. H. Pub. Co. Curr. Top. Mater. Sci. 141 (1994) 210–220.

[239] M. V Meissner, N. Spengler, D. Mager, N. Wang, S.Z. Kiss, J. Höfflin, P.T. While, J.G. Korvink, Ink-jet printing technology enables self-aligned mould patterning for electroplating in a single step, J. Micromechanics Microengineering. 25 (2015) 065015. https://doi.org/10.1088/0960-1317/25/6/065015.

[240] D. Zabetakis, W.J. Dressick, Selective electroless metallization of patterned polymeric films for lithography applications, ACS Appl. Mater. Interfaces. 1 (2009) 4–25. https://doi.org/10.1021/am800121d.

[241] U. Banerjee, P. Bit, Aggregation dynamics of particles in a microchannel due to an applied magnetic field, Microfluid Nanofluid, (2012) 565–577. https://doi.org/10.1007/s10404-012-1053-0.

[242] M. Goosey, M. Poole, An introduction to high performance laminates and the importance of using optimised chemical processes in PCB fabrication, Circuit World. 30 (2004) 34–39. https://doi.org/10.1108/03056120410539894.

[243] E. Uzunlar, Z. Wilson, P.A. Kohl, Electroless Copper Deposition Using Sn/Ag Catalyst on Epoxy Laminates, J. Electrochem. Soc. 160 (2013) D3237–D3246. https://doi.org/10.1149/2.039312jes.

Appendix

A. The details of the research ethics

Project information

Content removed on data protection grounds

Content removed on data protection grounds

Content removed on data protection grounds

Content removed on data protection grounds

Content removed on data protection grounds